Imperial College London

Blast performance of composite sandwich structures with hybrid laminate skins

Emily Louise Rolfe

Department of Mechanical Engineering

Imperial College London

A thesis submitted for the degree of Doctor of Philosophy
of Imperial College London and the Diploma of Imperial College

May 2019

Abstract

This research project has investigated the performance of composite sandwich panels with hybrid skins against air and underwater blast loading. The loads are equivalent to those that could arise from sea mine detonation. Composite sandwich materials offer many benefits over conventional ship building materials. However, due to their variability and subsequent unpredictability, widespread use of composite sandwich panels in structural applications across the naval industry has been slow. The panel variability and interactions between the various constituent materials can, however, be utilised. Hybrid composite skins aimed to increase the blast resilience of composite sandwich panels by promoting energy absorbing damage mechanisms caused by the differing skin materials.

Preliminary calculations and impact loading revealed the differences in panel performance that can be achieved by varying the hybrid skin layups. Placing glass-fibre as the outermost layer receiving the impact was shown to be beneficial. Additionally, it was advantageous to place carbon-fibre as the rearmost layer due to its high tensile strength and stiffness. These preliminary results were used to inform panel selection for full-scale blast testing. A number of full-scale air blast experiments were performed. Six types of composite sandwich panel were subjected to varying blast loads, benchmark conventional sandwich panels were tested where possible. The blast loads included large charges at large stand-off distances, small near-field charges as well as repeat blast loading. The experimental results revealed that hybrid composite panels with 50 % glass-fibre and 50 % carbon-fibre by volume achieve high blast resilience under the blast conditions tested. These 50:50 hybrids have the necessary strength and stiffness to prevent excessive skin or core damage whilst allowing an acceptable level of deflection. Under blast conditions, the presence of the two materials in the hybrid skin is the dominating factor. The layup of the hybrid skins has a minimal effect on overall performance. Instrumentation methods were extended compared to previous blast experiments. Spatial correlation between strain gauges mounted on the front skin and rear skin digital image corre-

lation strain was achieved and polyvinylidene fluoride gauges were used in a large scale blast environment. The repeatability of the experimental setup and method was demonstrated.

Lastly, one large scale underwater blast experiment was performed. Full-field panel response was recorded using digital image correlation. The results revealed the significant influence of water depth along with the severe deflection and damage sustained by the panel. Digital image correlation captured the underwater deflection profile of the panel from its initial position to the typically observed 'bath tub' shape for the first time. All experiments have demonstrated the significant blast resilience possessed by composite sandwich panels.

Acknowledgements

First and foremost I would like to thank my supervisor John Dear for giving me the opportunity to undertake this project and for all the support and guidance he has given me along the way. My thanks also go to Hari Arora for his immeasurable support, range expertise and good humour. This PhD would have been impossible without your help. I would also like to thank Rob Quinn who gave up a significant amount of time to help with my blast trials as well as Paul Hooper, who has provided technical expertise throughout. Thanks to Alex Sancho, Cihan Kaboglu, Jun Liu, Haibao Liu and George Irven for all your help with preparation for blast trials and other aspects of the project.

Secondly, my thanks go to Dr. Yapa Rajapakse at the Office of Naval Research (ONR) along with ONR Global for sponsoring this PhD and to the wider ONR Solid Mechanics family. It was a pleasure to be given this opportunity and to become involved in this research community. I would also like to thank EPSRC for supporting this PhD.

I am grateful to DNV GL and Centre for the Protection of National Infrastructure (CPNI) for allowing me to take part in a blast trial at RAF Spadeadam. Specifically I would like to thank Ian and Darren along with everyone else at the site who enabled a successful test. I would also like to thank Charles, Graeme, David and the entire team at Radnor Range Ltd for giving me the opportunity to use their test site. No job was too difficult for your team and I am very grateful for your perseverance. Thanks are also due to Mark Johnson from Slowmo Camera Ltd for his camera expertise and for introducing us to the guys at Radnor, and to Amy Johnson from GOM UK for her continued support in Digital Image Correlation.

I am grateful to all my friends at Imperial from both undergraduate and post-graduate days. I would like to thank Ruth and Suresh for their help in the labs over the years. Thanks are due to everyone in 506 and beyond, especially to Fabian for helping me move my panels so often.

Finally, I would like to thank my family. Ben and Alice, I hope this thesis helps to explain what I've been doing over the past few years! I am hugely grateful to my Mum and Dad for their unwavering support and encouragement. Lastly, thank you Rui for always putting a smile on my face at the end of each day.

Declarations

I, the author, declare that this work is my own unless otherwise stated, and any other contributions are appropriately acknowledged.

The copyright of this thesis rests with the author. Unless otherwise indicated, its contents are licensed under a Creative Commons Attribution-Non Commercial-No Derivatives 4.0 International Licence (CC BY-NC-ND).

Under this licence, you may copy and redistribute the material in any medium or format on the condition that; you credit the author, do not use it for commercial purposes and do not distribute modified versions of the work.

When reusing or sharing this work, ensure you make the licence terms clear to others by naming the licence and linking to the licence text.

Please seek permission from the copyright holder for uses of this work that are not included in this licence or permitted under UK Copyright Law.

Contents

List of Figures x

List of Tables xx

Nomenclature xxii

Acronyms xxvii

1 Introduction 1

1.1 Aims and Objectives . . . 3
1.2 Thesis Outline . . . 4
1.3 Published Literature . . . 5
1.3.1 Book Chapters . . . 5
1.3.2 Journal Articles . . . 6

2 Literature Review 7

2.1 Introduction . . . 7
2.2 Composites in Naval Structures . . . 8
2.3 Blast Testing of Composite Materials . . . 9
2.3.1 Air Blast Loading . . . 9
2.3.2 Underwater Blast Loading . . . 12
2.4 Post Blast Damage and Strength . . . 14
2.5 Hybrid Composite Structures . . . 17
2.5.1 Impact Testing of Hybrid Composites . . . 19
2.5.2 Blast Testing of Hybrid Composites . . . 21
2.6 Simulations of Blast Experiments . . . 21
2.6.1 Air Blast Simulation . . . 22
2.6.2 Underwater Blast Simulation . . . 24
2.6.3 Material Models . . . 26

2.7 Conclusion 27

3 Preliminary Analysis of Hybrid Composite Sandwich Panels 30
3.1 Introduction 30
3.2 Characterisation of Hybrid Face-Sheets 31
3.2.1 Laminate Stiffness 31
3.2.2 Sandwich Panel Stiffness 35
3.2.3 Micromechanics of Unidirectional Composites 36
3.2.4 Analytical Stiffness Results 37
3.2.5 Summary 42
3.3 High Velocity Hard Projectile Impact 43
3.3.1 Materials 44
3.3.2 Methods 47
3.3.3 Results 51
3.4 Post Impact Damage & Compression 63
3.4.1 Methods 63
3.4.2 Results 65
3.5 Discussion 69
3.6 Conclusion 72

4 Full Scale Air Blast Testing: Part 1 73
4.1 Introduction 73
4.2 Experimental 74
4.2.1 Materials 74
4.2.2 Methods 75
4.3 Results 85
4.3.1 Blast Wave Modelling 85
4.3.2 Data Filtering 87
4.3.3 Digital Image Correlation 87
4.3.4 Strain Gauges 95
4.3.5 Post Blast Damage Inspection 104
4.4 Discussion 107
4.4.1 Blast Wave Modelling and Work Done 107
4.4.2 Digital Image Correlation 108
4.4.3 Strain Gauge Data 109
4.4.4 Hybrid versus GFRP and CFRP 109

4.4.5 Post Blast Damage 110
4.5 Conclusion 110

5 Full Scale Air Blast Testing: Part 2 112
5.1 Introduction 112
5.2 Experimental 113
5.2.1 Materials 113
5.2.2 Methods 115
5.3 Results 122
5.3.1 Blast Wave Modelling 122
5.3.2 Digital Image Correlation 125
5.3.3 Strain Gauges 138
5.3.4 Pressure Gauges 139
5.4 Post Blast Damage & Compression 148
5.4.1 Methods 148
5.4.2 Results 150
5.5 Discussion 166
5.5.1 Blast Wave Modelling and Work Done 166
5.5.2 Digital Image Correlation 168
5.5.3 Post Blast Damage & Strength 168
5.6 Conclusion 170

6 Full Scale Underwater Blast Testing 172
6.1 Introduction 172
6.2 Experimental 173
6.2.1 Materials 173
6.2.2 Methods 175
6.3 Results 178
6.3.1 Digital Image Correlation 178
6.3.2 Strain Gauges & PVDF Pressure Gauges 183
6.3.3 Comparison of Air and Underwater Blast 184
6.4 Post Blast Damage & Compression 185
6.4.1 Methods 185
6.4.2 Results 185
6.5 Discussion 191
6.5.1 Experimental Design 191

6.5.2 Digital Image Correlation 192
6.5.3 Post Blast Damage & Compression 193
6.6 Conclusion 194

7 Conclusions **195**
7.1 Preliminary Analysis of Hybrid Composites 196
7.2 Full Scale Air Blast Testing 197
7.3 Full Scale Underwater Blast Testing 200
7.4 Future Work 202
7.5 Research Impact 204

References **206**

A Supplementary Data **218**

B Digital Image Correlation Uncertainty **225**

List of Figures

1.1 Photographs showing: (a) the Swedish Visby Class Corvette [1], (b) the French La Fayette Class Frigate [2], (c) the British Type 45 Destroyer [3] and (d) the Norwegian Skjøld Class Corvette [4]. 3

3.1 Schematic diagram showing lamina coordinate systems for: (a) a layup orientation aligned with global coordinate system and applied stresses and (b) a layup orientation not aligned with global coordinate system. 33
3.2 Layup configurations of the seven hybrid composite sandwich panels analysed. 39
3.3 Layup configurations of the six hybrid composite sandwich panels fabricated for high velocity hard projectile impact. 44
3.4 Diagram showing the impact panel size, bolt hole locations and unsupported area of the panel. 48
3.5 Top down schematic view of the experimental gas gun test up. 48
3.6 Diagram of camera location calculations for 3D DIC. 50
3.7 Photographs from high speed cameras showing: (a) and (b) calibration panel from left and right cameras, (c) and (d) panel held in fixture with speckle pattern applied. 52
3.8 Full field out-of-plane displacement from DIC of all panel types under impact velocity 75 ± 3 m s^{-1}. 53
3.9 Central point out-of-plane displacement versus time plot under impact velocity 75 ± 3 m s^{-1}. 53
3.10 Central point major strain versus time plot under impact velocity 75 ± 3 m s^{-1}. 55
3.11 Central point major strain rate versus time plot under impact velocity 75 ± 3 m s^{-1}. 55

3.12 Central horizontal cross-section of GFRP panel showing: (a) outward out-of-plane deflection and (b) panel return under impact velocity 75 ± 3 m s^{-1}. 56
3.13 Central horizontal cross-section of CFRP panel showing: (a) outward out-of-plane deflection and (b) panel return under impact velocity 75 ± 3 m s^{-1}. 56
3.14 Central horizontal cross-section of Hybrid-1A panel showing: (a) outward out-of-plane deflection and (b) panel return under impact velocity 75 ± 3 m s^{-1}. 57
3.15 Central horizontal cross-section of Hybrid-2 panel showing: (a) outward out-of-plane deflection and (b) panel return under impact velocity 75 ± 3 m s^{-1}. 57
3.16 Central point out-of-plane displacement versus time plot under impact velocity 90 ± 3 m s^{-1}. 59
3.17 Central point major strain versus time plot under impact velocity 90 ± 3 m s^{-1}. 59
3.18 Central point displacement and velocity for Hybrid-1B under impact velocity 90 ± 3 m s^{-1}. 60
3.19 Central horizontal cross-section of GFRP panel showing: (a) outward out-of-plane deflection and (b) panel return under impact velocity 90 ± 3 m s^{-1}. 60
3.20 Central horizontal cross-section of CFRP panel showing: (a) outward out-of-plane deflection and (b) panel return under impact velocity 90 ± 3 m s^{-1}. 61
3.21 Central horizontal cross-section of Hybrid-1A panel showing: (a) outward out-of-plane deflection and (b) panel return under impact velocity 90 ± 3 m s^{-1}. 61
3.22 Central horizontal cross-section of Hybrid-2 panel showing: (a) outward out-of-plane deflection and (b) panel return under impact velocity 90 ± 3 m s^{-1}. 61
3.23 Damage mapping of the front view and section view of Hybrid-1A panel after impact velocity 75 ± 3 m s^{-1}. 64
3.24 Schematic of the edgewise compression test method. 66
3.25 Effective compressive modulus for the hybrid panels following impact. 70
3.26 Maximum compressive stress for the hybrid panels following impact. . 70

4.1 Layup configurations of the two types of hybrid composite sandwich panel fabricated for full-scale air blast testing. Two Hybrid-1A panels and two Hybrid-2 panels were constructed. 75
4.2 Experimental setup showing: (a) a photograph of two hybrid composite sandwich panels bolted side-by-side onto the front of a steel cubicle and (b) a schematic diagram of the test pad setup. 77
4.3 Camera setup for the full scale air blast experiments showing: (a) a schematic diagram of the camera setup within the cubicle and (b) a photograph of the SAX2 cameras mounted vertically. 82
4.4 Photographs from the SAX2 high-speed cameras showing the calibration cross and speckle pattern from the bottom and top cameras. . . 82
4.5 Strain gauge locations used on panels Hybrid-1A(1) and Hybrid-2(1) showing: (a) a schematic diagram of the locations and (b) a photograph of Hybrid-2(1) once fully instrumented with strain gauges. . . . 84
4.6 Schematic diagram of (a) two-wire quarter-bridge strain gauge circuit and (b) three-wire quarter-bridge strain gauge circuit. 84
4.7 Diagram of the panel setup highlighting the area over which pressure distribution was modelled. 86
4.8 Comparison of reflected overpressure distribution across the panel. . . 86
4.9 Strain gauge data versus time shown as raw data and with moving average low pass filter applied. 88
4.10 Photographs showing the test pad setup and the progression of the blast wavefront. 88
4.11 Central out-of-plane displacement against time for Hybrid-1A(1) with and without RBMC along with recorded reflected overpressure against time. 89
4.12 Deflection at time intervals for the horizontal centre section showing (a) outward deflection without RBMC, (b) return without RBMC, (c) outward deflection with RBMC and (d) return with RBMC. . . . 90
4.13 DIC results for Hybrid-1A(1) showing: (a) out-of-plane displacement and major strain images, (b) deflection at time intervals for the horizontal centre section and (c) rebound at time intervals for the horizontal centre section. 91

4.14 DIC results for Hybrid-1A(2) showing: (a) out-of-plane displacement and major strain images, (b) deflection at time intervals for the horizontal centre section and (c) rebound at time intervals for the horizontal centre section. 91
4.15 DIC results for Hybrid-2(1) showing: (a) out-of-plane displacement and major strain images, (b) deflection at time intervals for the horizontal centre section and (c) rebound at time intervals for the horizontal centre section. 92
4.16 DIC results for Hybrid-2(2) showing: (a) out-of-plane displacement and major strain images, (b) deflection at time intervals for the horizontal centre section and (c) rebound at time intervals for the horizontal centre section. 92
4.17 Central out-of-plane displacement against time for the four composite sandwich panels along with the recorded reflected overpressure against time. 94
4.18 Cumulative work done against time for the four composite sandwich panels. 95
4.19 Central y-direction strain taken from DIC data for the rear skin and strain gauge data for the front skin. 96
4.20 Central point major strain versus time plot taken from rear skin DIC data. 97
4.21 Comparison of strain gauge readings at different locations across panel Hybrid-1A(1) and Hybrid-2(1). 99
4.22 Comparison of DIC strain and strain gauge readings at different locations across panel Hybrid-1A(1). 101
4.23 Comparison of DIC strain and strain gauge readings at different locations across panel Hybrid-2(1). 102
4.24 Photographs showing the damage to the core of Hybrid-1A(1) as viewed from the bottom. 106
4.25 Photographs showing the damage to the core of Hybrid-2(1) as viewed from the bottom. 106
4.26 Schematic diagrams showing the location and extent of damage for (a) Hybrid-1A(1) and (b) Hybrid-2(1). 107

5.1 Layup configurations of the four types of composite sandwich panel fabricated for full-scale air blast testing. 113

5.2 Photographs of panels mounted on the cubicle showing: (a) large 1.39 m × 1.23 m panels and (b) small 0.8 m × 0.8 m panels. 117
5.3 Photograph showing the camera setup for full scale blast experiments. 121
5.4 Photograph showing the setup of the strain gauges and PVDF pressure gauge at the centre of each panel. 122
5.5 Diagram of the panel setup highlighting the area over which pressure distribution was modelled. 124
5.6 Comparison of reflected overpressure distribution across the panel for 8 kg PE4 at 8 m stand-off with pendine blocks and roof extension. . . 124
5.7 Comparison of reflected overpressure distribution across the panel for 8 kg PE4 at 8 m stand-off without pendine blocks and roof extension. 125
5.8 Photographs showing the detonation of the charge and progression of the blast wavefront. 126
5.9 DIC results for GFRP(1) showing: (a) out-of-plane displacement and major strain images, (b) deflection at time intervals for the horizontal centre section and (c) rebound at time intervals for the horizontal centre section. 127
5.10 DIC results for CFRP(1) showing: (a) out-of-plane displacement and major strain images, (b) deflection at time intervals for the horizontal centre section and (c) rebound at time intervals for the horizontal centre section. 127
5.11 DIC results for Hybrid-3B(1) showing: (a) out-of-plane displacement and major strain images, (b) deflection at time intervals for the horizontal centre section and (c) rebound at time intervals for the horizontal centre section. 128
5.12 Central out-of-plane displacement against time for the three composite sandwich panels along with the recorded side-on blast pressure against time. 129
5.13 Cumulative work done against time for the three composite sandwich panels in test series A. 131
5.14 DIC results for Hybrid-3B(2) under the first 8 kg PE7 charge showing: (a) out-of-plane displacement and major strain images, (b) deflection at time intervals for the horizontal centre section and (c) rebound at time intervals for the horizontal centre section. 133

5.15 DIC results for Hybrid-3B(2) under the second 8 kg PE7 charge showing: (a) out-of-plane displacement and major strain images, (b) deflection at time intervals for the horizontal centre section and (c) rebound at time intervals for the horizontal centre section. 133
5.16 DIC results for Hybrid-4(1) under the first 8 kg PE7 charge showing: (a) out-of-plane displacement and major strain images, (b) deflection at time intervals for the horizontal centre section and (c) rebound at time intervals for the horizontal centre section. 134
5.17 DIC results for Hybrid-4(1) under the second 8 kg PE7 charge showing: (a) out-of-plane displacement and major strain images, (b) deflection at time intervals for the horizontal centre section and (c) rebound at time intervals for the horizontal centre section. 134
5.18 Central out-of-plane displacement against time for the two composite sandwich panels against both blast loadings along with the recorded side-on blast pressure against time for the first blast load. 135
5.19 Central out-of-plane displacement against time for CFRP(2) with and without RBMC along with the recorded side-on blast pressure against time. 137
5.20 Central out-of-plane displacement against time for the two composite sandwich panels against both blast loadings along with the recorded side-on blast pressure against time for the first blast load. 137
5.21 Cumulative work done against time for the composite sandwich panels in test series B. 138
5.22 Recorded static side-on pressure and calculated impulse for each of the two trials using 30 kg PE7 charges at 10.5 m.. 140
5.23 Recorded reflected overpressure at the centre of each panel from PVDF gauges along with reflected overpressure calculated from static pressure recorded by side-on gauge. 141
5.24 Recorded static side-on pressure and calculated impulse for each of the four trials using 8 kg PE7 charges at 8 m. 142
5.25 Recorded reflected overpressure at the centre of each panel from PVDF gauges along with reflected overpressure calculated from static pressure recorded by side-on gauge. 145
5.26 Recorded reflected overpressure at the centre of each panel from PVDF gauges along with reflected overpressure calculated from static pressure recorded by side-on gauge. 145

5.27 Photograph showing the setup for quasi-static compression test using Instron machine and DSLR camera. 150
5.28 Photographs showing the front skin following blast of (a) GFRP(1), (b) CFRP(1) and (c) Hybrid-3B(1). 152
5.29 Photographs showing the damage to the core of Hybrid-3B(1) as viewed from the bottom. 153
5.30 Schematic diagram showing the location and extent of internal panel damage for (a) GFRP(1), (b) CFRP(1) and (c) Hybrid-3B(1). 153
5.31 Post-blast effective modulus for the specimen taken from GFRP(1), CFRP(1) and Hybrid-3B(1). 155
5.32 Post-blast maximum compressive stress for the ten specimen taken from GFRP(1), CFRP(1) and Hybrid-3B(1). 155
5.33 Post-blast effective modulus versus damage percentage for the specimen taken from GFRP(1), CFRP(1) and Hybrid-3B(1). 156
5.34 Post-blast maximum compressive stress versus damage percentage for the specimen taken from GFRP(1), CFRP(1) and Hybrid-3B(1). . . . 156
5.35 Post-blast damage analysis showing: (a) photograph of Hybrid-3B(1) specimen, (b) 2D cross-sectional view in relatively undamaged region and (c) cross-sectional view in highly damaged region. 157
5.36 Post-blast damage analysis showing: (a) photograph of GFRP(1) specimen, (b) 2D cross-sectional view across highly damaged region and (c) perpendicular cross-sectional view across highly damaged region. 158
5.37 Photographs showing the front skin following blast of (a) Hybrid-3B(2) and (b) Hybrid-4(1). 159
5.38 Photographs showing the damage to the core of Hybrid-4(1) as viewed from the bottom. 160
5.39 Schematic diagram showing the internal panel damage for (a) Hybrid-3B(2) and (b) Hybrid-4(1). 161
5.40 Post-blast effective modulus for the ten specimen taken from Hybrid-3B(2) and Hybrid-4(1). 163
5.41 Post-blast maximum compressive stress for the ten specimen taken from Hybrid-3B(2) and Hybrid-4(1). 163
5.42 Post-blast effective modulus versus damage percentage for the ten specimen taken from Hybrid-3B(2) and Hybrid-4(1). 164

5.43 Post-blast maximum compressive stress versus damage percentage for the ten specimen taken from Hybrid-3B(2) and Hybrid-4(1). 165
5.44 Post-blast effective modulus versus damage percentage for the specimen taken from Hybrid-3B(1) and Hybrid-3B(2). 165
5.45 Post-blast maximum compressive stress versus damage percentage for the specimen taken from Hybrid-3B(1) and Hybrid-3B(2). 166

6.1 Layup configuration of the hybrid composite sandwich panel fabricated for full-scale underwater blast testing. 174
6.2 Photograph showing cubicle and pendine concrete block setup whilst under construction. 176
6.3 Schematic diagram of the test setup showing: (a) view of setup from above and (b) side-on section view of setup. 176
6.4 Photograph showing the camera setup for the full-scale underwater blast experiment. 177
6.5 Photograph showing the setup of the strain gauges and PVDF pressure gauges whilst the enclosure was being filled with water. 179
6.6 Photograph showing the detonation of the charge and progression of the water column. 179
6.7 DIC image series of the out-of-plane displacement and major strain showing: (a) deflection at intervals of time, (b) short rebound and (c) second deflection. 180
6.8 DIC results for the vertical centre cross-section showing: (a) deflection at intervals of time, (b) short rebound and (c) second deflection. . . . 181
6.9 DIC results for the horizontal centre cross-section showing: (a) deflection at intervals of time, (b) short rebound and (c) second deflection. 182
6.10 Central out-of-plane displacement against time for Hybrid-4(2) during underwater blast loading along with calculated initial central point velocity against time. 183
6.11 Photographs showing the front skin following underwater blast of Hybrid-4(2). The red dashed boxes highlight the sections removed for edgewise compression testing. 187
6.12 Photographs showing the damage to the core and skins of Hybrid-4(2) following underwater blast. 187
6.13 Post-blast effective modulus versus damage percentage for the eight specimen taken from Hybrid-4(2). 188

6.14 Post-blast maximum compressive stress versus damage percentage for the eight specimen taken from Hybrid-4(2). 189
6.15 Post-blast effective modulus versus damage percentage for the specimen taken from Hybrid-4(1) and Hybrid-4(2). 190
6.16 Post-blast maximum compressive stress versus damage percentage for the specimen taken from Hybrid-4(1) and Hybrid-4(2). 191

A.1 Central horizontal cross-section of Hybrid-1B panel showing: (a) outward out-of-plane deflection and (b) panel return under impact velocity 75 ± 3 m s^{-1}. 218
A.2 Central horizontal cross-section of Hybrid-3B panel showing: (a) outward out-of-plane deflection and (b) panel return under impact velocity 75 ± 3 m s^{-1}. 218
A.3 Central horizontal cross-section of Hybrid-1B panel showing: (a) outward out-of-plane deflection and (b) panel return under impact velocity 90 ± 3 m s^{-1}. 219
A.4 Central horizontal cross-section of Hybrid-3B panel showing: (a) outward out-of-plane deflection and (b) panel return under impact velocity 90 ± 3 m s^{-1}. 219
A.5 Central out-of-plane velocity against time for the four composite sandwich panels under 100 kg nitromethane charge at 15 m stand-off. . . . 220
A.6 Comparison of reflected overpressure distribution across the panel for 30 kg PE4 at 10.5 m stand-off with pendine blocks and roof extension. 220
A.7 Comparison of reflected overpressure distribution across the panel for 30 kg PE4 at 10.5 m stand-off without pendine blocks and roof extension. 221
A.8 Central out-of-plane velocity against time for the three composite sandwich panels under 30 kg PE4 charge at 10.5 m stand-off. 221
A.9 DIC results for CFRP(2) under the first 8 kg PE7 charge showing: (a) out-of-plane displacement and major strain images, (b) deflection at time intervals for the horizontal centre section and (c) rebound at time intervals for the horizontal centre section. 222
A.10 DIC results for CFRP(2) under the second 8 kg PE7 charge showing: (a) out-of-plane displacement and major strain images, (b) deflection at time intervals for the horizontal centre section and (c) rebound at time intervals for the horizontal centre section. 222

A.11 DIC results for GFRP(2) under the first 8 kg PE7 charge showing: (a) out-of-plane displacement and major strain images, (b) deflection at time intervals for the horizontal centre section and (c) rebound at time intervals for the horizontal centre section. 223
A.12 DIC results for GFRP(2) under the second 8 kg PE7 charge showing: (a) out-of-plane displacement and major strain images, (b) deflection at time intervals for the horizontal centre section and (c) rebound at time intervals for the horizontal centre section. 223

List of Tables

3.1 Mechanical properties of the composite sandwich panels materials and plies. . . . 37
3.2 Laminate stiffness results in order of increasing number of carbon-fibre layers. . . . 39
3.3 Sandwich panel mechanical properites calculated using the panel stiffness method. . . . 41
3.4 Mechanical properties of the composite sandwich panels materials and plies. . . . 45
3.5 Properties of the six hybrid composite sandwich panels fabricated for high velocity hard projectile impact. . . . 47
3.6 Details of the characteristics of each panel under high velocity hard projectile impact. . . . 62
3.7 Extent of the damage in each panel under high velocity impact. . . . 67
3.8 Details of the damage in each panel under high velocity impact. . . . 68

4.1 Mechanical properties of the composite sandwich panel materials and plies. . . . 76
4.2 Properties of the two hybrid composite sandwich panels. . . . 76
4.3 Failure indices according to the analytical solution outlined by Andrews and Moussa [66]. . . . 79
4.4 Details of the camera models and frame rate for each panel. . . . 81
4.5 Summary of DIC analysis results. . . . 100
4.6 Summary of pressure results. . . . 103
4.7 Comparison of hybrid panels to previous glass-fibre and carbon-fibre panels. . . . 104
4.8 Damage sustained by two hybrid panels identified using visual inspection and photographs. . . . 106

5.1 Details of the panel types tested in each series. . . . 114

5.2 Mechanical properties of the composite sandwich panel materials and plies. . . . 116
5.3 Properties of the composite sandwich panels. . . . 116
5.4 Failure indices for the 1.39 m × 1.23 m GFRP panel against a 30 kg PE7 charge according to the analytical solution outlined by Andrews and Moussa [66]. . . . 118
5.5 Failure indices for the 1.39 m × 1.23 m Hybrid-3B panel against an 8 kg PE7 charge according to the analytical solution outlined by Andrews and Moussa [66]. . . . 119
5.6 Summary of pressure results for test series B. . . . 143
5.7 Summary of DIC analysis results for test series A. . . . 146
5.8 Summary of pressure results for test series A. . . . 147
5.9 Visual inspection of damage sustained by the panels subjected to 30 kg PE7 charge. . . . 151
5.10 Visual inspection of damage sustained by the panels subjected to 2 × 8 kg PE7 charge. . . . 160

6.1 Mechanical properties of the composite sandwich panel materials and plies. . . . 174
6.2 Damage sustained by Hybrid-4(2) following underwater blast testing identified using visual inspection. . . . 186

A.1 Test matrix detailing hybrid panel types in each experimental investigation. . . . 224

B.1 Summary of the uncertainty estimates for out-of-plane displacement and major strain. . . . 226

Nomenclature

$\overline{\boldsymbol{Q}}$	Transformed Stiffness Matrix
$\overline{\boldsymbol{Q}}_k$	Transformed Stiffness Matrix for kth Layer
$\boldsymbol{\sigma}_{xy_k}$	Stress Matrix in xy Plane for kth Layer
$\boldsymbol{\varepsilon}^0$	In-Plane Strain Matrix
$\boldsymbol{A}$	In-Plane Stiffness Matrix
$\boldsymbol{B}$	Bending-Extension Coupling Matrix
$\boldsymbol{C}$	Asymmetrical Bending-Extension Coupling Matrix
$\boldsymbol{D}$	Bending Stiffness Matrix
$\boldsymbol{K}$	Plate Curvature Matrix
$\boldsymbol{M}$	Moment Resultant Matrix
$\boldsymbol{N}$	Stress Resultant Matrix
$\boldsymbol{Q}$	Laminate Stiffness Matrix
η	Krenchel Factor
γ_{12}	Maximum Shear Strain
γ_{xy}^0	In-Plane Shear Strain in xy Plane
γ_{xy}^c	Shear Strain in xy Plane for Core
γ_{yz}^c	Shear Strain in yz Plane for Core
ν_{12}	Major Poisson's Ratio
ν_{12}	Minor Poisson's Ratio

ν_f	Fibre Poisson's Ratio
ν_m	Matrix Poisson's Ratio
$\overline{C}^c_{ij}$	Transformed Core Transverse Shear Constants Matrix for ith Row and jth Column
$\overline{Q}_{ij}$	Transformed Stiffness Matrix Component for ith Row and jth Column
ρ	Ply Density
ρ_f	Fibre Density
ρ_m	Matrix Density
ρ_o	Ambient Density
ρ_s	Density Behind the Wavefront
ρ_w	Water Density
σ	Ply Failure Strength
σ_1	Maximum Principal Stress
σ_2	Minimum Principal Stress
σ_f	Fibre Failure Strength
σ_m	Matrix Failure Strength
σ_{xy}	Stress in xy Plane
σ_{xz}	Stress in xz Plane
σ_x	Stress in x-direction
σ_{yz}	Stress in yz Plane
σ_y	Stress in y-direction
τ_{12}	Maximum Shear Stress
θ	Blast Wave Decay Time Constant
υ_f	Lamina Fibre Volume Fraction

ε_1	Maximum Principal Strain
ε_2	Minimum Principal Strain
ε_x	Strain in x-direction
ε_x^0	In-Plane Strain in x-direction
ε_y^0	In-Plane Strain in y-direction
A_{ij}	In-Plane Stiffness Matrix Component for ith Row and jth Column
a_o	Speed of Sound at Ambient Conditions in Air
B_{ij}	Bending-Extension Coupling Matrix Component for ith Row and jth Column
BV	Bridge Voltage or Excitation Voltage
C_{ij}	Asymmetrical Bending-Extension Coupling Matrix Component for ith Row and jth Column
c_w	Speed of Sound in Water
D_1	Perpendicular Distance between Panel and Centre of Camera Sensor
D_2	Distance between Centre of Camera Sensors
D_c	Distance from Centre of Panel to Centre of Camera Sensor
D_{ij}	Bending Stiffness Matrix Component for ith Row and jth Column
E	Ply Longitudinal Modulus
E_1	Elastic Modulus in Longitudinal Direction
E_2	Elastic Modulus in Transverse Direction
E_{eff}	Effective Edgewise Stiffness
E_f	Elastic Modulus of Fibres
E_m	Elastic Modulus of Matrix
E_x	Elastic Modulus in x-direction
F	Applied Force

F_{ij}	Core Shear Stiffness Matrix for ith Row and jth Column
G_{12}	Shear Modulus in the 1-2 Axes
G_f	Shear Modulus of Fibres
G_m	Shear Modulus of Matrix
GF	Gauge Factor
h	Core Thickness
h_k	Thickness for kth Laminate Layer
k	Layer Number
K_{xy}	Plate Curvature in xy Plane
K_x	Plate Curvature in x-direction
K_y	Plate Curvature in y-direction
l	Camera Lens Length
M_{xy}	Moment Resultant in xy Plane
M_x	Moment Resultant in x-direction
M_y	Moment Resultant in y-direction
n	Number of Layers in Laminate
n_1	Number of Layers in Lower Skin
n_2	Number of Layers in Upper Skin
N_{xy}	Stress Resultant in xy Plane
N_x	Stress Resultant in x-direction
N_y	Stress Resultant in y-direction
$P(t)$	Pressure Acting at Time t
P_L	Longest Panel Length
P_m	Maximum Pressure at Shock Wavefront

P_o	Ambient Pressure
P_r	Reflected Overpressure
P_s	Static Overpressure
Q_{ij}	Laminate Stiffness Matrix Component for ith Row and jth Column
Q_x	Shear Resulant in x-direction
Q_y	Shear Resultant in y-direction
R	Stand-Off Distance from Charge Centre
R_1	Strain Gauge Resistance
R_C	Resistance of Bridge Arm in Series with Strain Gauge
s	Camera Sensor Size
T	Natural Response of Panel
t	Time
t_d	Positive Phase Duration of Blast Pressure
u	Particle Velocity in Water
u_s	Blast Wavefront Velocity
V_0	Output Voltage
V_c	Volume of Matrix in Lamina
V_f	Volume of Fibres in Lamina
W	Charge Mass Expressed in kg of TNT
w	Specimen Width
x_{dyn}	Dynamic Panel Deflection
x_{st}	Static Panel Deflection
Z	Scaled Distance
z	Laminate Thickness

Acronyms

3D Three-Dimensional

AC Alternating Current

BNC Bayonet Neill-Concelman

BVID Barely Visible Impact Damage

C4 Composition 4

CAI Compression After Impact

CFD Computational Fluid Dynamics

CFRP Carbon-Fibre Reinforced Polymer

CPNI Centre for Protection of National Infrastructure

CST Conical Shock Tube

CT Computed Tomography

CTE Coefficient of Thermal Expansion

DC Direct Current

DIC Digital Image Correlation

DIN Deutsches Institut fur Normung

DLF Dynamic Load Factor

DMA Dynamic Mechanical Analysis

DNV Det Norske Veritas

DNV GL Det Norske Veritas Germanischer Lloyd

DSLR Digital Single-Lens Reflex

EHSAPT Extended High-Order Sandwich Panel Theory

FE Finite Element

FOV Field Of View

FRPC Fibre Reinforced Polymer Composite

FSI Fluid Structure Interaction

GFRP Glass-Fibre Reinforced Polymer

IR Infrared

LED Light-Emitting Diode

MCMV Mine Countermeasure Vessel

NDE Non-Destructive Evaluation

ONR Office of Naval Research

PE Polyethylene

PE4 Plastic Explosive 4

PE7 Plastic Explosive 7

PEI Poly-Ether-Imide

PET Polyethylene Terephthalate

PP Polypropylene

PU Polyurea

PVC Polyvinyl Chloride

PVDF Polyvinylidene Fluoride

RBMC Rigid Body Motion Compensation

RDX Research Division Explosive

SAN Styrene Acrylonitrile

TNT Trinitrotoluene

TTL Transistor-Transistor Logic

UHMWPE Ultra High Molecular Weight Polyethylene

VARTM Vacuum Assisted Resin Transfer Moulding

VID Visible Impact Damage

Chapter 1

Introduction

Composite materials are being adopted for an increasing number of engineering applications. There has been some reluctance, however, to adopt these new materials in the marine industry. The design, manufacture, maintenance and disposal methods of steel and aluminium, which have been the main shipbuilding materials for over a century, are well established. However, fibre-reinforced polymer composites (FRPCs) possess many advantages over metallic materials traditionally used. These advantages include low radar signature, high strength to weight ratio and corrosion or chemical attack resistance. These advantages lead to enhanced stealth properties, higher velocity or greater payload, and reduced maintenance costs, respectively. These are all benefits in the marine and particularly the naval industry. Durability, dielectricity, non-magnetism and thermal insulation are further advantages possessed by FRPCs. Finally, the design of a vessel can be optimised through careful orientation of the composite fibres and complex forms can be manufactured with relative ease. However, composites behave in a different manner to metallic materials. Further understanding of composite material behaviour is required to achieve the necessary performance and safety standards.

There are some unique requirements demanded of materials used in the military marine environment. The movement of the vessel in the water results in cyclic flexural loading. Wave slamming against the hull adds to this cyclic loading and can cause loading peaks. Impact is another important factor. The vessel hull could collide with rocks or other debris. Naval hulls are expected to perform and withstand the loads mentioned at a range of temperatures in the presence of seawater, freshwater and even ice. The presence of water can lead to faster corrosion and material degradation. The effect of temperature on composite material properties is also important to understand as they contain temperature sensitive polymers.

Finally, a significant threat to the structural integrity of a naval vessel is caused by blast loading. Both airborne and underwater attacks on a naval vessels are possible.

This research forms part of an international research programme funded by the Office of Naval Research (ONR), USA. The programme investigates all aspects of composite sandwich panel use in military marine applications including, but not limited to, the challenges detailed here. The research presented in this thesis investigates the blast performance of composite sandwich panels.

The threats faced by a naval vessel that cause blast loading can be categorised into torpedoes, missiles and sea mines. Torpedoes and missiles are usually guided and will detonate once in contact with the vessels. Effective protection from these threats is to avoid detection or to destroy the weapon or source. Certain naval mines are also detonated by contact. Physical contact between the mine and vessel results in a very severe load which is unrealistic to protect against. However, sea mines can also be detonated by a change in water pressure and acoustic or radio detection caused by the proximity of a ship. The medium between the charge and vessel significantly reduces the blast energy experienced by the vessel. The response of FRPC structures to blast loads caused by these influence mines are the focus of this research.

In order to simulate this threat, composite sandwich panels were tested in air and underwater blast scenarios. Air blast loading replicates floating or surface mines loading a vessel's hull or superstructure above the water line. Underwater blast loading represents subsurface mines loading a vessel's hull beneath the water line. Following blast testing, the strength and damage sustained by the materials was analysed. This was carried out to assess whether a vessel made from composite materials could continue in service following a blast load. The material would have to support the structural loads until the vessel could be repaired or return to harbour.

Composite materials have been used in numerous vessels, a selection of these are shown in Figure 1.1. The Swedish Visby class and Norwegian Skjøld class corvettes, which are both stealth fast attack vessels, use composite materials in both the hull and superstructure. Many larger ships, including the French La Fayette frigate and the US Navy Zumwalt Class destroyer, utilise composite materials in their superstructures. India is the latest navy to develop vessels with composite superstructures. Other vessels, such as the UK Royal Navy Type 45 destroyer, have adopted composite materials in masts and radomes as well as other secondary components to reduce both weight and radar signature. These examples show that the use of composite materials in naval vessels is largely limited to non-structural



Figure 1.1: Photographs showing: (a) the Swedish Visby Class Corvette [1], (b) the French La Fayette Class Frigate [2], (c) the British Type 45 Destroyer [3] and (d) the Norwegian Skjøld Class Corvette [4].

components. There is a large potential for weight savings, cost savings and increased vessel speed or range if composite materials are used more widely throughout the naval industry. Further confidence in these materials needs to be established to overcome concerns. This project considers composite materials for structural use in the ship hull and seeks to further the understanding of how composite materials behave under blast loading.

1.1 Aims and Objectives

The primary goal of this research project was to assess the benefits of using hybrid composite laminate skins in composite sandwich panels for naval hull and superstructure designs. During blast loading, the larger the allowable deflection, the larger the blast impulse that can be resisted by the panel [5]. The maximum allowable deflec-

tion depends on panel span and allowable damage level. An optimal design would enable maximum deflection whilst avoiding excessive damage. The combination of glass-fibre and carbon-fibre in hybrid laminate skins aimed to take advantage of the higher strain to failure of glass-fibre. This would lead to greater panel deflection. Furthermore, the interactions between the dissimilar fibrous materials aims to reduce catastrophic brittle failure and promote energy absorbing failure mechanisms such as delamination. Provided the damage sustained is within allowable limits, hybrid skins could lead to greater impulse resistance. Furthermore, stress waves travelling through a material are partially reflected and partially transmitted at the interface between two dissimilar materials. This highlights the potential effectiveness of laminated composites, and particularly hybrid composites. A stress wave can be partially reflected at a series of interfaces to avoid large tensile stresses which can develop on the rear surface of a target [5]. The effect of material layup and proportions were investigated during full scale air blast experiments. The hybrid composite sandwich panels were also subjected to repeat blast loads to determine whether they retained comparable integrity to conventional composite sandwich panels.

Another objective set out in this project was to establish an underwater blast experimental setup with 3-dimensional digital image correlation (3D DIC) implemented to record the full-field response of the panel. Previous underwater blast experiments have relied soley on strain and pressure gauge data to interpret panel behaviour. This novel data acquisition approach would reveal the full-field panel deflection profile.

Post-blast strength tests were performed on the panels to quantify whether the damage sustained by the hybrids was allowable or not. These tests were performed to simulate the continued use of composite panels in a naval structure following a blast load. Damage present in the skins or core would cause a significant decrease in stiffness and strength. Since the core was kept consistent throughout the large scale blast tests, the variation in results would be driven by the different composite laminate skins.

1.2 Thesis Outline

The thesis is divided into seven chapters. The research aims and objectives are introduced here. The second chapter provides a review of literature that is relevant to the research topic. The main body of the thesis is divided into four experimental chapters.

Chapter 3 describes preliminary calculations along with high velocity gas gun experiments investigating the impact performance of hybrid composite sandwich panels. The results and panel behaviour observed during these experiments led to material selections for Chapters 4, 5 and 6.

Chapter 4 details a large scale open-air blast trial conducted at RAF Spadeadam, Cumbria, UK. An explosive charge of 100 kg trinitrotoluene (TNT) equivalent was used to test four hybrid composite sandwich panels at 15 m stand-off distance. High-speed 3D DIC was used to track displacement and strain on the rear surface of the panels. Front surface panel strains were recorded using strain gauges.

Chapter 5 describes a series of blast trials performed at Radnor Range Ltd, Wales, UK. Explosive charges of 8 kg and 30 kg plastic explosive 7 (PE7) were used to test seven composite sandwich panels at either 8 m or 10.5 m stand-off distances. Once again, high-speed 3D DIC was implemented to track the panel response. Different composite sandwich panel layups were investigated and subjected to single or repeated blast loading.

Chapter 6 aimed to develop an underwater blast experiment with 3D DIC implemented to record full-field panel underwater response. The experiment was carried out at Radnor Range Ltd. The experimental setup was trialled and proved successful, however, aspects of the experimental design that could be improved are highlighted. Conclusions and topics for further investigation are given in Chapter 7.

1.3 Published Literature

The following list provides publications resulting from or relating to the research presented in this thesis, which the author has directly contributed to.

1.3.1 Book Chapters

E. Rolfe, M. Kelly, H. Arora, P. A. Hooper, and J. P. Dear, "Blast performance and damage assessment of composite sandwich structures", in *Blast Mitigation Strategies for Marine Composite and Sandwich structures*, S. Gopalakrishnan, Y. Rajapakse, Eds., Singapore: Springer Singapore, 2018, ISBN 978-981-10-7170-6.

H. Arora, E. Rolfe, M. Kelly, and J. P. Dear, "Full-scale air and underwater blast loading of composite sandwich panels", in *Explosive Blast Response of Composites*, A. Mouritz, Y. Rajapakse, Eds., Woodhead Publishing, 2017, Chapter 7, ISBN 978-0-08-102093-7.

E. Rolfe, M. Kelly, H. Arora, and J. P. Dear, "Composite materials for blast applications in air and underwater", in *Dynamic Response and Failure of Composite Materials*, V. Lopresto, A. Langella, S. Abrate, Eds., Woodhead Publishing, 2017, Chapter 9, ISBN 978-0-08-100902-4.

1.3.2 Journal Articles

E. Rolfe, M. Kelly, H. Arora, P. A. Hooper, and J. P. Dear, "Failure analysis using X-ray computed tomography of composite sandwich panels subjected to full-scale blast loading", *Journal of Composites Part B: Engineering,* vol. 129, pp. 26-40, 2017.

E. Rolfe, C. Kaboglu, R. Quinn, P. A. Hooper, H. Arora, and J. P. Dear, "High velocity impact and blast loading of composite sandwich panels with novel carbon and glass construction", *Journal of Dynamic Behavior of Materials,* vol. 4, pp. 359-375, 2018.

E. Rolfe, R. Quinn, A. Sancho, C. Kaboglu, A. Johnson, H. Liu, P. A. Hooper, J. P. Dear, and H. Arora, "Blast resilience of composite sandwich panels with hybrid glass-fibre and carbon-fibre skins", *Multiscale and Multidisciplinary Modeling, Experiments and Design,* vol. 1, pp. 197-210, 2018.

Chapter 2

Literature Review

2.1 Introduction

This chapter seeks to evaluate the current published literature in the field of air and underwater blast loading of composite sandwich structures. Due to the complexity and cost, large scale explosive blast testing is performed infrequently. The chapter summarises the large scale experiments that have been carried out along with the techniques and methods used to replicate blast loading, such as shock tubes and soft projectile impact. The chapter discusses areas that could benefit from further experimental investigation.

The literature reveals the potential for use of hybrid composite laminates as the skins for composite sandwich panels. A significant amount of research has been carried out into the hybridisation of composites. Researchers have investigated various materials and loading conditions, including the impact behaviour of such laminates. However, the blast performance of hybrid laminates and hybrid composite sandwich panels has remained largely uninvestigated. Following this, the most relevant investigations into post-blast damage and strength are detailed. The ability for composite sandwich panels to continue in service following a blast event is critical for naval applications. The importance of quantifying the residual strength of sandwich panels following blast for calculations or simulations is highlighted by the literature. The development of analytical and computational simulations of blast loading is discussed in the final section. The literature highlights the current progress in this field. Simulations have been widely developed to reduce the number of large scale experiments required.

2.2 Composites in Naval Structures

There has been an increasing demand for composite materials in the naval industry since the 1960s when Swedish defence institutes began to develop composite sandwich panels for naval applications [6], [7]. Mouritz et al. highlighted that this demand has been due to the goals of reducing acquisition and maintenance costs whilst improving the operational performance of the vessels [8]. Parameters which are key for naval vessels include: range, stability, stealth, payload capacity and efficiency. Feasibility studies have shown composite patrol boats made from glass-fibre reinforced polymers (GFRPs) can achieve a weight saving of between 10 % and 36 % compared to aluminium and steel equivalents respectively [9]. The reduced mass of composite materials can lead to greater vessel efficiency along with improved range and/or greater payload [8]. Furthermore, composite materials are known to have superior corrosion resistance and reduced thermal and magnetic signatures, compared to steel or aluminium. Thereby meeting more of the criteria required of naval vessels. However, there are downsides to composite materials. This has resulted in slow uptake in the naval industry compared to other industries such as aerospace, automotive and renewable energy. The major drawbacks are cost, flammability and toxicity, seawater absorption and reduced stiffness compared to steel and aluminium. A study of 50 m long mine countermeasure vessels (MCMVs) has shown that the hull girder deflections of a composite ship are twice that of a steel ship due to the reduced stiffness of composites [8]. Furthermore, the low toughness of composite sandwich panels leads to the use of excessive safety factors limiting the benefits of composites. Traditionally, isotropic materials have been used throughout naval vessels, therefore, parts have been designed with manufacturing processes considered subsequently. With composite materials, the layup and fibre orientation must be considered during the design stage. This requires more in depth design processes and manufacturing techniques to ensure sufficient safety and integrity of the vessel is achieved. Although advanced composites are becoming more economically viable, a greater upfront cost is required. However, it has been shown that composite ships only require around 15 % of the maintenance costs required by similar steel vessels making this upfront investment worthwhile [10].

A number of vessels constructed partially or wholly from FRPCs are currently in service. These vessels include the Swedish Visby Class Corvette and the Norwegian Skjøld Class MCMV. The Skjøld Class MCMV has a hull constructed from glass-fibre and carbon-fibre composite laminates and sandwich panels infused with

vinylester and polyester resin [4]. The Visby Class corvette is made from carbon-fibre composite sandwich panels with a polyvinyl chloride (PVC) foam core and vinyl ester resin [1]. Composite sandwich structures consist of two FRPC skins separated by a lightweight core, typically made from structural foam or honeycomb. Composite sandwich structures have been adopted in naval vessels due to their increased bending stiffness, energy absorption and ability to withstand deflection. The increased bending stiffness of composite sandwich panels is achieved due to the distance between the composite laminate skins and the neutral axis [11]. The lightweight core only marginally increases the mass for a significant increase in bending stiffness. These two vessels have been designed to be lightweight, high-speed, manoeuvrable and undetectable. Along with these performance parameters, naval vessels are required to withstand a range of demanding loads due to the environment in which they operate. This can include wave slamming, high strain rate loading, impact loading and blast loading. These loading phenomena are very complex and can result in devastating consequences. Therefore, the performance of composite structures against such loads must be investigated.

2.3 Blast Testing of Composite Materials

2.3.1 Air Blast Loading

The detonation of explosive material generates a violent expansion of hot gases which produces a shockwave. The shock wave travels outwards from the explosive material and causes an almost instantaneous pressure rise in the surroundings. The pressure decays back to ambient before forming a negative phase due to the momentum of the explosive gases [5]. The charge material, charge weight and stand-off distance govern the characteristics of the blast event. These characteristics are impulse, static overpressure and reflected overpressure. Static overpressure is recorded using a gauge parallel to the blast wave, away from other objects. It is a property of the explosion. Reflected overpressure is measured on the face of a large obstruction within the wave path, it is a function of the surrounding environment and is dependent on the size of the object and its angle of incidence [12]. References [5] and [12] contain thorough descriptions and analyses of explosive blasts.

Due to the high experimental costs, there is relatively limited literature available on the air blast performance of composite structures. Furthermore, composite structures have a large potential for variation including: geometry (skin and core

thickness), materials (reinforcement, resin and core), configuration (layup order and weave type) as well as manufacturing method. This can be advantageous as it is possible to tune the structures for optimal performance. However, this can lead to a large range of potential experiments and qualitative experimental results limited to comparisons of different material responses. Comtois et al. [13] placed small explosive charges on the surface of glass-fibre and carbon-fibre laminates. The authors found that support conditions strongly influenced laminate damage and that damage was a function of both peak pressure and impulse. Furthermore, the carbon-fibre laminates suffered less fibre breakage compared to lower strength glass-fibre laminates. Yahya et al. [14], [15] have investigated the blast resilience of a number of glass-fibre and carbon-fibre laminates with different resins by subjecting them to near-field explosives. A ballistic pendulum was used to measure the impulse delivered to the specimen. The specimen were tested under a series of impulses. The results highlighted that the matrix material did not change the blast response of the woven carbon-fibre laminate under these conditions. The fibre material did affect the blast response. A glass-fibre laminate with poly-ether-imide (PEI) resin had superior blast resistance compared to a carbon-fibre laminate with PEI resin. Gargarno et al. [16], [17] subjected composite laminates to small scale charges to investigate the effects of glass-fibre versus carbon-fibre laminates and weave types. The authors found that glass-fibre woven laminates with vinyl ester resin demonstrated the best blast resilience compared to equivalent carbon-fibre laminates. Non-crimp continuous fibre fabrics with z-binder yarn were found to outperform woven fabric laminates using the same fibres and resin system. The z-binder yarn prevented delamination whereas the woven fabrics had poor interlaminar fracture toughness and shattered upon arrival of the shock wave. Franz et al. [18] observed that using a graded laminate configuration improves blast performance. The configuration consists of front layers with high energy absorption and damping properties, and rear layers with high flexural rigidity. This configuration is similar to that of a sandwich structure where the skins offer the rigidity and the core provides energy absorption. Composite sandwich panels, which are inherently more blast resilient than laminates [10], can therefore offer advantages over composite laminates under blast.

Large scale blast tests have been carried out by Arora on composite sandwich panels [19]. The author investigated panels with GFRP and carbon-fibre reinforced polymer (CFRP) skins along with the effects of core thickness, proximity to the charge and repeat loading. The panels adopted non-crimp continuous fibre fabrics with z-binder yarn. Stand-off distances between 8 m and 16 m were used and

charges of either 100 kg nitromethane or 30 kg composition 4 (C4) plastic explosive were selected. The panel with GFRP skins had a greater out-of-plane displacement and suffered from a large front skin crack compared to the CFRP panel despite having an equivalent mass per unit area of approximately 17 kg m^{-2}. The panel with CFRP skins suffered from minor cracks initiating at the bolt holes. Kelly [20] performed large scale blast testing, primarily investigating the effect of core material on panel response. The research showed that styrene acrylonitrile (SAN) structural foam had the best performance overall and implementing a stepwise graded core could further improve panel performance. This is a similar conclusion to Franz [18], whereby the front lower density core layers can absorb blast energy while the rearmost core layer has a higher flexural rigidity to support the rear skin. In addition, Kelly et al. [21] performed large scale blast tesing on panels with GFRP skins and polypropylene (PP) interlayers. The panel with PP interlayers deflected less than the panel with solely GFRP skins and an identical core. Upon post-blast inspection the panel with PP interlayers suffered from less front skin/core debonding and had no front skin cracks. Langdon et al. [22] carried out near-field blast experiments on composite sandwich panels with PVC foam cores and glass-fibre skins. A glass-fibre composite laminate with equivalent mass was also subjected to an identical charge at 50 mm stand-off distance. Under near-field loading, the composite sandwich panel was shown to have inferior blast resilience compared to the composite laminate. This appears counterintuitive. However, the authors concluded that this is due to the lower transverse stiffness of the sandwich panel resulting in a higher velocity causing greater deflection and hence material stresses and strains. The authors also concluded that a higher density foam core reduced sandwich panel damage as it increases the panel transverse stiffness.

Due to the high costs involved with blast testing, shock tubes are often used to simulate blast loading. Shukla and co-workers have performed a significant volume of research on the blast performance of composite laminates and sandwich structures using a shock tube. During shock tube loading, a rapid release of gas propagates a shock wave through a tube towards a specimen mounted at the end. Tekalur et al. [23] investigated the performance of woven glass-fibre versus stitched carbon-fibre laminates with the same resin system. The glass-fibre laminates demonstrated damage progression with various failure modes. The carbon-fibre laminates showed no signs of external damage until a threshold shock pressure beyond which the panel failed. The researchers have investigated the effects of using a stitched and unstitched foam core along with graded core composite materials [24], [25].

In agreement with Kelly [20], the authors concluded that a core configuration of low/medium/high density demonstrated superior blast performance compared to a panel with core configuration medium/low/high density. The same research group has looked into the addition of poly-urea (PU) interlayers into the skins of composite sandwich panels [26]. This was following a successful demonstration that PU layers improved the properties of concrete structures under blast loading [27]. The location of the PU layer was varied and it was found to affect deflection and strain of the sandwich panels. Placing the interlayer behind the front skin or behind the core was found to reduce back skin deflection, velocity and in-plane strain. This improves the overall blast performance of the panel. These results, along with those from Kelly [20], highlight the potential benefit of adding interlayers to composite sandwich panel skins.

Fleck and co-workers have developed another laboratory technique where the pressure versus time profile created by localised blast loads can be simulated [28]. This is achieved by firing an aluminium foam projectile at a specimen. The velocity, length and density of the foam projectile govern the impact magnitude and duration. The authors used this technique to compare the response and damage of composite sandwich beams, composite laminate beams and steel beams [29]. During this experiment, the sandwich beams outperformed the composite laminate beams. Both sandwich and laminate beams underwent smaller deflections compared to the steel beam for constant normalised impulse. However, both types of composite beam underwent catastrophic failure at lower normalised impulse compared to the steel beams.

This literature review has detailed the research that has been carried out on composite laminates and composite sandwich panels under air blast loading, however, sometimes with contradictory results. This highlights the importance of performing experiments on representative materials under realistic scenarios to gather results relevant to the final application.

2.3.2 Underwater Blast Loading

An underwater explosion results in two key energy dissipation mechanisms: a pulsating bubble of hot combustion gases, and a shock wave. Each mechanism is responsible for approximately 50 % of energy dissipation [5]. This gas bubble expands and contracts due to a difference in pressure between the bubble contents and surrounding water. The bubble rises to the surface and continues to pulsate until all the energy is dissipated. The effects of the gas bubble can be ignored for

analyses at sufficiently large stand-off distances [30]. If an explosion occurs underwater, the medium transferring the shock wave has increased in density. This results in a significant increase in speed of sound and a rise in pressure compared to air blast. An increase in peak pressure can have devastating consequences for structures. Conducting underwater explosive experiments is an equally expensive and high risk endeavour. Furthermore, detailed consideration is required to obtain high quality data that can be reliably interpreted.

The first instrumented large scale underwater blast experiments, to the authors knowledge, are detailed by Hayman [7]. These were carried out by Det Norske Veritas (DNV) and the Royal Norwegian Navy in the late 1980s. Over 50 experiments were performed investigating composite sandwich panels with glass-fibre skins and PVC foam core. Only up to 12 strain gauge channels per experiment were available. More recently, Arora and Kelly have performed large scale underwater blast tests adopting a similar set up. However, up to 28 strain gauges were used to monitor the panel behaviour during blast [19], [20]. Arora compared the underwater blast performance of composite sandwich structures with woven GFRP skins to structures with hybridised woven GFRP and aramid-fibre skins [19]. Both panel types had a SAN foam core. The hybridised glass-fibre and aramid-fibre panels were found to suffer greater damage. This was due to the presence of the aramid-fibres lowering the strength and stiffness of the panel overall. However, both panels used woven laminates as the skin materials. Previous literature has shown these fabrics are less blast resilient compared to non-crimp continuous fibre laminates. Kelly compared the underwater blast performance of sandwich panels with continuous fibre GFRP and CFRP skins both with a single density core and graded density core [20]. The high stiffness of carbon-fibre caused the panels with CFRP skins to suffer from extensive damage, especially the panels with a single density core. These two experiments highlight that glass-fibre skins demonstrate better performance during underwater blast loading due to their intermediate stiffness.

Once again, shock tubes and laboratory techniques have been developed to simulate underwater blast loading. The laboratory based simulations often enable improved instrumentation techniques to be implemented. Latourte et al. [31] have used a scaled down laboratory fluid structure interaction (FSI) experiment to compare the performance of composite laminates and composite sandwich panels. The pressure history is created by impacting a water piston with a flyer plate launched by a gas gun. The setup enabled deflection versus time recordings to be made using Moiré and high speed photography. Sandwich panels were shown to outperform

laminate panels at high specific impulses. LeBlanc et al. [32], [33] have used a conical shock tube (CST) to determine the effects of underwater blast loading on composite sandwich panels. The CST is a water filled tube with conical internal shape. The shock wave is initiated by an explosive at the open end of the tube. The initial experiment relied on strain gauge data to record panel response [32], however, the experimental setup was developed and transient plate response was recorded using 3D DIC [33]. High speed cameras were positioned behind the back face of the composite sandwich panel. This experiment investigated the effect that polyurea coatings have on composite sandwich panels with GFRP skins. The authors found, that for a given polyurea thickness, the panel responded best when it was applied to the back skin. High speed DIC has been used by Gupta et al. [34] to record and measure underwater implosions of composite tubes. This highlights the potential for further use of underwater DIC.

There is less experimental data and literature available on the underwater blast performance of composite structures compared to air blast. This is due to the cost and difficulties associated with performing underwater blast experiments. Since underwater explosions create a more severe loading regime, further experiments in this field are valuable to improve the understanding of material performance and to aid in improving computational simulations.

2.4 Post Blast Damage and Strength

Composite structures absorb blast energy through deformation and damage mechanisms. There are three key of failure modes in composite sandwich panels: skin failure, core failure and bond failure. The skin can fail via fibre fracture or skin wrinkling, which is caused by buckling of the skin into the core. The core often fails in shear as it is primarily transferring the shear forces between the skins. Core compression failure or core crushing is also common. Bond failure, or debonding is the failure between the skins and the core. The adhesives used for bonding are generally stronger than the core so for a perfect bond, debonding should not be an issue [11]. However, in practice, defects in bonds propagate under loading. Defects in the laminate resin are also common and lead to delamination of layers within the composite skins. Adhesion quality is, therefore, a priority in sandwich panel construction. The presence of damage in a composite panel can lead to reduced post blast strength. This can be problematic if a vessel is required to remain in service following a blast event. Understanding the effect of damage on composite strength

is, therefore, important. Delamination is a key energy absorbing mechanism for composite laminates and sandwich panels under blast. Debonding and delamination will certainly reduce the flexural and compressive properties of a composite sandwich panel or laminate due to the inability to transfer forces. Caprino and Teti carried out post-impact strength tests on composite sandwich panels with GFRP skins and PVC foam core [35]. The authors concluded that post-impact tensile strength was related to fibre failure and not the extent of delamination. Edgren et al. [36] performed compression after impact (CAI) experiments on continuous fibre CFRP sandwich panels to assess the failure mechanism during compression in the region of impact. These authors found that microbuckling dominated at the impact damage location.

The isolation of a single failure mode, however, is highly unlikely under blast loading. Furthermore, prediction of the dominant failure mode is not straightforward as it is affected by skin thickness, beam length and relative core density [11]. Multiple damage modes are expected to occur almost simultaneously under blast. Kelly [20] extensively mapped the damage in composite sandwich panels that had undergone large scale air blast loading. The majority of debonding was found to occur between the front skin and core. Very little damage took place at the centre of the sandwich panels. The author found that debonding dominated the flexural stiffness and strength far more so than core cracking. However, under edgewise compression, debonding was less problematic as the foam still prevented buckling of the skins unless the skins bowed away from the foam. Core cracking was a more significant problem under edgewise compression. Latourte et al. [31] performed an assessment of the damage performance of composite laminates and sandwich panels subjected to underwater blast loading using a CST. Cracks were formed at the centre through the panel thickness and extensive delamination was observed at the edges due to bending. Similar damage was observed in both the sandwich panels and the laminates, however, at much higher impulse per areal mass for the sandwich panels. The position of failure moved from the water side to the air side as peak pressure was decreased.

A key aspect of understanding the blast resilience of composite sandwich panels is to determine what is an acceptable size or level of damage following blast loading, regardless of the damage type. Zenkert et al. [10] have sought to establish the size and extent of damage that a structural ship component can have without the risk of growth or failure. Hence to determine whether a part needs repairing or replacement. The authors focussed their investigation on visible impact damage

(VID) and barely visible impact damage (BVID). Non-destructive evaluation (NDE) techniques are difficult to perform on composite structures due to their many layers. Furthermore, the size of naval structures prohibits the use of NDE techniques over the entire ship surface. Inspection performed by naval crews is likely to be limited to visual inspection, thereby only picking up on VID and some BVID. CAI was performed on composite sandwich panels with carbon-fibre skins, representative of the materials used in the Visby Class. Residual strength testing was limited to compressive loading as carbon laminates usually exhibit a considerably lower compressive than tensile strength. Thus compressive strength is usually the critical design criteria. In the same investigation, the authors also subjected panels with impact damage to hydrostatic pressure loading. The panels were subjected to a uniform pressure loading using a water-filled rubber bag. The authors successfully produced simple relationships between strength reduction and damage size for sharp and blunt impact damage. The authors concluded that damage certainly reduces the load bearing capacity of composite sandwich panels but many ship structures are not fully utilised and can allow for the presence of damage. Through laboratory based damage characterisation, comprehensive damage assessment schemes can be created. This enables inspection schemes to be mapped out and ensures the integrity of the ship structure after damage has been sustained.

The material choice is known to affect damage levels and post-blast strength of composite sandwich panels. Following large scale air blast testing, Arora et al. [37] investigated the edgewise compressive strength of sections of composite sandwich panels. The samples were large and contained a large amount of varied damage. The results revealed that the percentage drop in strength was greater for the panel with CFRP skins compared to the panel with GFRP skins. Kelly [20] found that the implementation of a compliant PP ply in the front skin prevented front skin cracking from occuring. X-ray computed tomography (CT) scanning has been performed on sections of composite sandwich panels which have undergone underwater blast testing to quantify damage [38]. Composite sandwich panels with glass-fibre or carbon-fibre skins and identical foam cores were subjected to a 1 kg plastic explosive 4 (PE4) charge underwater. The panels with CFRP skins were shown to suffer from 76.0 % front skin debonding whilst the panels with GFRP skins suffered from 26.9 %. The CFRP panel suffered 9.6 mm of core crushing compared to 4.0 mm for the GFRP panel. This illustrates that the brittle CFRP skins prevent panel deflection resulting in greater core crushing and greater damage in this loading regime.

The literature review has shown that a large body of research has been performed on the effect of core material on composite sandwich panel response and the behaviour of glass-fibre versus carbon-fibre laminates or skins. However, there is potential to further investigate the effect of skin material. GFRP has generally demonstrated superior blast performance due to its ability to undergo greater deformation before failure. However, under some circumstances GFRP panels developed damage sooner than equivalent CFRP laminates or panels due to their reduced strength. The CFRP laminates and panels suffer from sudden brittle failure particularly during underwater blast loading. A graded density foam core or graded laminate was shown to be advantageous. Extending this idea to sandwich panels could result in a sacrificial front skin made from a material with higher energy absorption and a stiffer rear skin made from a different material. Alternatively, a combination of glass-fibre and carbon-fibre in a hybrid composite could result in superior properties and improved performance.

2.5 Hybrid Composite Structures

Hybrid composites are usually considered to be composites with a matrix containing two or more types of reinforcement [39]. The second type of reinforcement could take the form of rubber or nano-scale reinforcements. However, the hybrids referred to here are composites containing two or more types of reinforcing fibres. After the invention of carbon-fibre [40], [41], hybridisation received a lot of research interest due to the prohibitive price of carbon-fibre and the desire to improve the failure strain. The replacement of some carbon-fibre layers with glass-fibre was an effective method of reducing cost. Furthermore, by hybridising glass-fibre and carbon-fibre, a number of researchers successfully increased the failure strain of hybrid laminates by up to 50 % compared to CFRP laminates [42], [43]. Achieving mechanical properties superior to the constituent materials is known as the hybrid effect. However, there is no widely accepted definition for calculating the hybrid effect. Some researchers have based hybrid effect on increased failure strain and others on comparison to the rule of mixtures. Recently there has been renewed interest in hybridisation with the aim of improving the toughness of composite materials along with improving damage resistance, reducing brittle behaviour and achieving warning before failure.

There are existing hypotheses regarding how the hybrid effect improves failure strain [39]. The mismatch in coefficient of thermal expansion (CTE) between the dissimilar fibres will cause glass-fibres to increase in length upon heating during

fabrication due to their greater CTE. Following curing, the glass-fibres will reduce in length resulting in compressive stresses on the carbon-fibres and tensile stresses on the glass-fibres. These compressive stresses counteract the applied stress on the carbon-fibres and the tensile stresses on the glass-fibres account for their reduced strain to failure compared to glass-fibre laminates alone. However, this hypothesis does not hold true for aramid-fibre and carbon-fibre hybrids. Aramid-fibres have a smaller CTE compared to carbon-fibres yet a positive hybrid effect has been observed [44]. A second hypothesis states that the higher elongation fibres, such as glass-fibre or aramid-fibres, will bridge the broken lower elongation fibres, carbon-fibre [43]. This will prevent broken fibre clusters from growing large enough to become unstable enough to lead to final failure [45].

As detailed by Swolfs et al. [39] composites can be hybridised in three main ways: layer-by-layer (interlaminar), within layers in a woven fabric (intralaminar) and within the yarn (intrayarn). Models suggest that expensive intrayarn hybrids are most likely to achieve significant failure strain enhancements. However, as detailed, achieving greater failure strain is no longer the sole driver behind developing hybrid composites. Interlaminar and intralaminar hybrids can enhance other material properties. Interlaminar hybrids have been widely investigated as they are the cheapest and simplest to manufacture. Murugan et al. [46] fabricated interlaminar GFRP/CFRP hybrid laminates and characterised their tensile strength, flexural strength, impact strength and performed dynamic mechanical analysis (DMA). This revealed that the stacking sequence of the laminae has an effect on the flexural properties of the hybrid laminate. Song [47] also investigated the performance of interlaminar GFRP/CFRP and aramid-fibre/CFRP hybrid composites under tensile and flexural tests. The author concluded that the tensile strength was dominated by the carbon-fibres and whether the second fibrous material was glass-fibre or aramid-fibre made little difference. In agreement with Murugan [46], the stacking sequence of fibre materials was shown to affect the mechanical properties of the composite laminates. Giancaspro et al. [48] noted that adding carbon-fibres on the tensile side of an interlaminar hybrid under flexure improved flexural strength. This was not the case when carbon-fibre was added to the compressive side, this promoted crushing on the compressive side. For interlaminar hybrids, the position of the layers can be tailored to suit expected loads.

2.5.1 Impact Testing of Hybrid Composites

The impact performance of GFRP/CFRP interlaminar hybrid laminates has been widely investigated. Improving toughness is a key goal for hybridisation and impact performance is linked to toughness [39]. Impact can be qualified as the near instantaneous application of an impulsive load to a structure. Low rate impacts are generally accepted to be those with projectile velocities less than 20 m s^{-1} [49]. Under low velocity impact, composite laminate and composite sandwich panel response is governed by flexural behaviour. Delamination and debonding are the main failure modes. This is caused by in-plane and out-of-plane shear stresses. As the impact velocity is increased, and the strain rate increased, the failure modes become more localised. At even higher impact velocities, the event time is shortened further. Perforation occurs and global structural response is not possible [49]. Impact differs from blast loading due to its more localised nature. Nevertheless, literature and results from impact experiments that result in global deflection and delamination can prove informative for understanding the blast performance of materials.

Enfedaque et al. [50] and Sevkat et al. [51] used drop towers to impact hybrid composite laminates. Enfedaque et al. elected to investigate impact energies between 30 and 245 J whilst Sevkat et al. investigated projectile velocities of 3.9 to 6.3 m s^{-1}. The authors separately concluded that the penetration impact resistance of such hybrid laminates can be improved when glass-fibre fabrics were the outermost layers. This is due to the higher failure strain of glass-fibre delaying damage within the laminates. Pavithran et al. [52] carried out Charpy impact tests on hybrid laminates fabricated from sisal fibres and glass-fibres. In this hybrid, the glass-fibres are the low elongation fibres and sisal fibres the high elongation fibres. The results showed that having the low elongation glass-fibres on the outside decreased Charpy impact energy. This agrees with the results from the GFRP/CFRP hybrid laminate experiments. Under repeated impact testing, Sevkat et al. [53] found that damage build-up and accumulation was reduced when glass-fibre layers were added as the outside layers into GFRP/CFRP hybrid laminates. The ability of hybrid composites to exhibit damage contributes directly to the amount of energy they can absorb. Sevkat et al. [53] showed that the damaged area in the GFRP/CFRP hybrids under low velocity impact was greater than the damaged areas in laminates made from either of the constituent composites. The authors attributed this to the incompatibility of the layers increasing the likelihood of delaminations. Park and Jang [54] compared the impact performance of interlayer and intralayer aramid-fibre and polyethylene (PE) fibre hybrids. The authors observed that the interlayer

hybrids had a greater penetration resistance due to the easier development of delaminations. However, this led to greater delaminated areas and should result in poorer post-impact mechanical properties. Peijs et al. [55] fabricated PE fibre and carbon-fibre interlaminar hybrids. The hybrids had differing levels of dispersion, achieved by using thinner or thicker plies. Thinner plies gave rise to more interfaces which enabled delamination and greater energy absorption. Czél et al. [56] have successfully controlled the damage mechanisms by reducing the thickness of the low elongation carbon-fibre layer. The authors sandwiched a 29 μm carbon-fibre layer between thicker glass-fibre layers. Under tensile testing, this led to several breaks in the carbon-fibre along the length of the sample with diffuse delamination before the glass-fibre layers broke. This failure mechanism absorbed a significant amount of energy.

Pandya et al. [57] have investigated the ballistic impact behaviour of hybrid GFRP/CFRP laminates. The authors concluded that for a constant laminate thickness, the ballistic limit was increased by replacing carbon-fibre laminate layers with glass-fibre layers. Furthermore, a higher ballistic limit was achieved when the carbon-fibre layers were placed within the glass-fibre layers compared to the inverse. For constant areal density, however, the carbon-fibre laminate achieved the highest ballistic limit followed by the glass-fibre laminate and then the hybrid composites. The performance of GFRP/CFRP hybrid laminates under high velocity impact was investigated by Reddy et al. [58]. The proportion of weight of the two fibres was varied and the authors concluded that a ratio of 50:50 in weight of the fibres demonstrated the maximum energy absorption. The ballistic impact performance of glass-fibre/aramid-fibre/carbon-fibre hybrid composite laminates was investigated using a gas gun by Randjbaran et al. [59]. The position of the glass-fibre and carbon-fibre layers was varied to observe the effect this has on energy absorption of the laminate. These experiments revealed that placing a glass-fibre layer at the front, experiencing the impact, is beneficial. The dispersion and positioning of the layers affects impact performance of hybrid composite laminates.

Researchers in this field widely agree that if fibres with the highest energy absorption are used as the outermost layers, the hybrid laminates are able to absorb more energy [39]. These ideas could be extended to blast loading. The positioning of the layers may affect blast performance in a similar way.

2.5.2 Blast Testing of Hybrid Composites

Investigations into the air blast response of hybrid composite laminates is limited. Some research has been carried out into the blast performance of alternative fibres, such as aramid and ultra high molecular weight polyethylene (UHMWPE). Karthikeyan et al. [60] impacted CFRP and UHMWPE laminates with metal foam projectiles at velocities between 140 and 890 m s^{-1} to simulate localised blast loading. The authors found that the UHMWPE beams outperformed the CFRP beams. The UHMWPE beams exhibited a lower central deflection, for a given impulse, and could tolerate a higher failure impulse. UHMWPE was subjected to localised air blast by Fallah et al. [61]. The UHMWPE laminate results were compared to numerical simulations of mild steel and armour steel plates with equal mass per unit area. The authors concluded that armour steel and UHMWPE plates offer potential displacement reductions of 50 % and 30 % respectively for the impulses tested.

The blast performance of hybrid composite laminates has remained uninvestigated. Futhermore, the literature detailed is concerned with hybrid composite laminates rather than composite sandwich panels with hybrid laminate skins. The benefits of hybrid composite laminates under impact have been demonstrated, there is potential to transfer these benefits across to blast loading. By implementing hybrid laminates as the skins on sandwich panels, the panel energy absorption could be significantly increased through material interactions and damage mechanisms.

2.6 Simulations of Blast Experiments

A large amount of research is dedicated to the development of simulations due to the high costs associated with blast experiments. Both analytical and numerical simulations have been developed. Experimental blast tests generate valuable data regarding failure modes and mechanics under blast, however, models can provide additional insight into material response that may be challenging to measure during experiments. Furthermore, simulations that have been validated against reliable experimental data can be used during the design process. This will reduce the number of experiments required along with the cost of the design process. This section details the most significant and relevant research currently within this field.

2.6.1 Air Blast Simulation

Librescu and co-workers developed an analytical solution for the response of sandwich panels to air and underwater blast loading [62]. The authors used the basic equations of sandwich plate theory and Hamilton's principle to drive the equations of motion of the panels [63]. The analytical models were used to determine the effects of a number of parameters on the accuracy of the solution. These included panel geometry, core orthotropy, ply thickness and stacking sequence [64]. The models were then used to predict the core compressibility and buckling of flat sandwich plates subjected to impulsive loading [65]. Andrews and Moussa developed an analytical solution for predicting failure of composite sandwich panels under blast loads. The failure took the form of front skin compressive failure, core shear failure or rear skin tensile failure. Failure mode maps were drawn for various sandwich panel dimensions. The static and dynamic response of the panel was considered by modelling the panel as a single degree of freedom mass-spring system [66]. Kardomateas, Frostig and Phan developed analytical solutions for the stress, strain and displacement response of sandwich panels to blast loading. These include a dynamic elasticity solution and extended high-order sandwich panel theory (EHSAPT) [67], [68]. The dynamic elasticity solution can be used as a benchmark to assess other advanced sandwich panel theories. Including the high-order core theory previously developed by Li, Kardomateas and Simitses [69], [70]. Yuan and Kardomateas went on to investigate deformation and rotation of sandwich panels under blast loading using the EHSAPT. Following comparison with other analytical solutions, the authors concluded that EHSAPT can successfully perform dynamic analysis with geometric nonlinearities. The authors demonstrated that it is a powerful approach and can be used in the analysis of complex sandwich panel responses [71]. Birman and Kardomateas present a comprehensive review regarding the latest developments in theoretical predictions of composite sandwich behaviour [72]. The authors highlight that the ever broadening use of composite sandwich panels and novel designs results in the need for continuous development of analytical solutions.

Hoo Fatt and Palla developed an analytical solution for circular sandwich panels with GFRP skins and PVC foam core under air blast loading. The response of these panels was split into core crushing and global bending. Finite element (FE) analysis in ABAQUS/Explicit was used to simulate the experiments and the analytical and FE predictions demonstrated close correlation rendering the analytical method a useful design tool [73]. Hoo Fatt and Sirivolu extended the work to consider both isotropic and transversely isotropic core properties. The isotropic foam behaviour

correlated well with a FE ABAQUS/Explicit model of the event. However, the use of isotropic properties overestimates the blast resilience of the panels for some geometries. Core yielding was predicted to occur at the centreline in regions approximately one quarter of the way in from the edges [74]. To support their experimental investigations, Langdon, Cantwell, Nurick and co-workers have extensively developed FE simulations in ABAQUS/Explicit. A FE model successfully predicted the post-blast deformed shapes of the composite sandwich panels with PVC foam cores and aluminium alloy skins [75]. The foam core was found to absorb over 50 % of the total energy. The effect of aramid fibre stitching within composite sandwich panels was also investigated via experiments and FE analysis [76]. The FE data was found to accurately predict panel response. However, the authors concluded that through-thickness stitching did not enhance blast resilience. Tagarielli et al. [77] developed a FE model to support their simulated blast experimental investigations. A crushable foam projectile was fired at monolithic and sandwich beams. The FE simulations correctly predicted the dynamic response of the beams. The authors concluded that core ductility and bonding interface toughness were key parameters in sandwich panel design and that shock resistance of a sandwich beam can be maximised by selecting composite fibres with high failure strain.

Tekalur et al. [24] used a 3D MOSAIC analysis approach to model the shock loading response of composite sandwich panels with woven skins and stitched foam core. LS-DYNA has also been used to create FE models of the blast behaviour of composite sandwich panels [78]. LS-DYNA FE simulations have been developed by Bahei-El-Din et al. [79], [80] to model the blast response of composite sandwich beams with stiff PU rubber and compliant polyethylene foam interlayers between the top CFRP skin and PVC foam core. The authors had similar aims to those authors implementing interlayers during experimental investigations, which were to limit delamination damage and core crushing. A variety of layups were investigated and the inclusion of both PU and polyethylene was found to be most effective. The presence of the interlayers was shown to reduce core crushing by over 50 % and dampen the transient response of the sandwich panel. This reduced panel displacement by 15 % and debond between the skin and core by a factor of five.

Arora developed ABAQUS/Explicit FE simulations of large-scale air blast experiments where the performance of composite sandwich panels with GFRP skins and CFRP skins were compared [81]. The panels had an identical SAN foam core. The author aimed to accurately capture the transient boundary conditions. The FE simulation successfully reproduced the experimental results from blast wave arrival

until first maximum deflection of the panel. The author identified that the deviations in results could be alleviated by using more detailed and accurate material models for both the skins and cores. The simulation was extended to capture the effects of different blast intensities and multiple blasts [82]. The updated model included Hashin damage criteria for the composite skins and a brittle failure condition for the core. Near linear trends between displacement and increased blast load were observed. Kelly [20] also developed a FE simulation to capture the response of composite sandwich panels with differing foam cores under large scale air blast. The author implemented a brittle cracking damage model for the foam core as this failure mode dominated post-blast visual observations. Debonding between the core and skins was also identified but not included in the model due to its complexity. The analysis revealed that implementing foam fracture improved the consistency of front skin predicted failure, however, prediction of foam fracture became unrealistic. The author concluded that further simulation work is necessary to accurately capture the panel response and damage mechanisms under air blast.

2.6.2 Underwater Blast Simulation

An analytical prediction for underwater blast on composite sandwich panels has been developed by Panciroli and Abrate [30]. The authors outlined an approach for determining the transient response accounting for core compressibility. The shape of the structure was found to dictate its behaviour. The first vibration mode dominates the response of beam and flat plates whilst superposition of higher modes dominates the response of curved structures.

A key problem with modelling blast loading of structures, particularly during underwater blast loading, is fluid structure interaction (FSI). The composite sandwich structures can displace while loading is incident on the surface and hence the loading of the panel changes. During underwater blast, the interaction between the water and panel causes cavitation. Schiffer and Tagarielli [83], [84] developed analytical and finite element simulations to capture this process. High speed photography during their experimental work revealed that previous theoretical models are not sufficiently detailed to predict FSI. In ABAQUS/Explicit the water was modelled with a specified cavitation limit. The analytical solution was divided into two phases. During the first phase, the water was in contact with the composite laminate plate whilst in the second phase cavitation began, this phase was informed by the FE simulation results. The analytical solution was compared to both FE and experimental results, all of which showed good correlation. The authors went

on to experimentally validate their predictions [85]. The FE simulation peak deflections and time responses correlated well with the experimental results and the authors concluded that GFRP laminates had a higher underwater blast resilience than CFRP laminates due to their higher ductility.

Further work by Schiffer and Tagarielli investigated the underwater blast performance of sandwich structures through their validated analytical predictions and FE [86]. The structures were in contact with water on both sides and the effect of water depth was studied. The authors concluded that stiffer cores of equal mass were advantageous and blast loading in deep water is less severe than shallow water. This is due to the impulse decreasing as initial static pressure for a water backed plate increases.

Hoo Fatt and Sirivolu have developed solutions for air and underwater blast response of composite sandwich panels with fluid-structure interaction introduced. Again, the sandwich panels had GFRP skins and PVC foam core. The authors found that the presence of water causes damping and results in greater pressures required to initiate damage. Panels with more ductile foams were found to be more blast resistant due to their ability to undergo core crushing [87]. Wei et al. [88] developed an FSI FE model in ABAQUS/Explicit using an Eulerian mesh for the water and a Langrangian mesh for the composite sandwich panel. Eulerian meshes tend to model the loading processes well but have limited capability for modelling material failure whereas Langragian meshes are better at modelling material and structural response but less so at the loading process [89]. Hashin failure was used to model the failure in the GFRP skins, a strain-rate sensitive cohesive law was used for delaminations between laminae and the PVC foam was modelled with a crushable foam plasticity model. The model accurately captured the spatial distribution and damage to a first-order approximation. Furthermore, the role of the foam in improving panel performance and reducing impulse imparted to the back skin was highlighted [88].

LS-DYNA was used by LeBlanc and Shukla to simulate the underwater shock performance of glass-fibre composite laminates and this was directly compared to experimental data [32]. The experimentally recorded strain gauge data and the FE results were shown to correlate well. The type and extent of damage in the glass-fibre composite laminate was captured by the simulation. The authors concluded that the results show computational simulations can support experimental results and be used as an alternative during design.

Arora also developed an ABAQUS FE simulation of a full scale underwater blast test performed [19]. The author created the model to aid in interpreting the results

from the sandwich panels during blast as they had been instrumented with strain gauges alone. A crushable foam model was implemented to capture the core damage and crushing, and acoustic elements were used to model the body of water surrounding the target. A strong agreement between experimental and simulational strains was achieved. Furthermore, the experimentally observed reduction in core thickness agreed well with that predicted by the FE simulation. Further detailed material models and FSI would improve the FE simulation. Once again, the author concludes that numerical models can be a powerful tool to minimise expensive experimental work [19].

2.6.3 Material Models

The accurate prediction of panel response under blast loading is driven by the material models implemented within the simulation. A number of simulations detailed in this chapter have sought to capture the dominant types of composite or foam failure. However, the results are generally limited by the lack of sufficiently detailed material models. Furthermore, the mechanical response of FRPCs is sensitive to loading rate, particularly for glass-fibre laminates and less so for carbon-fibre [90]. The use of static mechanical properties to predict high strain rate response is not strictly accurate. The stiffness and strength of composite materials increases at higher strain rates. Increased strength and stiffness is generally considered beneficial, however, under blast loading, deformation aids energy absorption. In this case, greater stiffness may not be advantageous. The material behaviour under high strain rates needs to be understood and captured. Many authors have sought to develop material models which accurately predict composite response under extreme conditions, such as blast loading and crashes. Some material models are oversimplifications whilst other models use complex damage formulations that require many material constants. Iannucci [91] developed a simple but effective predictive technique that includes rate dependency and allows for damage accumulation within composite laminates. This contiuum damage mechanics (CDM) approach was extended by Donadon et al. [92]. The panel stiffness reduction was calculated through irreversible damage variables. CDM allows different failure modes to be combined with stress and/or strain failure criteria and with fracture mechanics to capture the failure progression. The authors developed a 3D material model which was implemented for impact loading experiments in LS-DYNA and validated against experimental results. Delamination was not captured but could be implemented. A CDM composite laminate material model capturing delamination, or shear fracture

was developed by Faggiani and Falzon [93]. The approach also modelled fibre tensile and compressive breakage along with matrix tensile and compressive fracture under impact loading. The extent of both intralaminar and interlaminar panel damage and post-impact permanent indentation achieved very good agreement with experimentally obtained non-destructive evaluation of tested panels. The ability for this material model to capture interply interfaces and friction would be highly beneficial when considering hybrid composites. However, this highly detailed material model is computationally expensive.

This section has shown that a vast number of analytical and numerical blast models have been developed due to the prohibitive cost of large scale experiments. It is clear that simulations can be a useful tool during a design process and can minimise the requirement for expensive experiments. In order to validate and setup simulations a range of experimental data is required. The literature has revealed that panel response data needs to be gathered throughout blast loading. This will determine how well the model captures the panel response against time and will highlight if a simulation and experiment begin to deviate. Additionally, strain measurements should be taken at as many locations as possible as well as on the front skin and within the core of composite sandwich panels. Detailed damage analysis following a blast experiment is important to quantify the extent and locations of damage mechanisms. This information will demonstrate whether the correct material model has been used in the simulation. Finally, the load experienced by the panel should be recorded as accurately as possible. This will ensure that the experimental conditions are accurately replicated. The literature has revealed that some simulations have investigated the effect of skin material on blast performance. There is potential to further develop these simulations to determine whether the performance of various different skin materials can be easily captured. However, the detailed failure mechanisms and interactions between the materials are complex to model, computationally expensive and are beyond the scope of this research project.

2.7 Conclusion

This literature review has been performed to document the current published research regarding the blast performance of composite sandwich panels. The aim of the review was to aid and inform the research carried out in this project and to avoid duplicating existing work in this field. The review highlighted that limited experiments with explosive charges have been performed. This is due to the com-

plexity of such experiments along with cost. Although work is continuously being carried out over a range of scales, suitable scaling standards have not been established. Therefore, large scale explosive testing is highly valuable to industry and the research community and will be the focus of this investigation. Robust large scale data can be compared to small scale experiments and shock tube data to validate these methods. Once sufficient large scale data is gathered to do so, the number of large scale tests can be reduced.

The literature research into air and underwater blast testing highlighted the current interest in face-sheet materials and the inclusion of energy absorbing interlayers. These investigations have been carried out to determine the effect skin material has on overall damage. The literature has shown that the two most commonly used FRPCs in the naval industry, glass-fibre and carbon-fibre, both have advantages and disadvantages due to their inherent properties. The inclusion of interlayers has resulted in improvements. However, investigations into the blast performance of hybrid glass-fibre and carbon-fibre composite laminates or sandwich panels has not been performed. Hybrid composite laminates have been widely investigated under impact loading and have demonstrated their potential advantages and the variations that can be achieved due to material layup. These findings motivated the research into hybrid composite sandwich panels in this research project. Widely available material grades and existing manufacturing techniques were used to fabricate specimen to demonstrate their blast resilience and develop confidence in these materials. High speed cameras and DIC was the main method of recording panel deformation during the experiments in this research project. This technique is often used during blast and shock tube experiments. The recording methods adopted were well informed by the widely available literature. Furthermore, the use of high speed cameras and DIC during underwater shock tube loading, detailed in the review, motivated the use of DIC during a full scale underwater blast experiment, detailed in Chapter 6.

Post-blast damage assessments and strength after blast were investigated as a vessel may have to continue in service for a period of time following blast loading. Strength after blast of composite sandwich structures is limited but is increasingly being performed. The literature highlighted that the skin and core materials can increase or decrease the susceptibility of a panel to damage and loss of strength. The damage types present also influence the remaining strength or stiffness of the panel. If one failure mode is known to be less detrimental, it may be possible to tolerate or even promote failure in this manner. The use of hybrid composite laminate skins may result in improved post-blast strength, as one of the fibrous materials may pro-

tect the other. Alternatively, the presence of dissimilar fibre materials may promote delamination due to a mismatch. This literature motivated the investigations into post-blast damage and strength of hybrid composite sandwich panels as it is unclear whether hybridisation will have a positive or negative effect in practice. Furthermore, the results of post-blast strength could be used to develop residual models to simulate the response of such panels with damage present. This work could be extended to account for the effect this localised damage has on entire ship hulls.

Finally, this literature review highlighted that there is a vast amount of research into the analytical and numerical modelling of composite sandwich panels under blast. Models are continuously being improved and developed to capture the broadening designs of sandwich panels. Furthermore, increasingly complex material failure models and FSI is being introduced into computational simulations to more accurately model the blast phenomena and capture the material response. One analytical method was used during this project to select stand-off distance and charge sizes for experiments. The literature also highlighted the data that is necessary to setup a simulation and/or to validate the results against. This ensured that the experiments performed provided the necessary data for these simulations. The literature highlighted that the behaviour of composite sandwich panels under blast loading is complex and often difficult to predict. Hence experimental investigations are necessary to generate performance data. Once again, with sufficient data and validation, the number of large scale tests can be reduced.

Chapter 3

Preliminary Analysis of Hybrid Composite Sandwich Panels

3.1 Introduction

The motivations for and effects of hybridisation of composites have been outlined in the previous chapter. It is clear that hybrid composites could be beneficial within many industries including the naval industry. Naval structures are required to withstand a variety of load conditions. However, there is limited literature available regarding the performance of hybrid composites under loads, such as shock and blast. Furthermore, the vast amount of variables that can be altered during the fabrication of composites leads to a large range of hybrid composites that could be investigated. The number and variations of hybrid composites to be investigated must be narrowed down to those that could be feasibly adopted in naval structures currently. Due to the large volumes of material required for marine constructions, combinations of composites that are already commercially available are the most viable option. As a result of their commercial availability and relatively established use in the naval industry, glass-fibre and carbon-fibre are the focus of this study.

The weave architecture of a composite laminate affects its high strain rate response. The crimp created in woven fabrics leads to lower peak strength and modulus [49]. Previous research into blast performance of composite sandwich panels has focussed on unidirectional continuous fibre fabrics [19], [20]. To maintain consistency and reasonable material and manufacturing costs, interlaminar hybrids, manufactured from unidirectional non-crimp fabrics, were investigated in this project.

This chapter details the preliminary analysis carried out on interlaminar hybrid glass-fibre and carbon-fibre composite sandwich panels. Following analytical calcu-

lations, a number of hybrid composite panels were selected for fabrication and high velocity impact testing. The panels were subjected to solid projectile impacts at 75 m s^{-1} and 90 m s^{-1}. The damage sustained by each panel due to impact was analysed and compared along with post-impact compression strength and stiffness. Although impact testing results in a different loading regime compared to blast, the experiments demonstrated the high strain rate behaviour of the hybrid composite sandwich panels and the resulting difference in damage. This is not possible through analytical calculations alone. The analytical and experimental results aided in the selection of composite sandwich panels for full-scale air blast testing detailed in Chapter 4.

3.2 Characterisation of Hybrid Face-Sheets

Analytical calculations were performed to understand the advantages of interlaminar hybrids. These are hybrids where the unidirectional layers contain one fibre type and they are laid up so the fibre type in each subsequent layer could be different. The type of material and orientation of different layers can be tailored to achieve desired properties as layers and materials will interact under loading. The analysis was then extended to determine the effects of using interlaminar hybrids as the face-sheets on a composite sandwich panel. The results from this analysis have been used to decide which hybrid composite sandwich panels should be fabricated for experimental investigations.

3.2.1 Laminate Stiffness

In order to predict how interlaminar hybrid composites will behave, the laminate stiffness matrices for a number of layup configurations were calculated using classical laminate theory. The constitutive equations of a single ply, or lamina, can be easily calculated when the direction of the applied stress coincides with the principal material axis. A stiffness matrix, $\boldsymbol{Q}$, defined by engineering constants can be formulated that relates stress to strain as shown in Equation 3.1 [90]. It is assumed that the lamina is in a state of plane stress (through thickness stress is ignored) and that the thickness dimension is significantly smaller than the length and width dimensions (therefore, through thickness strain is ignored).

$$\begin{bmatrix} \sigma_1 \\ \sigma_2 \\ \tau_{12} \end{bmatrix} = \begin{bmatrix} Q_{11} & Q_{12} & 0 \\ Q_{12} & Q_{22} & 0 \\ 0 & 0 & Q_{66} \end{bmatrix} \begin{bmatrix} \varepsilon_1 \\ \varepsilon_2 \\ \gamma_{12} \end{bmatrix} \tag{3.1}$$

where:

$$Q_{11} = \frac{E_1}{1 - \nu_{12}\nu_{21}} \tag{3.2}$$

$$Q_{12} = \frac{\nu_{12}E_2}{1 - \nu_{12}\nu_{21}} = \frac{\nu_{21}E_1}{1 - \nu_{12}\nu_{21}} \tag{3.3}$$

$$Q_{22} = \frac{E_2}{1 - \nu_{12}\nu_{21}} \tag{3.4}$$

$$Q_{66} = G_{12} \tag{3.5}$$

However, composite laminates are frequently fabricated from layers not aligned with the applied stresses. These layers are subjected to off-axis loading. A material coordinate system, with axes 1, 2 and 3 as defined in Figure 3.1 (a) applies to each lamina in the face-sheet. This material coordinate system can differ from the global coordinate system due to layup orientation as shown in Figure 3.1 (b). The angle between the material coordinate system and the global coordinate system defines the lamina orientation. The stiffness matrix, $\boldsymbol{Q}$, can then be transformed from material coordinates to global coordinates resulting in the transformed stiffness matrix, $\overline{\boldsymbol{Q}}$. The inclusion of rotated layers in a laminate improves the stiffness and strength in the off-axis directions and can introduce extension-shear coupling [90]. This is a negative shear strain that arises as a result of an applied stress and in addition to the expected lateral material contraction.

The rotated stiffness matrix can be extended to apply to a laminate, rather than just one lamina. Laminates may be subjected to both in-plane and transverse loading. It is assumed that the strains caused by in-plane and transverse loading can be superposed. The strains caused by bending can be defined in terms of the plate curvature, K; $\varepsilon_x = zK_x$. Since all laminae are assumed to be perfectly bonded within a laminate, they have the same in-plane strains and curvatures [94]. For the kth layer, this results in Equation 3.6, where $\overline{\boldsymbol{Q}}_k$ is the transformed stiffness matrix for the layer.

$$\boldsymbol{\sigma}_{xy_k} = \overline{\boldsymbol{Q}}_k\boldsymbol{\varepsilon}^0 + z\overline{\boldsymbol{Q}}_k\boldsymbol{K} \tag{3.6}$$

$\overline{\boldsymbol{Q}}$ can then be used to calculate the stress resultant, $\boldsymbol{N}$, and moment resultant, $\boldsymbol{M}$, about the mid-plane. These terms define stresses acting along the edge of the

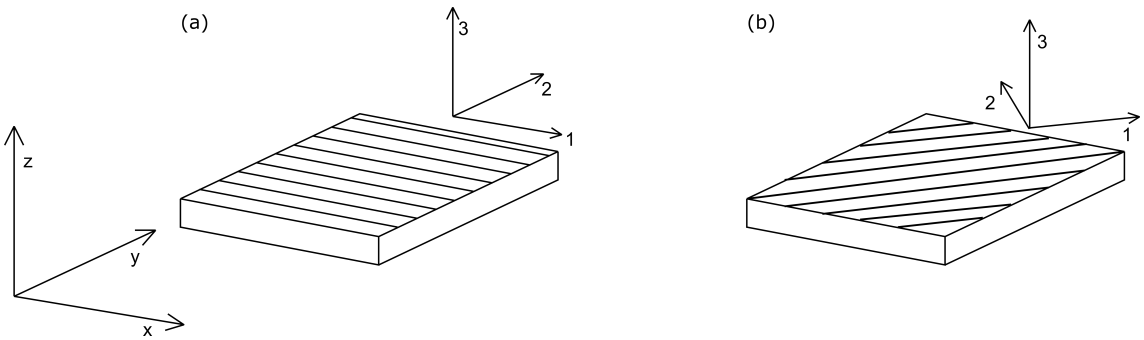


Figure 3.1: Schematic diagram showing lamina coordinate systems for: (a) a layup orientation aligned with global coordinate system and applied stresses and (b) a layup orientation not aligned with global coordinate system.

laminate in terms of equivalent forces and moments acting at the middle surface and are found by integrating the stress along the thickness of the laminate. The middle surface strains and curvatures are not a function of thickness so they can be removed from the integral. Additionally, the laminate stiffness matrix is constant for a given ply. Since the layers are a discrete thickness, the integration becomes a summation from 1 to n layers.

$$\begin{bmatrix} N_x \\ N_y \\ N_{xy} \end{bmatrix} = \boldsymbol{N} = \begin{bmatrix} \varepsilon_x^0 \\ \varepsilon_y^0 \\ \gamma_{xy}^0 \end{bmatrix} \sum_{k=1}^{n} \left[\overline{Q}_{ij}\right]_k \left(h_k - h_{k-1}\right) + \frac{1}{2} \begin{bmatrix} K_x \\ K_y \\ K_{xy} \end{bmatrix} \sum_{k=1}^{n} \left[\overline{Q}_{ij}\right]_k \left(h_k^2 - h_{k-1}^2\right) \tag{3.7}$$

$$\boldsymbol{N} = \boldsymbol{A}\boldsymbol{\varepsilon}^0 + \boldsymbol{B}\boldsymbol{K} \tag{3.8}$$

$$\begin{bmatrix} M_x \\ M_y \\ M_{xy} \end{bmatrix} = \boldsymbol{M} = \frac{1}{2} \begin{bmatrix} \varepsilon_x^0 \\ \varepsilon_y^0 \\ \gamma_{xy}^0 \end{bmatrix} \sum_{k=1}^{n} \left[\overline{Q}_{ij}\right]_k \left(h_k^2 - h_{k-1}^2\right) + \frac{1}{3} \begin{bmatrix} K_x \\ K_y \\ K_{xy} \end{bmatrix} \sum_{k=1}^{n} \left[\overline{Q}_{ij}\right]_k \left(h_k^3 - h_{k-1}^3\right) \tag{3.9}$$

$$\boldsymbol{M} = \boldsymbol{B}\boldsymbol{\varepsilon}^0 + \boldsymbol{D}\boldsymbol{K} \tag{3.10}$$

The laminate stiffness matrix and thickness terms can be combined to form new matrices defined in Equations 3.11 to 3.13. Using these newly defined matrices, the constitutive equations can be written in matrix form, known as the ABD matrix shown in Equation 3.14.

$$A_{ij} = \sum_{k=1}^{n} \left[\overline{Q}_{ij}\right]_k \left(h_k - h_{k-1}\right) \tag{3.11}$$

$$B_{ij} = \frac{1}{2} \sum_{k=1}^{n} \left[\overline{Q}_{ij}\right]_k \left(h_k^2 - h_{k-1}^2\right) \tag{3.12}$$

$$D_{ij} = \frac{1}{3} \sum_{k=1}^{n} \left[\overline{Q}_{ij}\right]_k \left(h_k^3 - h_{k-1}^3\right) \tag{3.13}$$

$$\begin{bmatrix} N_x \\ N_y \\ N_{xy} \\ M_x \\ M_y \\ M_{xy} \end{bmatrix} = \begin{bmatrix} A_{11} & A_{12} & A_{16} & B_{11} & B_{12} & B_{16} \\ A_{12} & A_{22} & A_{26} & B_{12} & B_{22} & B_{26} \\ A_{16} & A_{26} & A_{66} & B_{16} & B_{26} & B_{66} \\ B_{11} & B_{12} & B_{16} & D_{11} & D_{12} & D_{16} \\ B_{12} & B_{22} & B_{26} & D_{12} & D_{22} & D_{26} \\ B_{16} & B_{26} & B_{66} & D_{16} & D_{26} & D_{66} \end{bmatrix} \begin{bmatrix} \varepsilon_x^0 \\ \varepsilon_y^0 \\ \gamma_{xy}^0 \\ K_x \\ K_y \\ K_{xy} \end{bmatrix} \tag{3.14}$$

The $\boldsymbol{A}$ matrix represents in-plane stiffness, the $\boldsymbol{D}$ matrix represents bending stiffness whilst the $\boldsymbol{B}$ matrix contains the bending-extension coupling terms. When matrix $\boldsymbol{B}$ is non-zero, in-plane strains cause in-plane resultant forces and bending moments in the laminate. Equally bending strains result in bending moments and in-plane resultants [95]. Composite laminates are usually fabricated such that they have a balanced and symmetric structure. This eliminates $\boldsymbol{B}$ and the undesirable coupling terms. However, it may be beneficial to fabricate asymmetric sandwich panels to improve performance against loading from a particular direction.

It is then possible to calculate in-plane engineering constants for the laminates using matrix algebra [94]. To find the modulus in the x-direction, the x-direction stress over the x-direction strain must be calculated as in Equation 3.15. For symmetric laminates, this requires the solution of three equations as matrix $\boldsymbol{B}$ is zero. For non-symmetric laminates, however, six equations must be solved. This can be achieved using matrix algebra and Cramer's rule.

$$E_x = \frac{\sigma_x}{\varepsilon_x} = \frac{N_x/h}{\varepsilon_x} \tag{3.15}$$

3.2.2 Sandwich Panel Stiffness

The laminate stiffness analysis can be extended to sandwich panels. As defined previously, a composite sandwich panel is made from two composite laminate face-sheets, or skins, separated by a low density core. The core thickness is assumed to be much greater than the skin thicknesses and the core only transmits transverse shear stresses [95]. The in-plane resultants and bending moments are governed by the laminate skins, however, the distance from the mid-plane is increased by half the core thickness, $h/2$. The updated in-plane resultants and bending moments are shown in Equation 3.16 and 3.17. In these equations h_1 and h_2 are the thicknesses of the lower and upper skins, respectively.

$$\begin{bmatrix} N_x \\ N_y \\ N_{xy} \end{bmatrix} = \boldsymbol{N} = \int_{-(h/2+h_1)}^{-h/2} \begin{bmatrix} \sigma_x \\ \sigma_y \\ \sigma_{xy} \end{bmatrix} dz + \int_{-h/2}^{h/2+h_2} \begin{bmatrix} \sigma_x \\ \sigma_y \\ \sigma_{xy} \end{bmatrix} dz \tag{3.16}$$

$$\begin{bmatrix} M_x \\ M_y \\ M_{xy} \end{bmatrix} = \boldsymbol{M} = \int_{-(h/2+h_1)}^{-h/2} \begin{bmatrix} \sigma_x \\ \sigma_y \\ \sigma_{xy} \end{bmatrix} z dz + \int_{-h/2}^{h/2+h_2} \begin{bmatrix} \sigma_x \\ \sigma_y \\ \sigma_{xy} \end{bmatrix} z dz \tag{3.17}$$

In addition, a shear resultant arises due to the core. The shear stresses are a function of the shear stiffness of the core and the shear strains. The shear resultants are shown in Equation 3.18. The constitutive equations can be written in matrix form shown in Equation 3.19. In this case the $\boldsymbol{A}$, $\boldsymbol{B}$, $\boldsymbol{C}$ and $\boldsymbol{D}$ matrices are evaluated using Equations 3.20 to 3.23, where n_1 is the number of layers in the lower skin and n_2 the number of layers in the upper skin.

$$\begin{bmatrix} Q_x \\ Q_y \end{bmatrix} = \boldsymbol{Q} = \int_{-h/2}^{h/2} \begin{bmatrix} \sigma_{xz} \\ \sigma_{yz} \end{bmatrix} dz \tag{3.18}$$

$$\begin{bmatrix} N_x \\ N_y \\ N_{xy} \\ M_x \\ M_y \\ M_{xy} \\ Q_y \\ Q_x \end{bmatrix} = \begin{bmatrix} A_{11} & A_{12} & A_{16} & B_{11} & B_{12} & B_{16} & 0 & 0 \\ A_{12} & A_{22} & A_{26} & B_{12} & B_{22} & B_{26} & 0 & 0 \\ A_{16} & A_{26} & A_{66} & B_{16} & B_{26} & B_{66} & 0 & 0 \\ C_{11} & C_{12} & C_{16} & D_{11} & D_{12} & D_{16} & 0 & 0 \\ C_{12} & C_{22} & C_{26} & D_{12} & D_{22} & D_{26} & 0 & 0 \\ C_{16} & C_{26} & C_{66} & D_{16} & D_{26} & D_{66} & 0 & 0 \\ 0 & 0 & 0 & 0 & 0 & 0 & F_{44} & F_{45} \\ 0 & 0 & 0 & 0 & 0 & 0 & F_{45} & F_{55} \end{bmatrix} \begin{bmatrix} \varepsilon_x^0 \\ \varepsilon_y^0 \\ \gamma_{xy}^0 \\ K_x \\ K_y \\ K_{xy} \\ \gamma_{yz}^c \\ \gamma_{xy}^c \end{bmatrix} \tag{3.19}$$

$$A_{ij} = \sum_{k=1}^{n_1} \left[\overline{Q}_{ij}\right]_k \Big(h_k - h_{k-1}\Big) + \sum_{k=1}^{n_2} \left[\overline{Q}_{ij}\right]_k \Big(h_k - h_{k-1}\Big) \tag{3.20}$$

$$B_{ij} = \frac{h}{2}\Bigg(\sum_{k=1}^{n_2} \left[\overline{Q}_{ij}\right]_k \Big(h_k - h_{k-1}\Big) - \sum_{k=1}^{n_1} \left[\overline{Q}_{ij}\right]_k \Big(h_k - h_{k-1}\Big)\Bigg) \tag{3.21}$$

$$C_{ij} = \frac{1}{2}\Bigg(\sum_{k=1}^{n_1} \left[\overline{Q}_{ij}\right]_k \Big(h_k^2 - h_{k-1}^2\Big) + \sum_{k=1}^{n_2} \left[\overline{Q}_{ij}\right]_k \Big(h_k^2 - h_{k-1}^2\Big)\Bigg) \tag{3.22}$$

$$D_{ij} = \frac{h}{4}\Bigg(\sum_{k=1}^{n_2} \left[\overline{Q}_{ij}\right]_k \Big(h_k^2 - h_{k-1}^2\Big) - \sum_{k=1}^{n_1} \left[\overline{Q}_{ij}\right]_k \Big(h_k^2 - h_{k-1}^2\Big)\Bigg) \tag{3.23}$$

$$F_{ij} = h\overline{C}_{ij}^{c} \tag{3.24}$$

In Equation 3.24, $\overline{C}_{ij}^{c}$ are the transverse shear constants of the core. These are related to the shear stiffnesses of the core and are rotated with respect to the core's principal directions. Equation 3.19 has a similar form to Equation 3.14 with added transverse shear, however, matrix $\boldsymbol{C}$ introduces asymmetry in the stiffness matrix. In symmetric sandwich panels, the lower and upper skins are identical. This results in the $\boldsymbol{B}$ and $\boldsymbol{C}$ matrices becoming zero. There is no coupling between extension and bending and the constitutive equation takes the same form as the constitutive equation of a symmetric laminate with transverse shear [95].

3.2.3 Micromechanics of Unidirectional Composites

In order to calculate the initial stiffness matrix in Equation 3.1, engineering constants for the lamina are required for Equations 3.2 to 3.5. A lamina is assumed to be made up of uniform parallel continuous fibres, perfectly bonded to the matrix and loaded parallel to the fibres [90]. Perfect bonding results in strains that are equal in the fibres, matrix and composite. The volume fraction of a lamina is defined in Equation 3.25. The area fraction, which is the ratio of fibre to matrix cross-sectional area, is the same as the volume fraction for parallel fibres. Therefore, the rule of mixtures can be used to calculate the longitudinal modulus using Equation 3.26, where E_f is the elastic modulus of the fibres and E_m is the elastic modulus of the matrix. The transverse and shear moduli of the lamina can be calculated using Equations 3.27 and 3.28, respectively. The Poisson's ratio of the lamina can be calculated using Equation 3.29. For these analyses the fibre volume fraction was assumed to be 0.4 as this is an achievable volume fraction. The properties of the

Table 3.1: Mechanical properties of the composite sandwich panels materials and plies.

Material	Density (kg m^{-3})	Longitudinal modulus (GPa)	Shear modulus (GPa)	Poisson's ratio
Glass-fibres	2555 [96]	78.5 [96]	28.0 [96]	0.22 [96]
Carbon-fibres	1800 [97]	242.0 [97]	86.5 [96]	0.20 [96]
Gurit Prime 20LV epoxy & slow hardener	1144 [98]	3.5 [98]	0.86 [98]	0.40 [96]

glass-fibres and carbon-fibres along with resin used for these analytical calculations are shown in Table 3.1. These fibres and matrix were selected for this analysis as composite laminates will be fabricated from these materials in future experiments.

$$\upsilon_f = \frac{V_f}{V_c} \tag{3.25}$$

$$E_1 = E_f \upsilon_f + E_m(1 - \upsilon_f) \tag{3.26}$$

$$\frac{1}{E_2} = \frac{\upsilon_f}{E_f} + \frac{1 - \upsilon_f}{E_m} \tag{3.27}$$

$$\frac{1}{G_{12}} = \frac{\upsilon_f}{G_f} + \frac{1 - \upsilon_f}{G_m} \tag{3.28}$$

$$\nu_{12} = \nu_f \upsilon_f + \nu_m(1 - \upsilon_f) \tag{3.29}$$

3.2.4 Analytical Stiffness Results

The laminate stiffness method was used to calculate engineering constants for 13 different laminates. Previous research has demonstrated that laminates with 8 plies are suitable for full-scale blast experiments [19]. Fabrication using 8 plies of continuous fibre fabrics typically create a 2 mm thick laminate. Hence these calculations were performed for laminates with these parameters as they would be suitable for testing under full-scale blast. To ease large scale manufacture, stitched bi-axial glass-fibre and carbon-fibre fabrics were selected. The 13 different laminates, therefore, had 8 plies in total with varying positions and proportions of glass-fibre and carbon-fibre in groupings of 2 plies. The fibre orientation was kept constant for each laminate

analysis, $[0/90/+45/\text{-}45]_2$. This results in asymmetric laminates as this analysis is predicting the performance of one face-sheet. The engineering constants calculated for the hybrid laminates are detailed in Table 3.2. These results give an initial starting point for further investigation of these laminates.

As the number of carbon-fibre plies within a laminate is increased, the values of in-plane and transverse modulus generally increase. In addition, the direction of the carbon-fibre plies affects the laminate moduli. For laminates with an equal number of carbon-fibre plies, the presence of more [0/90] layers increases the moduli compared to laminates with more [+45/-45] layers. The proportions of glass-fibre and carbon-fibre will affect the mass per unit area of these laminates. This will in turn affect their performance under blast. Subsequently, it was desired to keep mass per unit area constant such that the effect of material positioning could be isolated. The greatest number of layup variations with constant mass per unit area can be achieved with the laminates consisting of 4 carbon-fibre plies and 4 glass-fibre plies. In addition, some of these laminates had moduli approaching or in excess of the laminates with 6 carbon-fibre bi-axial plies demonstrating that they would sufficiently highlight the effects of hybridisation.

Literature research has shown that composites are able to absorb more energy overall if the fibres with the highest energy absorption are placed as the outermost layer [39], [53], [90]. Laminates with glass-fibre layers at one outermost layer from the selected group were 4G4C, 2G4C2G and 2G2C2G2C. These laminates had the greatest moduli values within their group. Calculations were carried out for panels with these laminates positioned symmetrically and asymmetrically around the core. The analysis was also carried out for a benchmark carbon-fibre and glass-fibre sandwich panel. Panel stiffness calculations were performed for seven composite sandwich panels in total. A diagram illustrating the layup configurations for these panels is shown in Figure 3.2 along with a new naming convention. The fibre orientation for the composite sandwich panels was $[0/90/+45/\text{-}45]_2$CORE$[\text{-}45/+45/90/0]_2$ in all cases. The core material was assumed to be 20 mm thick. However, the transverse shear constants of the core were omitted as the core material will be kept the same for all sandwich panels. The $\boldsymbol{ABCD}$ stiffness matrices for the panels are shown in Equations 3.30 to 3.36. The engineering constants for the hybrid composite sandwich panels are shown in Table 3.3.

Table 3.2: Laminate stiffness results in order of increasing number of carbon-fibre layers.

Laminate Type	Longitudinal modulus (GPa)	Transverse modulus (GPa)	Shear modulus (GPa)	Poisson's ratio
Glass	13.1	13.1	4.9	0.35
6G2C	14.3	14.3	5.7	0.43
4G2C2G	21.9	21.9	4.9	0.21
2G2C4G	14.2	14.2	9.3	0.46
4G4C	22.3	22.3	5.7	0.26
2G4C2G	24.5	24.5	9.3	0.32
2C4G2C	16.2	16.2	5.7	0.40
2G2C2G2C	25.7	25.7	5.0	0.19
2C2G2C2G	15.3	15.3	11.4	0.54
2G6C	25.1	25.1	11.4	0.38
4C2G2C	17.1	17.1	11.5	0.47
2C2G4C	28.9	28.9	5.7	0.28
Carbon	30.5	30.5	11.5	0.35

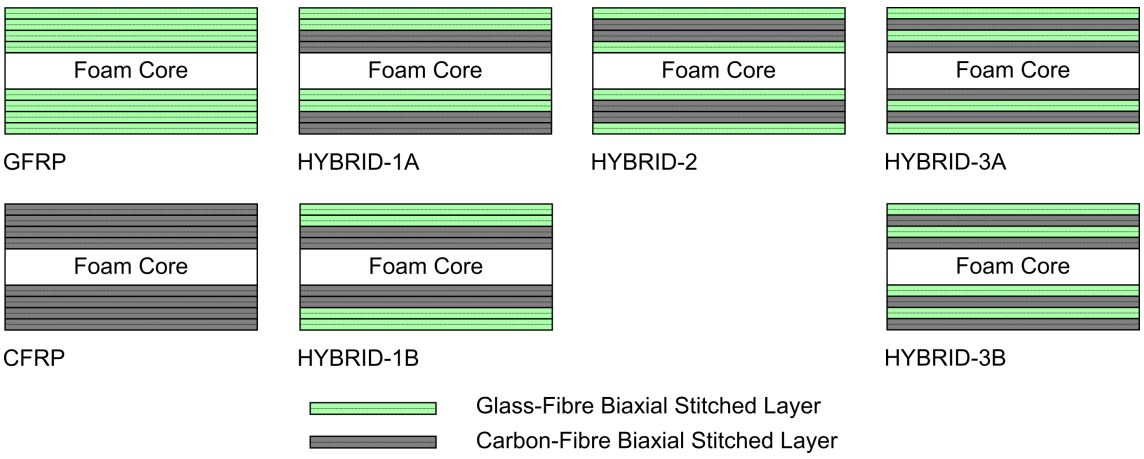


Figure 3.2: Layup configurations of the seven hybrid composite sandwich panels analysed.

GFRP:

$$\begin{bmatrix} 65.3 & 22.1 & 0 & 0 & 0 & 0 \\ 22.1 & 65.3 & 0 & 0 & 0 & 0 \\ 0 & 0 & 21.6 & 0 & 0 & 0 \\ 0 & 0 & 0 & 7250 & 2390 & 17.7 \\ 0 & 0 & 0 & 2390 & 7180 & 17.7 \\ 0 & 0 & 0 & 17.7 & 17.7 & 2340 \end{bmatrix} \times 10^9 Nm \tag{3.30}$$

CFRP:

$$\begin{bmatrix} 163.4 & 54.6 & 0 & 0 & 0 & 0 \\ 54.6 & 163.4 & 0 & 0 & 0 & 0 \\ 0 & 0 & 54.4 & 0 & 0 & 0 \\ 0 & 0 & 0 & 18200 & 5890 & 58.6 \\ 0 & 0 & 0 & 5890 & 18000 & 58.6 \\ 0 & 0 & 0 & 58.6 & 58.6 & 5870 \end{bmatrix} \times 10^9 Nm \tag{3.31}$$

Hybrid-1A:

$$\begin{bmatrix} 114.4 & 38.3 & 0 & 0 & 0 & 0 \\ 38.3 & 114.4 & 0 & 0 & 0 & 0 \\ 0 & 0 & 38.0 & 0 & 0 & 0 \\ -24.5 & -8.1 & 0 & 12700 & 4140 & 38.1 \\ -8.1 & -24.5 & 0 & 4140 & 12600 & 38.1 \\ 0 & 0 & -8.2 & 38.1 & 38.1 & 4100 \end{bmatrix} \times 10^9 Nm \tag{3.32}$$

Hybrid-1B:

$$\begin{bmatrix} 114.4 & 38.3 & 0 & 0 & 0 & 0 \\ 38.3 & 114.4 & 0 & 0 & 0 & 0 \\ 0 & 0 & 38.0 & 0 & 0 & 0 \\ 0 & 0 & 0 & 12500 & 4060 & 38.1 \\ 0 & 0 & 0 & 4060 & 12300 & 38.1 \\ 0 & 0 & 0 & 38.1 & 38.1 & 4020 \end{bmatrix} \times 10^9 Nm \tag{3.33}$$

Table 3.3: Sandwich panel mechanical properites calculated using the panel stiffness method.

Laminate Type	Longitudinal modulus (GPa)	Shear modulus (GPa)	Poisson's ratio
CFRP	36.3	13.6	0.33
GFRP	14.5	5.4	0.34
Hybrid-1A	25.4	9.5	0.34
Hybrid-1B	25.4	9.5	0.34
Hybrid-2	25.4	9.5	0.34
Hybrid-3A	16.9	13.6	0.56
Hybrid-3B	22.0	7.8	0.37

Hybrid-2:

$$\begin{bmatrix} 114.4 & 38.3 & 0 & 0 & 0 & 0 \\ 38.3 & 114.4 & 0 & 0 & 0 & 0 \\ 0 & 0 & 38.0 & 0 & 0 & 0 \\ 0 & 0 & 0 & 12700 & 4220 & 38.1 \\ 0 & 0 & 0 & 4220 & 12500 & 38.1 \\ 0 & 0 & 0 & 38.1 & 38.1 & 4190 \end{bmatrix} \times 10^9 Nm \tag{3.34}$$

Hybrid-3A:

$$\begin{bmatrix} 98.0 & 54.7 & 0 & 0 & 0 & 0 \\ 54.7 & 98.0 & 0 & 0 & 0 & 0 \\ 0 & 0 & 54.3 & 0 & 0 & 0 \\ 0 & 0 & 0 & 10800 & 5900 & 58.6 \\ 0 & 0 & 0 & 5900 & 10700 & 58.6 \\ 0 & 0 & 0 & 58.6 & 58.6 & 5860 \end{bmatrix} \times 10^9 Nm \tag{3.35}$$

Hybrid-3B:

$$\begin{bmatrix} 114.4 & 38.3 & 0 & -163.4 & 163.4 & 0 \\ 38.3 & 114.4 & 0 & 163.4 & -163.4 & 0 \\ 0 & 0 & 38.0 & 0 & 0 & 163.4 \\ -196.1 & 175.7 & 2.0 & 12700 & 4140 & 38.1 \\ 175.7 & -187.9 & 2.0 & 4140 & 12600 & 38.1 \\ 2.0 & 2.0 & 175.7 & 38.1 & 38.1 & 4100 \end{bmatrix} \times 10^9 Nm \tag{3.36}$$

The $\boldsymbol{ABCD}$ matrices and engineering constants for Hybrid-1A, Hybrid-1B and Hybrid-2 were very similar. The stiffness of these three hybrid composite sandwich panels clearly lies between the stiffness of the benchmark GFRP and CFRP panels. The asymmetry of Hybrid-1A causes coupling between stretching and bending which results in greater panel strain. Hybrid-1B should demonstrate a similar performance to Hybrid-1A whilst avoiding the coupling. Either surface of Hybrid-1B could be the absorption surface as glass-fibre is present on the outermost layer of each face. The components of the $\boldsymbol{D}$ matrix for the asymmetric Hybrid-1A are greater than for the symmetric Hybrid-1B. This is due to carbon-fibre plies in Hybrid-1A being a greater distance from the neutral axis. This indicates a reduced stiffness and strength in Hybrid-1B, however, the benefits of adopting a symmetric panel may counteract this reduction.

The stiffness calculations for Hybrid-2 are very similar to Hybrid-1A, however, the layup of Hybrid-2 could prove beneficial. As detailed by Czél et al. [56]. Placing lower elongation carbon-fibre layers between higher elongation glass-fiber layers should result in high energy absorbing failure mechanisms. In theory, the carbon-fibre layers should fracture and then delaminate from the intact glass-fibre layers.

The $\boldsymbol{ABCD}$ matrices for Hybrid-3A and Hybrid-3B, shown in Equation 3.35 and Equation 3.36 respectively, demonstrate that Hybrid-3A has a reduced stiffness compared to the other hybrid panels. Again, this is due to the plies of carbon-fibre lying closer to the neutral axis reducing the bending stiffness and due to the orientation of the carbon-fibre plies. The stiffness reduction may enable the panels to undergo greater deflection and energy absorption. Hybrid-3B has a similar stiffness to the other hybrid panels. The $\boldsymbol{B}$ and $\boldsymbol{C}$ matrices for Hybrid-3B are non-zero as the sandwich panel is asymmetric. Hybrid-3A will no longer be considered due to its significantly lower stiffness. This lower stiffness is caused by a lack of [0/90] carbon-fibre plies. Hybrid-3B will be investigated further as the intricacy of hybridisation and utilisation of thinner layers could be beneficial in energy absorption during a loading event such as blast.

3.2.5 Summary

There are a vast range of hybrid composite sandwich panels which could be fabricated. Narrowing the material selection and fabric type is necessary to investigate the effects of hybridisation systematically. This chapter has only considered unidirectional plies made from glass-fibre and carbon-fibre materials. The analytical calculations performed in this chapter highlight the effect of varying the number

of material plies and orientations even within this narrowed selection. Replacing half the glass-fibre plies within a laminate with carbon-fibre results in moduli values reaching up to 80 % of carbon-fibre laminate moduli. A number of laminates with an equal mass per unit area can be created from 4 plies of bi-axial glass-fibre and 4 plies of bi-axial carbon-fibre. Therefore, laminates with these material proportions were selected for further calculations and ultimately for experimental investigations. These analytical methods have been used to calculate the quasi-static material constants. However, the calculations do not illustrate the laminate out of plane constants, the laminate response under high strain rate loading, the strain to failure or the damage mechanisms that arise due to ply positioning and interactions. Additionally, a number of factors will affect the validity of the analytical approach. For example, the thickness of the laminates fabricated may differ from the thickness used in the calculations. Furthermore, despite using biaxial fabrics there may still be fibre misalignment. These calculations have been used to aid initial material selection. High strain rate loading is required to understand the behaviour of the laminates under representative conditions.

3.3 High Velocity Hard Projectile Impact

The overall aim of this research is to understand the blast performance of composite sandwich structures with hybrid laminate skins. However, the number of blast trials available is limited. Laboratory based high velocity impact testing was, therefore, carried out to aid further material selection prior to full-scale blast testing. Impact loading results in a high strain testing regime, approaching that of blast and shock loading. Impact and blast loading will both cause stress waves to propagate through the panels. However, impact loading is localised [49] whilst a blast wave causes a more uniform pressure across a panel surface. The response of the composite sandwich panels under impact may differ to their response under blast loading. Nevertheless, the results will help demonstrate the high strain rate behaviour of the hybrid composite skins. Furthermore, there is relatively limited available literature on high strain rate response of hybrid composite sandwch panels so experimental data, investigating both impact and blast loading, is valuable. A proportion of the following work has been published [99].

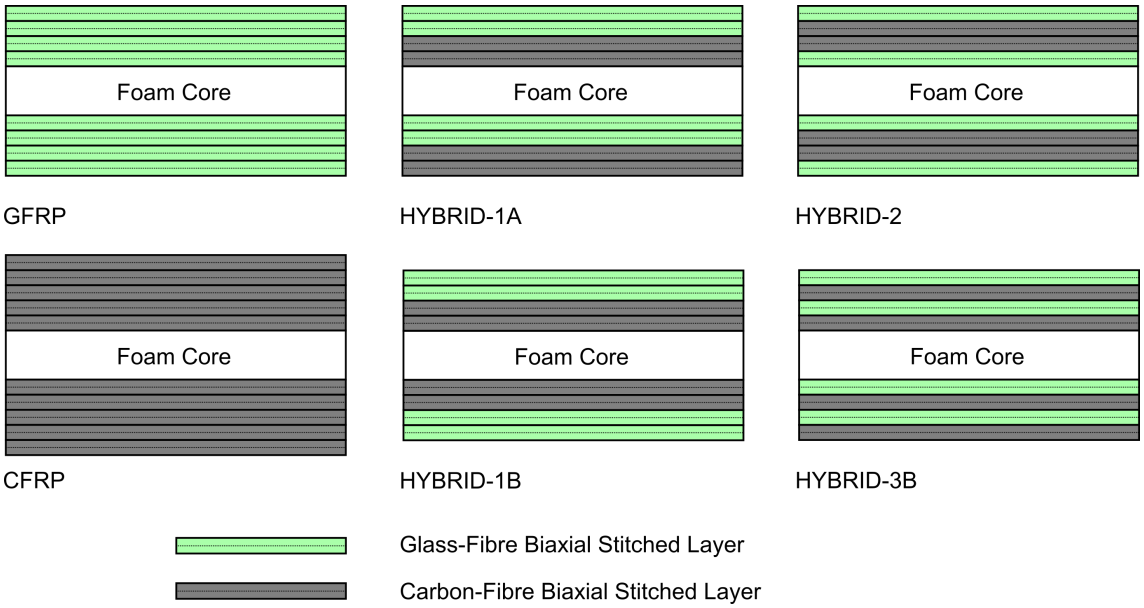


Figure 3.3: Layup configurations of the six hybrid composite sandwich panels fabricated for high velocity hard projectile impact.

3.3.1 Materials

Composite sandwich panels with glass-fibre and carbon-fibre hybrid skins were manufactured for high velocity hard projectile impact experiments. Four hybrid panels were compared to a benchmark carbon-fibre sandwich panel and a benchmark glass-fibre sandwich panel. The hybrid layups were selected based on the analytical calculations performed previously. The sandwich panel configurations are shown in Figure 3.3. All panels had a 20 mm polyethylene terephthalate (PET) foam core and approximately 2 mm thick skins made from 4 plies of bi-axial stitched continuous fibre fabrics. The panels were fabricated using vacuum assisted resin transfer moulding (VARTM) using Gurit Prime 20 LV epoxy resin and slow hardener. During VARTM the dry composite reinforcement fibres are stacked between layers of flow media and peel ply. This stack is placed on a heat plate and sealed within a vacuum bag. The resin and hardener are drawn over the fabric stack using a partial vacuum. The epoxy and resin system was selected due to its mechanical properties and high water resistance. This resin system is commonly used in naval applications. The strain to failure of the epoxy and hardener is 3.5 % which is well matched with the strain to failure of the glass-fibres used in the laminate skins.

The laminate skins were fabricated from biaxial E-glass fibre, 600 gsm, and high strength biaxial carbon fibre, 400 gsm. The plies were oriented in a quadriaxial

Table 3.4: Mechanical properties of the composite sandwich panels materials and plies.

Material	Density (kg m^{-3})	Longitudinal modulus (GPa)	Longitudinal tensile strength (MPa)	Shear strength (MPa)	Longitudinal compressive strength (MPa)
Glass-fibres	2555 [96]	78.5 [96]	2000.0 [96]	-	4500.0 [96]
Carbon-fibres	1800 [97]	242.0 [97]	4500.0 [97]	-	4950.0 [96]
Gurit Prime 20LV epoxy & slow hardener	1144 [98]	3.5 [98]	0.86 [98]	0.40 [96]	
XE603/epoxy bi-axial GFRP ply	1618	16.5	409.6	47.0	882.6
XC411/epoxy bi-axial CFRP ply	1310	40.5	758.6	47.0	850.0
PET GR150 foam core	150 [100]	0.2 [100]	3.3 [100]	1.4 [100]	2.6 [100]

layup, to create quasi isotropic laminates, $[0/90/+45/-45]_2$CORE$[-45/+45/90/0]_2$. The properties for the materials used, taken from the manufacturer data sheets and a materials database, along with bi-axial laminate properties calculated using the rule of mixtures are detailed in Table 3.4. The material properties, therefore, are only approximations as the manufacturing procedures vary from those described in the material data sheets. The fibre volume fractions for each panel were calculated using the fibre densities and the areal densities of the dry fibre plies provided by the manufacturers. The volume of fibres within each ply was calculated by dividing the weight of the fabric in each dry fibre ply by the fibre density. Once manufactured, the skin thickness of the panels was measured to determine the volume of each ply including the resin. The total volume occupied by the fibres within a ply could then be calculated.

The rule of mixtures was then used to calculate the laminate bulk density (ρ) using Equation 3.37 where ρ_f is the fibre density, ρ_m is the matrix density and υ_f is the fibre volume fraction. The longitudinal modulus of the bi-axial laminate was calculated using the rule of mixtures shown in Equation 3.38. The Krenchel factor or composite efficiency factor, η, takes into account the contribution of the fibres to ply stiffness and strength depending on their orientation. It is a simplification of the stiffness matrix calculation shown in Section 3.2. The Krenchel factor was

taken as 0.5 for a bi-axial ply. The tensile and compressive strengths of each ply were calculated using Equation 3.39 where σ_f and σ_m are the failure strengths of the fibres and matrix respectively. In tension this equation holds true when the breaking strain of the fibres is greater than the breaking strain of the matrix. In addition, σ_f should strictly be the fibre stress at a strain corresponding to matrix failure. Tensile strength calculated here is, therefore, likely to be an overestimation. In addition, the equation neglects fibre strength variation and flaws [90]. The compressive strength of a laminate is difficult to predict due to voids, fibre bunching and fibre misalignment or waviness. Alternative equations exist which relate the compressive strength of a laminate to the shear modulus of the matrix as shear or buckling in compression is the most likely failure mode. However, agreement between predicted and experimental compressive strength is poor. Equation 3.38 gave the most conservative estimate for compressive strength, however, it is certainly an overprediction. The shear strength given in Table 3.4 for the composite plies are the interlaminar shear strength properties taken from manufacturer data sheets for slightly different layup configurations. All the material properties detailed for the foam core are taken from manufacturer data sheets.

$$\rho = \rho_f \upsilon_f + \rho_m(1 - \upsilon_f) \tag{3.37}$$

$$E = \eta E_f \upsilon_f + E_m(1 - \upsilon_f) \tag{3.38}$$

$$\sigma = \eta \sigma_f \upsilon_f + \sigma_m(1 - \upsilon_f) \tag{3.39}$$

The modulus and strength of bi-axial laminates has been calculated using the rule of mixtures as the true volume fraction can be calculated following panel fabrication. In addition, the rule of mixtures enables the calculation of tensile and compressive strength. The values in Table 3.4 act to highlight the predicted difference between the glass-fibre and carbon-fibre laminate properties. A more thorough calculation was performed to generate the $\boldsymbol{ABCD}$ stiffness matrices for the hybrid composite panels using an estimated volume fraction. These are shown in Equations 3.30 to 3.36. This matrix enables the calculation of in-plane moduli shown in Table 3.3.

The carbon-fibre panel had 5 plies of bi-axial fibre fabric within each skin to maintain a comparable mass per unit area between each panel. By increasing the ply count in the CFRP panel, the equivalent bending stiffness of the panel was increased by 7.72 kN m^{-2}. Table 3.5 details the calculated mass per unit area, bending stiffness

Table 3.5: Properties of the six hybrid composite sandwich panels fabricated for high velocity hard projectile impact.

Panel type	Areal density (kg m^{-2})	Equivalent bending stiffness (kN m^{-2})	Fibre volume fraction
GFRP	9.47	11.1	0.36
CFRP	9.55	31.1	0.31
Hybrid-1A	8.86	18.2	0.37
Hybrid-1B	8.86	19.0	0.34
Hybrid-2	8.86	16.5	0.40
Hybrid-3B	8.86	16.5	0.40

and fibre volume fraction for the six panels. The fibre volume fraction is an average for each panel calculated from the mean of the volume fraction in the glass-fibre plies and carbon-fibre plies.

3.3.2 Methods

To investigate the impact performance of the panels, experiments were performed using a gas gun apparatus. An aluminium projectile with a hemispherical nose was selected. The projectile had a diameter 24.90 ± 0.05 mm, length 25.45 ± 0.05 mm and weight 25.5 ± 0.2 g. Impact velocities of 75 ± 3 m s^{-1} and 90 ± 3 m s^{-1} were selected as this would lead to projectile kinetic energies of 77 ± 3 J and 100 ± 3 J respectively. The higher velocity resulted in a 30 % increase in projectile kinetic energy. These velocities were chosen as they would cause significant panel damage and deflection under impact but would not lead to full penetration of the panel by the projectile. The projectiles were accelerated along a 3 m long barrel and the velocity was measured using two pairs of infrared sensors (IR) just before the barrel exit. The end of the barrel and the sandwich panels were contained within a transparent safety box constructed from thick polycarbonate panels, steel panels and aluminium extrude. The composite sandwich panels were 160 × 160 mm in size and were bolted into a steel fixture using twelve M8 bolts tightened to a torque of 30 Nm. The steel fixture had an opening 75 × 75 mm. A diagram showing the panel size and bolt hole locations is shown in Figure 3.4. In order to record the deflection of the panels under impact, two high speed cameras (Phantom Miro LC310) were synchronised and located behind the target outside the chamber. 3D DIC was performed on the high speed images recorded. A top down view of the gas gun and camera setup is shown in Figure 3.5.

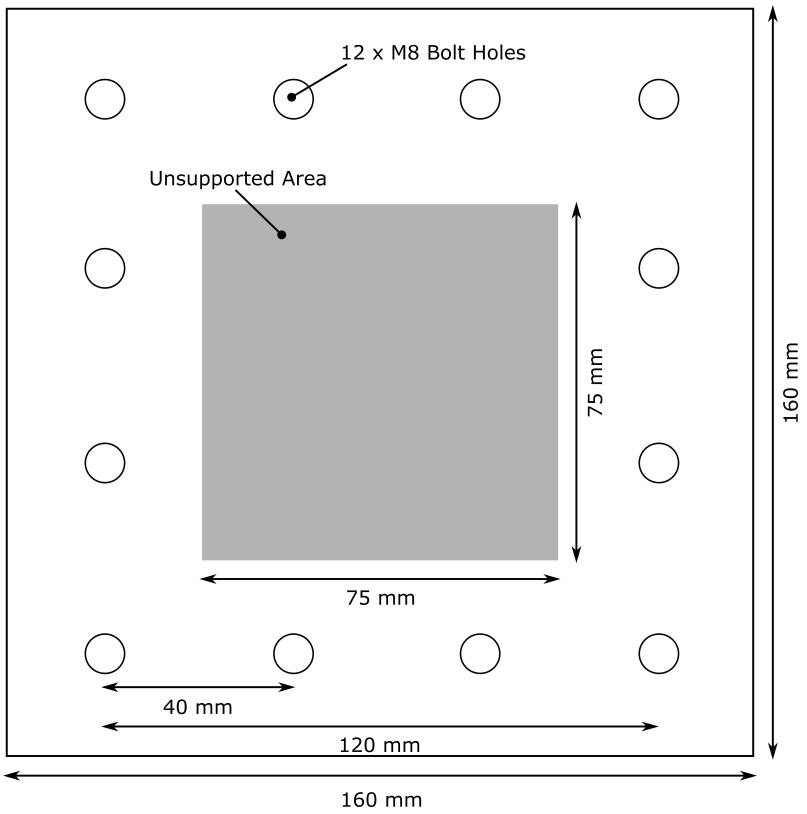


Figure 3.4: Diagram showing the impact panel size, bolt hole locations and unsupported area of the panel.

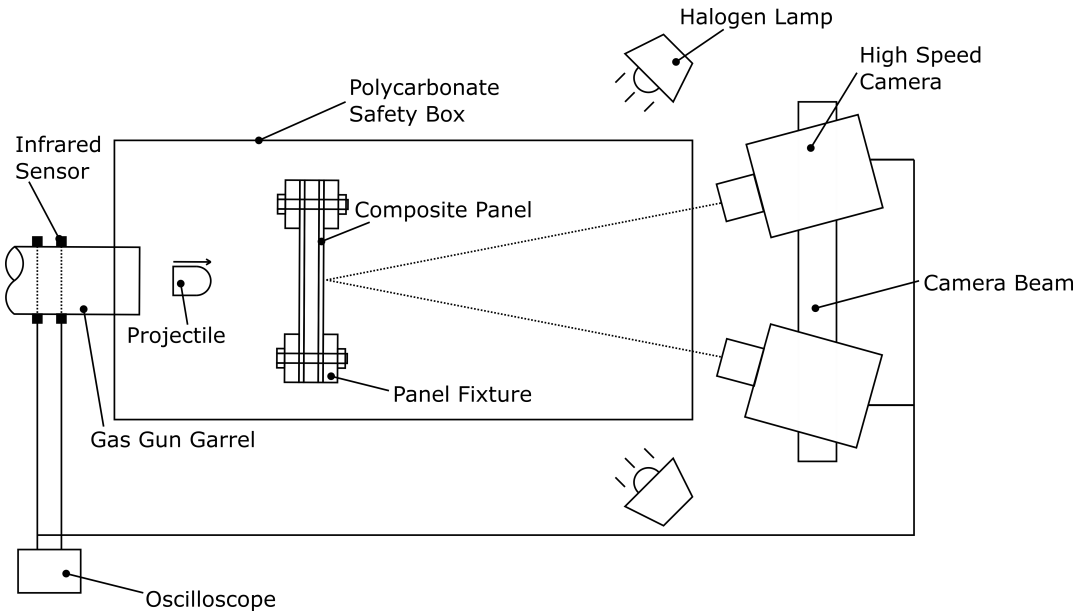


Figure 3.5: Top down schematic view of the experimental gas gun test up.

3.3.2.1 Three-Dimensional Digital Image Correlation

3D DIC is the main measurement technique used throughout the experiments performed. To perform 3D DIC, two cameras must be placed with an angle of 25° between the camera sensors and focussed on the centre of the target [101]. A diagram detailing the camera setup and distances required are shown in Figure 3.6.

It is necessary to calculate the distance from the centre of the panel to the centre of the camera sensor, D_{C}, the perpendicular distance between the centre of the panel and the camera sensor, D_1, and the distance between the high speed cameras, D_2. The longest panel length, P_L, lens length, l, and camera sensor size, s, will dictate these distances. The formulae for calculating angles A and B from the camera sensor size and lens length are shown in Equation 3.40 and 3.41 respectively. The distance between the centre of the panel and the camera sensor is calculated using Equation 3.42. Equation 3.43 provides the perpendicular distance from the camera sensor to the panel surface and Equation 3.44 gives the distance between the two cameras. For the high velocity impact experiment, fixed focal length lenses of 50 mm were used on both cameras hence the perpendicular distance between the centre of the target and the centre of the camera sensors was 970 mm. The two cameras were separated by a distance of 430 mm to achieve this angle.

$$A = \tan^{-1}\left(\frac{s/2}{l}\right) \tag{3.40}$$

$$B = 180^\circ - (77.5^\circ + A) \tag{3.41}$$

$$D_C = \frac{\left(\frac{P_L}{2}\right)\sin B}{\sin A} \tag{3.42}$$

$$D_1 = D_C \cos(12.5^\circ) \tag{3.43}$$

$$D_2 = 2D_C \sin(12.5^\circ) \tag{3.44}$$

The cameras are then calibrated such that their relative distance to one another is recorded. To carry out calibration, a calibration object known to the GOM Correlate software is held in multiple orientations and photographs are simultaneously taken using the two cameras. From the image series, the location of the two cameras in 3D space is determined. For the high velocity impact experiment a 120 mm × 96 mm uncoded calibration panel was used. Figure 3.7 (a) and (b) shows calibration images

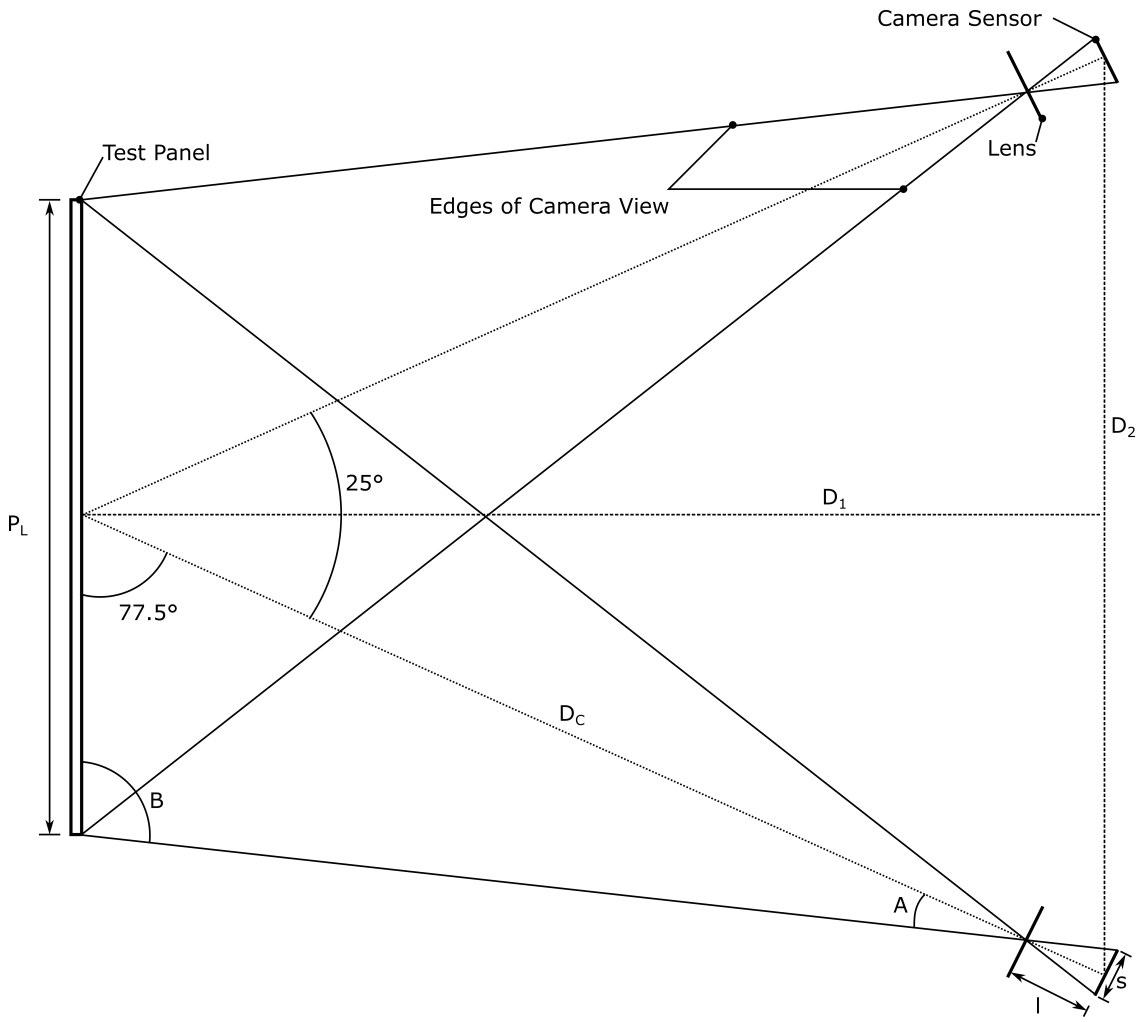


Figure 3.6: Diagram of camera location calculations for 3D DIC.

of the calibration panel from the left and right camera. In order to facilitate DIC, a specimen has to have a random black and white speckle pattern applied to its surface. Therefore, the panels were spray painted matt white and a random black speckle pattern was appplied to the back surface of the panel. It is recommended that the specimen have roughly 50 % coverage from speckles on the surface [101]. The DIC algorithm is then able to track each facet containing a unique speckle pattern and calculates the deformation from the sequence of synchronised images. The recommended speckle pattern is 3-5 pixels. The largest dimension of interest was 70 mm and the resolution of the Phantom Miro LC310 cameras at the required frame rate of 39,000 fps is 256 pixels across this length. This means that each pixel represents 0.3 mm on the panel surface. Therefore each speckle was required to be between 0.9 mm and 1.5 mm. A black marker was used to create the speckles this size. Figure 3.7 (c) and (d) shows the speckled test panel from the left and right cameras. Full details of the DIC technique are provided in Sutton et al. [102].

39,000 frames per second were recorded on each camera following activation of the camera trigger. During the gas gun experiments, the trigger was activated by a signal generated by the IR sensors at the barrel exit. The cameras are synchronised using a 5 V transistor-transistor-logic (TTL) signal produced by one camera and received by both each time the shutter opens, to ensure they open on both cameras at the same time. During camera recording, the panels were illuminated using halogen lamps. The lamps were turned on shortly before the test to prevent any heating effects.

3.3.3 Results

3.3.3.1 75 m s^{-1} Impact Velocity

Full-field deflection contour images of all six panel types, when subjected to impact velocity 75 m s^{-1} are shown in Figure 3.8. These image series show that the GFRP panel experiences the greatest and most widespread deflection at this impact velocity. This is a result of its reduced stiffness as shown in the $\boldsymbol{ABCD}$ matrix, Equation 3.30. The CFRP panel demonstrates the lowest deflection due to its high stiffness. For the hybrid panels, panel stiffness negatively correlates with out-of-plane deflection as expected.

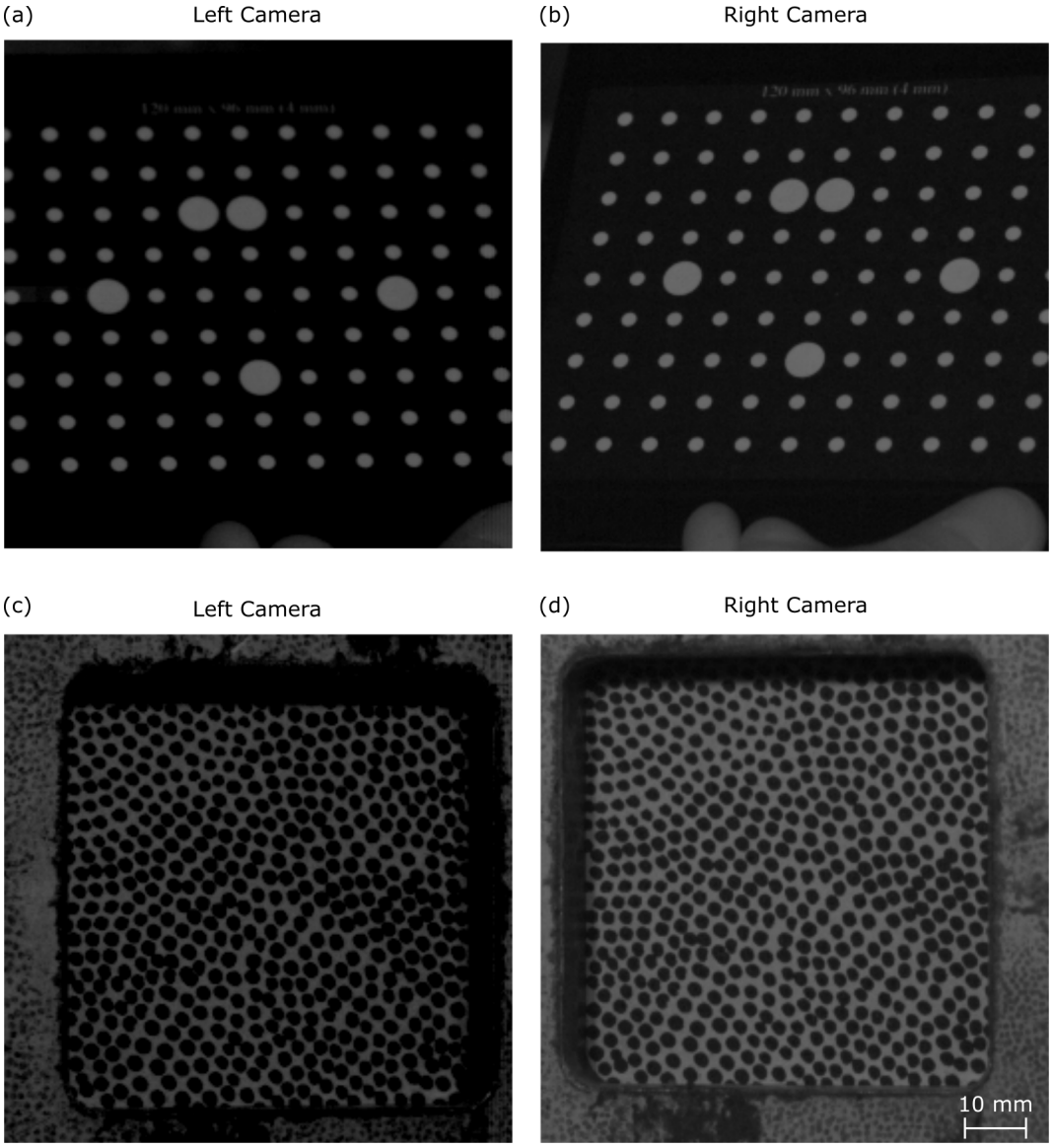


Figure 3.7: Photographs from high speed cameras showing: (a) and (b) calibration panel from left and right cameras, (c) and (d) panel held in fixture with speckle pattern applied.

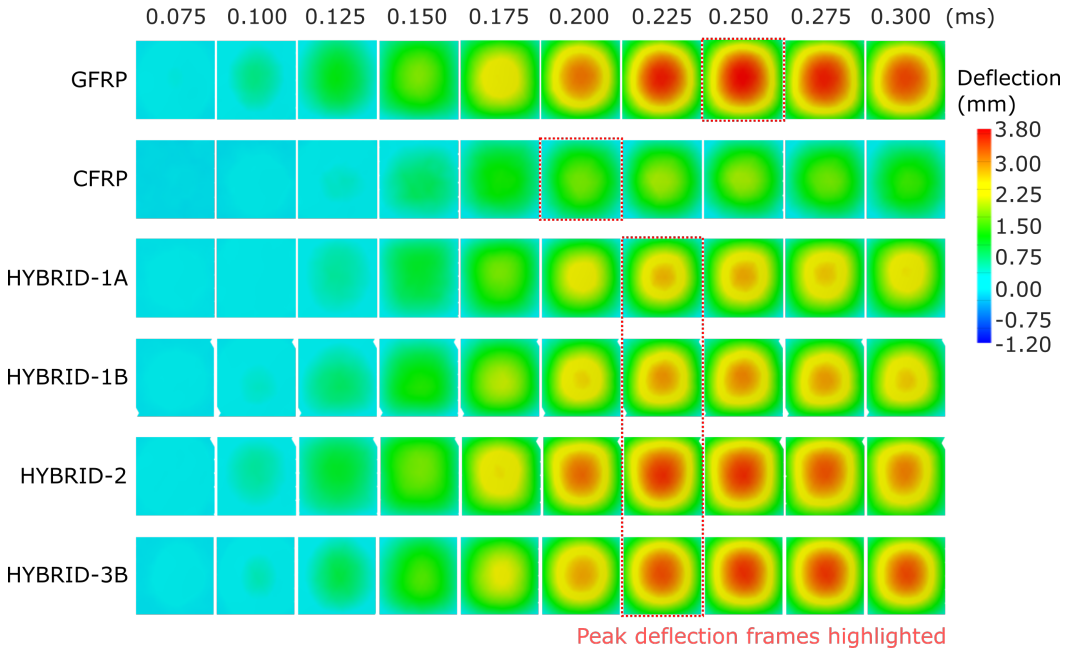


Figure 3.8: Full field out-of-plane displacement from DIC of all panel types under impact velocity 75 ± 3 m s^{-1}.

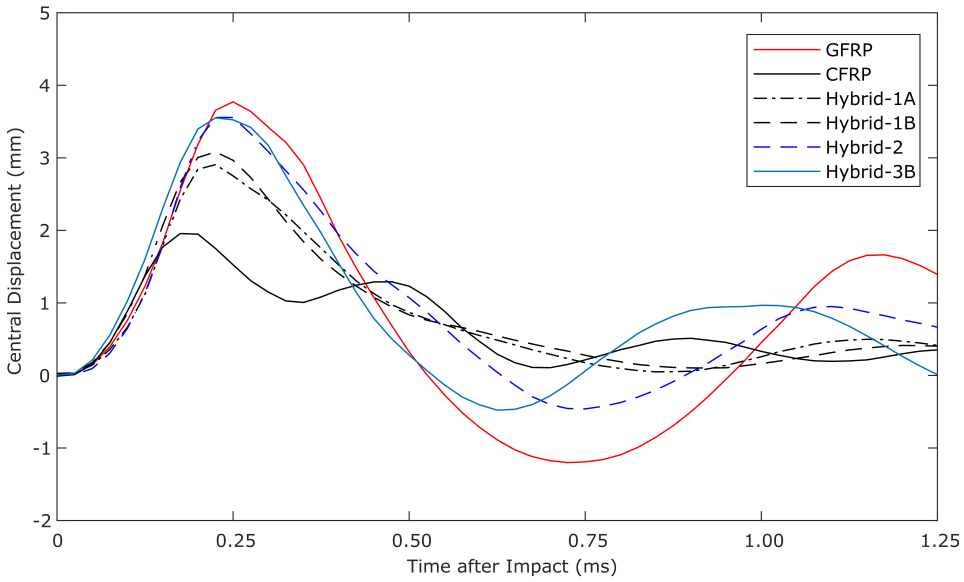


Figure 3.9: Central point out-of-plane displacement versus time plot under impact velocity 75 ± 3 m s^{-1}.

The out-of-plane deflection of the centre point of each panel is shown in Figure 3.9. The maximum central deflection of the GFRP panel was 3.8 mm, this panel experienced a negative rebound of -1.2 mm. The maximum deflection of the CFRP panel was 1.96 mm at 0.2 ms and it experienced another smaller peak at 0.5 ms without returning to zero deflection in between. The maximum central displacement of Hybrid-1A was 2.9 mm. Hybrid-1A does not return to zero before deflecting again. The behaviour of Hybrid-1B was similar to Hybrid-1A when subjected to impact velocity 75 m s^{-1}. Hybrid-1B deflected by 3.1 mm. Hybrid-2 and Hybrid-3B reach maximum deflections of 3.56 mm and 3.55 mm, respectively. These hybrid panels experienced a negative rebound, like the GFRP panel, before oscillating again. Along with high deflection, the GFRP panel experiences the greatest major strain on the rear skin, 1.06 %, as shown in Figure 3.10. Magnitude of central major strain correlates with central deflection for all panels. The central point strain rate for each panel is shown in Figure 3.11. This is calculated by differentiating the central point major strain for each panel, shown in Figure 3.10, with respect to time. The GFRP panel experiences a peak strain rate of 124 s^{-1}. The peak strain rate for all other panels lies between 50 s^{-1} and 100 s^{-1}.

The deflection of the horizontal cross-section at discrete intervals of time for the GFRP panel can be seen in Figure 3.12. Due to the thickness of the steel fixture used to clamp the sandwich panels in place, shadows were cast at the edges of the exposed panel hence the boundaries appear to displace under impact in the cross-section plots. The cross-sectional displacement is shown for the CFRP panel in Figure 3.13. It is clear from Figure 3.13 that the CFRP panel deflects less and the cross-section does not return to zero at 0.375 ms before making another positive deflection. Figure 3.14 shows the displacement of the central cross-section for Hybrid-1A. The distance between deflection lines in Figure 3.14 (b), as the panel nears zero, is significantly reduced. This is due to the deceleration of Hybrid-1A, caused by damage within the panel. Figure 3.15 shows the horizontal cross-sectional deflection for Hybrid-2. This hybrid undergoes a typical deflection and negative rebound. The cross-section diagrams for Hybrid-1B and Hybrid-3B can be found in the Appendix. Hybrid-1A and Hybrid-2 have been included here as these were the hybrid panels which experience the least and the greatest deflection, respectively.

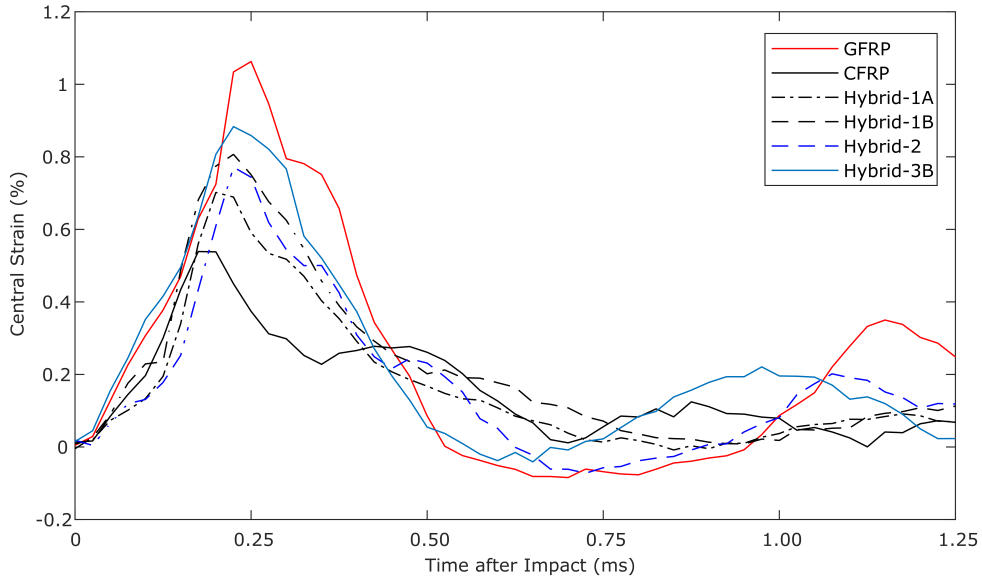


Figure 3.10: Central point major strain versus time plot under impact velocity 75 ± 3 m s^{-1}.

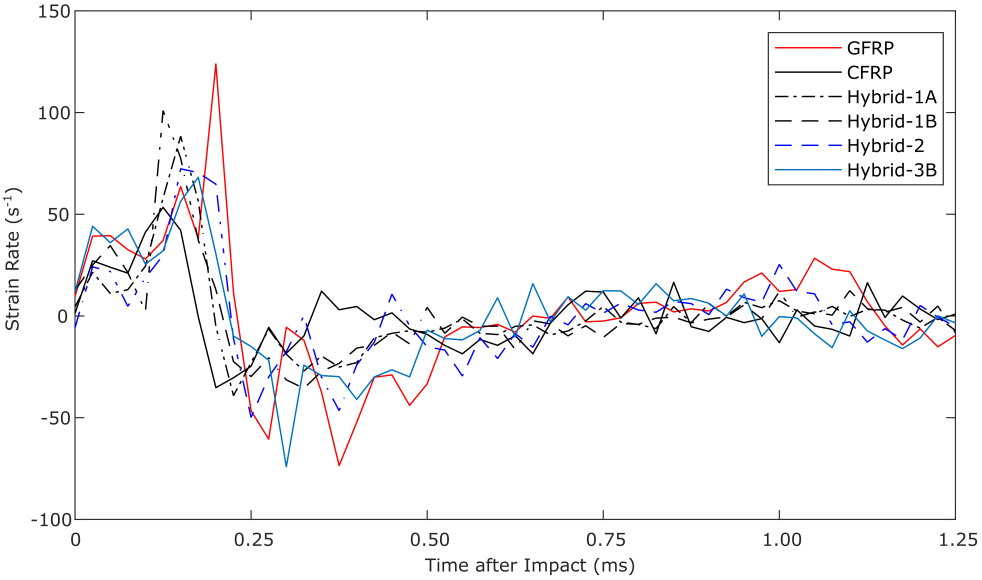


Figure 3.11: Central point major strain rate versus time plot under impact velocity 75 ± 3 m s^{-1}.

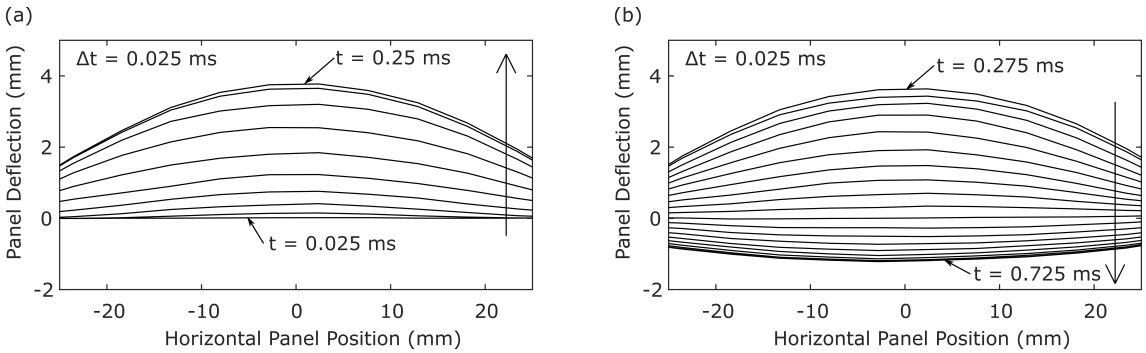


Figure 3.12: Central horizontal cross-section of GFRP panel showing: (a) outward out-of-plane deflection and (b) panel return under impact velocity 75 ± 3 m s^{-1}.

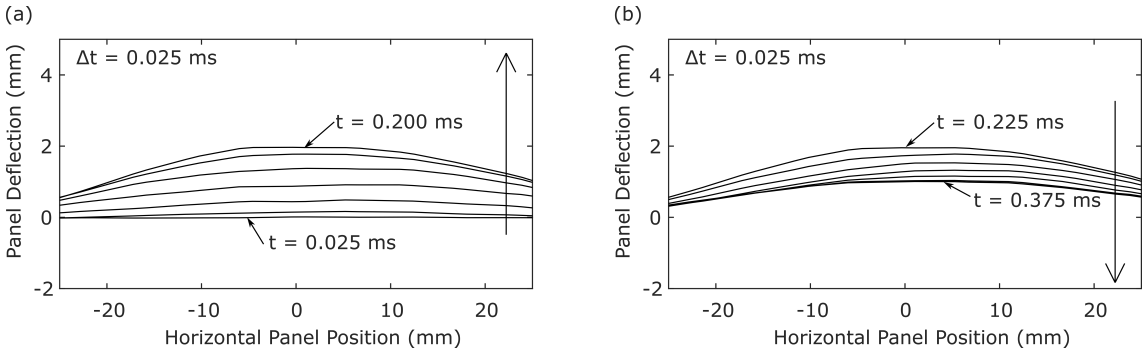


Figure 3.13: Central horizontal cross-section of CFRP panel showing: (a) outward out-of-plane deflection and (b) panel return under impact velocity 75 ± 3 m s^{-1}.

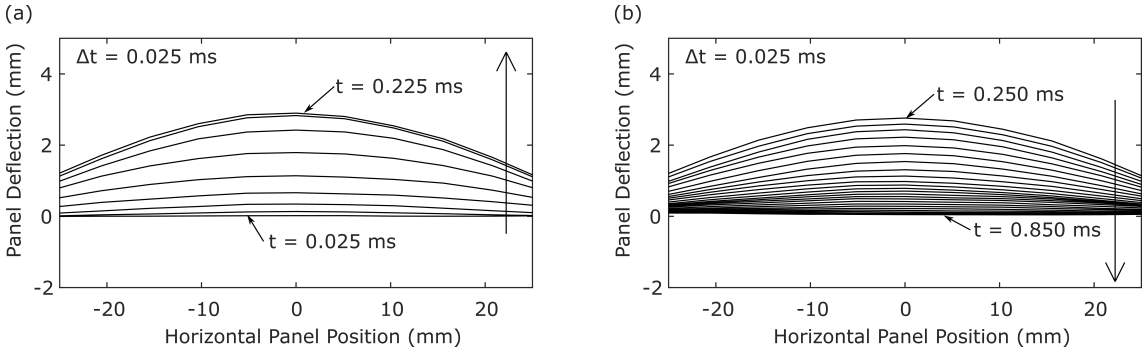


Figure 3.14: Central horizontal cross-section of Hybrid-1A panel showing: (a) outward out-of-plane deflection and (b) panel return under impact velocity 75 ± 3 m s^{-1}.

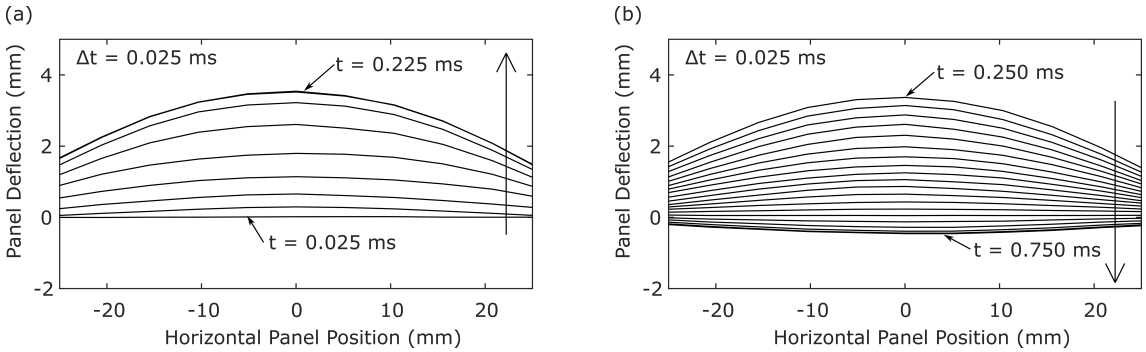


Figure 3.15: Central horizontal cross-section of Hybrid-2 panel showing: (a) outward out-of-plane deflection and (b) panel return under impact velocity 75 ± 3 m s^{-1}.

3.3.3.2 90 m s^{-1} Impact Velocity

The out-of-plane deflection of the centre point of each panel under 90 m s^{-1} impact is shown in Figure 3.16. The central point major strain is shown in Figure 3.17. The GFRP panel experiences the greatest deflection and strain during the first deflection. The deflection and strain of this panel are 4.02 mm and 1.12 % respectively. Hybrid-1A, Hybrid-2 and Hybrid-3B have maximum deflections of 2.86 mm, 3.62 mm and 3.71 mm, respectively. Again, the hybrids lie between the CFRP and the GFRP panels. These three hybrids then undergo an overdamped return towards zero due to the damage decelerating the panels and preventing a damped oscillatory response. Since the GFRP panel does oscillate after impact, it implies that the GFRP panel has experienced the least damage. Once again, panel stiffness negatively correlates with initial deflection under impact.

Under 90 m s^{-1} impact, the CFRP and Hybrid-1B panels exhibited two deflections with the second deflection greater than the initial one. Neither of the panels returned to zero displacement between deflections. The projectile remained embedded in the Hybrid-1B panel. A repeat experiment of this impact demonstrated the same behaviour. The double deflection peaks, shown in Figure 3.16 are likely to be caused by significant panel damage reducing the overall stiffness and enabling a greater second deflection. The velocity of Hybrid-1B during the second peak is reduced indicating the added mass of the embedded projectile in this panel contributes to its increased deflection. The velocity of Hybrid-1B is shown in Figure 3.18. The projectile embedding into Hybrid-1B indicates that the ballistic limit for this panel is lower than any other panel configuration tested.

The deflection of the horizontal cross-section for the GFRP panel under impact velocity of 90 m s^{-1} is shown in Figure 3.19. This panel demonstrates a symmetric outward deflection and rebound with uniform spacing. This indicates that the panel suffers from little damage. The horizontal cross-section for the CFRP panel under the higher velocity impact is shown in Figure 3.20. This CFRP panel reaches its rebound minimum at 0.4 ms before deflecting in a positive direction again. The contours highlight where damage may be present in the cross-section. Hybrid-1A has a relatively symmetric deflection, as shown in Figure 3.21. The rebound stroke indicates deceleration as the panel approaches zero. Finally, the cross-section for Hybrid-2 is shown in Figure 3.22. Hybrid-2 experiences a long and significantly decelerated return to zero and does not deflect positively again. The damage suffered by Hybrid-2 causes panel deceleration rather than a reduction in stiffness like the CFRP and Hybrid-1B panels.

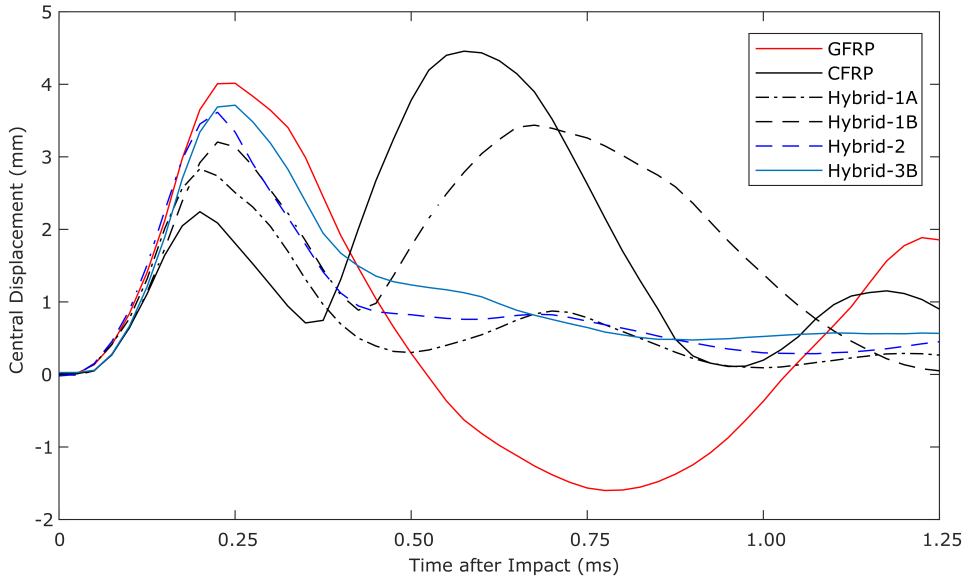


Figure 3.16: Central point out-of-plane displacement versus time plot under impact velocity 90 ± 3 m s^{-1}.

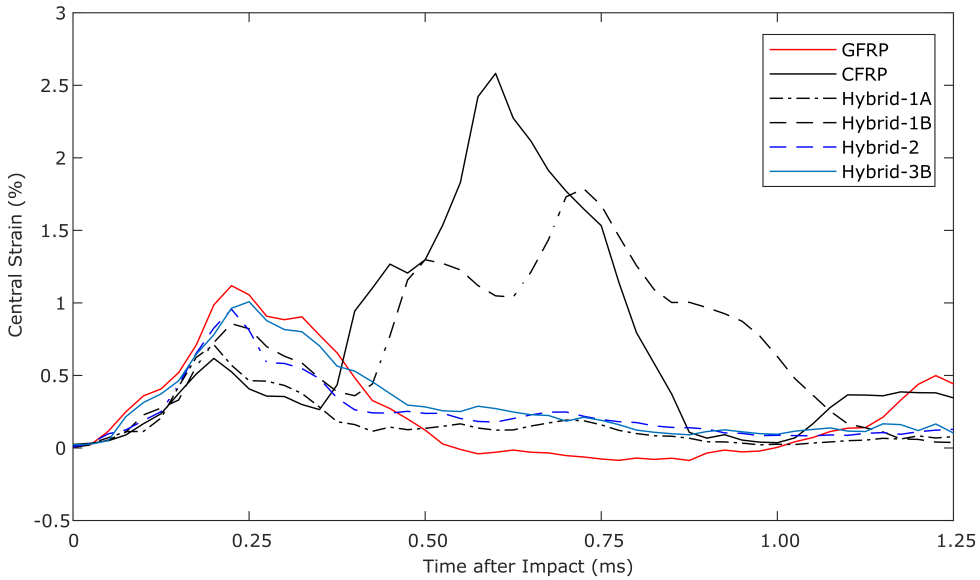


Figure 3.17: Central point major strain versus time plot under impact velocity 90 ± 3 m s^{-1}.

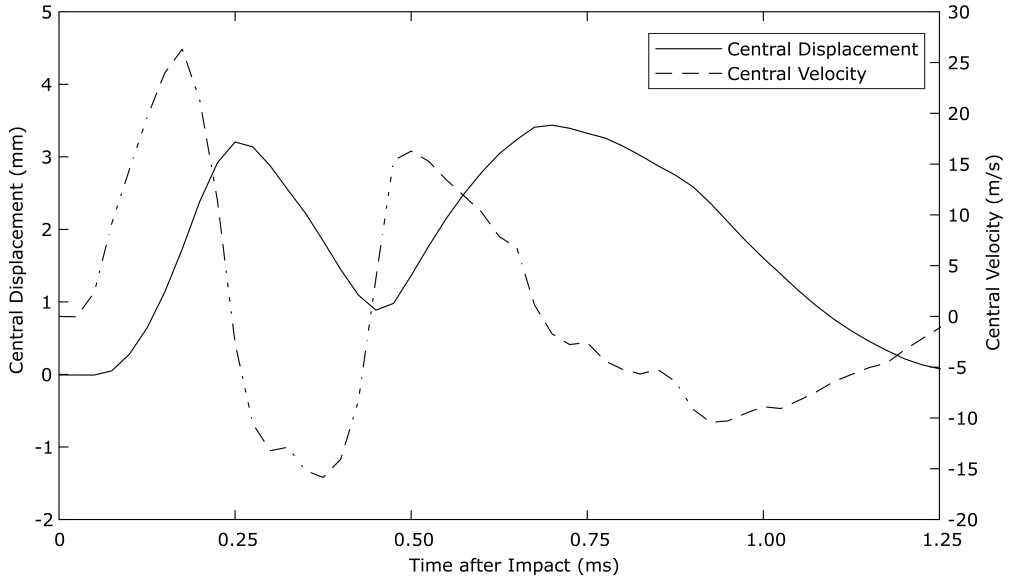


Figure 3.18: Central point displacement and velocity for Hybrid-1B under impact velocity 90 ± 3 m s^{-1}.

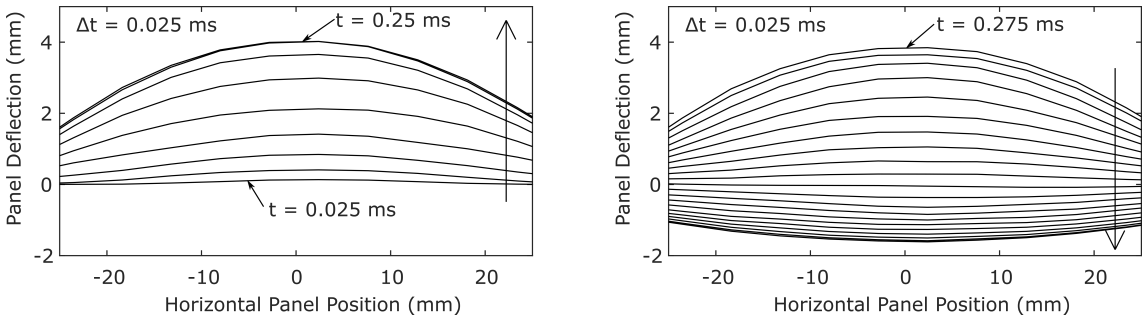


Figure 3.19: Central horizontal cross-section of GFRP panel showing: (a) outward out-of-plane deflection and (b) panel return under impact velocity 90 ± 3 m s^{-1}.

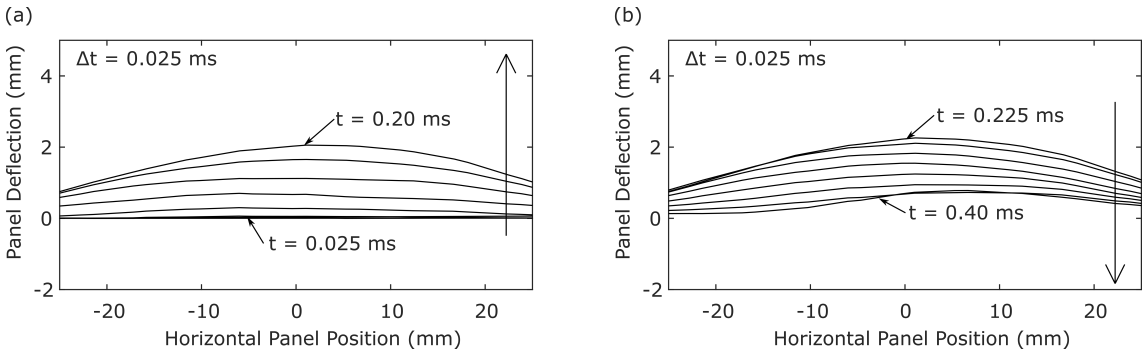


Figure 3.20: Central horizontal cross-section of CFRP panel showing: (a) outward out-of-plane deflection and (b) panel return under impact velocity 90 ± 3 m s^{-1}.

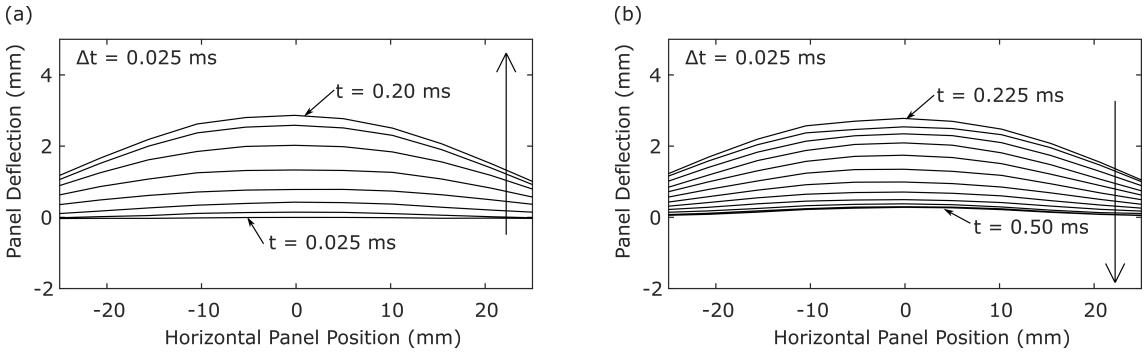


Figure 3.21: Central horizontal cross-section of Hybrid-1A panel showing: (a) outward out-of-plane deflection and (b) panel return under impact velocity 90 ± 3 m s^{-1}.

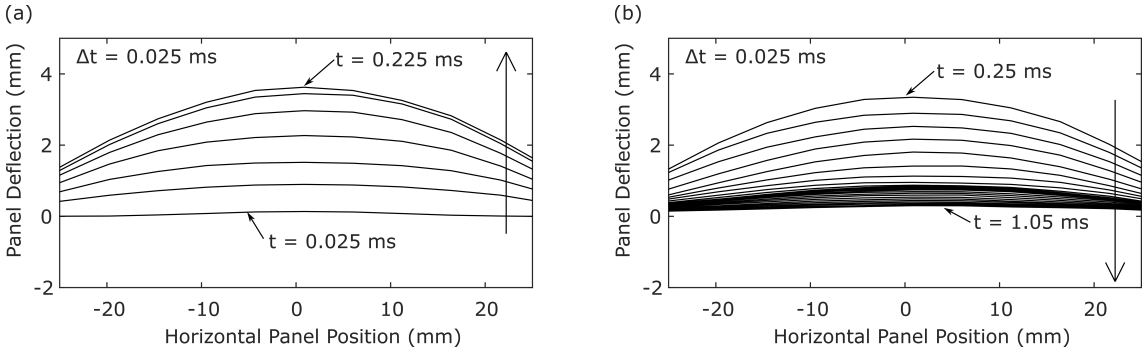


Figure 3.22: Central horizontal cross-section of Hybrid-2 panel showing: (a) outward out-of-plane deflection and (b) panel return under impact velocity 90 ± 3 m s^{-1}.

Table 3.6: Details of the characteristics of each panel under high velocity hard projectile impact.

Panel type	Impact velocity (m s^{-1})	Max centre deflection (mm)	Max centre strain (%)	Specific deflection (mm kg^{-1} m^2)	Specific strain (% kg^{-1} m^2)
GFRP	78	3.77	1.06	0.400	0.113
	89	4.02	1.12	0.428	0.119
CFRP	73	1.96	0.54	0.194	0.054
	88	4.46†	2.58†	0.442	0.256
Hybrid-1A	78	2.91	0.70	0.322	0.077
	89	2.86	0.71	0.316	0.079
Hybrid-1B	78	3.08	0.81	0.341	0.090
	89	3.44†	1.79†	0.381	0.198
Hybrid-2	78	3.56	0.77	0.394	0.085
	89	3.62	0.96	0.400	0.106
Hybrid-3B	74	3.55	0.88	0.393	0.097
	90	3.71	1.01	0.410	0.112

†Maximum deflection and strain from second peak

Table 3.6 details the maximum deflection and strain for each panel at its centre point, along with these values normalised by the panel areal density. An increase in panel areal density should theoretically improve panel impact resilience, therefore, the specific results remove this influencing factor. The lowest specific deflection is exhibited by CFRP under 75 m s^{-1} impact. Under impact velocity of 90 m s^{-1}, however, the CFRP panel suffers from the greatest specific deflection and experiences major damage. Overall the lowest specific deflections are demonstrated by Hybrid-1A, this panel also exhibits the lowest specific strains, despite the coupling effect caused by asymmetry of the panel layup. Although reduced specific deflection and strain would appear to be beneficial for a panel under impact, it is important to consider the damage sustained by each panel configuration and the post-impact behaviour and strength.

3.4 Post Impact Damage & Compression

Materials implemented on a naval vessel may be required to continue in service following projectile impact or blast loading. Hence damage analysis and post-impact edgewise compression tests were performed on the composite sandwich panels, following high velocity impact. The type of hybrid utilised in the skin is expected to affect the extent and type of damage, hence influence the post-impact compressive strength of the panels. Post-impact flexure and flatwise compression would primarily test the strength of the core, whereas the motivation for these experiments was to assess the influence of the skins.

3.4.1 Methods

3.4.1.1 Damage Analysis

Following impact testing, the front skin of the panels were photographed. The panels were then sectioned through the centre-line and photographed again. All photographs were taken in line with a steel rule, to allow for size calibration of the images. A MATLAB script was created which loaded each image to the screen and enabled the user to click on each corner of a straight section of a core crack as well as debonds and delaminations. The extent of front view skin delamination, cross-sectional view skin delamination, core damage length and projectile penetration depth was recorded. The cross-sectional skin delamination was calculated as a percentage of the total panel cross-sectional length. All other damage parameters were recorded in millimeters. In addition, each panel was inspected for qualitative damage catagories. Figure 3.23 shows an example of the images used and an example of how the user would select a damage path using the MATLAB script.

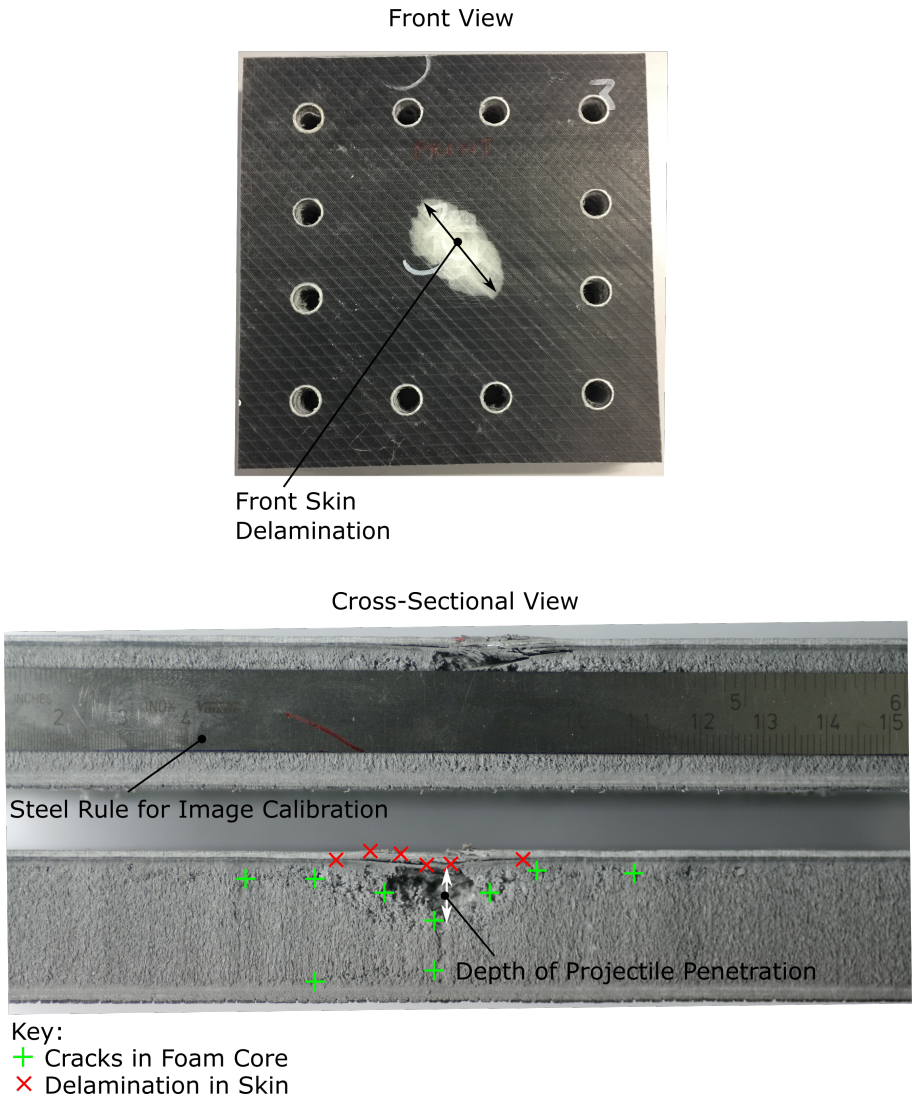


Figure 3.23: Damage mapping of the front view and section view of Hybrid-1A panel after impact velocity 75 ± 3 m s^{-1}.

3.4.1.2 Edgewise Compression

Edgewise loading of the sandwich specimens was performed at a quasi-static rate to simulate structural forces caused by a vessel. Testing was performed using an ESH hydraulic test machine with compression rate of 2 mm min^{-1}. A Canon EOS 350D digital single-lens reflex (DSLR) camera was used to capture one photo every two seconds to measure the axial two-dimensional DIC strain during testing. To ensure even loading is applied by the test machine plattens and to prevent slip, 10 mm thick rubber spacers were placed between the machine plattens and the test specimen. Although care was taken when the panels were originally cut and sectioned, these rubber spacers would mitigate any inconsistency in the cut along the specimen edges. The experimental setup is shown in Figure 3.24.

Two-dimensional DIC was adopted because strain within the rubber sheets, and possible slipping at the plattens, would result in the machine displacement being inaccurate. The DIC images were processed for in-plane strain using GOM Correlate. The strain across the surface of the damage specimens was irregular, therefore, an average strain was measured to determine an effective compressive modulus. To avoid the necessity of aligning the camera frame with the load, the sandwich panel stiffnesses were calculated using Equation 3.45. Where E_{eff} is the effective edgewise stiffness, σ_y is the in-plane engineering stress, and ε_y is the in-plane engineering strain. The in-plane engineering stress was calculated using Equation 3.46, where F is the applied force, and w and z are the specimen width and skin thickness respectively. Negligible stress would be present in the foam core compared to in the skins, hence these dimensions were adopted for the engineering stress calculations.

$$E_{eff} = \frac{\partial \sigma_y}{\partial t} \cdot \frac{\partial t}{\partial \varepsilon_y} \tag{3.45}$$

$$\sigma_y = \frac{F}{2wz} \tag{3.46}$$

3.4.2 Results

3.4.2.1 Damage Analysis

Table 3.7 shows the quantitative damage recorded during visual inspection of the panels. The qualitative damage suffered by each panel is detailed in Table 3.8. The results from these tables reveal that the GFRP panel suffered from the least damage. The projectiles deflected off the GFRP panels at both velocities leaving

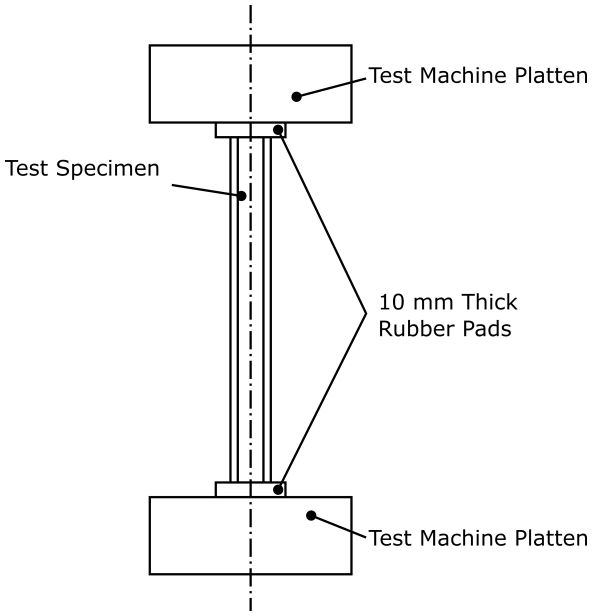


Figure 3.24: Schematic of the edgewise compression test method.

minor indentation and minor local delamination. The GFRP panels only suffered from debonding between the core and front face-sheet. At the other extreme, the projectiles punctured the CFRP panels at both velocities and caused significant damage. The projectile travelling at 90 m s^{-1} damaged the rear skin of the CFRP panel. Front view delamination in the CFRP panels is lower than expected as it is not visible due to the opaque carbon-fibre plies. Damage suffered by the hybrid panels lies between that of the GFRP and CFRP panels. The extent of damage to the panels correlates with their stiffness. Higher stiffness results in lower panel deflection and major strain but greater damage. This is due to the higher stiffness leading to brittle skin failure. Hybrid-3B suffers from the least damage and the lowest projectile penetration depths. The front view delaminations for Hybrid-3B were 9 % and 19 % and penetration depths were 9 mm and 11 mm under impact at 75 m s^{-1} and 90 m s^{-1}, respectively. Hybrid-2 and Hybrid-3B suffered from a similar extent of damage, therefore, the intricacy of the Hybrid-3B skins may not be worth the added complexity. The damage caused by the projectiles on the Hybrid-1A and Hybrid-1B panels was very similar. Delamination in the front skins in a local central region and minor fibre fracture of the front-most glass fibre layers was caused. The projectile travelling at 90 m s^{-1} embedded itself into the Hybrid-1B panel and caused fibre fracture in the front skin and rear skin/core debonding. Adopting symmetry did not have a beneficial effect on reducing panel damage.

Table 3.7: Extent of the damage in each panel under high velocity impact.

Panel type	Impact velocity (m s^{-1})	Front view delamination (mm)	Cross-section view delamination (%)	Foam damage length (mm)	Projectile penetration depth (mm)
GFRP	78	4	0	98	0
	89	6	0	120	0
CFRP	73	0	21	129	13
	88	0	14	191	20
Hybrid-1A	78	4	17	142	11
	89	6.5	18	51	17
Hybrid-1B	78	2	18	226	10
	89	4	21	260	20
Hybrid-2	78	2	10	182	9
	89	3	20	184	15
Hybrid-3B	74	2	9	173	9
	90	3	19	182	11

3.4.2.2 Edgewise Compression

There is a greater amount of damage in all the panels that underwent impact at 90 m s^{-1} compared to impact at 75 m s^{-1}. Under edgewise compression, the panels with greater stiffness prior to impact would be expected to exhibit greater post-impact stiffness. However, the extent of damage and brittle failure of the stiffer panels will affect their post-impact modulus. Edgewise compression was also performed to reveal whether initiating damage between the dissimilar fibres in the hybrid panels results in catastrophic delamination. Hence whether the hybrid panels buckle and collapse more easily than either the GFRP or CFRP panel.

Figure 3.25 shows the effective compressive modulus of the panels for 75 m s^{-1} impact velocity and 90 m s^{-1} impact velocity. The figure shows that all panels, not only the hybrid panels, experience a drop in effective modulus when suffering from greater damage under 90 m s^{-1} impact velocity. This implies that the combination of dissimilar fibres does not result in catastrophic delamination. Despite having the lowest stiffness, the GFRP panel exhibits a high effective modulus as it suffered from the least damage so retains a greater proportion of its undamaged stiffness. Although the CFRP panel suffered from the greatest damage, it also retains an effective modulus higher than three of the hybrids. Hybrid-1A has a high effective compressive modulus, despite significant damage suffered. This indicates that the

Table 3.8: Details of the damage in each panel under high velocity impact.

Panel type	75 ± 3 m s^{-1}	90 ± 3 m s^{-1}
GFRP	Front skin/core debonding	Front skin/core debonding
CFRP	Front skin/core debonding Front skin delamination Front skin broken fibres Core crushing	Front skin/core debonding Front skin delalmination Front skin broken fibres Core crushing Rear skin/core debonding Rear skin delamination Rear skin broken fibres
Hybrid-1A	Front skin/core debonding Front skin delamination Front skin broken fibres Core crushing	Front skin/core debonding Front skin delalmination Front skin broken fibres Core crushing
Hybrid-1B	Front skin/core debonding Front skin delamination Front skin broken fibres Core crushing	Front skin/core debonding Front skin delalmination Front skin broken fibres Core crushing Rear skin/core debonding
Hybrid-2	Front skin/core debonding Front skin delamination	Front skin/core debonding Front skin delalmination Front skin broken fibres Core crushing
Hybrid-3B	Front skin/core debonding Front skin delamination	Front skin/core debonding Front skin delalmination Front skin broken fibres Core crushing

less intricate hybridisation may be beneficial as it results in a large cross-section of in tact carbon-fibre at the rear of the panel which will significantly contribute to high effective stiffness. In these experiments, the whole sandwich cross-section was compressed rather than the impacted face-sheet alone. This leads to the compressive load bypassing through the non-impacted face-sheet and hence an overestimation of the residual compressive strength [103]. This accounts for the high compressive modulus of the CFRP panel despite significant front skin damage, as the rear skin significantly contributes. Nevertheless, all panels underwent the same edgewise compression method.

The panel maximum compressive stresses are shown in Figure 3.26. The hybrid panels exhibit a drop in maximum stress with increased damage whereas the GFRP and CFRP panels do not. This implies that the extent of damage affects compressive strength of the hybrid panels. The increased damage in the GFRP and CFRP panels affects their compressive moduli but not their compressive strength. Once again, the damaged CFRP panel has a greater maximum stress than the lesser damaged hybrid panels. Hybrid-1A has the highest strength out of the hybrid panels, adopting a symmetrical version, Hybrid-1B, does not appear to be beneficial. Hybrid-3B suffers the greatest drop in compressive strength. This indicates that its thinner hybrid layers are more susceptible to strength reduction when damage is increased. The results for Hybrid-2 are counterintuitive. It is possible that the panel was not exactly aligned during testing, resulting in off-axis loading. All hybrid panels achieve compressive strength to within 15 % of the GFRP panel. Compressive strength is often the critical design criterion in naval composites as fibre misalignment worsens and voids open up under compression. High compressive strength can lead to ductile materials, whereas high compressive modulus leads to brittle materials. Compressive strength is, therefore, a more critical parameter [10]. This indicates that Hybrid-1A is, overall, the most suitable hybrid panel under impact loading.

3.5 Discussion

Analytical calculations revealed that a significant improvement in stiffness of glass-fibre composite laminates can be achieved by replacing a proportion of the glass-fibre plies with carbon-fibre plies. The fibre orientations and distance of materials from the neutral axis affects the predicted laminate stiffness. High velocity impact testing was performed on composite sandwich panels with laminate skins selected from the analytical calculations. Although impact causes more localised loading

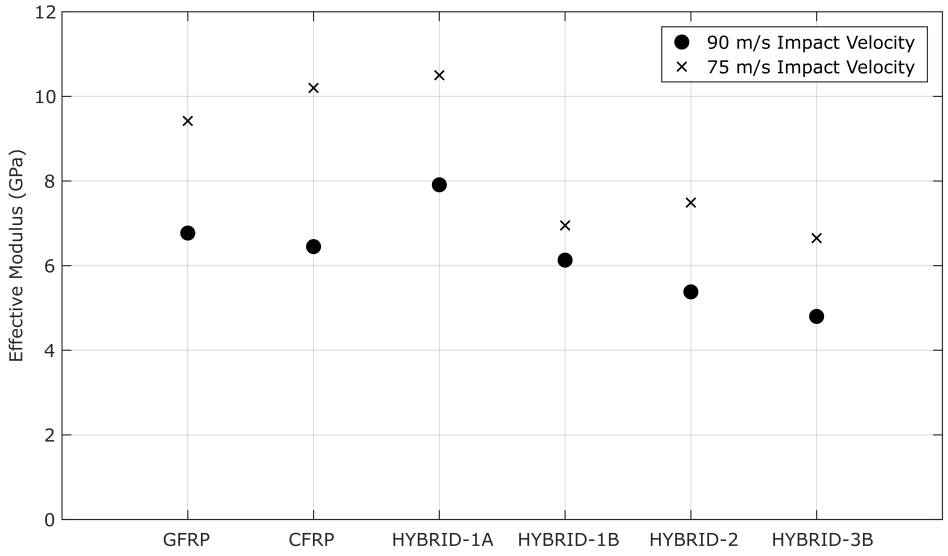


Figure 3.25: Effective compressive modulus for the hybrid panels following impact.

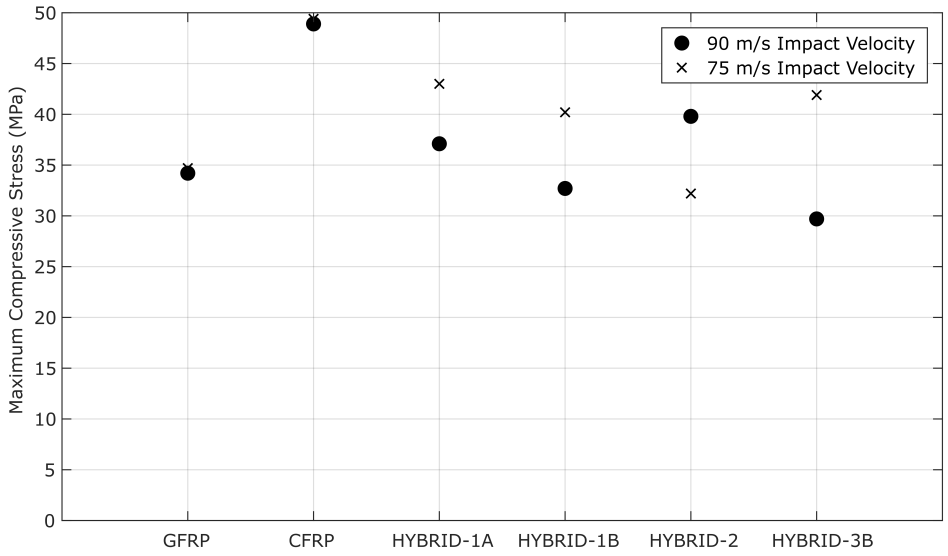


Figure 3.26: Maximum compressive stress for the hybrid panels following impact.

and failure compared to blast, stress wave propagation occurs during both loading types. Furthermore, representative high strain rate experiments are necessary to understand panel behaviour as prediction is complex.

High velocity impact experiments were performed at 75 ± 3 m s^{-1} and 90 ± 3 m s^{-1} as these velocities would cause front skin and core panel damage whilst leaving the rear skin and speckle pattern intact. The experiments revealed that the GFRP panel experiences the greatest deflection and strain under both impact velocities. However, due to the greater strain to failure of the glass-fibres, the panel absorbs and redistributes the impact energy. The GFRP panel suffers from the lowest damage. Conversely, the CFRP panel experiences the lowest deflection and lowest strain on the initial peak. Due to the brittle behaviour of the carbon-fibres, the CFRP panels suffer from the most extensive damage. In addition, this damage causes a greater second deflection peak under 90 m s^{-1} impact. These results indicate that GFRP skins have superior impact performance compared to CFRP, or any hybrid skins, when mass per unit area is kept constant. However, the aim of this research is to understand the blast performance of composite sandwich panels with various skin configurations. Previous research has demonstrated that under blast loading, GFRP panels with equal areal densities to CFRP panels suffer from greater damage [19]. This is due to impact loading being localised and blast loading requiring a global panel response. Although the hybrid composite sandwich panels have a lower impact performance, the potential for hybrid skins to improve blast resilience can not be discounted.

The deflection, strain and damage response of the hybrid composite sandwich panels lie between those of the GFRP and CFRP panels as expected. The results from Hybrid-1A and Hybrid-1B show that there is no advantage in adopting a symmetric skin configuration under these conditions. Hybrid-1B exhibits an unpredictable double deflection and rear skin/core debonding under 90 m s^{-1} impact. Hybrid-1A exhibits greater post-impact compressive modulus and maximum stress compared to Hybrid-1B. This could be due to the positioning of the carbon-fibre and glass-fibre layers within the rear skin. The carbon-fibre plies are placed at the very rear of Hybrid-1A, resulting in the glass-fibre plies protecting the carbon-fibre. Hence a greater cross-section of carbon-fibre remains intact for post-impact strength. In addition, the configuration for Hybrid-1A takes advantage of the high tensile strength of carbon-fibre. When the panel is impacted, the glass-fibre layers experience compression whilst the carbon-fibre layers experience tension in both

skins. Hybrid-1A was selected for full-scale air blast testing as the panel performed well under impact testing.

Hybrid-2 and Hybrid-3B exibited similar deflections, strain and damage. Hybrid-3B suffered from the greatest decrease in compressive strength between 75 and 90 m s^{-1} impact. The intricate layup and thinner hybrid layers result in a thinner cross-section available to withstand compressive forces. Hybrid-2 was selected for full-scale air blast testing. Comparison of Hybrid-1A and Hybrid-2 under air blast would reveal the effects of a symmetric layup and the distance of carbon-fibre plies from the neutral axis.

3.6 Conclusion

This chapter has introduced the preliminary analysis and experiments carried out on hybrid composite sandwich panels. The calculations demonstrated the potential for hybrid laminate skins to improve stiffness and strength compared to conventional composite sandwich panels. In-plane and transverse moduli of hybrid laminates were shown to increase as the number of carbon-fibre plies increases. This is more pronounced by the addition of [0/90] layers compared to the addition of [+45/-45] layers. However, blast loading does not cause in-plane loading alone. Therefore, high velocity impact testing was carried out as a preliminary trial. This helps to reveal the energy absorption and failure mechanisms caused by hybridisation. The performance of four hybrid composite sandwich panels with equal mass per unit area were investigated and compared to benchmark GFRP and CFRP panels. Impact testing highlighted differences in panel deflection and strain, dictated by the positioning of different material plies. In addition, the types of damage that can be sustained by composite sandwich panels were exhibited. The results showed that brittle behaviour of carbon-fibre results in significant damage whereas glass-fibre is able to undergo greater deflection and strain with minimal damage. The deflection, strain and damage of the hybrid composite sandwich panels lay between the benchmark panels. Additionally, the asymmetry of Hybrid-1A was shown to have no detrimental effects on impact performance. Impact loading does, however, differ to blast loading. The localised force and resulting damage are not present in blast loading. Therefore, these experiments have been used to inform material selection. Hybrid-1A and Hybrid-2 were selected for full-scale air blast testing.

Chapter 4

Full Scale Air Blast Testing: Part 1

4.1 Introduction

This chapter investigates the full-scale air blast performance of hybrid composite sandwich panels. The experiments were carried out at a specialised test facility, located at RAF Spadeadam, Cumbria, UK. The large scale experimental setup aimed to represent the typical scale of both naval structures and the explosive charges that could be encountered by naval vessels. Scaling the blast response of composites from small to large scale is challenging and under continuous development. Therefore, large scale data is an important contribution to this research field. The composite sandwich panels tested could be used in both ship hulls and superstructures. This air blast experiment simulates a surface or open-air blast against the vessel superstructure or hull section above the waterline.

Four composite sandwich panels were simultaneously subjected to a 100 kg nitromethane charge at 15 m stand-off distance. The analytical and experimental results, detailed previously, aided in the selection of hybrid composite sandwich panels for this series of full-scale experiments. The selected panels aimed to highlight differences between symmetric and asymmetric sandwich panels under blast. The effects of differing bending stiffness, caused by positions of the fibre material in the layup, would also be revealed. All panels adopted a PVC foam core. This foam material is known to perform well at high strain rates and was kept consistent such that differences in the skins could be identified. This chapter outlines the tests performed along with the instrumentation techniques used to record the material response under blast. The displacement-time histories of the composite sandwich

panels were recorded using high-speed 3D DIC. High-speed cameras are able to capture the full-field displacement of the rear surface of the sandwich panels. In addition, foil strain gauges were implemented on the front surface of the panels to enable evaluation of the front skin behaviour. These instrumentation methods were adopted to generate sufficient data for the validation of future numerical models. Following blast testing, the damage sustained by each panel was evaluated. This was performed to compare the blast resilience of the panels and to ensure future numerical models capture the correct extent and type of damage. A proportion of this experimental work and associated results have been published [104].

4.2 Experimental

4.2.1 Materials

Four composite sandwich panels were constructed for full-scale air blast testing. Two panels adopted the hybrid skin layup of Hybrid-1A and two had Hybrid-2 skin layups. Unfortunately, due to a manufacturing error, the skins were constructed from eight bi-axial stitched ply face-sheets either side of a PVC foam core, rather than four bi-axial stitched plies. The core was 30 mm thick Divinycell H100 with a density of 100 kg m^{-3}. The panels were 1.75 m $\times$ 1.55 m in size. A schematic of the hybrid layups of the two panel types is shown in Figure 4.1. Two types of each hybrid were fabricated to determine the repeatability and reliability of the large scale test method adopted. The skin fabrics were bi-axial E-glass-fibre, 600 gsm, and bi-axial carbon-fibre, 400 gsm HexTow AS4, infused with SR8100 epoxy resin and SD8824 hardener. The panels were fabricated using resin infusion and were ambient cured and then held under vacuum for 24 h before being demoulded.

The properties of the materials used, taken from the manufacturer data sheets and a materials database, along with face-sheet properties calculated using the rule of mixtures are detailed in Table 4.1. The rule of mixtures method, as detailed in Chapter 3, was used to calculate these properties. Hence, the values are only approximations as the manufacturing procedures vary from those described in the material data sheets. Furthermore, the laminate compressive strengths are overpredictions as the calculation neglects the effects of voids, fibre misalignment or fibre bunching. The Krenchel factor was taken as 0.375 for a quadriaxial ply and 0.5 for a bi-axial ply. The shear strength given in Table 4.1 for the composite plies are the interlaminar shear strength properties taken from manufacturer data sheets for

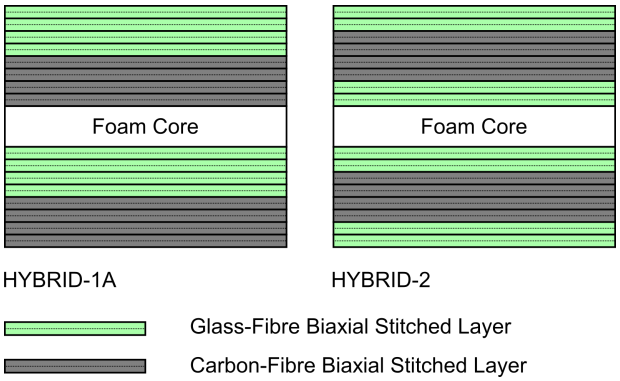


Figure 4.1: Layup configurations of the two types of hybrid composite sandwich panel fabricated for full-scale air blast testing. Two Hybrid-1A panels and two Hybrid-2 panels were constructed.

layup configurations with a different epoxy resin. All the material properties detailed for the foam core are taken from manufacturer data sheets. Due to the varying positions of the carbon-fibre and glass-fibre layers, a difference in stiffness between Hybrid-1A and Hybrid-2 is expected. Table 4.2 details the measured mass per unit area, calculated bending stiffness and fibre volume fraction for the two panels.

4.2.2 Methods

Full-scale blast testing was performed at the DNV GL test site at RAF Spadeadam. During testing, the composite sandwich panels were bolted side-by-side into two steel cubicles, as shown in Figure 4.2 (a). 5 mm thick steel frames were adhered to the front and back of the panels using Sikaflex 291i marine sealing adhesive. The adhesive was not intended to provide any structural contribution to the boundary conditions during the test, but was simply to fix the steel frames to the panels. The panels were secured to the steel cubicles using 20 $\times$ M11 bolts around the perimeter. To prevent the sandwich panels from being crushed upon tightening of the bolts, steel tubes were placed inside the holes in the sandwich panel and sat flush against the front and rear surface of the panel. The steel cubicles were 3.2 m $\times$ 3.2 m with 1.3 m $\times$ 1.6 m openings over which the panels were mounted. A schematic of the experimental setup is shown in Figure 4.2 (b). A spherical charge was raised to the centre height of the panels, 1.5 m from the ground, by placing it on polystyrene blocks which absorb little blast energy. A large steel plate was situated underneath the polystyrene blocks to prevent cratering of the ground. A spherical charge was

Table 4.1: Mechanical properties of the composite sandwich panel materials and plies.

Material	Density (kg m^{-3})	Elastic modulus (GPa)	Tensile strength (MPa)	Shear strength (MPa)	Compressive strength (MPa)
Glass-fibres	2555 [96]	78.5 [96]	2000.0 [96]	-	4500.0[96]
Carbon-fibres (HexTowAS4)	1790 [105]	230.0 [105]	4410.0 [105]	-	4950.0 [96]
SR8100 epoxy & SD8824 hardener	1119 [106]	2.7 [106]	50.0 [106]	48.0 [106]	103.0 [96]
QX600/epoxy quadriaxial GFRP ply	1829	15.9	396.1	48.0	886.4
FCIM105/epoxy bi-axial CFRP ply	1441	56.6	1084.1	48.0	1241.2
PVC H100 foam core	100 [107]	0.1 [107]	3.0 [107]	2.1 [107]	2.7 [107]

Table 4.2: Properties of the two hybrid composite sandwich panels.

Panel type	Areal density (kg m^{-2})	Equivalent bending stiffness (kN m^{-2})	Fibre volume fraction
Hybrid-1A	14.66	79.3	0.36
Hybrid-2	14.66	79.1	0.36

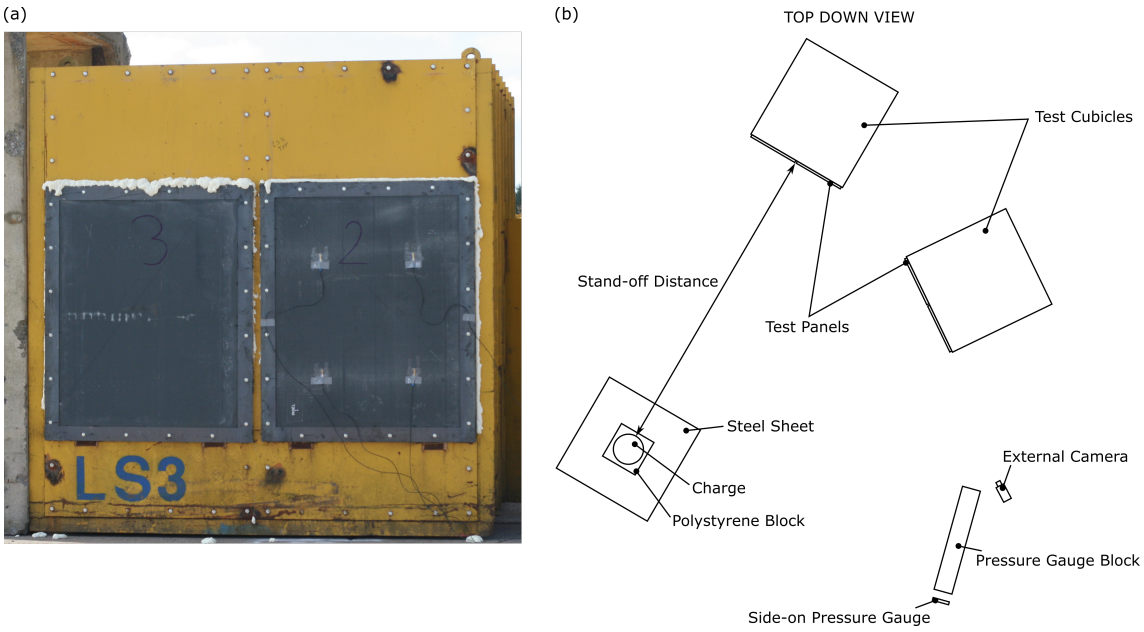


Figure 4.2: Experimental setup showing: (a) a photograph of two hybrid composite sandwich panels bolted side-by-side onto the front of a steel cubicle and (b) a schematic diagram of the test pad setup.

used as it creates a non-biased spherical pressure wave. The detonator was placed into the top of the charge at the centre.

4.2.2.1 Blast Wave Modelling

The charge size was set at 100 kg nitromethane, equivalent to 100 kg TNT, by the test range. Therefore, an appropriate stand-off distance was required to cause sufficient damage to the composite panels yet not damage instrumentation situated behind the panels. An analytical method outlined by Andrews and Moussa [66] was used to calculate the stand-off distance at which core shear failure, front skin wrinkling and tensile skin failure would occur. This method assumes that the blast pressure is approximately uniform across the panel face and the panel is simply supported at its boundaries. Using this method, the loads required to cause these three failure modes, and static panel deflection that would result from the quasi-static application of these loads, are calculated based on the material and geometric properties of the panel.

Following this, the maximum reflected overpressure and positive phase duration caused by a 100 kg TNT equivalent charge at set stand-off distances were generated from Pro S Air models detailed later in this section. The peak panel deflection

caused by both static and dynamic effects of these blast pressures were calculated. The static deflection is calculated from the quasi-static application of the pressure load and the stiffness of the panel based on material and geometric properties. Dynamic effects are included in the method by modelling the panel as a single-degree-of-freedom mass-spring system. The natural response of the panel, T, is compared to the positive phase duration of the blast pressure, t_d. As the ratio of positive phase duration to natural panel response period, t_d/T, increases, the loading regime moves from impulsive loading, to dynamic loading and finally quasi-static loading. When the ratio is small, blast loading has finished and the panel has not experienced a full oscillation response, hence impulsive loading. Whereas when the ratio is large, the blast wave loading is ongoing and the panel undergoes a number of oscillations hence approaching quasi-static loading. As t_d/T varies it affects the maximum dynamic load factor (DLF). The definition of DLF is shown in Equation 4.1 where x_{dyn} is the dynamic deflection produced by the blast wave and x_{st} is the static deflection produced by the blast wave [5]. Since the maximum DLF and static displacement as a result of each blast wave is known, the peak dynamic deflection caused by the blast pressure can be calculated. Finally, a failure index is calculated by comparing the peak deflection caused by the blast pressure against the static deflection necessary to cause panel failure modes. If the failure index is greater than 1 then the panel is expected to fail via this failure mode.

$$DLF = \frac{x_{dyn}}{x_{st}} \tag{4.1}$$

The outlined method assumes that the failure modes have no influence on each other. This is inaccurate as core shear failure will lead to stress concentrations in the skins, increasing the likelihood of skin failure. After failure, the stiffness of the structure will change, hence the natural response of the panel and DLF will change. A series of equations would need to be specified and solved to accurately capture the panel behaviour under blast loading. Conversely, the method assumes simply supported boundary conditions. The boundary conditions in the experiment are quasi-built-in. Therefore, the analytical method provides a conservative result with respect to the boundary conditions. Despite these limitations, the analytical method serves to give an indication of the first failure mode expected and the suitability of stand-off distance selected. To ensure confidence in the selected stand-off distance, it was compared to previous blast testing research performed by Arora [19] and Kelly [21].

Table 4.3: Failure indices according to the analytical solution outlined by Andrews and Moussa [66].

Stand-off distance (m)	Peak reflected overpressure (kPa)	Positive phase duration (ms)	Core shear failure index	Front skin wrinkling index	Tensile skin failure index
14	393.0	7.80	4.00	1.17	0.66
15	328.9	7.70	3.40	1.01	0.56
16	278.8	7.90	3.01	0.88	0.49

Failure mode calculations were carried out for stand-off distances of 14 m, 15 m and 16 m. The failure indices were calculated for the Hybrid-1A layup. Since both panel types were equal in size and had an equal mass per unit area, the failure indices are valid for both Hybrid-1A and Hybrid-2. These intial distances were based on previous research mentioned [19], [21]. Increments of 1 m were selected as more accurate positioning of the test cubicle on the test pad would not be practically achievable due to the nature of the field based experiments. The peak reflected overpressure, positive phase duration and failure indices for a 100 kg TNT equivalent charge is shown in Table 4.3. It is clear that the first expected failure mode is core shear failure. With failure indices greater than three in all cases, core shear failure is extremely likely to occur. A stand-off distance of 15 m was selected as this distance is predicted to result in front skin damage but no rear skin tensile failure. The camera equipment behind the panels will, therefore, be protected. Any rear skin damage that might occur would be minor.

To support the analytical calculations, the air blast computational fluid dynamics (CFD) solver, Pro S Air, was used to model the blast wave arriving at and travelling over the cubicle. The analytical method assumes a uniform pressure across the panel front. In reality the pressure distribution across the cubicle front would vary due to blast clearing effects. It was not possible to position concrete blocks alongside the cubicle to mitigate these effects. As a result, the centre of the cubicle is expected to experience a greater pressure than the edges. The Pro S Air model can generate reflected overpressure at multiple locations and be compared against analytical predictions and the reflected overpressure recorded during the experiment.

It is only possible to define infinitely rigid obstacles in the CFD solver as it has no structural capabilities. Nevertheless, it will provide an estimate of the reflected overpressure across the test panels. A spherical geometry, cylindrical geometry and

3D geometry were used in turn to efficiently model separate stages of the blast wave and its interactions with the surroundings. Each geometry stage had an appropriate cell size and problem time as recommended by the software user guides [108], [109] and previous investigations [20]. The spherical geometry modelled the pressure from detonation until the blast wave reached the closest boundary, the floor. The cylindrical geometry modelled the blast wave between reaching the floor and reaching the next boundary, the cubicle. The 3D geometry stage took over to model the blast wave as it encountered the 3D test cubicle as an object. For computational efficiency, a plane of symmetry was assumed to run through the centre of the test cubicle. This symmetry boundary was assumed to be reflective along with the floor, 100 % of the blast energy was reflected. All other boundaries were 100 % transmissive. In the 3D geometry stage, the control volume that was modelled was from the ground to 5 m in height and from the centre of the charge to 25 m in length and to 4 m in width. The reflected overpressure was measured 25 mm in front of the cubicle, as this is representative of the distance from the charge to the front of the panels due to their thickness. A measurement was taken at 400 target points across the panel front.

4.2.2.2 Instrumentation

4.2.2.2.1 Three-Dimensional Digital Image Correlation

To capture the response of the composite panels under blast loading, high-speed images of the rear skins of all panels were recorded. 3D DIC was performed on the images to calculate the rear skin deflection and strain. A total of eight high-speed Photron cameras were used, a pair for each panel. The camera specifications are detailed in Table 4.4. The cameras in each pair were triggered by a TTL signal produced by one camera but received by both to ensure frame synchronisation. The cameras were initially triggered upon charge detonation. This was achieved by taping the open ends of the TTL signal circuit to the charge. The circuit was completed by the ionising air around the charge upon detonation.

The cameras were housed within the test cubicles to protect them from the blast wave. Due to the restricted length of the cubicles, and in order to achieve the desired 25° angle between the cameras, 24 mm lenses were used on each camera. The cameras were mounted vertically, as shown in Figure 4.3. This was to capture the longest panel length within the frame and to ensure two pairs could fit into each cubicle. Using Equations 3.40 to 3.44 the perpendicular distance between the panel and cameras was calculated to be 2.19 m and the distance between the cameras

Table 4.4: Details of the camera models and frame rate for each panel.

Panel type	Camera 1	Camera 2	Frame rate (fps)
Hybrid-1A(1)	SA1.1 mono	SA5 mono	4 000
Hybrid-1A(2)	SA1.1 colour	SA5 colour	4 000
Hybrid-2(1)	AX100	AX100	4 000
Hybrid-2(2)	SAX2	SAX2	12 000

was 0.97 m. Each camera was bolted to a 5 mm steel plate which was attached to an aluminium extrude bar using T-slot nuts. The camera bar was mounted on a heavy duty steel camera stand which was weighed down with sand bags once placed in the correct position. This setup allowed easy movement of the cameras if distance and angles required adjusting for calibration. Banks of light emitting diode (LED) lights and halogen lamps were used to illuminate the panels during blast testing. Calibration of the cameras was achieved by taking numerous photographs of a 1000 mm CC20 coded calibration cross supplied by GOM UK. This calibration object is known by the GOM Correlate Professional software so the location of the two cameras in space can be determined. Figure 4.4 shows images taken during the calibration sequence from both cameras. The figure also shows the random black speckle pattern on a white painted background that was applied to each test panel. This pattern enabled tracking of the panel using the DIC software. For this camera setup, the speckles were required to be between 5 mm and 10 mm in diameter. The cubicle columns either side of the test panel were also speckled such that the rigid body movement of the cubicle front during blast could be recorded and removed from the analysis.

An additional GoPro camera was setup to record the progression of the blast wavefront and ensure no debris impacted the front of the panels. This camera was mounted on the ground behind a concrete block to protect it from the blast wave.

4.2.2.2.2 Foil Strain Gauges

One of each hybrid type was instrumented with 14 foil strain gauges on the front skin. Single axis gauges (CEA-06-125UW-350) were adhered to the centre of the panel and along the edges, 200 mm in from the steel frame. In the centre of the panel, one gauge was aligned with the major vertical axis of the panel and the second was aligned with the minor horizontal axis. The position of all the strain gauges is shown in Figure 4.5. The strain gauges and terminal pads were adhered to the panel surface using Vishay M-Bond AE-10. Before adhesion, the panel surface was

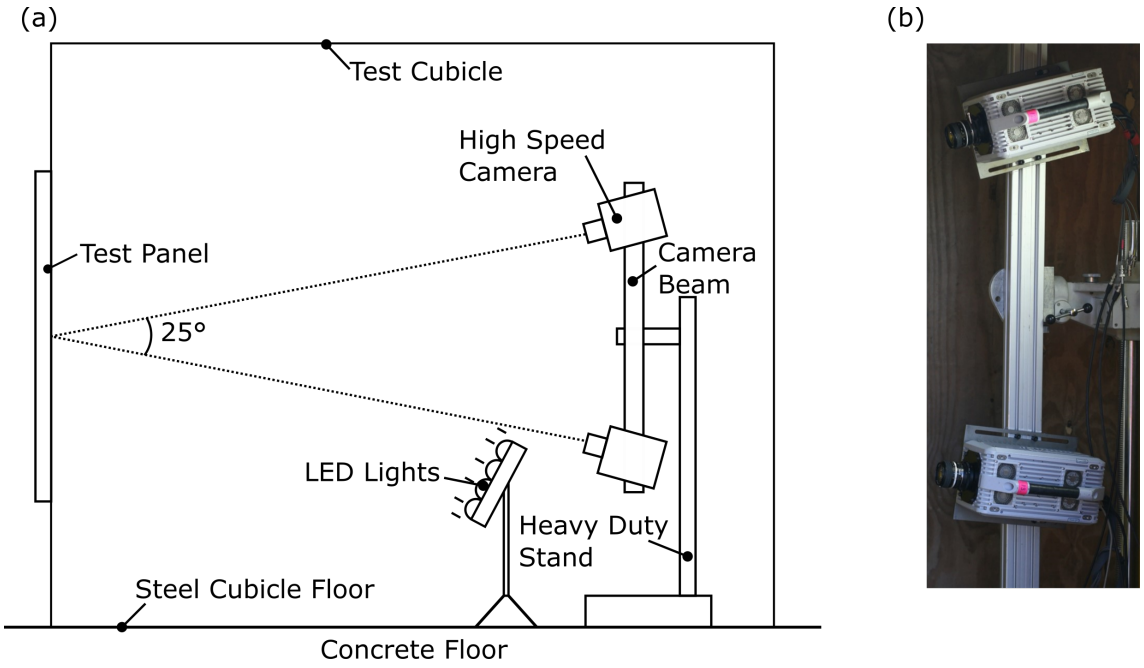


Figure 4.3: Camera setup for the full scale air blast experiments showing: (a) a schematic diagram of the camera setup within the cubicle and (b) a photograph of the SAX2 cameras mounted vertically.

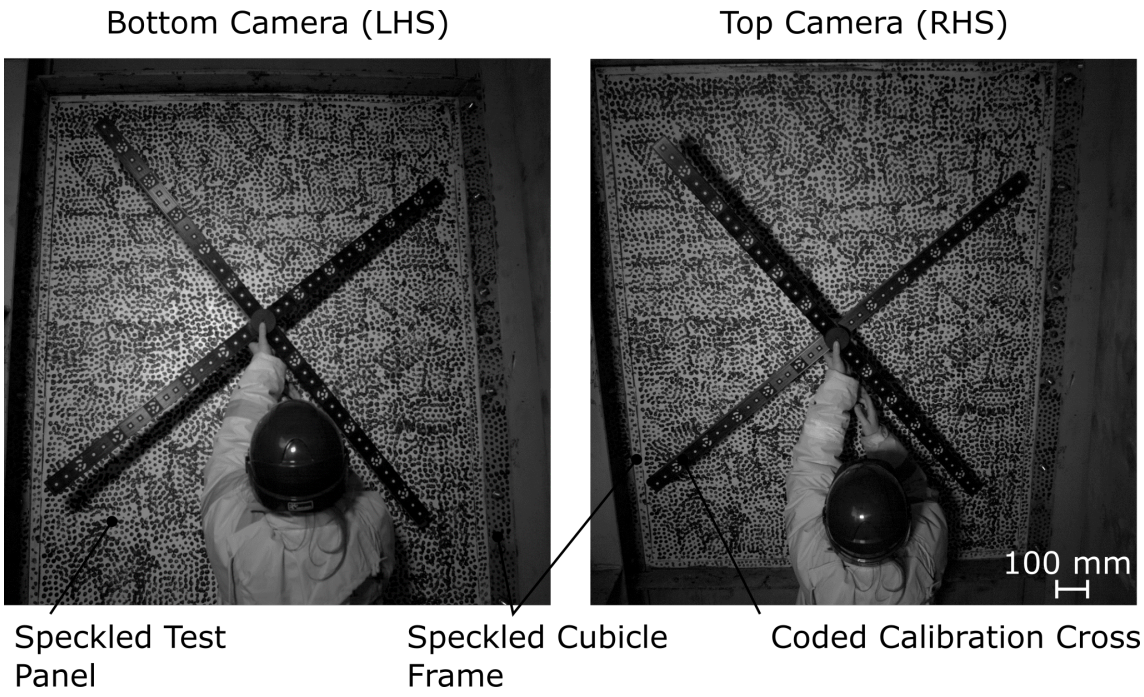


Figure 4.4: Photographs from the SAX2 high-speed cameras showing the calibration cross and speckle pattern from the bottom and top cameras.

roughened with two grades of sand paper and cleaned with isopropyl alcohol. A single wire was soldered between the gauge and terminal pads and the data cables were soldered to the terminals. The gauges, single wires and solder terminals were then covered with a liberal coating of M-Coat A for protection. 30 m long three-core shielded cables were used for the data cables. The cables were taped to the front of the panel and were given slack to prevent the gauges tearing away from the panel whilst deflecting. The connections to the transducer amplifier were via Amphenol bayonet connectors.

A three wire quarter-bridge circuit was selected over a two wire quarter-bridge circuit. Schematic diagrams of the two-wire and three-wire circuits are shown in Figure 4.6 (a) and (b), respectively. In the three wire circuit, the negative output bridge corner is moved from the top of R_2, to the bottom strain gauge tab at the end of B. In the three wire circuit, leadwire C and the strain gauge R_1 comprise one arm of the bridge and A with resistor R_2 form the adjacent arm. The three wire strain gauge bridge will remain balanced provided data wires A and C are made from the same material, have the same resistance and remain at the same respective temperature. The bridge is symmetric about a line through the bridge output corners, hence the bridge is balanced. Only data wire C is in series with the strain gauge which reduces leadwire sensitivity by up to 50% compared to a two wire quarter-bridge configuration. Data wire B is a voltage-sensing wire only, it is not in series with either of the bridge arms and has no effect on balance or temperature stability. With a three wire quarter-bridge the same conditions as a half-bridge circuit are achieved [110]. The relative bridge output voltages for the two wire and three wire bridge circuits are given in Equations 4.2 and 4.3 [111]. In these equations V_0 is the output voltage, BV is the bridge voltage or excitation voltage, which was 5V, GF is the gauge factor, ε_1 is the strain and R is the resistance of the data wires or resistors. In a two wire quarter-bridge, both lead wires affect the relative bridge output voltage. Whereas in a three wire circuit, the variation in resistance of the data wire connected in series with the gauge has the same effect as the gauge resistance itself on the output voltage. Mitigation of lead wire effects is important as very long length lead wires are required for this experimental setup.

$$\frac{V_0}{BV} = \frac{GF}{4} \cdot \varepsilon_1 \cdot \frac{R_1}{R_1 + R_A + R_B} \tag{4.2}$$

$$\frac{V_0}{BV} = \frac{GF}{4} \cdot \varepsilon_1 \cdot \frac{R_1}{R_1 + R_C} \tag{4.3}$$

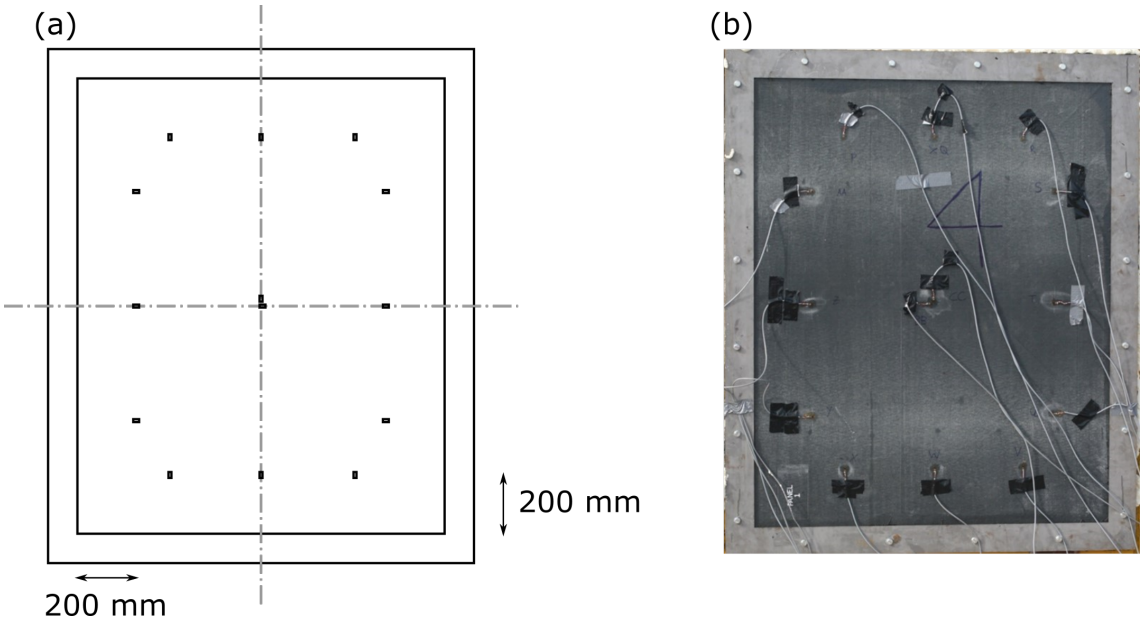


Figure 4.5: Strain gauge locations used on panels Hybrid-1A(1) and Hybrid-2(1) showing: (a) a schematic diagram of the locations and (b) a photograph of Hybrid-2(1) once fully instrumented with strain gauges.

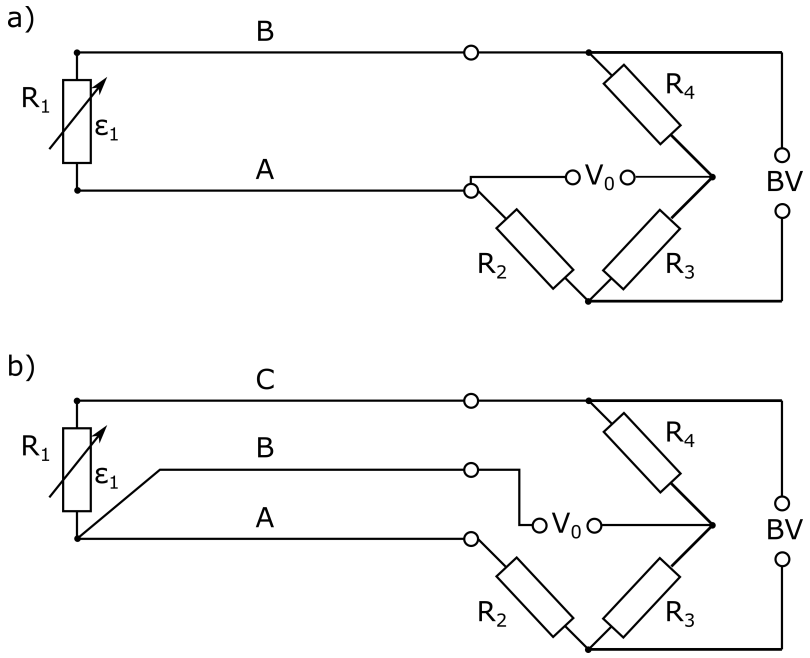


Figure 4.6: Schematic diagram of (a) two-wire quarter-bridge strain gauge circuit and (b) three-wire quarter-bridge strain gauge circuit.

4.2.2.2.3 Reflected Pressure Gauge

A reflected pressure gauge was positioned within a concrete pressure block at the same stand-off distance from the charge as the targets. The concrete pressure block had a similar area to the front of the cubicle such that similar blast clearing effects occurred. The reflected pressure sensor was situated normal to the blast wave direction, measuring the pressure as the air particles came to rest against the surface. A side-on pressure gauge was also situated at the same stand-off distance from the charge. The gauge was positioned parallel to the blast wave and measured the static pressure as the blast wave moved over the sensor.

4.3 Results

4.3.1 Blast Wave Modelling

Figure 4.7 illustrates the panels mounted in the test cubicle. The area highlighted by the red dashed line indicates the area where pressure distribution was modelled. Figure 4.8 shows the reflected overpressure distribution across the panel mounted on the right-hand side of the cubicle. The bottom left-hand corner of the panel, at (0,0), lies at the cubicle centre and 0.725 m up from the ground, as shown in Figure 4.7. The pressure distribution at discrete intervals of time, when subjected to 100 kg TNT equivalent charge at 15 m stand-off distance, are shown. The pressure has been interpolated between the 400 measured target points to create continuous maps. Due to the position of the charge and ground reflections, the blast wave first interacts with the bottom left-hand corner. The pressure increases with a radial profile across the panel. The highest reflected overpressure at the centre of the panel is recorded at 18.10 ms after detonation. Following the peak pressure, blast clearing begins to affect the pressure distribution. As the average pressure across the panel decreases, the outer edge of the panel experiences relative lower pressure. As time continues, the average overpressure decreases but the pressure difference between the central left-hand edge and outer right-hand edge becomes more prominent. At 19.01 ms and 19.47 ms the difference between maximum and minimum overpressure remains at over 60 kPa. This reveals that the central left-hand edge of the panel experiences a greater pressure for a longer period of time.

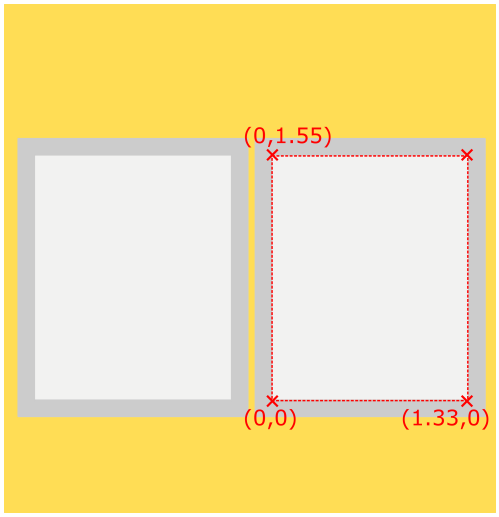


Figure 4.7: Diagram of the panel setup highlighting the area over which pressure distribution was modelled.

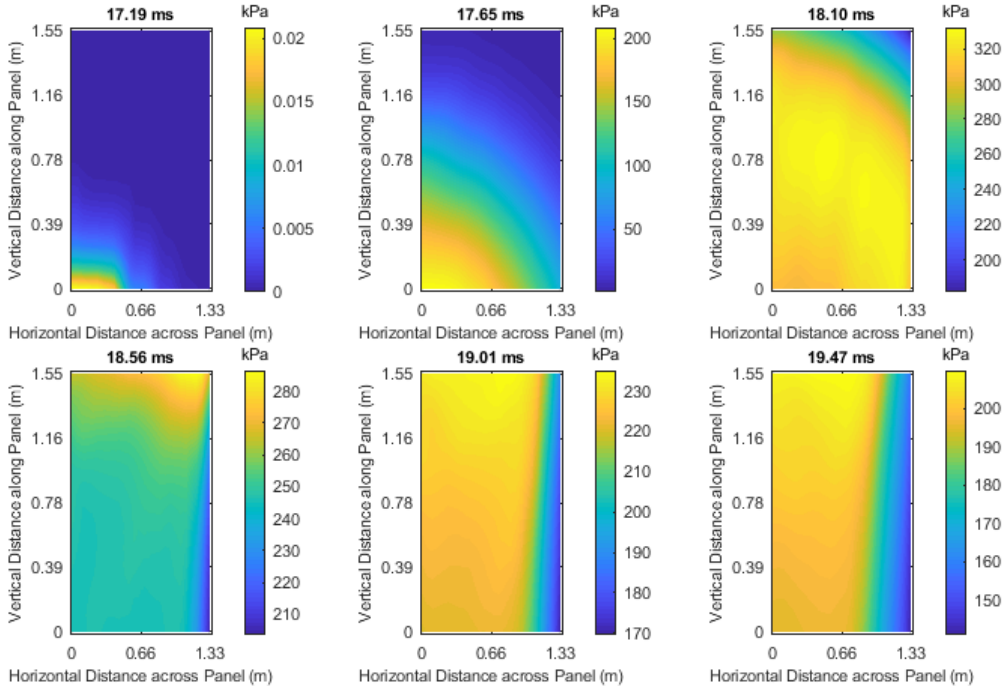


Figure 4.8: Comparison of reflected overpressure distribution across the panel.

4.3.2 Data Filtering

The raw strain gauge data and pressure gauge data obtained during the blast experiments had clear data patterns with random noise. A filter was applied to the data since the noise frequencies were significantly higher than the data response. A moving average filter with span of 10 data points was used. This results in average data values calculated across every section of 10 data points. The random noise was eliminated whilst the signal trace was maintained. 10 data points did not result in a significant shift of the data in time due to the moving average. An example of raw and filtered strain gauge data is shown in Figure 4.9.

4.3.3 Digital Image Correlation

The progression of the blast wave during the experiment is shown in Figure 4.10. The first image shows the test setup on the pad whilst the following images show the blast wave travelling across the ground. The deflection of the panels can be seen in the final image. This camera was not connected to the charge trigger, so the time at which the images were taken relative to detonantion was not recorded.

4.3.3.1 Rigid Body Motion Compensation

The inside supports of the steel test cubicle were also speckled such that the displacement of these supports could be analysed using DIC. It is possible to remove the movement of the supports from the displacement of the composite sandwich panels using GOM Correlate DIC software. This is known as rigid body motion compensation (RBMC) and gives the panel response relative to its boundaries. Figure 4.11 shows a plot of the displacement of the central point of Hybrid-1A(1) under blast loading from DIC data. Two displacement versus time traces are shown for the panel. One with RBMC and one without. The reflected overpressure recorded during the blast is also shown to highlight the response relative to the blast wave arrival. Without RBMC the overall central displacement is greater and the panel experiences more gradient discontinuities on the return stroke due to panel damage and interactions between the panel and cubicle structure. Figure 4.12 (a) and (b) show the displacement and return at 0.25 ms intervals for the horizontal cross-section at the mid-plane of Hybrid-1A(1) without RBMC. Figure 4.12 (c) and (d) show the displacement and return of the same cross-section with RBMC for the same number of time intervals. Without RBMC the left-hand boundary can be seen to deflect by 17.5 mm and the right-hand boundary by approximately 8 mm during the outward

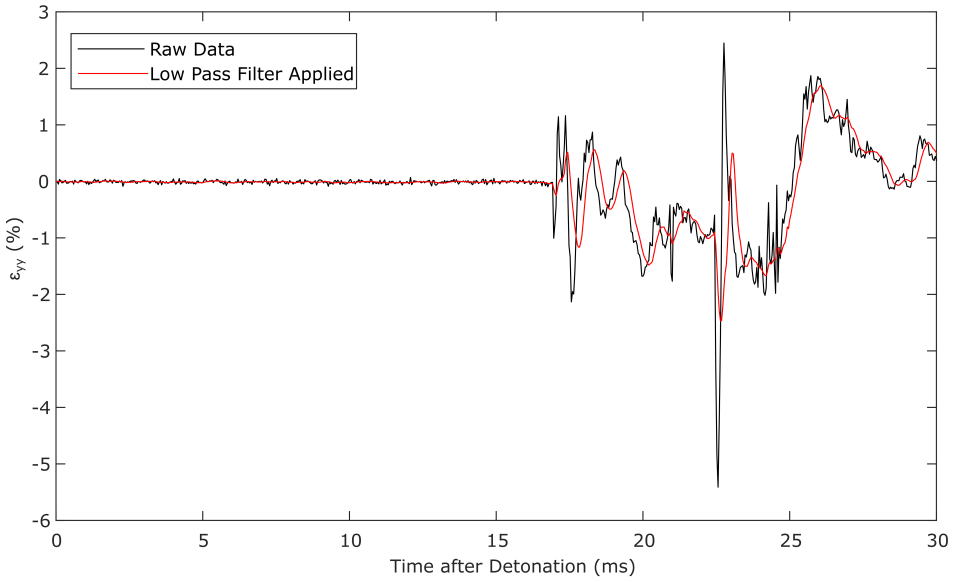


Figure 4.9: Strain gauge data versus time shown as raw data and with moving average low pass filter applied.



Figure 4.10: Photographs showing the test pad setup and the progression of the blast wavefront.

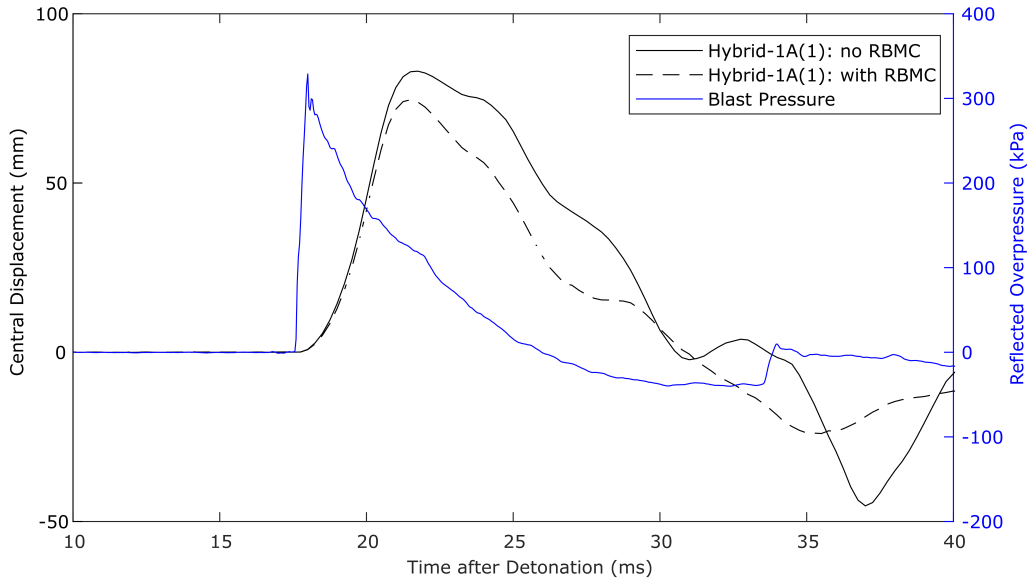


Figure 4.11: Central out-of-plane displacement against time for Hybrid-1A(1) with and without RBMC along with recorded reflected overpressure against time.

deflection. During the rebound stroke, the left-hand and right-hand boundaries deflect by -25.7 mm and 24.6 mm respectively. This is clearly caused by movement due to the fixing method and deflection of the cubicle. Since it is panel behaviour that is of interest, and not the response of the system, all DIC data presented has RBMC implemented. In this frame of reference, the behaviour of the panels govern the response rather than the blast cubicle and fixing method.

4.3.3.2 Full-field Analysis

Figure 4.13 (a) shows a sequence of contour images of the out-of-plane deflection and major strain for Hybrid-1A(1) at intervals of time calculated using DIC. The major strain reaches a maximum at the centre of 0.70 %. This occurs sooner than the displacement reaches a maximum. The remaining high strain on the right-hand side of the panel in the final two images, which reaches 0.54 %, indicates permanent damage to the panel following blast loading. Figure 4.13 (b) shows the displacement of the horizontal cross-section at the mid-plane of Hybrid-1A(1) at discrete intervals of time from zero displacement to maximum displacement. The horizontal cross-section is shown rather than the vertical as it experiences a greater gradient of deflection. Figure 4.13 (c) shows the return phase of this horizontal cross-section. In Figure 4.13 (c), the asymmetrical return of the panel, highlighted in the final four

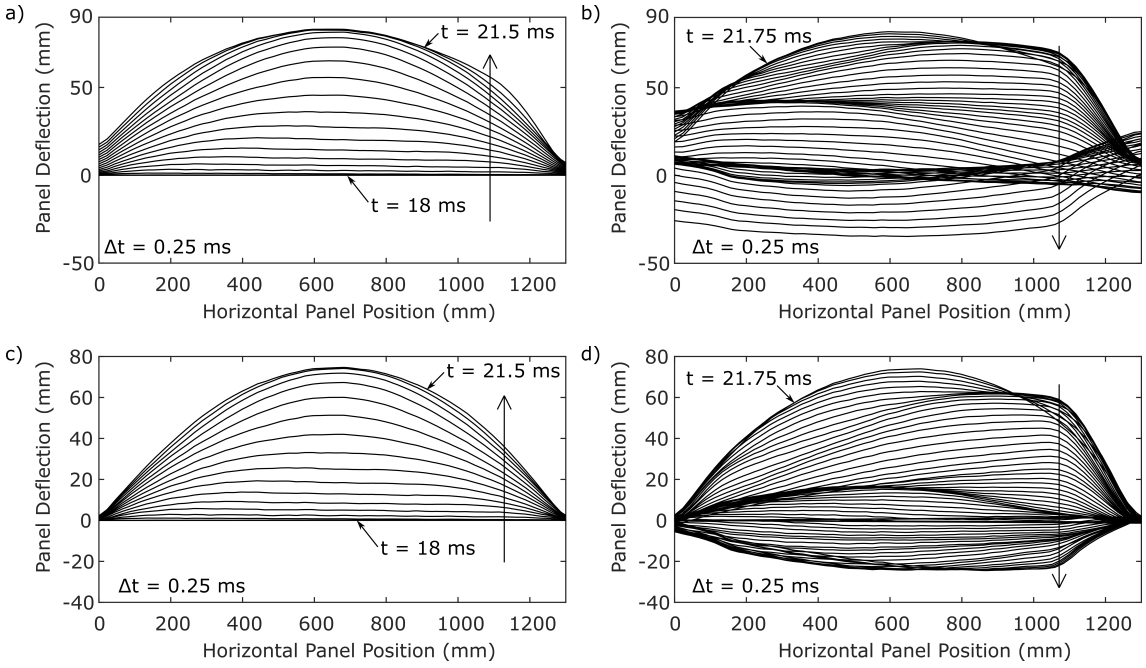


Figure 4.12: Deflection at time intervals for the horizontal centre section showing (a) outward deflection without RBMC, (b) return without RBMC, (c) outward deflection with RBMC and (d) return with RBMC.

images in Figure 4.13 (a), can be seen in an alternative visualisation. The damage to the panel is prominent in this return stroke with gradient discontinuities and deceleration of the panel shown where deflection lines are closer together. Hybrid-1A(1) experiences a maximum central displacement of 74.6 mm.

Figure 4.14 (a) shows the out-of-plane displacement and major strain image sequences for Hybrid-1A(2). The displacement of the horizontal cross-section at the mid-plane of Hybrid-1A(2), as shown in Figure 4.14 (b), is similar to that of Hybrid-1A(1). Figure 4.14 (c) shows the return stroke of this cross-section. The gradient discontinuities indicate that there is permanent damage on both the right-hand side and left-hand side of this panel. The maximum central displacement of Hybrid-1A(2) is 72.8 mm and maximum central major strain is 0.67 %. Maximum major strain was reported with a difference of 0.03 % and maximum displacement with a difference of 1.8 mm for these panels both fabricated with Hybrid-1A skins.

The sequence of images of out-of-plane displacement and major strain for Hybrid-2(1) are shown in Figure 4.15. The remaining high strain, 0.69 %, on the left-hand side of the panel in the final three images indicates permanent damage to the panel following blast loading. Figure 4.15 (b) shows the out-of-plane displacement of the horizontal cross-section at the mid-plane of Hybrid-2(1). Maximum central

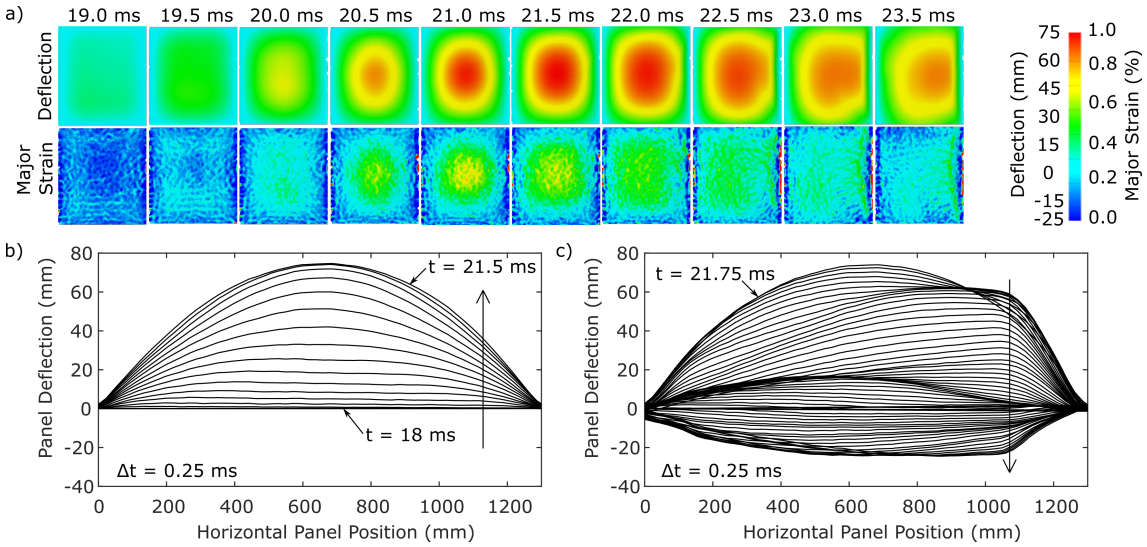


Figure 4.13: DIC results for Hybrid-1A(1) showing: (a) out-of-plane displacement and major strain images, (b) deflection at time intervals for the horizontal centre section and (c) rebound at time intervals for the horizontal centre section.

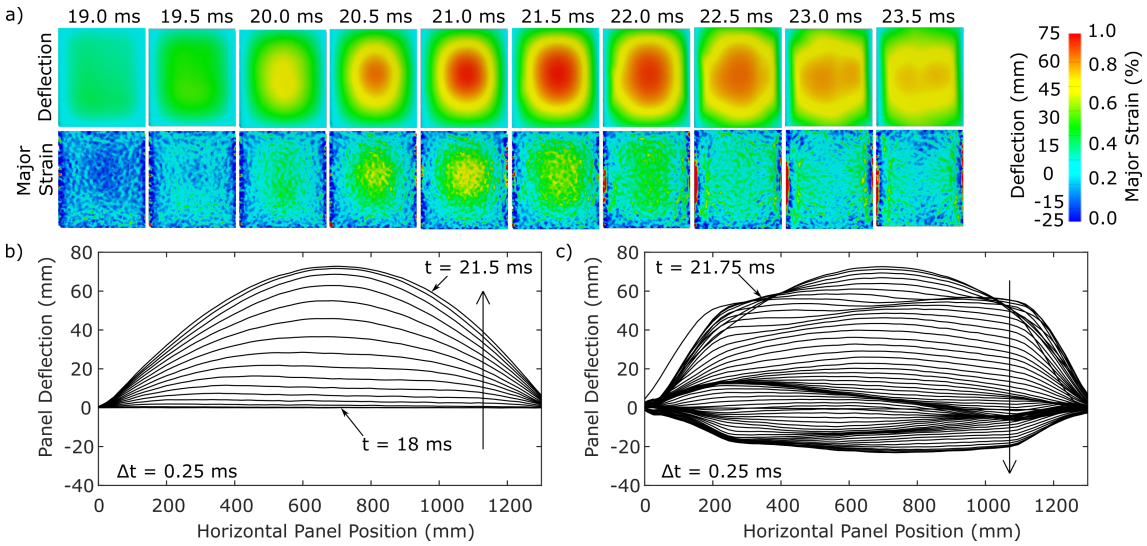


Figure 4.14: DIC results for Hybrid-1A(2) showing: (a) out-of-plane displacement and major strain images, (b) deflection at time intervals for the horizontal centre section and (c) rebound at time intervals for the horizontal centre section.

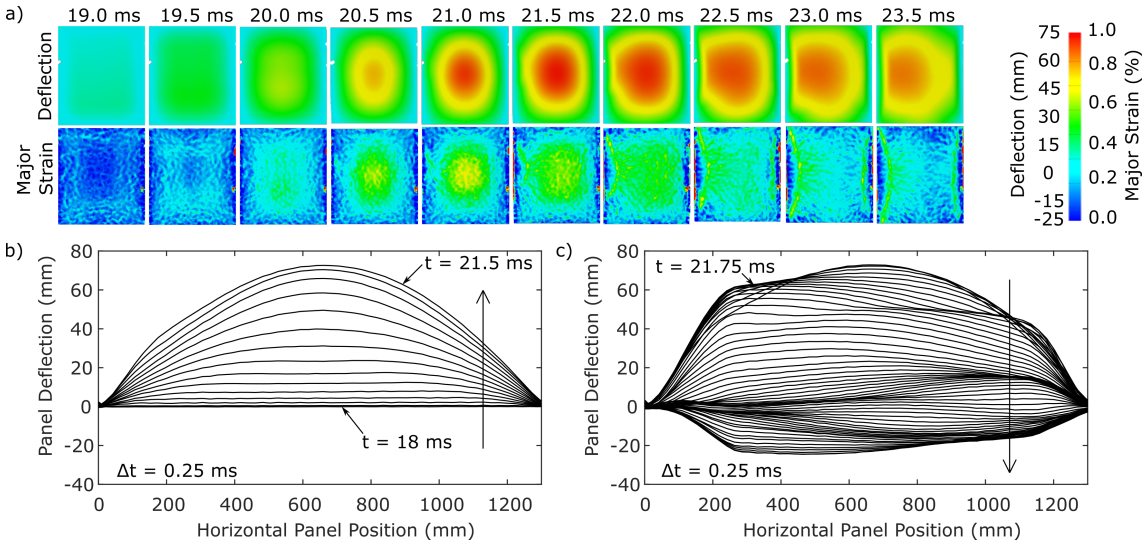


Figure 4.15: DIC results for Hybrid-2(1) showing: (a) out-of-plane displacement and major strain images, (b) deflection at time intervals for the horizontal centre section and (c) rebound at time intervals for the horizontal centre section.

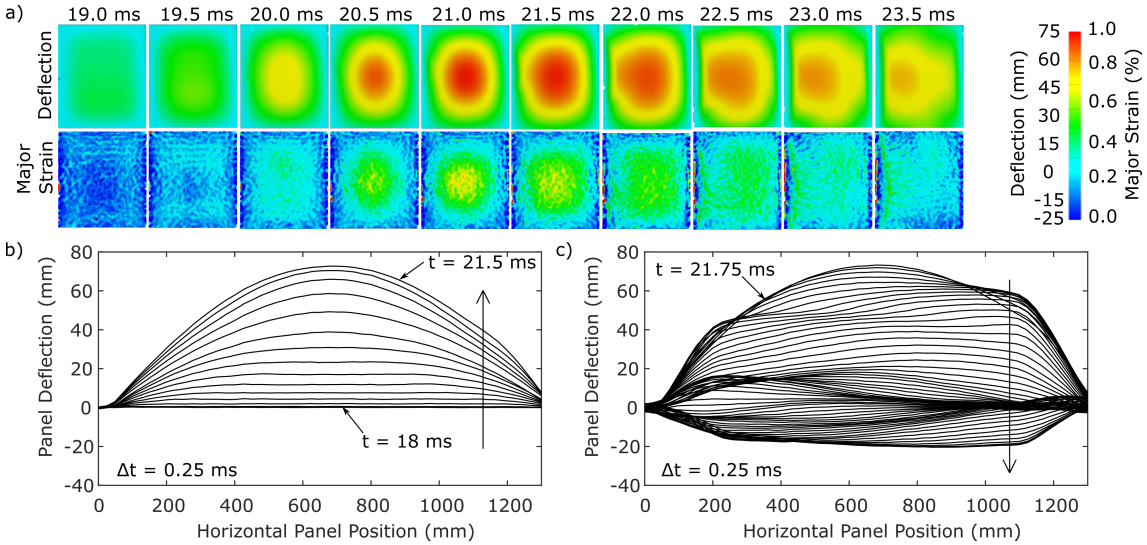


Figure 4.16: DIC results for Hybrid-2(2) showing: (a) out-of-plane displacement and major strain images, (b) deflection at time intervals for the horizontal centre section and (c) rebound at time intervals for the horizontal centre section.

displacement reached by this panel is 72.8 mm. The return stroke of this cross-section is shown in Figure 4.15 (c). In Figure 4.15 (a) and (c), sharp changes in deflection gradient, as seen one quarter of the way across the panel width, indicate damage to the panel. The maximum central major strain experienced by Hybrid-2(1) is 0.65 %.

Figure 4.16 (a) shows the DIC image series for out-of-plane deflection and major strain for Hybrid-2(2). Figure 4.16 (b) shows the displacement of the horizontal cross-section at the mid-plane for Hybrid-2(2). The maximum displacement of the centre point is 72.8 mm. The return phase of this cross-section is shown in Figure 4.16 (c). The asymmetrical return of the panel can be seen and, once again, correlates with the DIC image sequence in Figure 4.16 (a). The panel experiences a maximum central major strain of 0.70 %. The Hybrid-2 panels showed no difference in central maximum displacement and a 0.05 % difference in maximum central major strain.

4.3.3.3 Central Point Analysis

Figure 4.17 shows a plot of the incident blast pressure along with the displacement of the centre points of all four panels tested. The reflected overpressure reaches a maximum of 328.9 kPa before slowly reducing to zero. The deflection against time of both hybrid types is similar as damage is not yet present within the panels. The deceleration and variation in gradient of the centre points during the return to zero is caused by damage within the panels. Based on the theoretical blast wave velocity and results analysis, the DIC data was deemed reliable until 40 ms. After this time, vibrations from the cubicle base and from the blast wave transmit through the camera stands affecting the relative positions and orientation of the cameras compared to their initial position. This is sufficient time to capture the peak deflection and rebound of each panel. Comparison of the positive phase duration of the pressure signal and time taken to reach peak panel displacement show that the panels are tested in the dynamic regime [5]. Under the blast conditions, both hybrids types demonstrate similar deflection and rebound behaviour. A plot of blast impulse versus time is included in Figure 4.17.

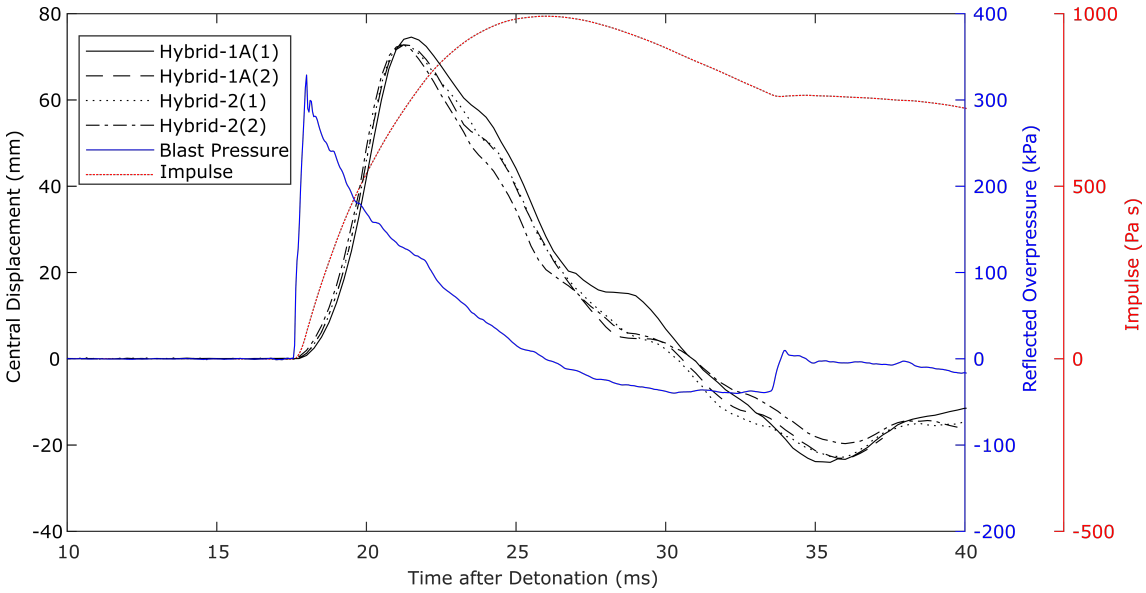


Figure 4.17: Central out-of-plane displacement against time for the four composite sandwich panels along with the recorded reflected overpressure against time.

4.3.3.4 Work Done

The work done in displacing the entire panel by the distributed blast pressure has been calculated. The Pro S Air results, detailed in Section 4.3.1, were used to generate a normalised pressure value at the 400 target point locations for each time step between 17.25 ms and 22.00 ms after detonation. This is the time between the pressure wave arrival and panel maximum displacement. The normalised pressure values were multiplied by the experimentally recorded blast pressure recorded at each corresponding time step. This gives a pressure distribution across the panel that estimates what would have occured during the experiment. The displacement of the 400 corresponding locations across the panel were extracted from DIC data for each time step. The work done at each location was calculated by multiplying the displacement at that location by the pressure experienced at that location and by the small area encompassing that point. The sum of work done at all 400 locations was calculated for each time step. Figure 4.18 shows a plot of cumulative work done against time for all four panels tested.

Both Hybrid-2 panels undergo greater work done than both Hybrid-1A panels. Since all four panels experienced the same pressure wave, the difference in work done is due to differing panel displacements. More locations on the Hybrid-2 panels experienced a greater deflection compared to Hybrid-1A despite both panel types having a similar centre point displacement. This indicates that Hybrid-2 undergoes a more

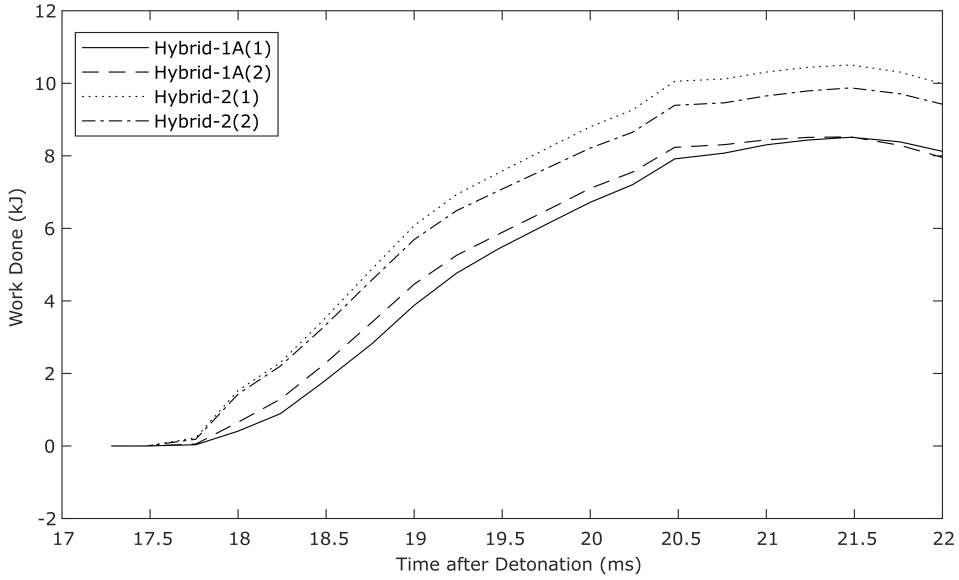


Figure 4.18: Cumulative work done against time for the four composite sandwich panels.

widespread global deflection under blast loading. This could be due to the slightly reduced bending stiffness of Hybrid-2 and ability for this layup to undergo greater deflection. Conversely, the widespread deflection could be due to more widespread damage within the panel. Post-blast damage assessment of the panels will help to reveal whether the widespread deflection is beneficial or not.

4.3.4 Strain Gauges

4.3.4.1 Central Point Strain

Two panels, Hybrid-1A(1) and Hybrid-2(1), were instrumented with strain gauges on the front skins to understand the panel response. Figure 4.19 shows the strain recorded at the centre of panel Hybrid-1A(1) using a strain gauge on the front skins versus the strain recorded on the rear skin using DIC. The rear skin y-direction strain from DIC data peaks at 0.57 % at 21 ms after detonation. The front skin strain recorded by the strain gauge initially experiences oscillations due to stress waves travelling through the panel thickness. When the blast wave loads the panel it sends a compressive stress wave through the panel. Upon reaching the rear face, the stress wave is reflected back as a tensile wave. As this occurs, compressive loading is maintained on the front of the panel until the blast overpressure reduces

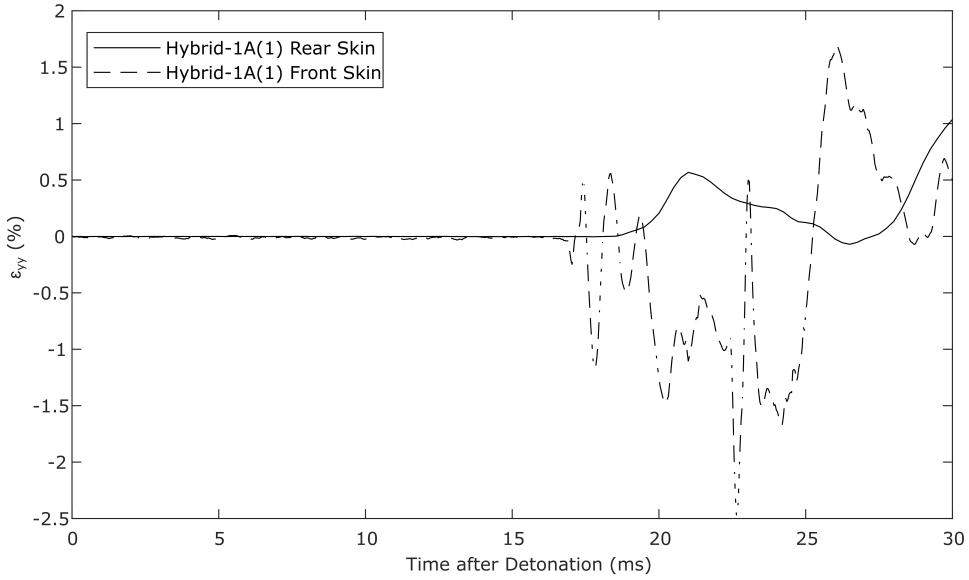


Figure 4.19: Central y-direction strain taken from DIC data for the rear skin and strain gauge data for the front skin.

to zero. The stress waves generated by the initial load and ongoing load superpose through the panel thickness. In addition, the stress wave propagation velocity varies depending on whether the panel materials are loaded within their elastic or plastic regions. The different material layers within the composite sandwich panel reflect and transmit the stress waves to varying degrees. All of these factors combine and result in multiple stress waves travelling through the panel thickness at different velocities. The strain gauge on the panel front experiences oscillations between tension and compression due the the stress waves between 17 ms and 19.5 ms before the deflection of the panel occurs and dominates the strain recording. When the panel deflects under the blast load from 19.5 ms onwards, the front skin experiences compression as the front skin strain is largely negative. This compressive strain peaks at -2.47 % at 22.46 ms after detonation. The panel then rebounds resulting in tensile strain on the front skin, reaching a maximum of 1.69 %, and the rear skin goes into compression with a small magnitude of -0.07 %. Both skins experience tension during the transition. This indicates that the panel experiences stretching. Unforunately the strain gauges located at the centre of Hybrid-2(1) did not record so the central response of the two panels can not be compared.

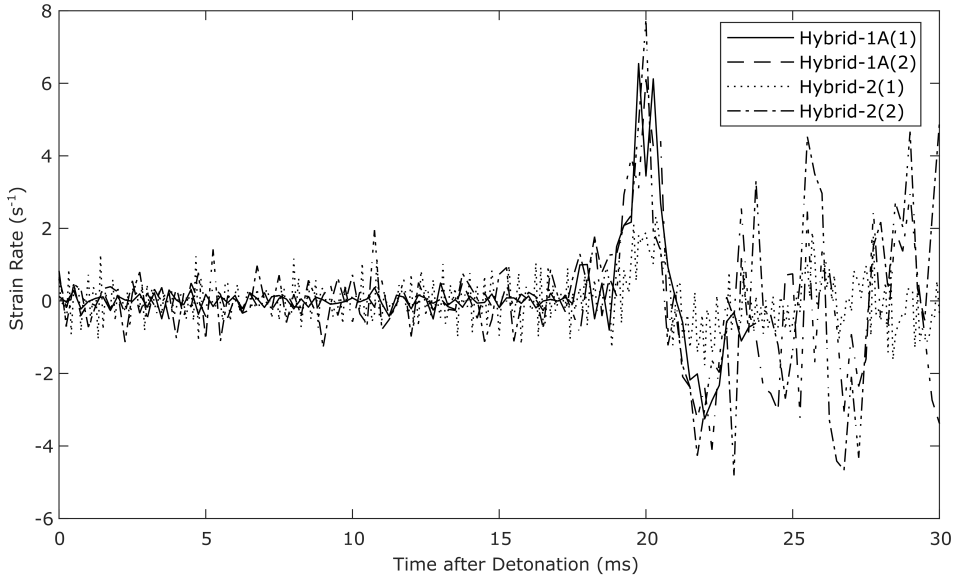


Figure 4.20: Central point major strain versus time plot taken from rear skin DIC data.

4.3.4.2 Central Point Strain Rate

The strain rate of the central point on each panel is shown in Figure 4.20. This is calculated by differentiating the back skin strain, recorded using DIC, with respect to time. Hybrid-2(2) experiences a peak strain rate of 7.76 s^{-1}. The time to reach peak strain from zero is up to 16 times slower for this blast experiment compared to the high velocity impact experiment detailed in Chapter 3. The peak strain rate under 75 m s^{-1} impact was recorded as 124 s^{-1} for the GFRP panel. The differences between the loading conditions and panel dimensions result in the differing strain rates. Although the impact experiment results in a greater strain rate, the results were informative. The impact experiment captures greater variation in the panel results aiding layup selection. Furthermore, the ability of a panel to withstand a more severe loading regime is beneficial. The experiments capture the behaviour of hybrid panels under blast and impact loading which are both loading types that a naval vessel could encounter.

4.3.4.3 Influence of Test Cubicle

Figure 4.21 shows the comparison of front skin strain for the two instrumented panels at four locations on the front skin. The strain readings clearly demonstrate that the panel is not supported equally around the perimeter due to the steel cubicle

design. Furthermore, the panel does not experience a uniform load due to blast clearing effects as detailed in Section 4.3.1. This accounts for the asymmetrical response, particularly during rebound. The central column between the two panels has a lower stiffness than the edge columns and experiences the greatest loading during blast as the blast clears the edges. The central column, therefore, deflects under blast loading. The strain gauges along the centre edges of the panels record lower strain readings. The outer edges experience strain up to twice the magnitude, -5.74 %, due to the greater constraint imposed by the stiffer edge of the steel cubicle. These support conditions dictate the location of damage observed in the composite sandwich panels, highlighted by areas of high strain in the DIC data. Uniform support conditions would result in damage appearing along all panel edges. However, the formation of a crack would result in stress relief elsewhere so symmetric crack formation is unlikely to occur without sustained or increased loading. Support structure design can aid in the blast resilience of composite sandwich panels or any other material by making support movement permissible [5].

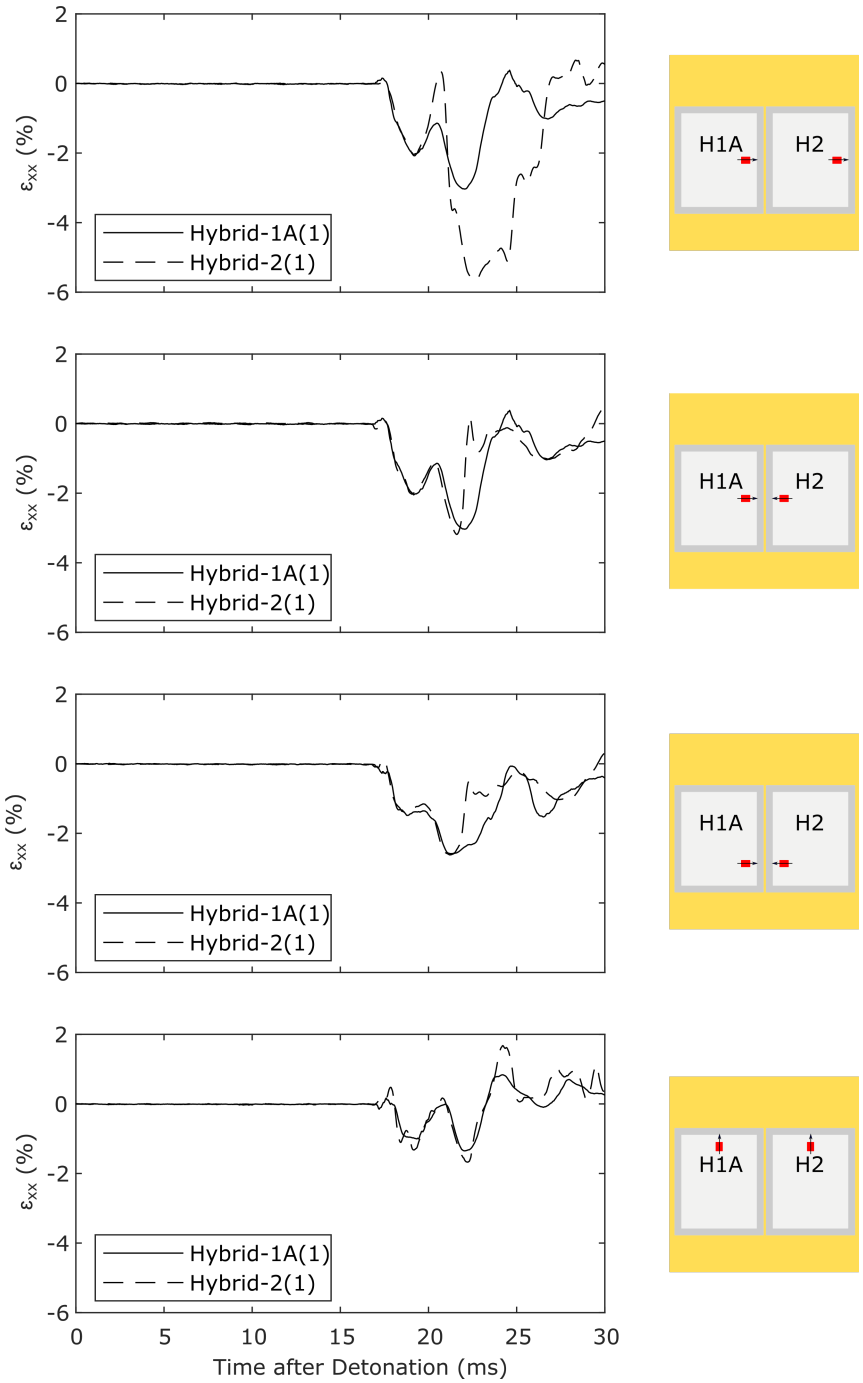


Figure 4.21: Comparison of strain gauge readings at different locations across panel Hybrid-1A(1) and Hybrid-2(1).

4.3.4.4 Strain Gauge versus DIC

Although the magnitude of the strain experienced by the front and rear skin is different, the spatial strain variations can be compared. Figure 4.22 shows plots of the areal minimum, maximum and average in the region of the strain gauge, taken from DIC data, against the front strain gauge data for Hybrid-1A(1). Figure 4.23 shows plots of strain gauge versus DIC data at locations on Hybrid-2(1). The DIC and strain gauge data generally agree in terms of deflection time. The rear skin experiences tension and front skin compression with the skins returning to zero strain at a similar time before deflecting again. The strain gauge readings on the left-hand side of Hybrid-1A(1) in Figure 4.22, the outer edge of the cubicle, show high strain readings after 22 ms post-detonation peaking at -4.8 %. This correlates with the DIC areal maximum strain readings which also remain high compared to other areas of the panel. This is visible in Figure 4.13 (a) and is due to the bending moment being greatest towards the built-in supports. There are low gauge and DIC strain readings near the top and bottom of the panel. The DIC strain at the centre of the panel shows a clear peak and return to near zero which correlates with the strain gauge reading. Hybrid-2(1) was mounted next to Hybrid-1A(1) hence the outer edge of the cubicle is on the right-hand side of this panel. As shown in Figure 4.23, the strain gauge in the centre of the right-hand side records -5.6 % strain. Again this correlates with the DIC strain readings, highlighting the influence of the stiff outer support. The strain towards the top and bottom of Hybrid-2(1) is lower than the strain recorded towards the centre of the panel. Overall, both panels demonstrate a similar response. The DIC images in Figures 4.13, 4.14, 4.15 and 4.16 are viewed from behind the panel hence are the opposite of the strain gauge readings. The DIC data from the rear face can reliably be used to comment on the spatial strain variations experienced by the whole panel. The DIC results are summarised in Table 4.5.

Table 4.5: Summary of DIC analysis results.

Panel type	Peak centre point deflection (mm)	Peak centre point strain (%)	Peak cumulative work done (kJ)
Hybrid-1A(1)	74.6	0.70	8.51
Hybrid-1A(2)	72.8	0.67	8.52
Hybrid-2(1)	72.8	0.65	10.51
Hybrid-2(2)	72.8	0.70	9.87

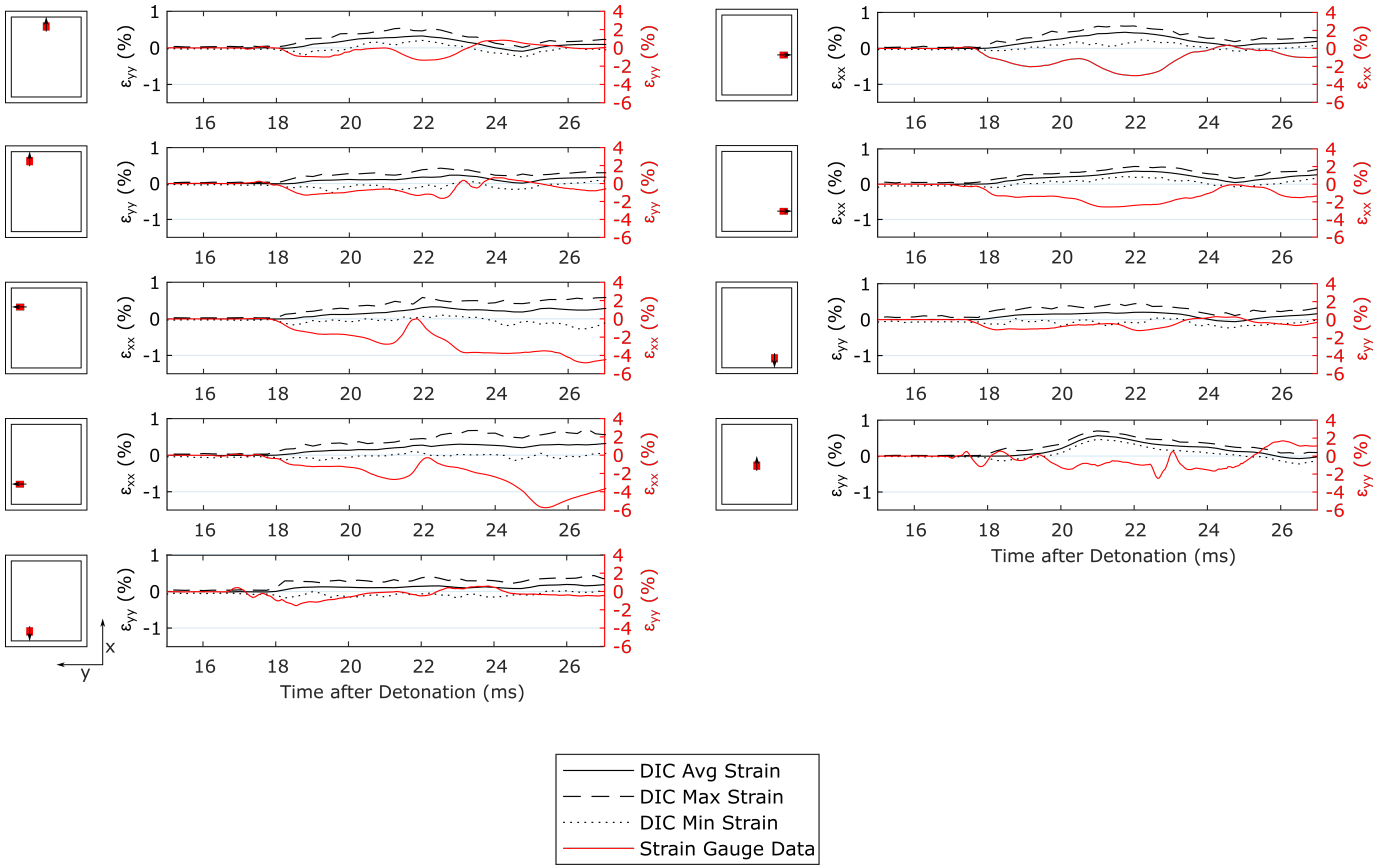


Figure 4.22: Comparison of DIC strain and strain gauge readings at different locations across panel Hybrid-1A(1).

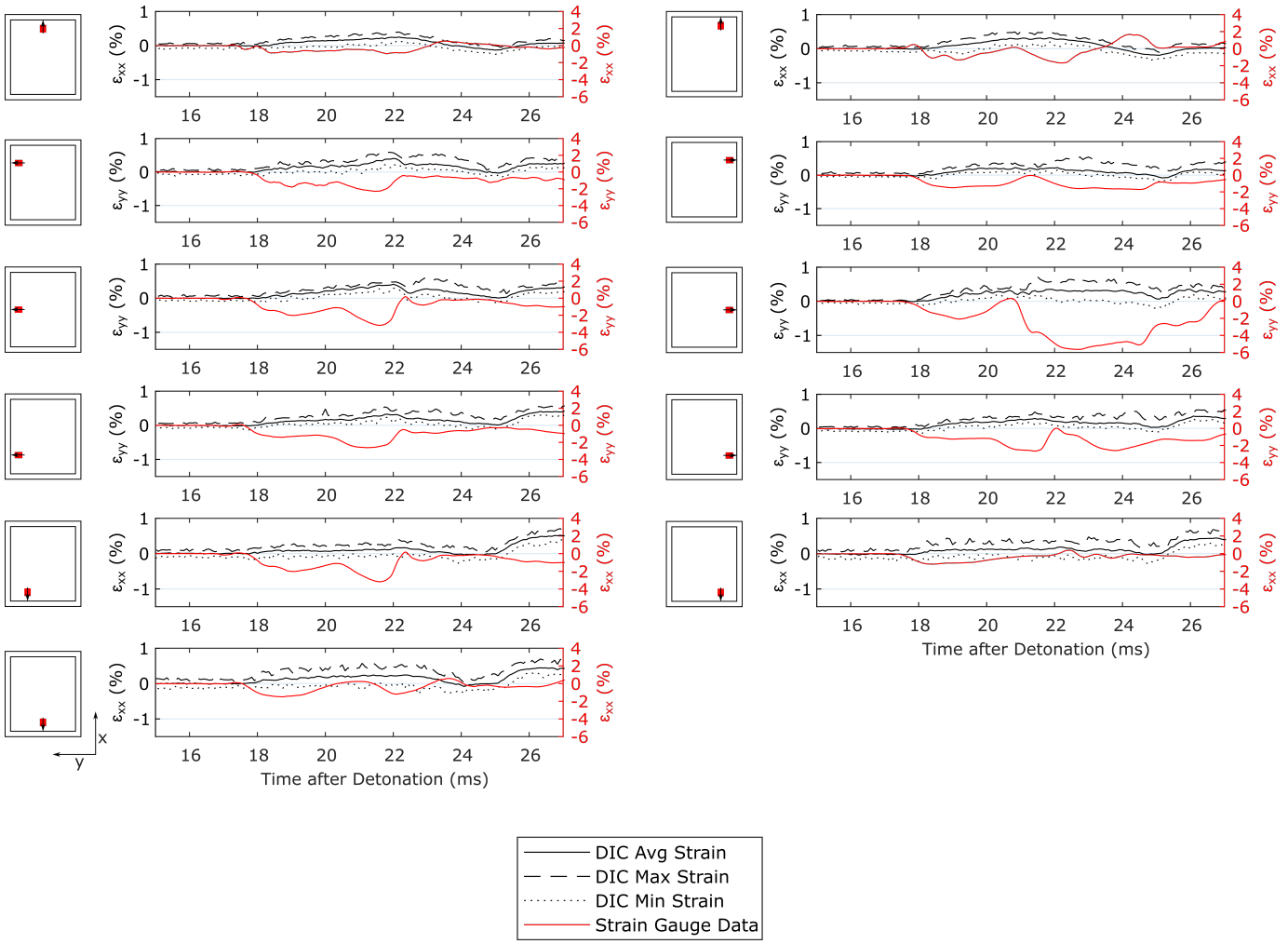


Figure 4.23: Comparison of DIC strain and strain gauge readings at different locations across panel Hybrid-2(1).

Table 4.6: Summary of pressure results.

	Peak reflected pressure (kPa)	Peak reflected impulse (Pa s)	Positive phase duration (ms)
Experimentally recorded	328.9	986.2	8.4
Pro S Air predicted	328.9	890.5	7.7

4.3.4.5 Pressure Data

Table 4.6 summarises the recorded and predicted pressures from this experimental setup. The experimentally recorded pressure was filtered using a moving average filter with a span of 10 points, identical to the filter applied to the strain gauge data. The peak pressure from this filtered data and the peak Pro S Air pressure agreed exactly. The peak pressures were expected to differ. The Pro S Air model was expected to overpredict the reflected pressure as it assumes the cubicle is perfectly rigid. During the experiment, however, the reflected pressure gauge was housed at the centre of a concrete block. This concrete block would offer more resistance against the blast wave compared to the steel cubicle. Additionally, the exact size of the concrete block was not measured. The size of the obstacle affects blast wave clearing and hence the reflected pressure recorded. The Pro S Air model reliably predicted the reflected pressure, impulse and positive phase duration all to within 10 %. The results provide confidence in the accuracy of both the experimental data and the CFD predictions. Although the peak pressures agreed exactly, this is not expected to be the case for future Pro S Air models.

4.3.4.6 Hybrid Skins versus Glass-Fibre & Carbon-Fibre Skins

Due to the costs associated with large scale blast testing, it was only possible to test four composite panels during this trial performed at RAF Spadeadam. Furthermore, repeat tests on the hybrid types were desired to ascertain whether the method and results were repeatable and reliable. Therefore, it was not possible to directly compare the hybrid panels to conventional panels with solely glass-fibre and carbon-fibre skins. Data from a previous experiment performed by Arora et al. [37] is shown in Table 4.7 alongside the data gathered during the experiment detailed in this chapter. The studies adopted different panel areal densities, core thicknesses and stand-off distances. In order to draw a comparison between the panel deflections, the deflection was divided by the panel areal density and multiplied by the explosive scaled distance. These values are shown in the sixth column of the ta-

Table 4.7: Comparison of hybrid panels to previous glass-fibre and carbon-fibre panels.

Panel type	Areal density (ρ_A) (kg m^{-2})	Panel core thickness (t) (mm)	Scaled distance (Z) (m kg$^{-1/3}$)	Peak centre point deflection (dz_{max}) (mm)	$\frac{dz_{max}}{\rho_A} \times Z$	$dz_{max} \times t \times Z$
Hybrid-1A(1)	14.66	30	3.23	74.6	16.5	7232.4
Hybrid-1A(2)	14.66	30	3.23	72.8	16.2	7057.9
Hybrid-2(1)	14.66	30	3.23	72.8	16.2	7057.9
Hybrid-2(2)	14.66	30	3.23	72.8	16.2	7057.9
GFRP †	17	25	3.02	140	24.9	10556.7
CFRP †	17	25	3.02	107	19.0	8086.4

†Data taken from Arora et al. [37]

ble. The values show that even when scaled distance and panel areal density are accounted for, to some extent, the hybrid panels undergo a lower deflection compared to panels with soley GFRP or CFRP skins. Another comparative value which takes into account the core thickness and scaled distance is shown in the seventh column of Table 4.7. This value is calculated by multiplying the deflection by the core thickness and the scaled distance. Once again, the hybrid panels exhibit a lower deflection when these two parameters, core thickness and scaled distance, are taken into consideration. Reduced deflection, however, does not guarantee improved blast performance. Significant blast energy can be absorbed through deflection provided that the deflection does not lead to panel damage. The deflection of the GFRP panel detailed in Table 4.7 led to severe panel damage [37]. This indicates that the GFRP panel deflection was beyond an allowable level thereby causing damage. The low deflection of the hybrid panels indicates that excessive deflection has not occurred. However, damage analysis of the hybrid panels is required. An optimal panel design would enable maximum deflection whilst sustaining an allowable level of damage.

4.3.5 Post Blast Damage Inspection

Following blast testing, Hybrid-1A(1) and Hybrid-2(1) were cut into eight sections. All edges were photographed and visually inspected for core cracks, front skin/core debonding and rear skin/core debonding. All photographs were taken in line with a steel rule, to enable size calibration of the images. Using the same MATLAB script as detailed in Chapter 3, the core cracks, debonding and delaminations were recorded. The total length of core cracks and debonds were recorded in millimeters.

No visual damage on the front or rear skins was observed for either Hybrid-1A(1) or Hybrid-2(1). Figure 4.24 (a) shows cross-sections of Hybrid-1A(1) as viewed from the bottom of the panel. Figure 4.24 (b) highlights a cross-section at the mid-plane where a shear core crack is visible approximately 200 mm in from the panel edge. Shear core cracks are visible around 200 mm in from the edge on both sides of the panel on multiple cross-sections. This implies that the shear cracks have propagated vertically for over half the panel length. The cross-sectional views for Hybrid-2(1) are shown in Figure 4.25. Shear core cracks are, again, located approximately 200 mm in from both panel edges. Figure 4.25 (b) highlights debonding between the front skin and core along with a shear core crack that is visible. The shear cracks in the foam core are all at approximately 45° to the through thickness direction. As shown in Figures 4.24 (b) and 4.25 (b) the shear cracks are angled towards the centre of the panel at the front skin. Front skin/core debonding propagates from the point where the shear crack reaches the front skin towards the panel centre. Figure 4.26 shows schematic diagrams of the locations and extent of visible core shear cracking and front skin/core debonding for Hybrid-1A(1) and Hybrid-2(1). Table 4.8 details the visual damage assessment based on the photographs taken. The results highlight that the analytical prediction performed in Section 4.3.1 accurately predicted the occurence of core shear failure. However, a front skin wrinkling index of 1.01 was not sufficient to cause visible front skin damage.

Hybrid-1A(1) and Hybrid-2(1) underwent a similar central point deflection, however, the work done calculation illustrates that Hybrid-2(1) experiences a more widespread global deflection. The damage assessment reveals that this greater deflection leads to greater damage. As discussed before, a larger allowable deflection results in a greater blast impulse that can be resisted by the panel. However, larger deflections can lead to greater panel damage and it is clear that this is the case for the two types of panels investigated in this study. Based on these results the lower deflection, caused by the higher stiffness of Hybrid-1A, is advantageous. An increase in panel stiffness could lead to greater brittle failure yet this is not the case for Hybrid-1A indicating that this layup is approaching a good trade-off between stiffness and deflection. Although there is a difference in panel damage, overall both panels demonstrate minimal damage following a significant blast load demonstrating the exceptional blast resilience of hybrid composite sandwich panels.

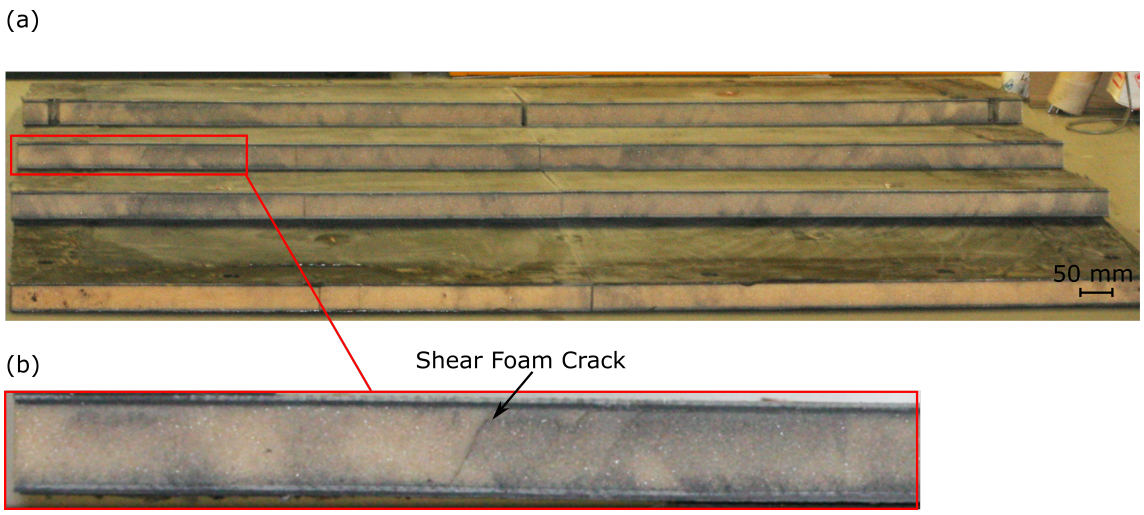


Figure 4.24: Photographs showing the damage to the core of Hybrid-1A(1) as viewed from the bottom.

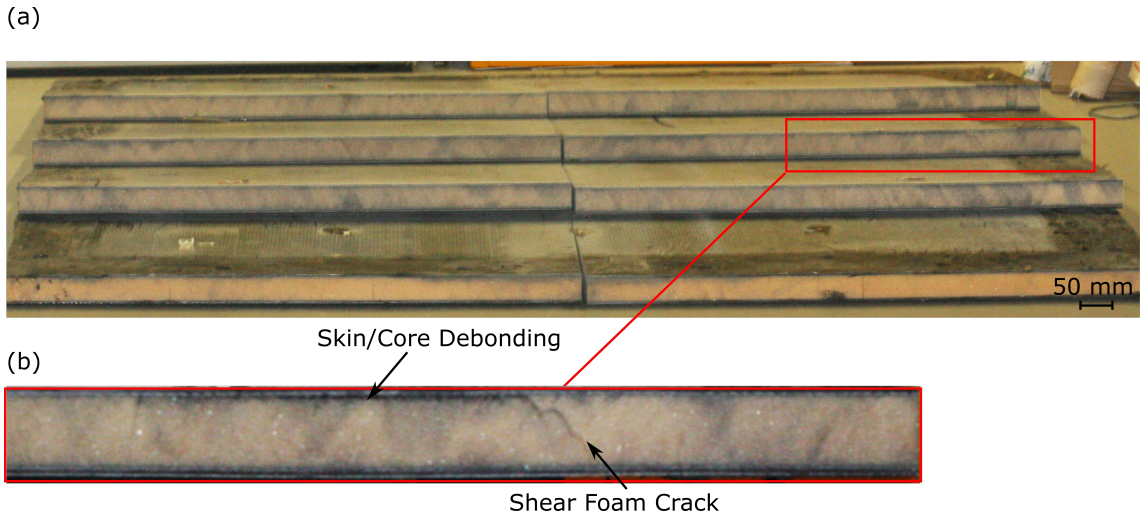


Figure 4.25: Photographs showing the damage to the core of Hybrid-2(1) as viewed from the bottom.

Table 4.8: Damage sustained by two hybrid panels identified using visual inspection and photographs.

Panel type	No. of core cracks	Length of core cracks (mm)	No. of core/front skin debonds	Length of front debonds (mm)
Hybrid-1A(1)	8	279	1	22
Hybrid-2(1)	12	424	1	101

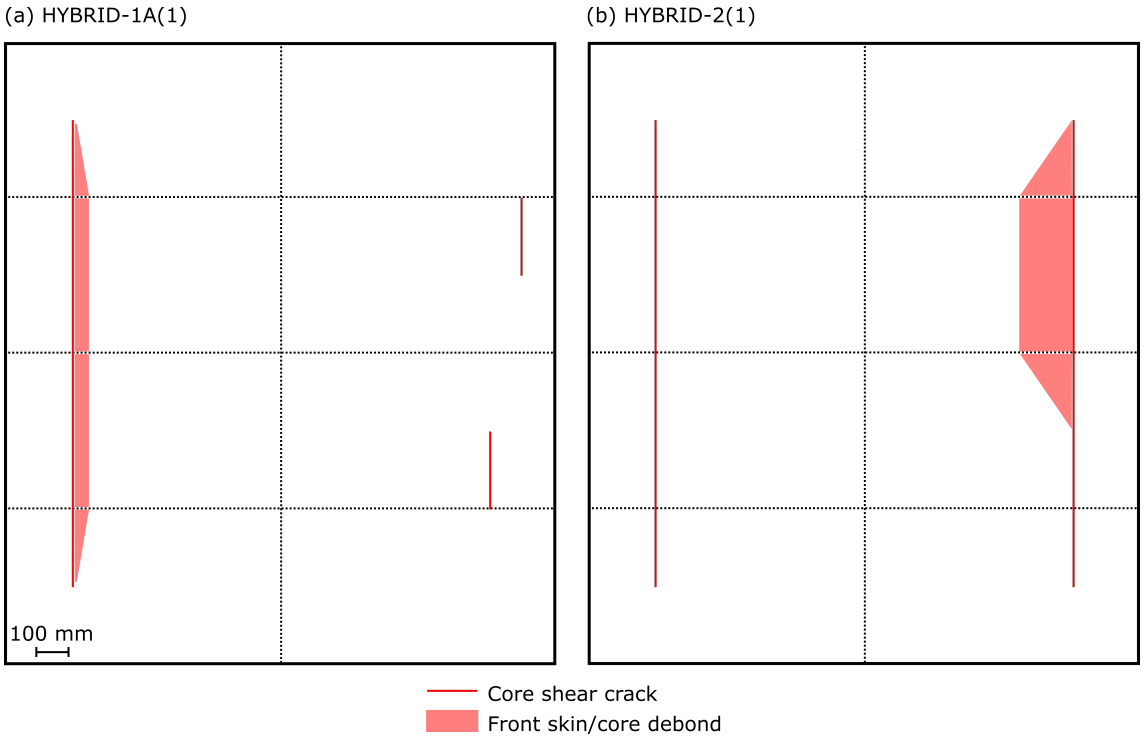


Figure 4.26: Schematic diagrams showing the location and extent of damage for (a) Hybrid-1A(1) and (b) Hybrid-2(1).

4.4 Discussion

4.4.1 Blast Wave Modelling and Work Done

Pro S Air CFD software was used to predict the expected blast loading on the sandwich panels. This was performed to aid experimental design, to validate experimentally recorded pressure and to reveal blast clearing effects. Differences between the experiment and model were expected to arise due to the assumptions made during modelling. These assumptions included an infinitely rigid target and a perfectly elastic floor. Nevertheless, the computationally predicted and experimentally recorded peak reflected overpressures were identical. Furthermore, the positive phase duration and hence blast wave impulse showed good agreement. Identical correlation is not expected for future models. The blast wave model was used to generate a pressure distribution across the sandwich panel. This revealed the non-uniform pressure load experienced by the sandwich panel and accounts for the asymmetric deflection captured using DIC. This pressure distribution was then made dimensionless, multiplied by the experimentally recorded pressure and displacement of each

facet to obtain work done on each panel under blast. The cumulative work done by each panel under blast revealed a difference in performance between Hybrid-1A and Hybrid-2. Hybrid-2 was shown to undergo more widespread deflection due to its reduced stiffness.

4.4.2 Digital Image Correlation

DIC enabled rear skin out-of-plane displacement and strain tracking. Rigid body motion compensation was implemented across all the DIC data. This removes the movement of the cubicle and fixing system and isolates the panel response relative to its boundaries. The full-field DIC results showed that all four panels demonstrate similar deflection and strain behaviour under the blast load experienced. The results are summarised in Table 4.5. The deflection and return beyond zero were similar for all four panels. In addition, the DIC data for all panels showed that they experienced internal damage at one quarter and three quarters along the horizontal cross-section. This is visible in the form of sharp gradient changes caused by a local drop in bending stiffness, where the foam core has failed. The DIC data also demonstrates the repeatability of the experimental setup. Good agreement between the two Hybrid-1A panels and between the two Hybrid-2 panels were achieved demonstrating the reliability of the results and method. Based on these results, specimen repeats are not required in future experiments.

Under small scale impact in Chapter 3, these hybrids were shown to exhibit different deflections and strains. This is because under the impact experiment, the panels experience a localised load at a higher velocity and higher strain rate. Due to the localised loading, the front skin, core and rear skin are engaged independently. In addition, the projectile punctured the front skins of the panels and core. Through this mechanism, the skin and core absorb energy yet the load remains localised as the panel does not distribute load through bending. Different deflections and strains may have been exhibited because the front skins were perforated and hence tested to a more extreme extent. Under large scale blast loading, the pressure load is more uniform across the panel. The panel, therefore, responds globally. Under these circumstances, the skin layups and core are engaged simultaneously in the global bending response. Under blast loading, the presence, and hence interactions, of both types of fibres is more dominant compared to the position of each fibre fabric layer.

4.4.3 Strain Gauge Data

Hybrid-1A(1) and Hybrid-2(1) were each instrumented with 14 strain gauges. In total, 8 gauges failed to record data. Due to the nature of the experiment, limited time was available to identify and resolve the issue. The blast test, therefore, continued with 20 functioning gauges. The strain gauge data revealed the non-uniform support of the steel test cubicle. Coupled with blast clearing effects, these support conditions result in a compliant central column and more rigid edge supports. The external panel edges experience greater constraint. This correlates with the DIC deflection profiles. The more constrained external panel edges experience a greater deflection gradient which in turn leads to damage. The strain gauge data also highlights the greater strain magnitude experienced by the front skin confirming the major role that is played by the foam core in energy absorption through elastic compression and damage mechanisms. Finally, the strain gauge data and DIC data were shown to correlate spatially. Panel areas with high DIC strain were shown to have high strain gauge readings. Although the front and rear skins experience different strain magnitudes, the DIC data from the rear skin can reliably be used to comment on the spatial strain variation across the whole panel.

4.4.4 Hybrid versus GFRP and CFRP

The blast performance of Hybrid-1A and Hybrid-2 were compared to data from a previous experiment performed by Arora et al. [37] in which panels with solely GFRP or CFRP skins were blast tested. Since a large number of parameters differed between the tests, only a qualitative comparison between the different composite sandwich panels can be made. Two performance indices were calculated to compare the different panels. These indices took panel areal density, core thickness and stand-off distance into account, as far as possible. The values demonstrated that the hybrid panels underwent a lower deflection. As stated previously, panel deflection can absorb significant blast energy provided it is not excessive and does not lead to severe damage. Although these comparative results appear promising, an optimal panel design would allow large deflections whilst minimising damage. Therefore, a direct comparison of hybrid composite sandwich panels against panels with conventional skin materials is required.

4.4.5 Post Blast Damage

Post-blast visual damage inspection revealed no significant damage to the front or rear skins of the panels. Shear core cracks, 200 mm in from both edges spanning the panel vertically, are visible for both Hybrid-1A(1) and Hybrid-2(1). The core shear crack angles and direction of front skin/core debond propagation have been highlighted by the post-blast photographs. The work done calculation shows that Hybrid-2(1) underwent a more widespread deflection which leads to greater post-blast visual damage, as shown in Table 4.8. These results illustrate that under this blast load, the higher stiffness of Hybrid-1A is advantageous. Overall, the damage sustained by both hybrid panels was minimal and did not significantly affect their structural integrity. These results revealed the considerable blast resilience of both panel types. Due to a manufacturing error, the skins were constructed from eight bi-axial fabric plies instead of four. Had the panels been fabricated from four bi-axial plies, as intended, the panels would have had a reduced stiffness leading to greater deflection, skin damage and core damage. A more significant difference between the hybrid layups may have been observed.

The asymmetry of Hybrid-1A was not detrimental to the overall panel performance under these blast conditions. Although Hybrid-1A(1) did suffer from a greater central point deflection, the work done calculations revealed the more widespread deflection of the Hybrid-2 panels. Furthermore, the damage sustained by Hybrid-1A(1) was lower than that sustained by the symmetric Hybrid-2(1). The results demonstrate that when loading direction is known, the coupling in the composite laminate skins introduced by asymmetry is not detrimental.

Based on the results from this chapter, further investigations were deemed necessary during a second set of blast trials. Panels with four bi-axial plies would be tested to cause more considerable damage. Hybrid composite sandwich panels with more significantly different bending stiffnesses and areal densities would be compared. Panels with conventional GFRP or CFRP skins would be directly compared to the performance of hybrid composite sandwich panels.

4.5 Conclusion

Four hybrid composite sandwich panels were simultaneously subjected to a 100 kg nitromethane charge at 15 m stand-off distance. The investigation was carried out to compare the blast resilience of two different hybrid skin layups and to demonstrate the repeatability of the test method. The main difference between the two hybrids

can be seen in the work done calculation. Both Hybrid-2 panels underwent greater work done caused by a more widespread panel deflection. Hybrid-2 has a reduced bending stiffness compared to Hybrid-1A. This subsequently lead to greater internal panel damage in the form of core shear cracks and skin/core debonding. Hybrid composite sandwich panels have demonstrated more significant variations under impact due to the localised nature of the loading. Under blast loading, the panels are able to respond in a global manner; hence both skins and cores are engaged simultaneously. Under blast loading, the presence of both fibre types was found to be more dominant than the position of each fibre layer. The hybrid composite sandwich panels appear to offer advantages over previously tested GFRP and CFRP panels. However, a direct comparison is required as a number of parameters differed between the two tests.

Implementation of strain gauges on panels during blast loading has revealed that front skins experience a greater magnitude of strain than the rear skins. This confirms that the foam core plays a major role in energy absorption during loading. This occurs through elastic compression and damage to the core. Although the magnitude of rear skin strain from DIC is lower, the spatial strain distribution correlates between front and rear, hence the number of strain gauges can be reduced in future experiments.

The test cubicle design was shown to influence the location of panel damage. The more rigid constraint imposed by the cubicle edges resulted in higher strain readings, greater deflection gradients and hence core shear cracking. This experiment set out to investigate the blast performance of the panels alone, however, it is well known that the blast resilience of an entire structure can be improved by allowing a permissible level of deflection.

Chapter 5

Full Scale Air Blast Testing: Part 2

5.1 Introduction

Further full-scale air blast experiments were performed on hybrid composite sandwich panels at Radnor Range Ltd, Wales. Once again, a large scale experimental setup was adopted to simulate the loading and response representative of naval structures and their threats.

Two test series were carried out, subjecting a total of seven composite sandwich panels to PE7 charges. The first test series investigated the response of three composite sandwich panels to a 30 kg charge at 10.5 m stand-off distance. This created pressure and impulse signatures similar to those detailed in Chapter 4. The second series involved loading four panels against a repeated 8 kg PE7 charge at 8 m stand-off distance. Repeated loading aimed to highlight whether the damage initiated in hybrid composite sandwich panels under the first blast would be exacerbated by a repeat blast loading.

This chapter continues the investigation into air blast performance of hybrid composite sandwich panels. During the previous chapter, the stiffness and mass per unit area of the selected panels were very similar. Only the panel work done highlighted a difference in panel performance. Therefore, two hybrid composite sandwich panels with more significantly different layups were fabricated and compared. Benchmark composite sandwich panels with GFRP and CFRP skins were manufactured such that the difference in performance could be directly compared and quantified. All panels adopted a PVC foam core.

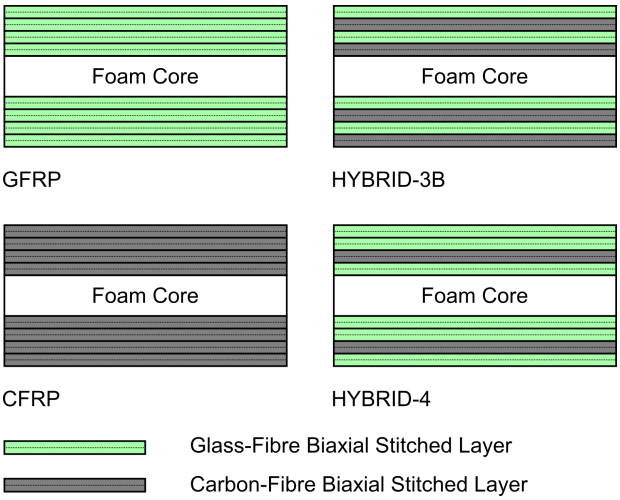


Figure 5.1: Layup configurations of the four types of composite sandwich panel fabricated for full-scale air blast testing.

These experiments utilised a similar setup to those performed in Chapter 4. High-speed DIC was adopted to record the response of the panels. Due to the spatial correlation achieved in Chapter 4, a reduced number of foil strain gauges were adhered to the front skins of the panels. Polyvinylidene fluoride (PVDF) film pressure senors were implemented during the blast experiments to extend the pressure recording methods. Understanding the post-blast behaviour of these panels was extended to include both damage analysis and compression testing.

This test series was the first of its nature carried out at Radnor Range. This chapter details how the test setup and instrumentation techniques, which had been trialled over previous years at RAF Spadeadam, were successfully adapted to Radnor Range.

5.2 Experimental

5.2.1 Materials

Hybrid composite sandwich panels were directly compared to panels with solely GFRP or CFRP skins in two test series. A schematic of the layups of these panels is shown in Figure 5.1. During test series A, three panels were subjected to a 30 kg PE7 charge at 10.5 m stand-off distance. Test series B involved subjecting four panels to a repeat load. The panels experienced two 8 kg PE7 charges at 8 m stand-off distance. The types of panels evaluated in each test are detailed in Table 5.1.

Table 5.1: Details of the panel types tested in each series.

Test series	PE7 charge (kg)	Stand-off distance (m)	Panel type	Panel dimension (m × m)
A	30	10.5	GFRP(1)	1.39 × 1.23
			CFRP(1)	1.39 × 1.23
			Hybrid-3B(1)	1.39 × 1.23
B	2 × 8	8	GFRP(2)	0.80 × 0.80
			CFRP(2)	0.80 × 0.80
			Hybrid-3B(2)	1.39 × 1.23
			Hybrid-4(1)	1.39 × 1.23

5.2.1.1 Test Series A

The panels in test series A were 1.39 m × 1.23 m in size. The cubicle size dictated the maximum panel width. The panel length was selected such that the aspect ratio was equal to the panels detailed in Chapter 4. The panels were constructed from four layers of bi-axial stitched fabric either side of a 30 mm thick Divinycell H100, 100 kg m^{-3}, PVC foam core. The fabric layers were arranged quadriaxially $[0/90/-45/+45]_2$CORE$[+45/\text{-}45/90/0]_2$. The same fibres, matrix and fabrication method as detailed in Chapter 4 was used again. 600 gsm E-glass-fibre and 400 gsm HexTow AS4 carbon-fibre were used along with SR8100 epoxy resin and SD8824 hardener. The panels were fabricated using resin infusion and were ambient cured and then held under vacuum for 24 h before being demoulded. GFRP, CFRP and Hybrid-3B panels were selected for this experiment. Hybrid-3B was constructed from an equal number of plies of glass-fibre and carbon-fibre. The GFRP and CFRP panels would act as benchmarks and quantify the advantages or disadvantages of adopting hybrid composite skins under the same blast conditions. Furthermore, this test series aimed to result in a pressure and impulse signature similar to that of Chapter 4. Therefore, a qualitative comparison between the panels tested in this series and in Chapter 4 could be drawn.

5.2.1.2 Test Series B

The Hybrid-3B and Hybrid-4 panels adopted in test series B were identical in size, material and fabrication method to those in test series A. The two hybrid panels in Chapter 4 demonstrated similar performance, therefore, Hybrid-3B and Hybrid-4 were selected due to their more significant differences. Hybrid-3B has a greater proportion of carbon-fibre and a greater mass per unit area. The hybrid layers are thinner resulting in a reduced cross-sectional area of each material and more inter-

faces between the dissimilar fibre materials. Based on the analytical calculations performed in Chapter 3, the composite skins in Hybrid-4 have a high modulus considering they contain only one bi-axial carbon-fibre ply. Due to supplier constraints, the GFRP(2) and CFRP(2) panels in this test series were 0.8 m × 0.8 m in size. The panels were constructed from four layers of bi-axial stitched fabric either side of a 40 mm thick, 130 kg m^{-3} PVC foam core (Divinycell H130). The fibre layers were arranged with the same quadriaxial layup. 600 gsm E-glass-fibre and 400 gsm Toray T700 carbon-fibre were used along with high elongation vinylester resin and hardener.

As in Chapter 4, the properties of the materials used and the approximate face-sheet properties calculated using the rule of mixtures are detailed in Table 5.2. Once again, due to the varying positions and quantities of carbon-fibre and glass-fibre layers, a difference in panel stiffness is expected. Table 5.3 details the measured areal density, calculated bending stiffness and fibre volume fraction for each panel type.

5.2.2 Methods

During testing, the composite sandwich panels were mounted side-by-side onto a steel cubicle. The dimensions and panel mounting method were adapted to suit the new test cubicle at Radnor. The front of the cubicle had two sections with clamps welded around the perimeter. Two 10 mm thick steel sheets were fabricated to slide into the cubicle front and provide support for the panels. These sheets had 1.03 m × 1.19 m openings over which the panels were mounted. To prevent excessive deflection of the steel front, steel bars were welded across the width of the cubicle behind the sheets. Steel sheets with 0.60 m × 0.60 m openings for the smaller panels were also fabricated. Figure 5.2 shows photographs of the front of the cubicle with the larger and smaller panels mounted. As shown in Figure 5.2 (b), the 0.8 m × 0.8 m panels were bolted using 12 × M12 bolts around the perimeter. The 1.39 m × 1.23 m panels were bolted to the steel sheet along the top and bottom edges using 8 × M12 bolts. These panels were clamped using the cubicle clamps along the vertical edges. A 5 mm thick steel frame was placed up against the panel to help distribute the bolting and clamping forces, however, adhering steel frames to the front and rear of each panel was deemed unnecessary. Figure 5.2 also shows pendine concrete blocks placed alongside the cubicle, to prevent blast clearing effects. In addition the vertical height of the cubicle was extended using a steel sheet supported by welded struts. This would mitigate the effects of blast clearing over the top of the cubicle.

Table 5.2: Mechanical properties of the composite sandwich panel materials and plies.

Material	Density (kg m^{-3})	Elastic modulus (GPa)	Tensile strength (MPa)	Shear strength (MPa)	Compressive strength (MPa)
Glass-fibres	2555 [96]	78.5 [96]	2000.0 [96]	-	4500.0[96]
Carbon-fibres (HexTowAS4)	1790 [105]	230.0 [105]	4410.0 [105]	-	4950.0 [96]
Carbon-fibres (Toray T700)	1800 [112]	230.0 [112]	4900.0 [112]	-	4950.0 [96]
SR8100 epoxy & SD8824 hardener	1119 [106]	2.7 [106]	50.0 [106]	48.0 [106]	103.0 [96]
Vinyl ester resin & hardener	1045 [96]	3.5 [96]	85.5 [96]	57.0 [96]	94.8 [96]
BX600/epoxy bi-axial GFRP ply	1913	22.9	574.9	48.0	1289.3
FCIM105/epoxy bi-axial CFRP ply	1425	53.9	1032.4	48.0	1184.3
BX600/vinyl ester bi-axial GFRP ply	1754	20.3	515.0	57.0	1107.0
T700/vinyl ester bi-axial CFRP ply	1464	65.4	1399.1	57.0	1417.1
PVC H100 foam core	100 [107]	0.1 [107]	3.0 [107]	2.1 [107]	2.7 [107]
PVC H130 foam core	130 [107]	0.2 [107]	4.2 [107]	2.1 [107]	2.7 [107]

Table 5.3: Properties of the composite sandwich panels.

Panel type	Areal density (kg m^{-2})	Equivalent bending stiffness (kN m^{-2})	Fibre volume fraction
GFRP(1)	10.21	19.8	0.55
CFRP(1)	8.98	55.5	0.46
GFRP(2)	12.22	36.7	0.47
CFRP(2)	11.06	70.5	0.56
Hybrid-3B	9.94	48.7	0.39
Hybrid-4	9.88	38.9	0.39

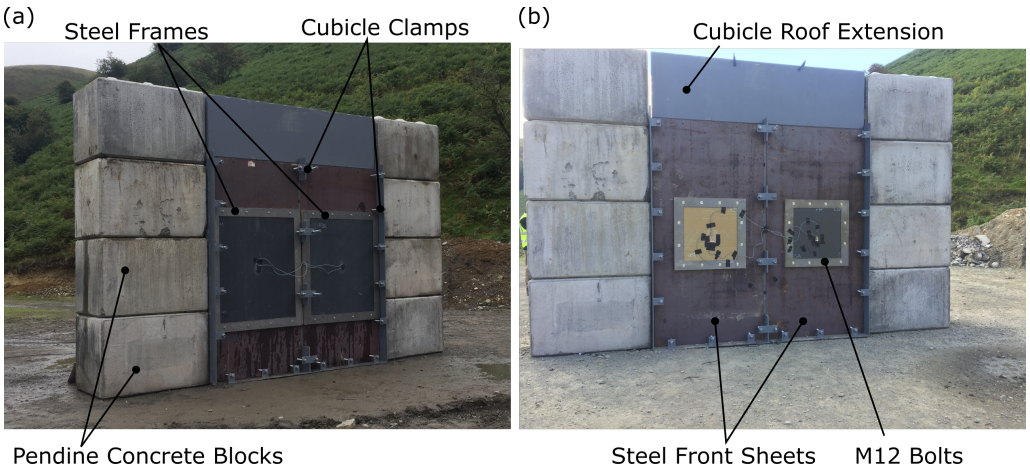


Figure 5.2: Photographs of panels mounted on the cubicle showing: (a) large 1.39 m × 1.23 m panels and (b) small 0.8 m × 0.8 m panels.

5.2.2.1 Blast Wave Modelling

The charge size and stand-off distance were calculated to cause sufficient damage to the composite panels without damaging instrumentation situated behind the panels. Spherical charges were used in all trials to create a non-biased spherical pressure wave. Furthermore, it was desired to maintain the same Hopkinson-Cranz scaled distance for the charge and stand-off distance as used in the experiment detailed in Chapter 4. The calculation for scaled distance is shown in Equation 5.1, where R is the stand-off distance from the charge centre in metres and W is the charge mass expressed in kilogrammes of TNT. It is recommended that a charge weight enhancement factor of 1.8 is assumed for surface explosions to take into account wave reflections caused by the ground [5]. For the experiments in Chapter 4, Z was equal to 2.66. At Radnor Range, the available explosive was PE7 and the charge sizes available were 30 kg, 8 kg and 1 kg. 30 kg charges were selected to create a large uniform pressure wave across the panel surface, and create similar peak overpressure, positive phase duration and hence impulse as the 100 kg nitromethane charge at 15 m stand-off distance in Chapter 4. 8 kg charges were selected to cause near-field, non-uniform pressure loading across the panels and to investigate the effect of repeat blast loads on the panels. Using a TNT equivalence of 1.33, the stand-off distances for these charges based on the Hopkinson-Cranz scaled distance were calculated as 11 m for the 30 kg PE7 charge and 7 m for the 8 kg PE7 charge.

$$Z = \frac{R}{W^{\frac{1}{3}}} \tag{5.1}$$

Table 5.4: Failure indices for the 1.39 m × 1.23 m GFRP panel against a 30 kg PE7 charge according to the analytical solution outlined by Andrews and Moussa [66].

Stand-off distance (m)	Peak reflected overpressure (kPa)	Positive phase duration (ms)	Core shear failure index	Front skin wrinkling index	Tensile skin failure index
10	388.8	5.60	4.62	1.92	1.30
10.5	341.8	5.80	4.20	1.75	1.18
11	305.0	6.00	3.83	1.60	1.08

The analytical method outlined by Andrews and Moussa [66] was used alongside Pro S Air modelling to determine whether these stand-off distances were appropriate and further refine the distances. Experience from the experiments performed in Chapter 4 revealed that positioning of the charge and cubicle to 0.5 m accuracy would be achievable. Failure mode calculations were, therefore, carried out for stand-off distances of 10 m, 10.5 m and 11 m for the 30 kg PE7 charge. The failure indices were calculated for all panel types. The peak reflected overpressure, positive phase duration and failure indices for the most severe case at these stand-off distances, which was the 1.39 m × 1.23 m GFRP panel, are shown in Table 5.4. Since a different explosive material and charge size were used, the same maximum reflected overpressure and impulse as Chapter 4 could not be achieved. A satisfactory trade-off between these two parameters at a stand-off distance of 10.5 m was selected. Experience from Chapter 4 revealed that a failure index of 1.01 was not sufficient to cause front skin wrinkling failure. Furthermore, these failure indices were for the most severe case. To cause damage in the other panels, these severe failure indices would have to be pushed to their limit. Only one 1.39 m × 1.23 m GFRP panel would be subjected to a 30 kg blast, therefore, it was determined that the likelihood of catastrophic panel failure and damage to the cameras under loading at this stand-off distance would be highly unlikely.

Failure mode calculations were carried out for stand-off distances of 7 m, 7.5 m and 8 m for the 8 kg PE7 charge. The peak reflected overpressure, positive phase duration and failure indices for the most severe case at these stand-off distances, which was the 1.39 m × 1.23 m Hybrid-3B panel, are shown in Table 5.5. A more conservative distance of 8 m was selected as the panels would undergo a repeat load at this stand-off. This distance was selected as the analytical method does not take into account existing panel damage.

As well as aiding in charge and stand-off distance selection, a Pro S Air model of the new experimental setup was created to determine whether the blast pressures

Table 5.5: Failure indices for the 1.39 m × 1.23 m Hybrid-3B panel against an 8 kg PE7 charge according to the analytical solution outlined by Andrews and Moussa [66].

Stand-off distance (m)	Peak reflected overpressure (kPa)	Positive phase duration (ms)	Core shear failure index	Front skin wrinkling index	Tensile skin failure index
7	297.3	4.57	3.76	0.92	0.53
7.5	252.1	4.54	3.27	0.79	0.46
8	217.2	4.50	2.88	0.70	0.40

measured using the PVDF sensors and side-on pressure sensor, detailed later, correlated with the model. Once again, a spherical geometry, cylindrical geometry and a 3D geometry were used in turn to efficiently model the blast wave propagation. The same planes of symmetry and boundary conditions as described in Chapter 4 were implemented in the model. The control volume that was modelled in the 3D geometry stage spanned from the ground to 4 m in height, from the centre of the charge to 13.5 m or 11.5 m in length, depending on the stand-off distance, and from the centre of the cubicle to 4 m in width. The reflected overpressure was measured 25 mm in front of the cubicle to take into account the panel thickness. A measurement was taken at 400 target points across the panel. Pro S Air only has the capability to model PE4 not PE7. However, considering both plastic explosives consist of 88 % Research Department Explosive (RDX) and have the same TNT equivalence, the error in the pressure predictions was deemed to be negligible. In the 3D geometry stage, the cubicle, pendine blocks and roof extension were defined as infinitely rigid obstacles. Models with the cubicle alone, without the pendine blocks and roof extension, were also run. This would reveal their influence on blast clearing and determine whether comissioning of the cubicle roof extension and placement of the pendine blocks was necessary.

5.2.2.2 Instrumentation

5.2.2.2.1 Three-Dimensional Digital Image Correlation

3D DIC was implemented to capture the response of the panels during blast loading. Since two panels were tested per charge, four high-speed cameras were used. The cameras used were a pair of Photron SAX2s and a pair of Photron AX100s recording at 12,500 fps and 4000 fps, respectively. The camera signal circuit input

was connected to a trigger switch. This camera trigger switch was pressed at the same time as the charge detonation switch.

The cameras were, once again, housed within the test cubicles. An identical camera setup to that described in Chapter 4 was adopted. Due to the restricted length of the test cubicle, 24 mm lenses were used on all cameras to ensure the panels were entirely within the field of view (FOV). Using Equations 3.40 to 3.44 the perpendicular distance between the panel and cameras was calculated to be 1.74 m and the distance between the cameras was 0.77 m for the 1.39 m $\times$ 1.23 m panels. For the smaller 0.80 m $\times$ 0.80 m panels the perpendicular distance between the panel and cameras was calculated to be 1.00 m and distance between the cameras was 0.44 m. The cameras were mounted vertically on an aluminium extrude bar using steel plates and the bar was attached to a heavy duty camera stand. Banks of LED lights were used to illuminate the back skin of the panels during blast testing. Calibration of the cameras was carried out using a 700 mm CC coded calibration cross supplied by GOM UK. This calibration cross was selected due to the reduced size of the panels. The rear skin of the panels were painted matt white and a random black speckle pattern was applied to facilitate DIC processing. For the 1.39 m $\times$ 1.23 m panels, the speckles were required to be between 4 mm and 7 mm. For the 0.8 m $\times$ 0.8 m panels the speckles were between 2.5 mm and 4 mm. A photograph of the camera and light setup within the cubicle, along with the panel speckle pattern, is shown in Figure 5.3.

During test series A, an additional high speed Photron SA1 colour camera was setup to record the progression of the wavefront. This camera was mounted on a tripod on the bank of the test arena such that it was protected from the blast wave. The camera recorded at a frame rate of 25,000 fps.

5.2.2.2.2 Foil Strain Gauges

Each panel was instrumented with two single axis gauges (CEA-06-250UW-350) at the centre of the panel to capture the front skin strain magnitude. Fewer gauges were required due to the successful spatial correlation achieved between strain gauge and DIC data during the first air blast experiment. The primary aim of the strain gauges was to record the difference in magnitude between front and rear skin central point strain. One gauge was aligned with the major vertical axis of the panel and the second was aligned with the minor horizontal axis. The same surface preparation, adhesion and coating technique as described in Chapter 4 was used. A three wire quarter-bridge circuit was implemented for the strain gauges to miti-

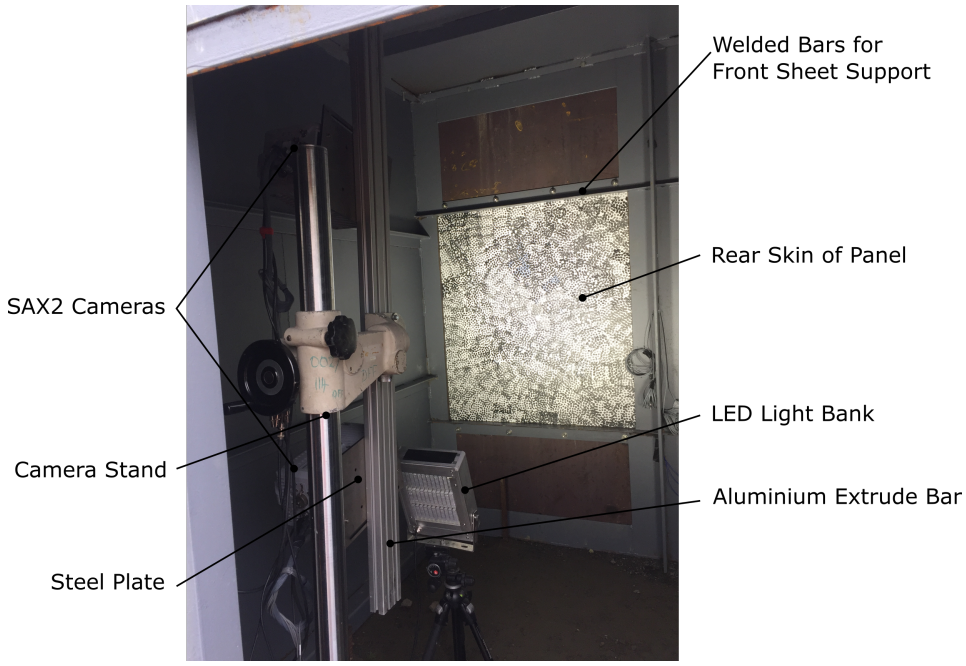


Figure 5.3: Photograph showing the camera setup for full scale blast experiments.

gate the influence of leadwires and ensure a balanced bridge as detailed previously. For these experiments, 5 m long three-core shielded cables with a DIN connector were soldered to the gauge terminal pads and ran into the cubicle to the transducer amplifiers. Two amplifiers were placed in the steel cubicle within an ammunition box and padded with foam. The horizontally aligned gauges were connected to a low frequency Flyde FE-579-TA bridge amplifier and the vertically aligned gauges were connected to a high frequency Flyde H379TA bridge amplifier. The data cables were taped to the front of the panel with slack to prevent the gauges tearing away from the panel during deflection. 200 m of coaxial cable with BNC (Bayonet Neill-Concelman) connectors were used between the amplifiers and the oscilloscopes located in the reinforced cabin recording the data.

5.2.2.2.3 Pressure Gauges

PVDF film pressure sensors were implemented during the blast experiments. These pressure sensors are lightweight thin films that can be taped directly onto the surface of the panels or cubicle adding negligible mass to the system. A PVDF sensor was fixed to the centre of both panels for each blast experiment. The PVDF sensors used have a 25 mm^2 active area and were connected via a 5 m long, low noise coaxial cable to a charge amplifier. The charge amplifier was housed within the

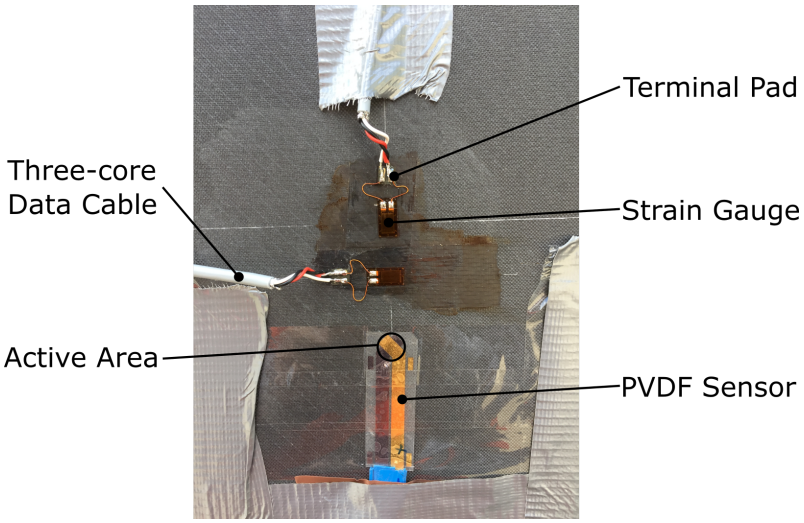


Figure 5.4: Photograph showing the setup of the strain gauges and PVDF pressure gauge at the centre of each panel.

ammunition box in the steel cubicle. Movement of the cable between the PVDF sensor and amplifier during blast would create charge and result in noise within the signal. Therefore, the cable was fixed to the panel front using self-adhesive cable ties. 200 m of coaxial cable with BNC connectors was used between the charge amplifier and the oscilloscope recording the data in the reinforced cabin. A photograph of the strain gauge and PVDF gauge setup is shown in Figure 5.4.

A side-on pressure gauge was situated at the set stand-off distance for each test, 10.5 m for test series A and 8 m for test series B. The pressure gauge was positioned at the centre height of the charge. The sensor was positioned parallel to the blast wave and it measured the static pressure as the air particles moved over the sensor. To reduce the disruption of the flow a thin steel plate was placed over the sensor face.

5.3 Results

5.3.1 Blast Wave Modelling

Figure 5.5 shows a diagram of the panels mounted in the test cubicle. The pressure distribution across the right hand panel was modelled, as highlighted by the red dashed box. The coordinates on the illustration correspond to the coordinates of the blast modelling results shown in Figures 5.6 and 5.7. Figure 5.6 shows the pressure distribution across the right-hand panel with pendine blocks and roof extension in

situ. This reflected overpressure is for 8 kg of PE4 at 8 m stand-off distance. The blast wave impinges on the bottom left-hand corner of the panel first. The pressure increases in a band radially across the panel. Peak reflected overpressure at the panel centre is recorded at 11.41 ms after charge detonation. In the first three time steps, the dark blue regions in the top right-hand corner illustrate that this area of the panel is not yet loaded. The pressure then continues across the panel in a radial direction with the top right-hand corner experiencing the greatest pressure from 11.80 ms onwards. In the final three time steps, the entire panel experiences pressure loading. As time continues, the average overpressure decreases and the pressure across the panel becomes more uniform with an overpressure difference of only 25 kPa at 12.58 ms.

The overpressure maps for 8 kg of PE4 at 8 m stand-off distance without pendine blocks and cubicle roof extension are shown in Figure 5.7. The first three time steps are identical to those in Figure 5.6. The final three, however, differ significantly. At 11.80 ms the top right-hand corner again experiences greatest pressure, however, the pressure drops at the right-hand outside edge of the panel due to blast wave clearing. As time continues the average overpressure decreases but the pressure difference between the central left-hand edge and outer right-hand edge becomes more prominent. At 12.19 ms and 12.58 ms the difference between maximum and minimum overpressure remains at 50 kPa indicating that the pressure across the panel becomes uniform at a slower rate. As a result of these simulations, the comissioning of the cubicle roof extension and placement of the pendine blocks during the blast experiments was deemed necessary to mitigate blast clearing effects.

The pressure distribution across the panels for the 30 kg PE4 charge at 10.5 m stand-off distance with and without the pendine blocks and roof extension show similar characteristics. The peak reflected overpressure and average overpressure for the 30 kg charge at 10.5 m is higher than for the 8 kg charge at 8 m as expected. The two figures illustrating the effect of the pendine blocks and roof extension for the 30 kg charge can be found in Appendix A. The 8 kg charges at 8 m were intended to cause more localised, non-uniform loading of the panel. The pressure distribution plots, however, show that these parameters do not result in more localised loading. Despite this, the charge size and stand-off distance was still selected for the experiment as the failure calculations detailed in Section 5.2.2.1 indicate that damage would be caused in these panels after two blast loads. Reducing the stand-off distance further to create a more localised blast load was not an option as protection of instrumentation behind the panel was critical.

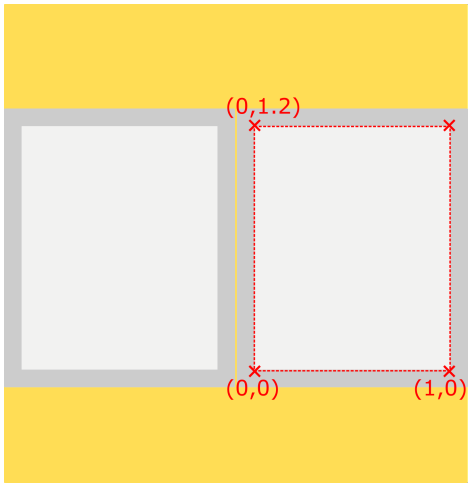


Figure 5.5: Diagram of the panel setup highlighting the area over which pressure distribution was modelled.

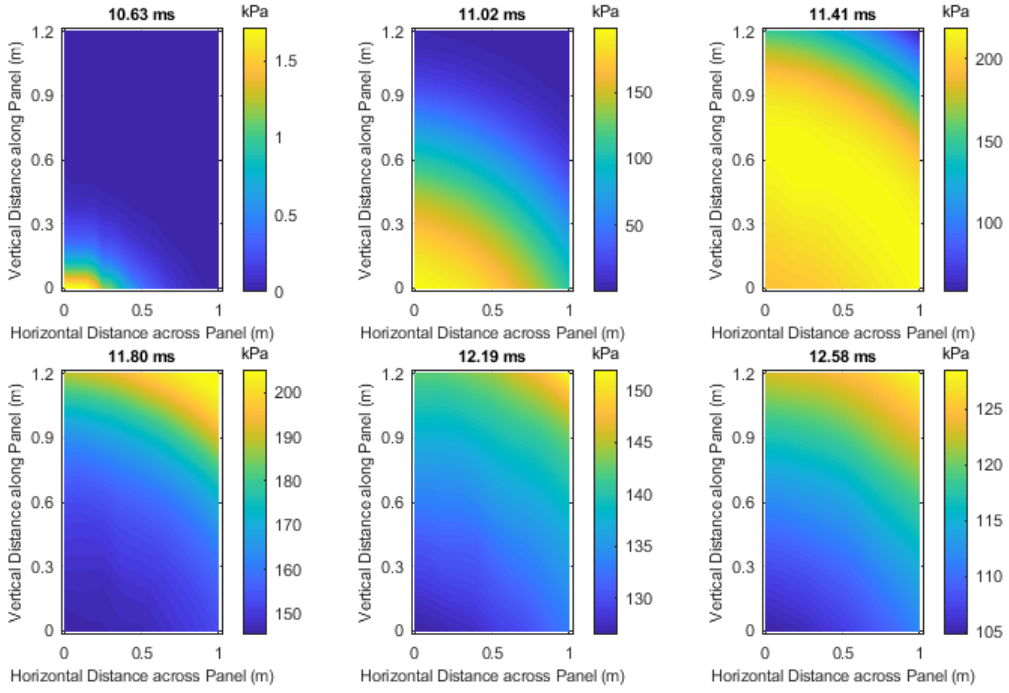


Figure 5.6: Comparison of reflected overpressure distribution across the panel for 8 kg PE4 at 8 m stand-off with pendine blocks and roof extension.

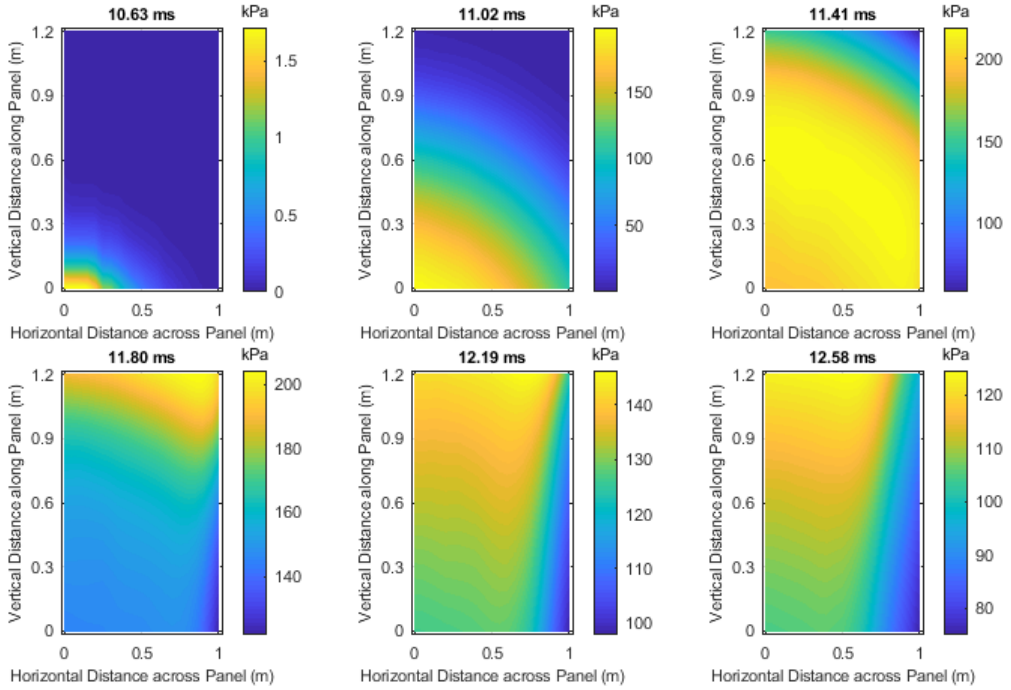


Figure 5.7: Comparison of reflected overpressure distribution across the panel for 8 kg PE4 at 8 m stand-off without pendine blocks and roof extension.

5.3.2 Digital Image Correlation

5.3.2.1 Test Series A

The progression of the blast wave during the first trial in test series A is shown in Figure 5.8. The first image clearly shows the detonation of the charge and the test cubicle. The blast wave front travelling across the ground can then be seen in the subsequent images. The camera exposure was set to a minimum to prevent overexposure caused by light emitted during the explosion. This makes the final two images less clear. The blast wave can be seen reaching the cubicle between 11.2 ms and 14.0 ms after charge detonation.

5.3.2.1.1 Full-field Analysis

Figure 5.9 (a) shows a sequence of contour images of the out-of-plane deflection and major strain for GFRP(1) at intervals of time under a 30 kg PE7 blast load. The major strain reaches a maximum at the centre of 1.46 %. This occurs sooner than the maximum displacement. GFRP(1) experiences a maximum central displacement of 77.6 mm. The remaining band of high strain at the centre of the panel indicates permanent damage. This is supported by the displacement contours which show a

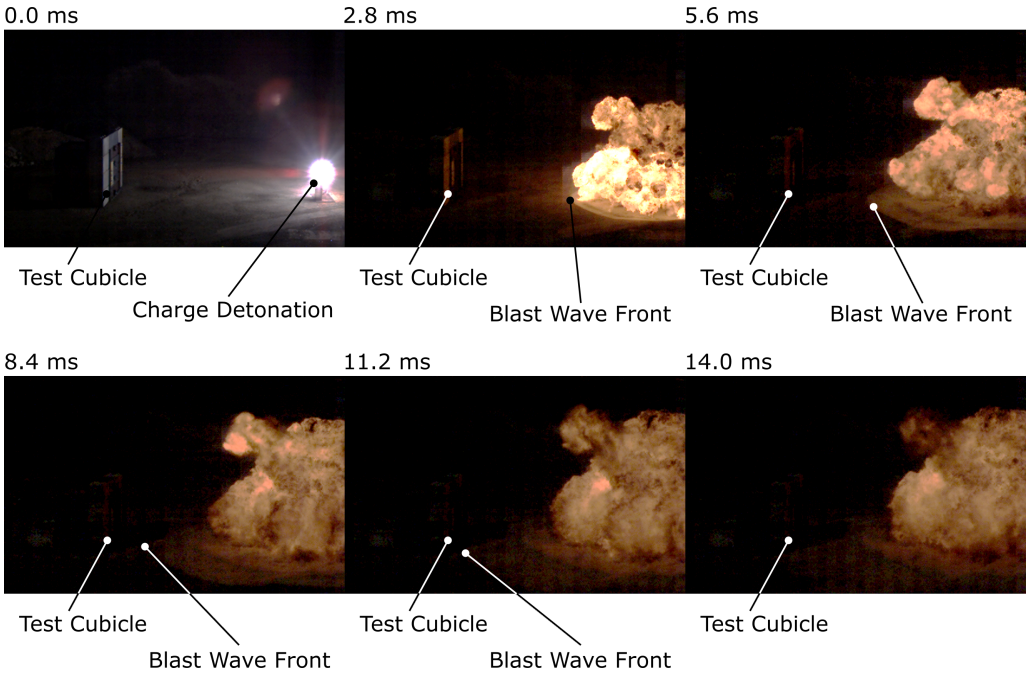


Figure 5.8: Photographs showing the detonation of the charge and progression of the blast wavefront.

higher magnitude of deflection in this region, indicating a loss in panel integrity. Figure 5.9 (b) shows the displacement of the horizontal cross-section at the mid-plane of GFRP(1) at discrete intervals of time from zero displacement to maximum displacement. Figure 5.9 (c) shows the return phase of this horizontal cross-section. In Figure 5.9 (c) the gradient discontinuity highlights the location of panel damage. RBMC has been used to remove movement of the cubicle from the displacement profiles in all DIC analyses. This enables a comparison of the panel response to blast loading.

The sequence of contour images of out-of-plane displacement and major strain for CFRP(1) are shown in Figure 5.10. It is clear that CFRP(1) experiences a lower deflection and strain compared to GFRP(1) due to the higher stiffness of the carbon-fibre skins. The deflection and strain images indicate a region of damage running vertically down the centre of the panel. The band of high strain in the final images for CFRP(1) are less widespread than the band of strain visible for GFRP(1). Figure 5.10 (b) shows the out-of-plane displacement of the horizontal cross-section of CFRP(1). The panel experiences a symmetric deflection but damage is clear on the return stroke in Figure 5.10 (c). The maximum central displacement of CFRP(1) is 61.4 mm and maximum central major strain is 0.79 %.

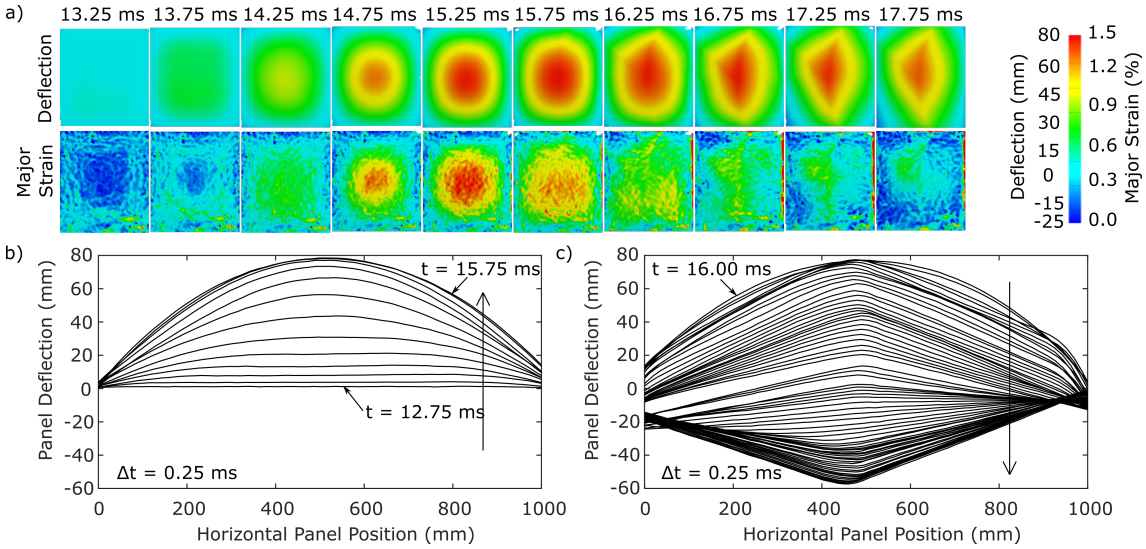


Figure 5.9: DIC results for GFRP(1) showing: (a) out-of-plane displacement and major strain images, (b) deflection at time intervals for the horizontal centre section and (c) rebound at time intervals for the horizontal centre section.

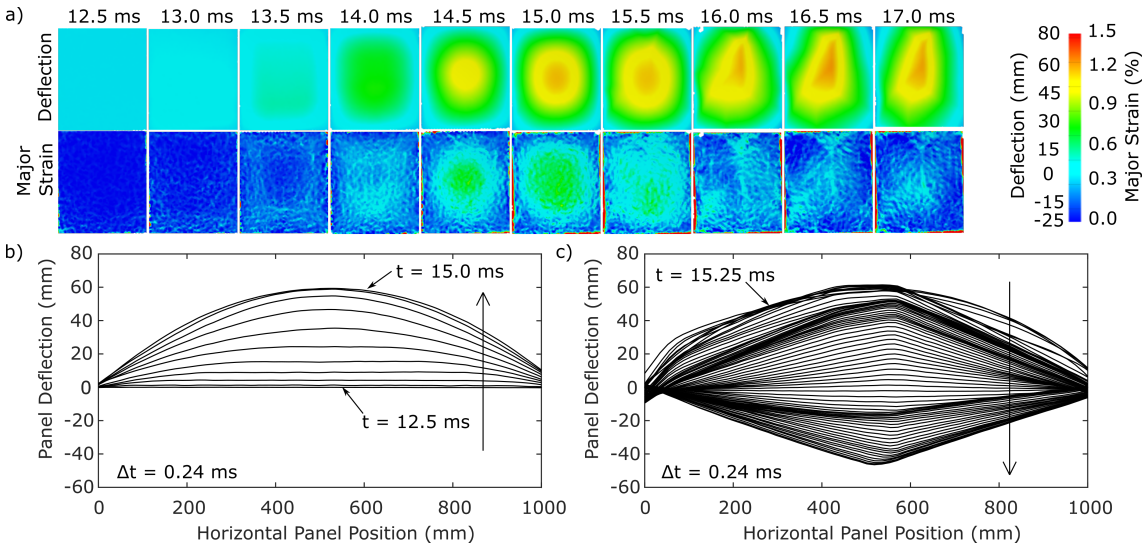


Figure 5.10: DIC results for CFRP(1) showing: (a) out-of-plane displacement and major strain images, (b) deflection at time intervals for the horizontal centre section and (c) rebound at time intervals for the horizontal centre section.

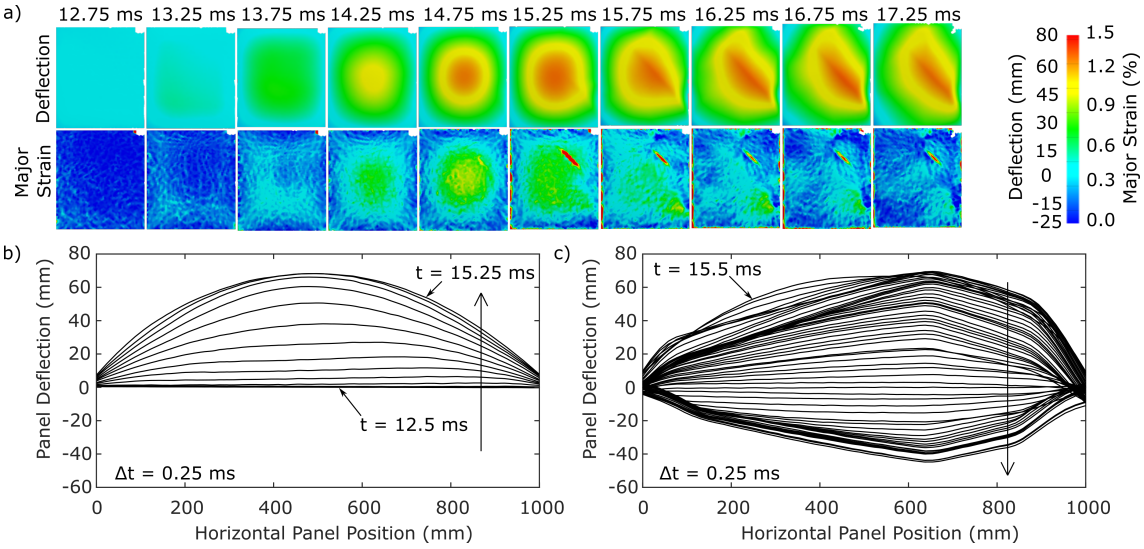


Figure 5.11: DIC results for Hybrid-3B(1) showing: (a) out-of-plane displacement and major strain images, (b) deflection at time intervals for the horizontal centre section and (c) rebound at time intervals for the horizontal centre section.

Figure 5.11 (a) shows the DIC contour image series for Hybrid-3B(1). The panel experiences an area of high strain towards the top right-hand side of the panel. The deflection and strain images indicate a region of damage running diagonally across the panel. Figure 5.11 (b) shows the displacement of the horizontal cross-section at the mid-plane for Hybrid-3B(1). The maximum displacement of the centre point is 68.0 mm and maximum major strain at the centre point is 0.96 %. The return phase of this cross-section is shown in Figure 5.11 (c). The panel returns asymmetrically and this correlates with the damage in the DIC image sequences in Figure 5.11 (a). However, when the return stroke of Hybrid-3B(1) is compared to that of GFRP(1) and CFRP(1), the gradient discontinuity in the damaged region is less steep. This is partly due to the damage running diagonally across the panel. Additionally, the damage in Hybrid-3B(1) appears to be spread across a wider area which could be beneficial.

RBMC has been applied to all DIC data detailed here, however, the movement of the panels at the boundaries is more significant compared to the results in Chapter 4. This is because the vertical edges of the panels were only clamped during these experiments due to the cubicle setup. This has led to slipping at these locations hence the movement at the boundaries can not be fully eliminated.

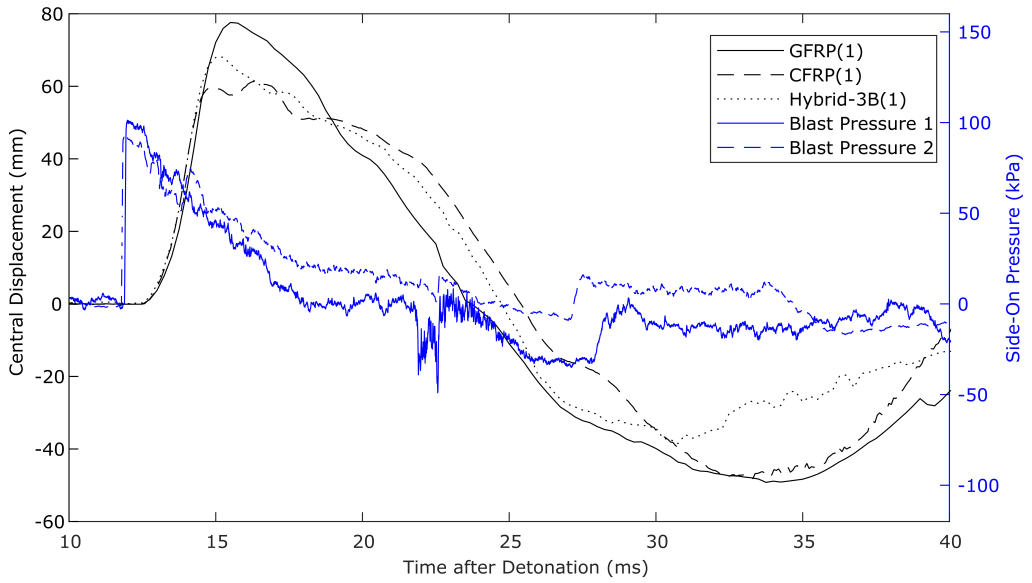


Figure 5.12: Central out-of-plane displacement against time for the three composite sandwich panels along with the recorded side-on blast pressure against time.

5.3.2.1.2 Central Point Displacement

A low pass filter was applied to the pressure data since the noise frequencies were significantly higher than the data response. The filter span was set to 10 data points resulting in average data values calculated across every section with this interval.

Figure 5.12 shows a plot of the side-on blast pressure from the two trials along with the displacement of the centre points of all three panels. GFRP(1) and CFRP(1) were tested side-by-side, Hybrid-3B(1) was tested following this. GFRP(1) and CFRP(1) experienced a peak side-on pressure of 100.8 kPa whilst Hybrid-3B(1) experienced a peak side-on pressure of 93.8 kPa. Although the tests were performed one after the other, this change in pressure could be caused by atmospheric or weather conditions. The pressure difference may have been caused by variability between the charges. The plastic explosive charges were prepared by site personnel using their explosive material, an existing mold and weighing scales. Due to safety restrictions, it was not possible to inspect the sphericity or weight of the charge prior to testing. Additionally, a change in the positioning of the charge or a change in the positioning of the side-on pressure gauge could have caused this pressure difference. The ratio between positive phase duration of the pressure and time to reach peak panel displacement indicates that all panels were tested within the dynamic regime. Based on the theoretical blast wave velocity and results analysis, the DIC data was

deemed reliable until 40 ms. After this time, vibrations from the ground and from the blast wave transmit through the camera stands moving the cameras out of their initial calibrated position. Although the stand-off was reduced compared to previous blast testing, the test cubicle did not have a steel base so was not as susceptible to vibrations. The DIC analysis was, therefore, reliable for the same length of time. The initial deflection against time slope in Figure 5.12 for all three panel types is similar as damage is not yet present. As expected, the deflection of the panels negatively correlates with their stiffness. The deflection of Hybrid-3B(1) lies between the deflections of GFRP(1) and CFRP(1). CFRP(1) demonstrates a double maximum peak, this could be caused by damage occuring as the panel reaches its maximum due to blast energy being distributed through the structure. Damage also causes the elongated return of CFRP(1). Due to its high stiffness and low mass, CFRP(1) should have the shortest time period of response followed by Hybrid-3B(1). Figure 5.12 shows that this is not the case. The panel stiffness, or flexural rigidity, is reduced due to damage resulting in a longer period of response. This indicates that CFRP(1) and Hybrid-3B(1) have suffered from greater damage or are more susceptible to the effects of damage compared to GFRP(1).

5.3.2.1.3 Work Done

The work done on the panel by the distributed blast pressure has been calculated for this test series. The same method as detailed in Chapter 4 was used. The static pressure recorded using the side-on gauge was used to calculate reflected overpressure using the Rankine-Hugonoit relationship shown in Equation 5.2. In this equation P_r is reflected overpressure, P_s is static pressure and P_o is ambient pressure. This relationship assumes the wave encounters an infinitely large rigid wall with a zero angle of incidence. The normalised pressure at the 400 target point locations from the Pro S Air model were multiplied by this calculated reflected pressure at the corresponding time steps between 11.75 ms and 16.25 ms. This gives a pressure distribution across the panel that estimates the loading that occurs during the experiment. The displacement of the 400 corresponding locations across the panel were extracted from DIC data for each time step. The work done at each location was calculated by multiplying the displacement at that location by the pressure experienced at that location and by the small area encompassing that point. Figure 5.13 shows a cumulative work done versus time plot for the all three panels tested.

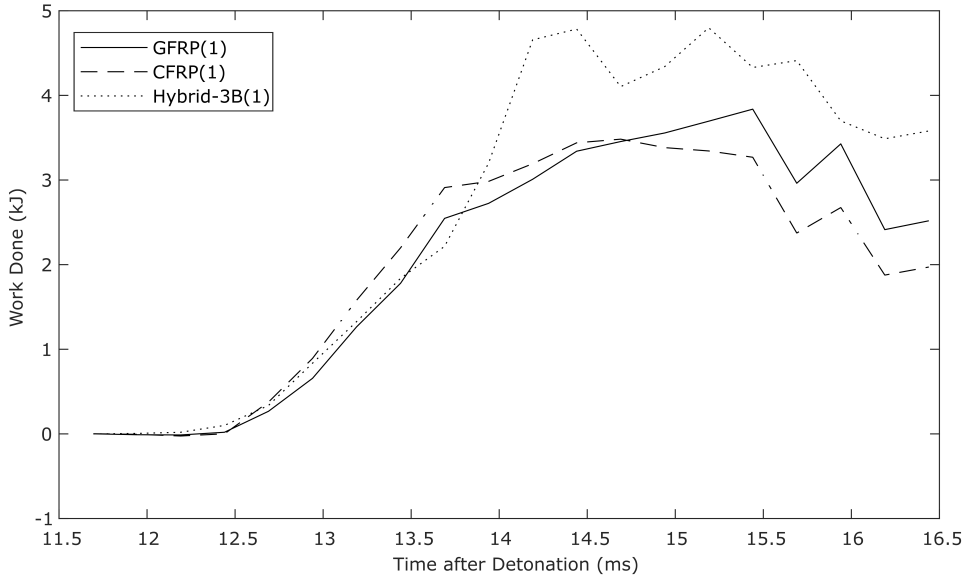


Figure 5.13: Cumulative work done against time for the three composite sandwich panels in test series A.

$$P_r = 2P_s \left[\frac{7P_o + 4P_s}{7P_o + P_s} \right] \tag{5.2}$$

Despite data filtering, the signal recorded using the side-on pressure gauge has significant noise. This results in sharp gradient changes in the cumulative work done shown in Figure 5.13. Further data filtering was not carried out as masking of the recorded pressure was not desired. Figure 5.13 shows that GFRP(1) and CFRP(1) experience similar cumulative work done. Since these two panels were subjected to the same blast loading, as they were tested side-by-side, this implies that the panels experienced a similar global displacement. Figure 5.12 shows that the central point of GFRP(1) experiences a greater deflection. Therefore, the work done on CFRP(1) must be caused by deflection of a more widespread area. Beyond 14.7 ms, the work done by GFRP(1) exceeds that of CFRP(1). This indicates that the deflection of GFRP(1) is sustained for a longer period of time. Figure 5.13 shows Hybrid-3B(1) undergoes greater work done. This is partially caused by the differing pressure signatures shown in Figure 5.12. Although the two trials demonstrate a similar peak pressure, the pressure decay differs. This results in a greater impulse being delivered to Hybrid-3B(1). The increased work done on Hybrid-3B(1) is also partially caused by the deflection of the panel. Although the deflection of the centre point of Hybrid-3B(1) lies between that of CFRP(1) and GFRP(1), Figure 5.11 (a)

clearly shows a band of diagonal damage. Deflection in this band is greater than deflection at the centre point after approximately 15.25 ms post detonation. The increased work done by Hybrid-3B(1) is caused by a combination of the deflection of this band and a greater blast impulse delivered to the panel. Panel deflection can absorb a significant amount of blast energy, provided that the deflection does not cause excessive damage. Post-blast panel assessment will reveal whether Hybrid-3B(1) is able to undergo a greater blast impulse and greater deflection without excessive damage. If this is the case, the layup utilised in Hybrid-3B(1) is beneficial.

5.3.2.2 Test Series B

5.3.2.2.1 Full-field Analysis

Figure 5.14 (a) shows a sequence of contour images of the out-of-plane displacement and major strain for Hybrid-3B(2) under the first 8 kg PE7 blast load. The panel experiences a relatively symmetric outward deflection and return. Figure 5.14 (b) shows the displacement of the horizontal cross-section at the mid-plane of Hybrid-3B(2). The panel reaches a maximum central displacement of 47.2 mm at 14 ms and maximum central major strain of 0.66 %. The symmetric response of the panel can be clearly seen in the cross-sectional displacement until the final few cross-sections of the return stroke. Deceleration is visible on the left hand side of the panel, indicating the presence of damage. Figure 5.15 shows the DIC data for the same panel, Hybrid-3B(2), under the second 8 kg PE7 blast load. The panel experiences a greater deflection with a maximum of 50.9 mm at 14.25 ms and maximum central major strain of 0.61 %. The accumulation of damage results in an asymmetric deflection and distorted return stroke.

Figure 5.16 illustrates the response of Hybrid-4(1) to the first 8 kg PE7 blast load. Hybrid-4(1) experiences a greater central deflection and major strain compared to Hybrid-3B(2) under the first blast load with values of 51.9 mm and 0.78 %, respectively. There is a greater extent of panel deceleration and a gradient discontinuity in the return stroke of Hybrid-4(1). The response of Hybrid-4(1) to the second blast load is shown in Figure 5.17. The deflection and strain images in Figure 5.17 (a) indicate the location of a severe crack. The maximum central out-of-plane displacement of Hybrid-4(1) under the second blast load was 58.0 mm and maximum central major strain was 0.77 %. Hybrid-4 has a lower equivalent bending stiffness than Hybrid-3B caused by a lower proportion of carbon-fibre layers in the layup. The repeated blast loading widens the difference in performance between the two panels due to damage accumulation.

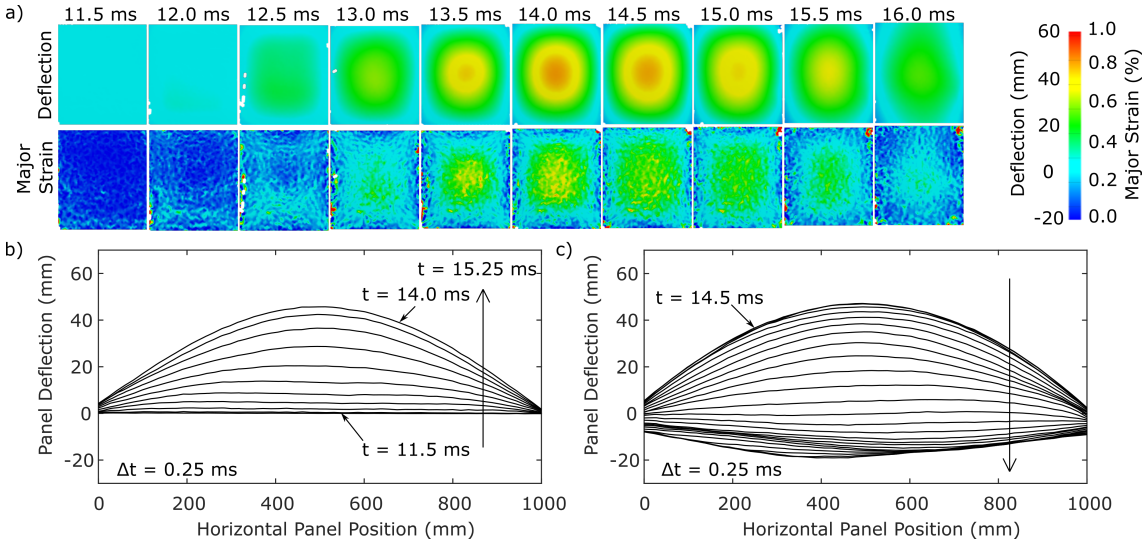


Figure 5.14: DIC results for Hybrid-3B(2) under the first 8 kg PE7 charge showing: (a) out-of-plane displacement and major strain images, (b) deflection at time intervals for the horizontal centre section and (c) rebound at time intervals for the horizontal centre section.

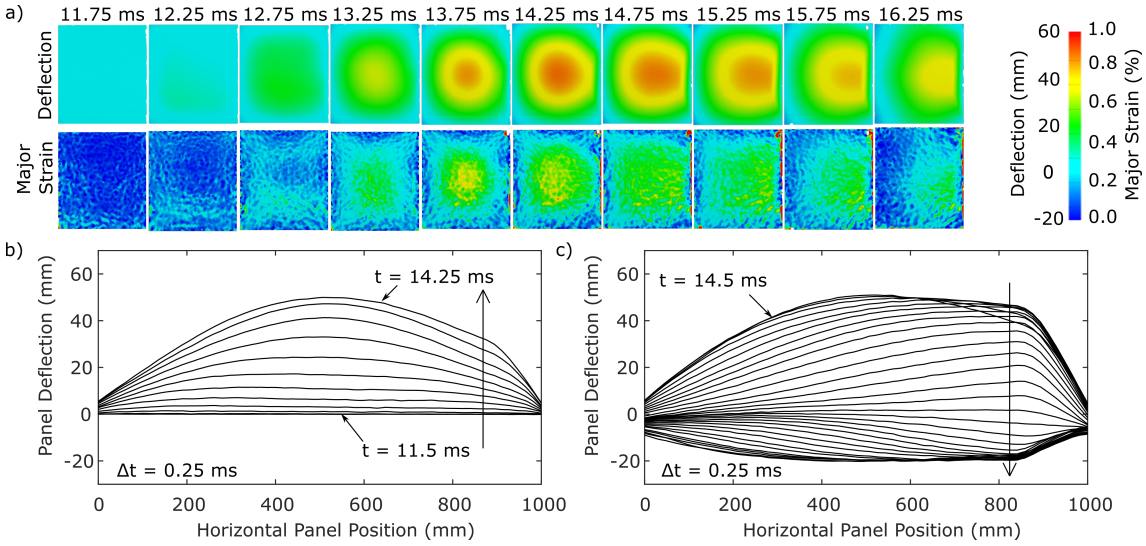


Figure 5.15: DIC results for Hybrid-3B(2) under the second 8 kg PE7 charge showing: (a) out-of-plane displacement and major strain images, (b) deflection at time intervals for the horizontal centre section and (c) rebound at time intervals for the horizontal centre section.

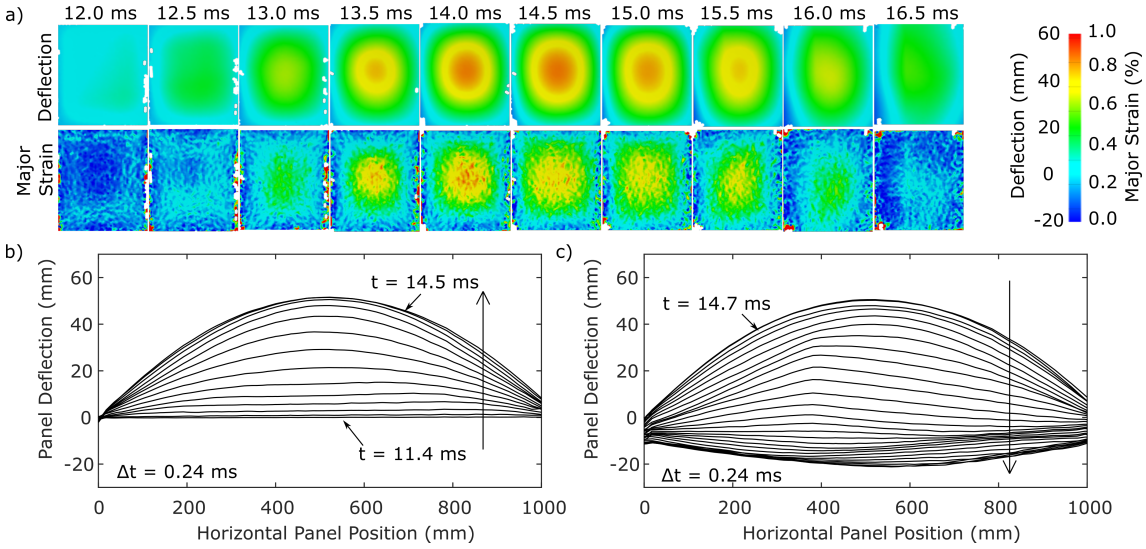


Figure 5.16: DIC results for Hybrid-4(1) under the first 8 kg PE7 charge showing: (a) out-of-plane displacement and major strain images, (b) deflection at time intervals for the horizontal centre section and (c) rebound at time intervals for the horizontal centre section.

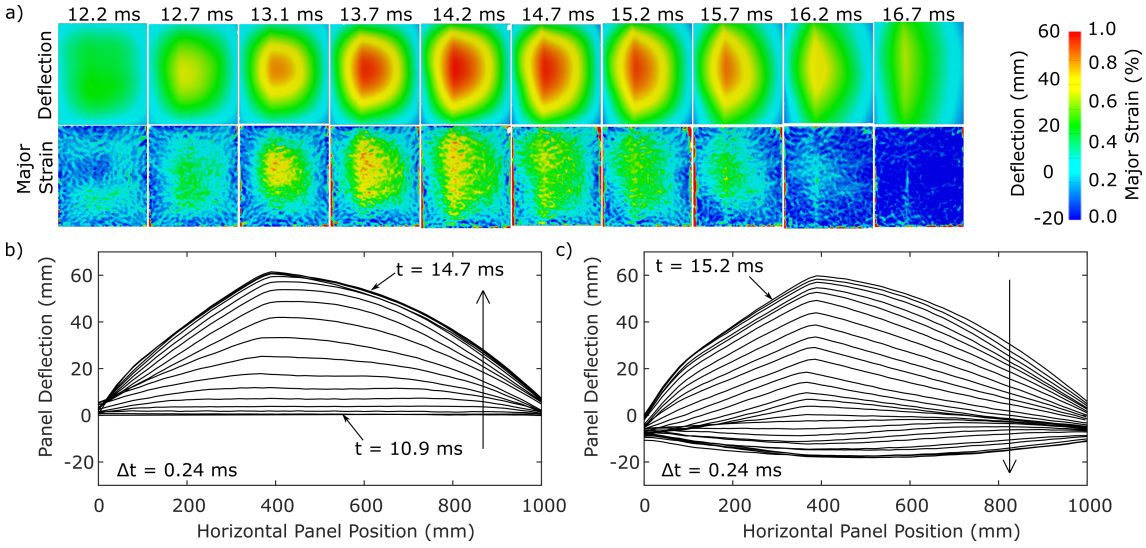


Figure 5.17: DIC results for Hybrid-4(1) under the second 8 kg PE7 charge showing: (a) out-of-plane displacement and major strain images, (b) deflection at time intervals for the horizontal centre section and (c) rebound at time intervals for the horizontal centre section.

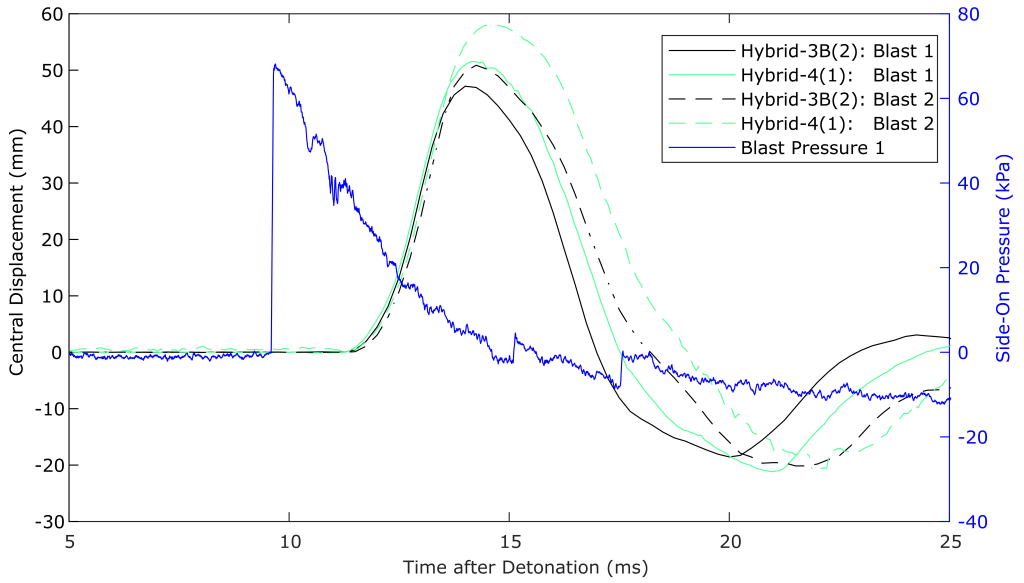


Figure 5.18: Central out-of-plane displacement against time for the two composite sandwich panels against both blast loadings along with the recorded side-on blast pressure against time for the first blast load.

5.3.2.2.2 Central Point Displacement

Figure 5.18 shows a plot of the side-on blast pressure recorded during the first blast trial along with the displacement of the centre points of the panels under both trials. Comparison of the positive phase duration of the pressure signal and time taken to reach peak panel displacement show that the panels are tested in the dynamic regime [5]. Hybrid-3B(2) and Hybrid-4(1) were tested side-by-side in the test cubicle and thus underwent the same explosive charges under the same conditions. The peak side-on pressure during the first blast trial was 67.7 kPa and peak pressure for the second blast trial was 68.9 kPa. The increase in displacement between the first and second trials for both panels can be clearly seen. Additionally, the response period for both panels increases between the first and second blast. This is likely to be due to greater damage present during the second trial resulting in an elongated return of both panels. As expected, the period of response for Hybrid-3B(2) is shorter than that of Hybrid-4(1) during both trials. Hybrid-4(1) experiences greater deflection than Hybrid-3B(2) during both the first and second blasts. Furthermore, Hybrid-4(1) experiences a greater relative increase in central deflection indicating that this panel has a lower blast resilience and has experienced a greater loss of integrity. The initial deflection against time slope for all panels under both blast trials is similar.

This indicates that minimal damage is present within the panels, even following the first blast load, as response is dominated by material properties. Additionally, there is no deceleration or gradient discontinuities during the return to zero for any panel. The DIC data was deemed reliable until 25 ms after which excessive vibrations affected the positions of the cameras.

Figure 5.19 shows a displacement and side-on blast pressure versus time plot recorded during the first blast loading of the 0.8 m × 0.8 m CFRP(2) panel against an 8 kg PE7 charge. The plot with RBMC shows the deflection of the composite sandwich panel relative to the steel frame. Whereas the plot without RBMC gives the total magnitude of deflection including the deflection of the front steel sheet and any deflection of the cubicle or fixings. The reduced size of the GFRP(2) and CFRP(2) panels required a greater surface area of front steel sheet. Since the steel sheet was more compliant than expected, the deflection of GFRP(2) and CFRP(2) relative to their boundaries was significantly reduced compared to Hybrid-3B(2) and Hybrid-4(1). The response of the GFRP(2) and CFRP(2) panels under their first and second 8 kg PE7 blasts with RBMC implemented, which were the third and fourth blast trials in test series B, are shown in Figure 5.20. There are no decelerations or gradient discontinuities during the return to zero for any panel. As expected the deflection of both panels increases during the second blast trial. The lower stiffness of GFRP(2) results in greater deflection compared to CFRP(2) for both blast loads. GFRP(2) experiences peak central deflection of 5.1 mm and 6.0 mm during the first and second blast, respectively. CFRP(2) experiences maximum central deflections of 4.4 mm and 5.1 mm. GFRP(2) experiences a greater relative increase in central deflection. Neither panel showed clear signs of damage, due to the minor levels of deflection experienced. Comparison of the positive phase duration of the pressure signal and time taken to reach peak panel displacement show that the panels are tested in the dynamic regime, however, this trial is approaching the impulsive regime [5]. The DIC data was deemed reliable until 25 ms after which point excessive vibrations affected the positions of the cameras.

The full-field DIC data images for GFRP(2) and CFRP(2) under the third and fourth blasts can be found in Appendix A. Due to the influence of boundary conditions and deflection of the front steel sheet, neither the deflection nor the damage in GFRP(2) and CFRP(2) can be compared to Hybrid-3B(2) and Hybrid-4(1).

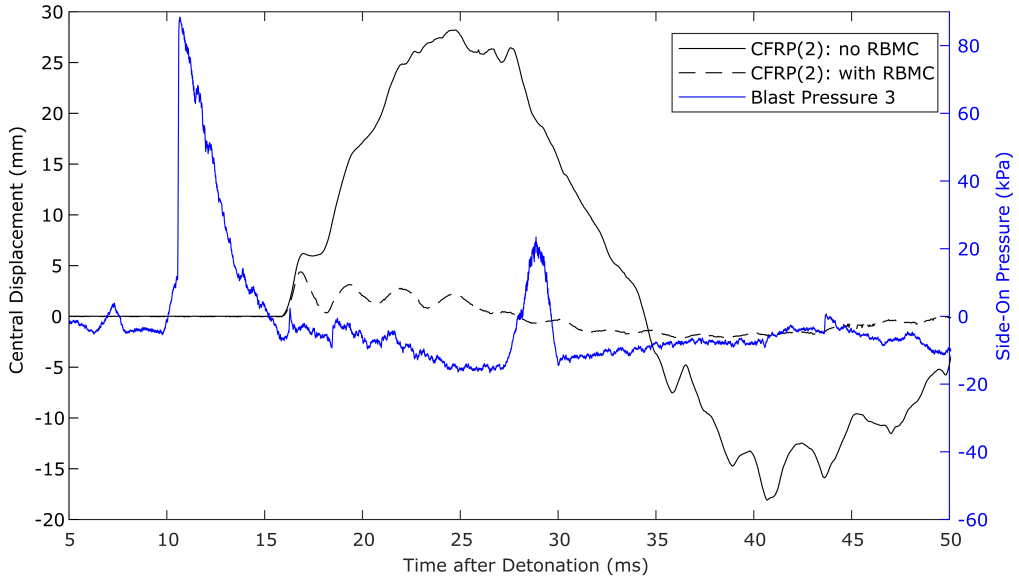


Figure 5.19: Central out-of-plane displacement against time for CFRP(2) with and without RBMC along with the recorded side-on blast pressure against time.

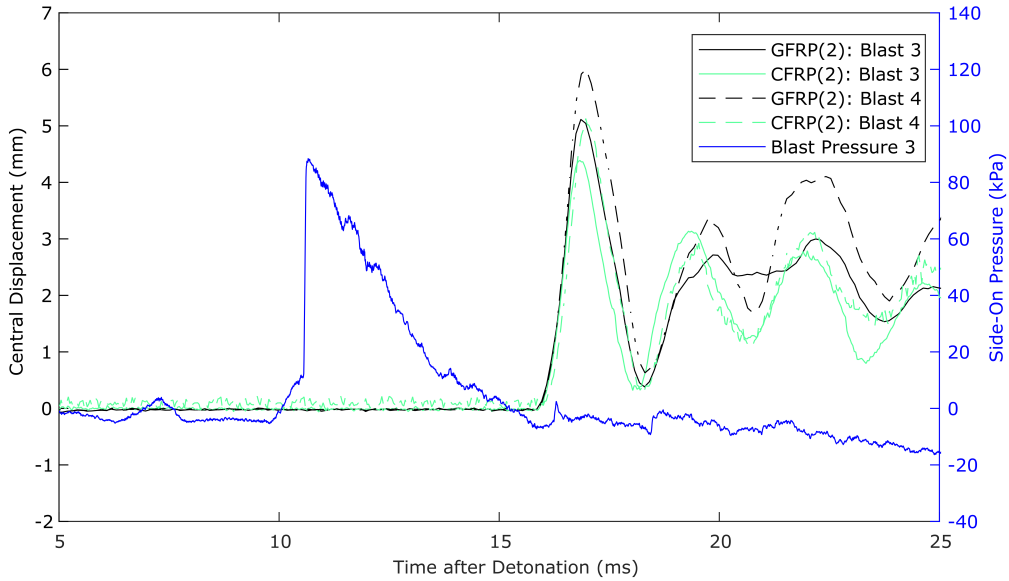


Figure 5.20: Central out-of-plane displacement against time for the two composite sandwich panels against both blast loadings along with the recorded side-on blast pressure against time for the first blast load.

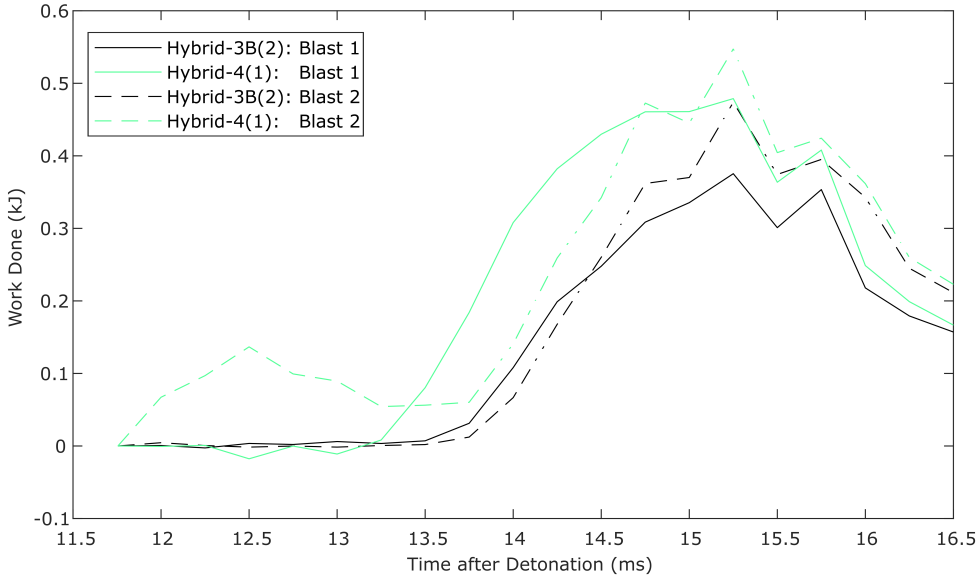


Figure 5.21: Cumulative work done against time for the composite sandwich panels in test series B.

5.3.2.2.3 Work Done

The work done on the Hybrid-3B(2) and Hybrid-4(1) by the distributed blast pressures during the first and second trials of test series B have been calculated. The same method as previously detailed was used. The reflected overpressure was calculated from the recorded static pressure using the Rankine-Hugonoit relationship. Figure 5.21 shows a plot of cumulative work done versus time for all four cases. Figure 5.21 shows that Hybrid-3B(2) undergoes less work done during both trials compared to Hybrid-4(1). Since these panels were tested side-by-side and subjected to the same blast loads, this implies that Hybrid-4(1) underwent greater deflection. Figure 5.18 shows that the central point of Hybrid-4(1) undergoes greater displacement. Furthermore, Figures 5.16 (a) and 5.17 (a) illustrate that the deflection of Hybrid-4(1) is more widespread than the deflection of Hybrid-3B(2). The gradient changes in Figure 5.17 (c) indicate damage to Hybrid-4(1) which is the cause of greater deflection over a more widespread area.

5.3.3 Strain Gauges

Due to an unidentifiable issue, the oscilloscope failed to trigger and record strain gauge data during all of the experimental trials. The high frequency amplifier re-

quired an alternating current (AC) power supply, this was supplied by a diesel generator which created a noisy signal. The generator with the lowest noise was selected to power the amplifier. Power cables running into the cubicle to the high-speed cameras, lights and amplifier were separated from the data cables running out of the cubicle to prevent further interference and noise. The low frequency amplifier could be supplied by a direct current (DC) power supply. This power supply was also placed within the test cubicle. All data and power connections were taped in place to prevent movement due to the blast wave. During one trial, a laptop and oscilloscope were also placed within the cubicle to eliminate the 200 m of coaxial data cable. Despite these steps, no data was recorded. Due to the nature of the experiments and time constraints, the trials continued without gathering strain gauge data.

5.3.4 Pressure Gauges

5.3.4.1 Test Series A

A comparison of the pressure signatures recorded using the side-on pressure gauge during the two 30 kg PE7 trials is shown in Figure 5.22. The two trials demonstrate a similar peak side-on pressure, however, the decay of the curve differs. This results in an increased impulse during the second trial, in which Hybrid-3B(1) was tested, as the overpressure does not fall below zero. As discussed previously, there are many factors which could cause this difference. The difference in impulse between the two trials needs to be considered whilst the performance of the panels relative to one another is analysed.

The reflected overpressure recorded using the film PVDF pressure gauges at the centre of each panel are shown in Figure 5.23. The static pressure recorded using the side-on gauge was used to calculate reflected overpressure using the Rankine-Hugonoit relationship shown in Equation 5.2. This reflected overpressure has been calculated to help verify the results from the PVDF gauges since this instrumentation method has not been used during large scale blast experiments before. The peak calculated reflected overpressure for the first blast trial investigating GFRP(1) versus CFRP(1) was 278.5 kPa and for the second trial investigating Hybrid-3B(1) was 253.3 kPa. The peak reflected pressures recorded by the PVDF gauges at the centre of panels GFRP(1), CFRP(1) and Hybrid-3B(1) were 357.8 kPa, 320.6 kPa and 334.5 kPa, respectively. Although the Rankine-Hugonoit relationship assumes an infinitely large rigid wall, hence no blast clearing, the reflected overpressures

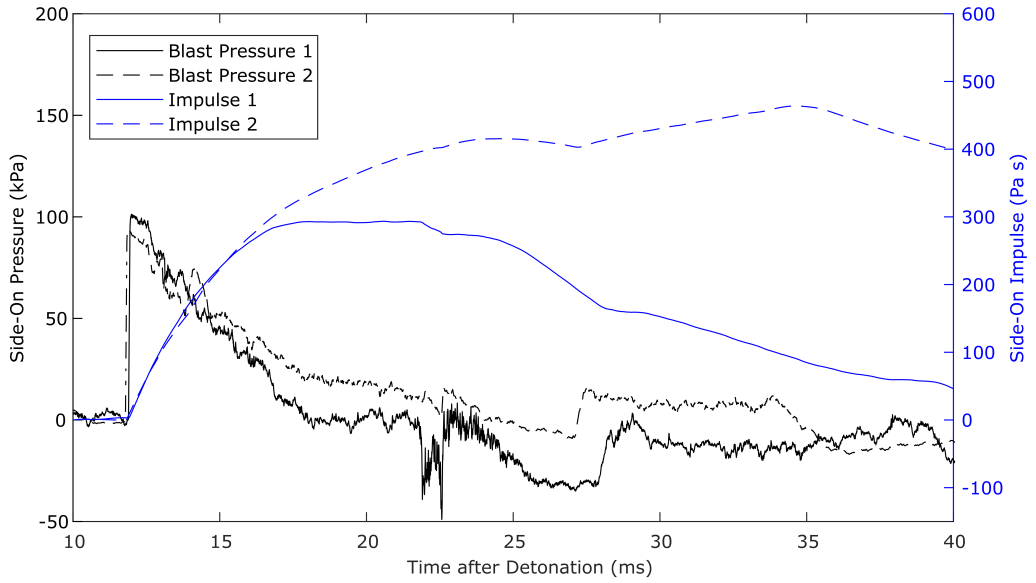


Figure 5.22: Recorded static side-on pressure and calculated impulse for each of the two trials using 30 kg PE7 charges at 10.5 m..

calculated with this method are lower than the PVDF recorded pressures. This could be due to side-on pressure data recorded. Misalignment of the side-on pressure gauge and blast clearing or flow disruption around the gauge would result in pressure lower than the true value being recorded.

There is approximately a 0.50 ms difference between the pressure signature peak recorded by the side-on gauge in the first trial and the GFRP(1) and CFRP(1) PVDF gauges. By calculating the blast wavefront velocity using Equation 5.3, the difference in distance which causes this delay in arrival time can be calculated. In this equation u_s is the blast wavefront velocity and a_o is the speed of sound at ambient conditions, which is taken as 343 m s^{-1}. This time difference could be caused by a distance misalignment of 234 mm. Despite efforts to ensure accurate positioning of the charge and side-on pressure gauge, it is highly likely that the stand-off distance between the side-on pressure gauge and the charge or the stand-off distance between the charge and cubicle varied by 234 mm. Although the cubicle was fixed in place with steel ground stakes and concrete blocks, preceding blast trials could have moved it from its original position. This time difference can, therefore, be accounted for due to the nature of the field experiments.

$$u_s = \sqrt{\frac{6P_s + 7P_o}{7P_o}} \cdot a_o \tag{5.3}$$

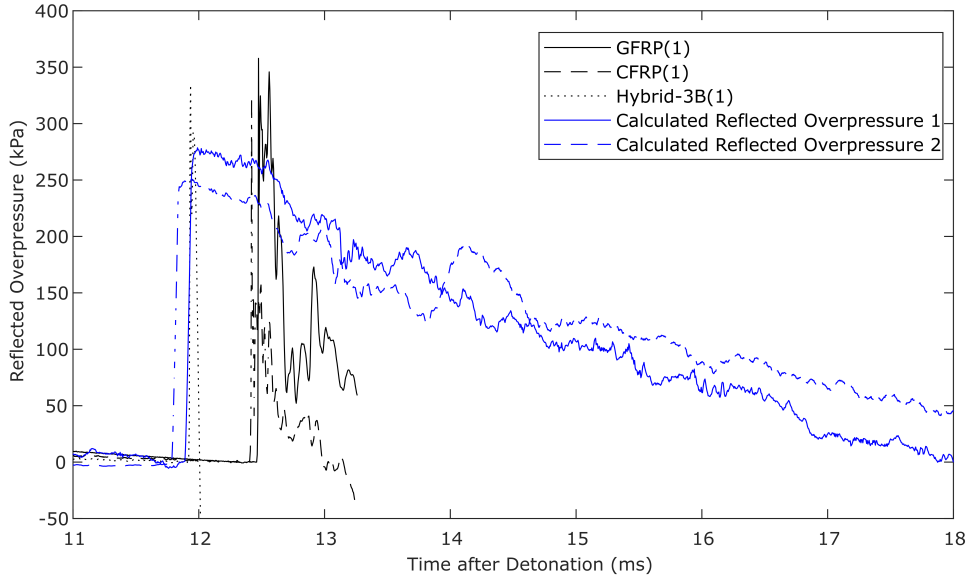


Figure 5.23: Recorded reflected overpressure at the centre of each panel from PVDF gauges along with reflected overpressure calculated from static pressure recorded by side-on gauge.

5.3.4.2 Test Series B

The side-on static pressure recorded during each of the four test series B blast trials are shown in Figure 5.24. The impulse versus time has been calculated for each trial and is included. Although an 8 kg charge at 8 m was specified for each blast load, variability in the peak pressure and arrival time is observed. This could be caused by slight variations in the charge material and shape, changes in environmental conditions, misalignment of the side-on pressure gauge and variations in stand-off distance between the charge and pressure gauge and indeed the charge and test cubicle. The first blast pressure wave, shown in Figure 5.24 (a), reached a peak pressure at 9.9 ms whilst the second blast pressure, shown in Figure 5.24 (b), reached a peak at 12.0 ms. In addition, the peak pressure of the third blast pressure wave, shown in Figure 5.24 (c), was recorded as 88.2 kPa whilst the first blast pressure wave had a peak of only 68.1 kPa. Despite these differences, the panels all experienced a largely similar impulse loading considering the nature and complexity of the experiments. Details of the pressures and impulse experienced by each panel during test series B are shown in Table 5.6.

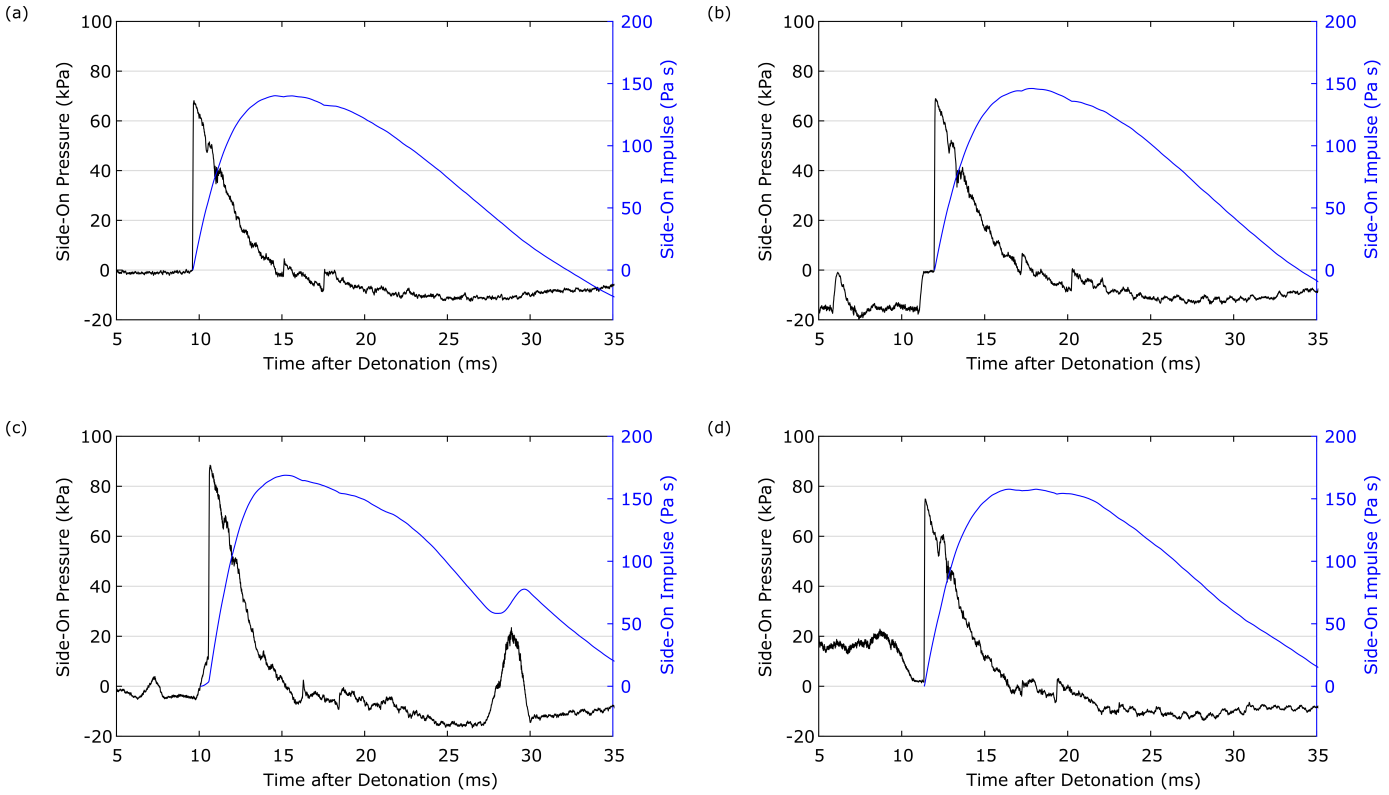


Figure 5.24: Recorded static side-on pressure and calculated impulse for each of the four trials using 8 kg PE7 charges at 8 m.

Table 5.6: Summary of pressure results for test series B.

Trial number	Panel type	Peak side-on pressure (kPa)	Positive phase duration (ms)	Calculated reflected pressure (kPa)	Calculated peak reflected impulse (Pa s)	PVDF peak reflected pressure (kPa)	Pro S Air predicted reflected pressure (kPa)	Pro S Air predicted reflected impulse (Pa s)	Pro S Air predicted positive phase duration (ms)
B1	Hybrid-3B(2) Hybrid-4(1)	68.1	5.01	172.1	327.6	305.8 310.4			
B2	Hybrid-3B(2) Hybrid-4(1)	68.9	5.11	174.5	294.7	- -	217.2	384.3	4.50
B3	GFRP(2) CFRP(2)	88.2	5.17	235.6	407.7	308.9 291.8			
B4	GFRP(2) CFRP(2)	74.9	5.09	192.8	398.2	- -			

The reflected overpressure recorded using the PVDF pressure gauges for the first trial in test series B is shown in Figure 5.25. This trial compared Hybrid-3B(2) and Hybrid-4(1) under their first 8 kg PE7 charge at 8 m. The gauge at the centre of Hybrid-3B(2) records a peak pressure of 305.8 kPa and Hybrid-4(1) records a peak pressure of 310.4 kPa. The reflected overpressure calculated from the recorded side-on pressure using the Rankine-Hugonoit relationship is only 172.1 kPa for this blast load. However, Figure 5.24 shows that the side-on pressure recorded for the first blast is low compared to the recorded pressure for subsequent trials. This may be due to poor alignment and placement of the side-on pressure gauge along with flow disruption around the side-on pressure gauge itself. Unfortunately, the amplifier gain for the second blast trial was set incorrectly such that the voltage generated by the pressure gauges exceeded the cut off voltage for data acquisition. This was rectified for future trials. This indicates that the peak pressure during the second trial exceeded 243.7 kPa according to the PVDF gauges on both Hybrid-3B(2) and Hybrid-4(1), however, the exact values of the peak pressures were not recorded.

Figure 5.26 shows the reflected overpressure recorded during the third trial in test series B. This trial compared GFRP(2) and CFRP(2) under their first 8 kg PE7 charge at 8 m. The peak pressure recorded at the centre of GFRP(2) was 308.9 kPa and at the centre of CFRP(2) was 291.8 kPa. The reflected overpressure calculated from the side-on pressure gauge peaked at 235.6 kPa. This calculated reflected pressure is more comparable to the overpressures recorded using the PVDF gauges. There is a 0.46 ms time difference between the blast wave arrival recorded using the side-on pressure gauge and the PVDF pressure gauges. Using blast wavefront velocity shown in Equation 5.3, this time difference equals a difference in distance of 215 mm. As detailed previously, 215 mm variability in positioning of the charge, side-on pressure gauge and cubicle was highly possible due to the nature of the experiments. The pressure signals for the fourth trial, investigating the second 8 kg PE7 blast on GFRP(2) and CFRP(2) did not record.

The peak pressures recorded using the PVDF gauges during the first trial for Hybrid-3B(2) and Hybrid-4(1) are comparable to the pressures recorded during the third trial, as shown in Table 5.6. This gives confidence that the PVDF gauges are reliably recording the reflected overpressure experienced by each panel and that each panel has undergone a very similar load as intended. The PVDF gauges, however, only record the peak pressure and do not capture the pressure decay during these experiments. This could be due to the cables becoming disconnected from the gauges following blast or becoming untaped from the panel front as the cables are

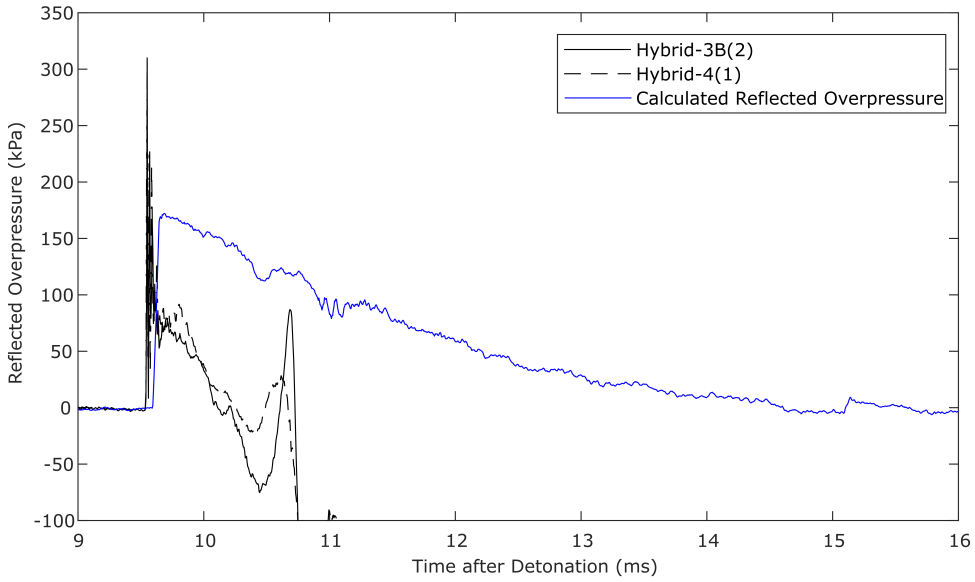


Figure 5.25: Recorded reflected overpressure at the centre of each panel from PVDF gauges along with reflected overpressure calculated from static pressure recorded by side-on gauge.

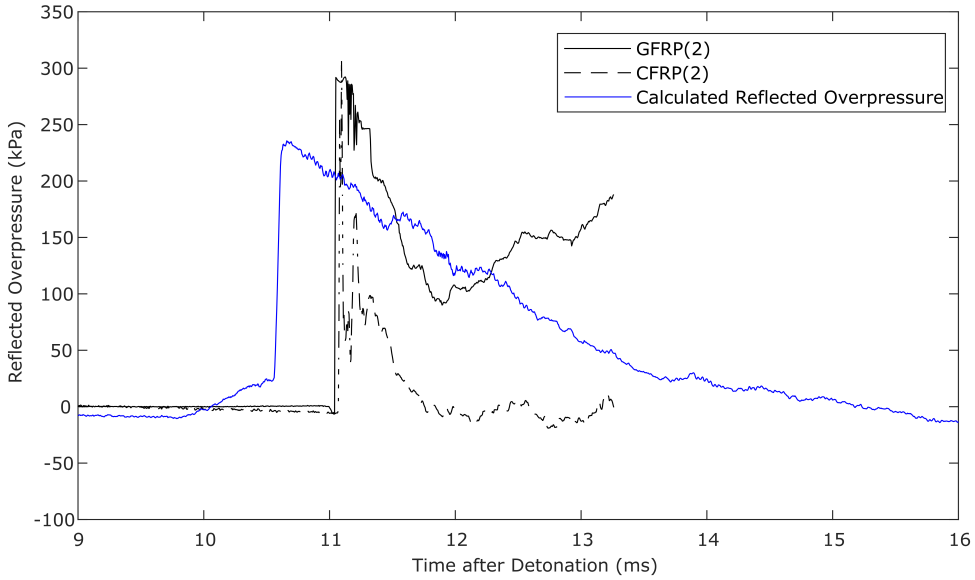


Figure 5.26: Recorded reflected overpressure at the centre of each panel from PVDF gauges along with reflected overpressure calculated from static pressure recorded by side-on gauge.

Table 5.7: Summary of DIC analysis results for test series A.

Trial number	Panel type	Peak centre point deflection (mm)	Peak centre point strain (%)	Peak cumulative work done (kJ)
A1	GFRP(1)	77.6	1.46	3.84
	CFRP(1)	61.4	0.79	3.48
A2	Hybrid-3B(1)	68.0	0.96	4.80
B1	Hybrid-3B(2)	47.2	0.66	0.38
	Hybrid-4(1)	51.9	0.78	0.47
B2	Hybrid-3B(2)	50.9	0.61	0.48
	Hybrid-4(1)	58.0	0.77	0.55
B3	GFRP(2)	5.1	0.24	-
	CFRP(2)	4.4	0.12	-
B4	GFRP(2)	6.0	0.29	-
	CFRP(2)	5.1	0.18	-

whipped around by the blast wave. Although the cables were fixed to the panel fronts before each trial, they were found to have moved and become disconnected on some occasions. Movement of the cables will result in charge generation and could account for noisy and anomalous results following the peak pressure recordings.

The DIC results for test series A and B are summarised in Table 5.7. Tables 5.8 and 5.6 summarise the recorded and predicted pressures from this experimental setup in test series A and B, respectively.

Table 5.8: Summary of pressure results for test series A.

Trial number	Panel type	Peak side-on pressure (kPa)	Positive phase duration (ms)	Calculated reflected pressure (kPa)	Calculated peak reflected impulse (Pa s)	PVDF peak reflected pressure (kPa)	Pro S Air predicted reflected pressure (kPa)	Pro S Air predicted reflected impulse (Pa s)	Pro S Air predicted positive phase duration (ms)
A1	GFRP(1) CFRP(1)	100.8	6.12	278.5	732.5	357.8 320.6	348.1	684.2	5.80
A2	Hybrid-3B(1)	93.8	12.23	253.3	999.1	334.5			

5.4 Post Blast Damage & Compression

5.4.1 Methods

5.4.1.1 Damage Analysis

Following blast testing the panels were cut into eight sections. All edges were photographed and visually inspected for core cracks, front skin/core debonding and rear skin/core debonding. As detailed previously, the core cracks, debonding and delaminations were recorded and calibrated against a steel rule using a MATLAB script. Visual assessment was carried out as inspections performed by naval crews are likely to be limited to visual methods. Furthermore, previous damage assessment performed by Kelly [20] revealed that the damage that dominates post blast performance can be identified with visual inspection. Kelly also identified minimal damage at the centre of the sandwich panels [20]. A large proportion of panel damage occured towards the panel edges. Further sectioning of the panel centre was, therefore, deemed unnecessary. The visual damage assessment led to ten 300 mm $\times$ 200 mm sections being removed from each panel for edgewise compression testing. These compression specimen were taken from various locations across the panel and had sustained varying amounts of damage during the blast test. The visual inspection also led to 20 mm $\times$ 20 mm cuboids of interest being cut from Hybrid-3B(1) and GFRP(1) for analysis using X-ray CT scanning.

5.4.1.2 Edgewise Compression Testing

Sections of the composite sandwich panels containing varying amounts of damage were subjected to edgewise compression loading. Post blast testing was limited to compressive loading as the compressive strength of composite laminates is usually considerably lower than their tensile strength. Therefore, compressive strength is usually the critical design criteria. The specimen were 300 mm $\times$ 200 mm in size and ten specimen were taken from each panel. The composite sandwich panels are expected to support structural loads during service. Quasi-static compression loading of these panels aimed to simulate the structural loads caused by the weight of the vessel. Furthermore, the experiments aimed to understand the compressive performance of the sandwich structures. The results would reveal how the skins and core interact rather than generate an exact compressive performance of the skin materials. Previous edgewise compression testing performed by Kelly [20] on post blast composite sandwich panels showed that the panel stiffness and strength did not

demonstrate dependence on test rate. Furthermore, higher test rates led to reduced strength and stiffness as the panels were not aligned correctly. Therefore, a quasi-static test rate of 2 mm min^{-1} was selected for all specimen. Testing was performed using an Instron 5985 universal testing machine. A Nikon D7100 DSLR camera was used to capture one photograph every second to measure the strain using 2D DIC. A speckle pattern was painted along one edge of each specimen to facilitate DIC. To ensure even loading, 10 mm thick rubber spacers were placed between the machine plattens and the steel plates. Care was taken during specimen cutting, however, this would reduce inconsistency along the specimen edge. 2D DIC was adopted due to potential slipping at the plattens resulting in inaccurate machine displacement readings. An effective edgewise stiffness was calculated from the in-plane engineering stress and average strain as detailed in Equation 5.4. The in-plane engineering stress was calculated using Equation 5.5, where F is the applied force, and w and z are the specimen width and skin thickness, respectively. Negligible stress would be present in the foam core compared to in the skins, hence these dimensions were adopted for the engineering stress calculations. A photograph of the test setup is shown in Figure 5.27.

$$E_{eff} = \frac{\partial \sigma_y}{\partial t} \cdot \frac{\partial t}{\partial \varepsilon_y} \tag{5.4}$$

$$\sigma_y = \frac{F}{2wz} \tag{5.5}$$

5.4.1.3 X-ray CT Analysis

A 20 mm × 20 mm × 35 mm specimen was taken from a highly damaged region of the Hybrid-3B(1) and GFRP(1) panels. The specimen were evaluated using x-ray CT scanning to compare the damage being exhibited by each skin layup. Hybrid-3B(1) and GFRP(1) specimen were selected as both panels had been subjected to the same size charge, 30 kg PE7. Furthermore, previous visual inspection revealed that minimal damage was suffered by a glass-fibre skin under impact. Therefore, GFRP(1) was selected as a benchmark against which a hybrid layup could be compared. 20 mm × 20 mm × 35 mm cuboids were selected in order to capture the required level of detail and optimise scanning efficiency. A voxel resolution of 17 μm was achieved. The accelerating potential used was 60 kV and the tube current was 60 μA.

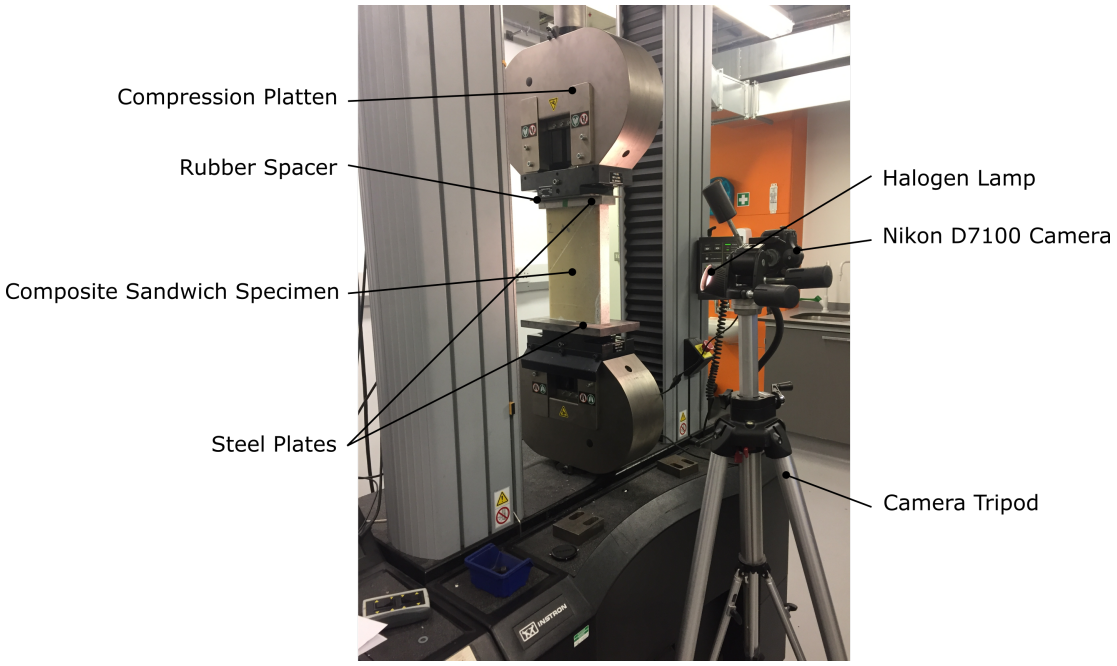


Figure 5.27: Photograph showing the setup for quasi-static compression test using Instron machine and DSLR camera.

5.4.2 Results

5.4.2.1 Test Series A

5.4.2.1.1 Damage Analysis

Figure 5.28 shows the front views of GFRP(1), CFRP(1) and Hybrid-3B(1) following sectioning. The red dashed boxes highlight the 300 mm × 200 mm regions that were removed from the panel for edgewise compression. All panels suffer from severe front skin fibre breakage. The front skin damage for all three panels correlates with the suspected damage observed in the DIC analysis shown in Figures 5.9, 5.10 and 5.11. The DIC data for both GFRP(1) and CFRP(1) show sharp gradient discontinuities and deflection peaks at the panel centre which corresponds to the severe cracks running down the centre of the panels. GFRP(1) also suffers from a diagonal crack towards the top of the panel. This is visible in the DIC contour plot in Figure 5.9 (a) from 16.25 ms onwards. The DIC data for Hybrid-3B(1), shown in Figure 5.11, highlights a crack running diagonally across the panel. This corresponds with the crack running from the bottom left-hand side of the panel to the middle right-hand side observed in Figure 5.28. The total length of the front skin cracks are detailed in Table 5.9.

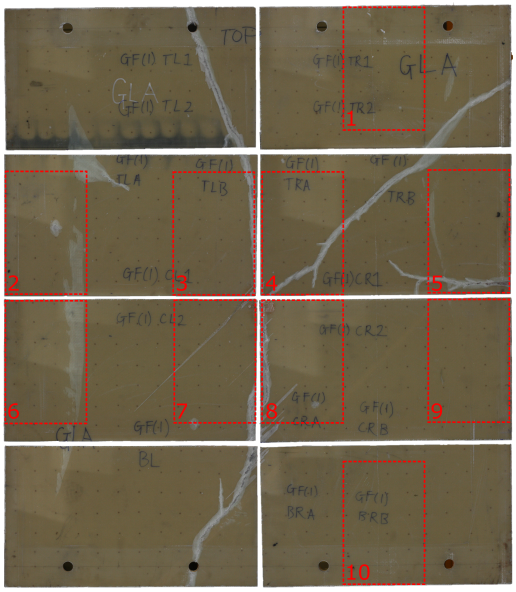
Table 5.9: Visual inspection of damage sustained by the panels subjected to 30 kg PE7 charge.

Panel type	No. of core cracks	Length of core cracks (mm)	No. of core/front skin debonds	Length of front debonds (mm)	No. of core/rear skin debonds	Length of rear debonds (mm)	Length of front skin cracks (mm)
GFRP(1)	11	426	6	243	4	129	2468
CFRP(1)	14	448	4	72	1	44	2180
Hybrid-3B(1)	11	420	2	137	2	51	2958

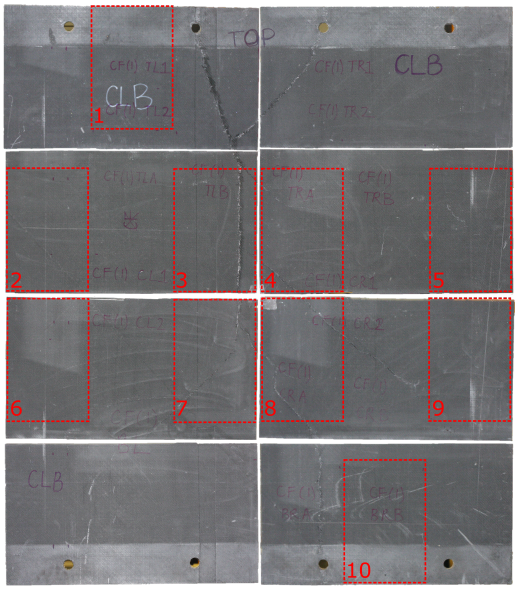
Core shear cracks are visible approximately 150 mm in from the panel edges on all panels. As detailed in Chapter 4, the shear cracks occur at 45° to the through thickness direction. The cracks are angled such that they point towards the panel centre at the front skin. Front skin/core debonding initiates at the point where the crack reaches the top skin and travels towards the panel centre. Rear skin/core debonding propagates from the point where the crack reaches the rear skin and extends towards the panel edge. An example of the crack angle and debond regions are shown in Figure 5.29. Figure 5.29 (a) shows cross-sections of Hybrid-3B(1) as viewed from the bottom of the panel. Figure 5.29 (b) highlights a cross-section where a shear core crack and debonding is visible. A large number of core shear cracks occur at this location as this is the transition region between the constrained edge and the deflecting central region. A schematic diagram showing the location and extent of internal damage to each of the three panels is shown in Figure 5.30. The damage observations from this study and Chapter 4 reveal that core shear cracking is the first damage type to occur followed by front skin/core debonding and then rear skin/core debonding. Table 5.9 details the quantified visual damage assessment based on the photographs.

Despite undergoing differing central point deflections, all three panels experience a similar extent of core shear cracking and front skin damage. GFRP(1) suffers from greater front skin and core debonding. This could be due to the reduced stiffness of the glass-fibre skins allowing greater deflection compared to the core. The extent of damage to Hybrid-3B(1) lies between that of GFRP(1) and CFRP(1). Considering Hybrid-3B(1) underwent more widespread deflection and was subjected to a greater impulse, the ability for Hybrid-3B(1) to only sustain comparable levels of damage demonstrates that this hybrid layup is advantageous.

(a) GFRP



(b) CFRP



(c) HYBRID-3B(1)

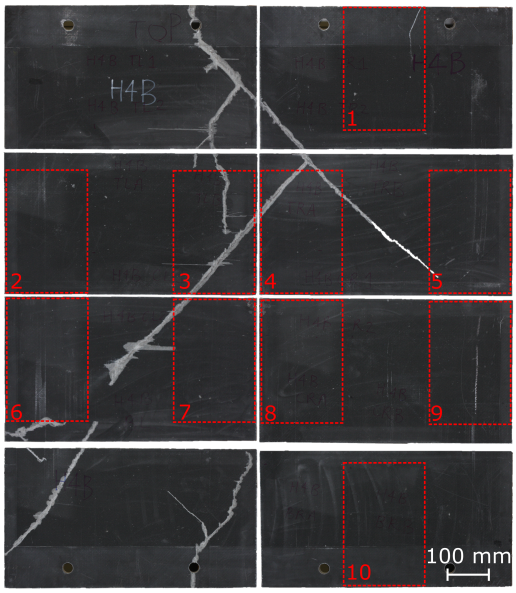


Figure 5.28: Photographs showing the front skin following blast of (a) GFRP(1), (b) CFRP(1) and (c) Hybrid-3B(1).

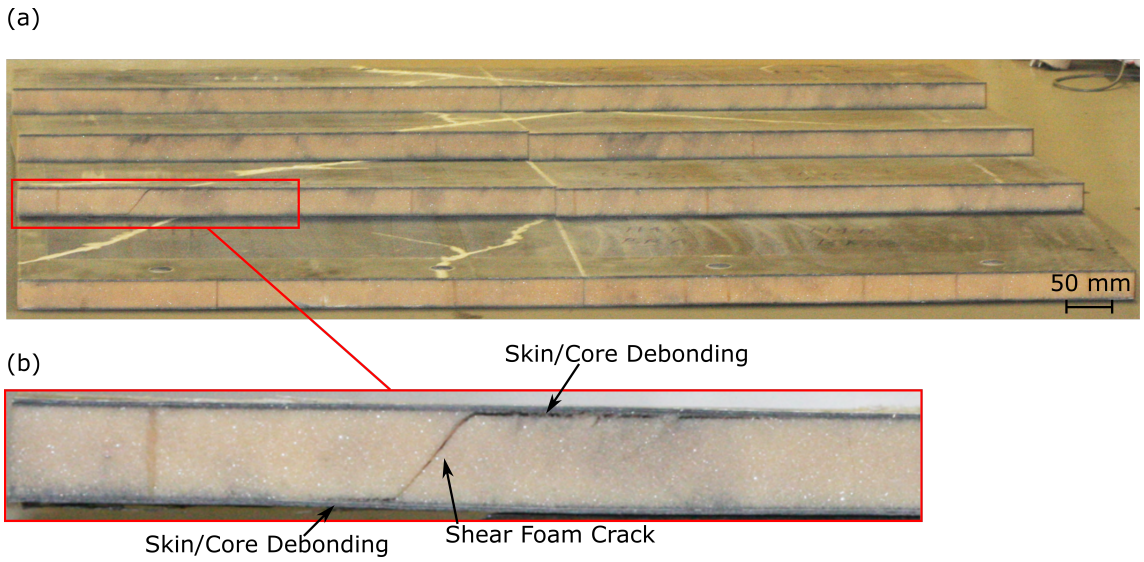


Figure 5.29: Photographs showing the damage to the core of Hybrid-3B(1) as viewed from the bottom.

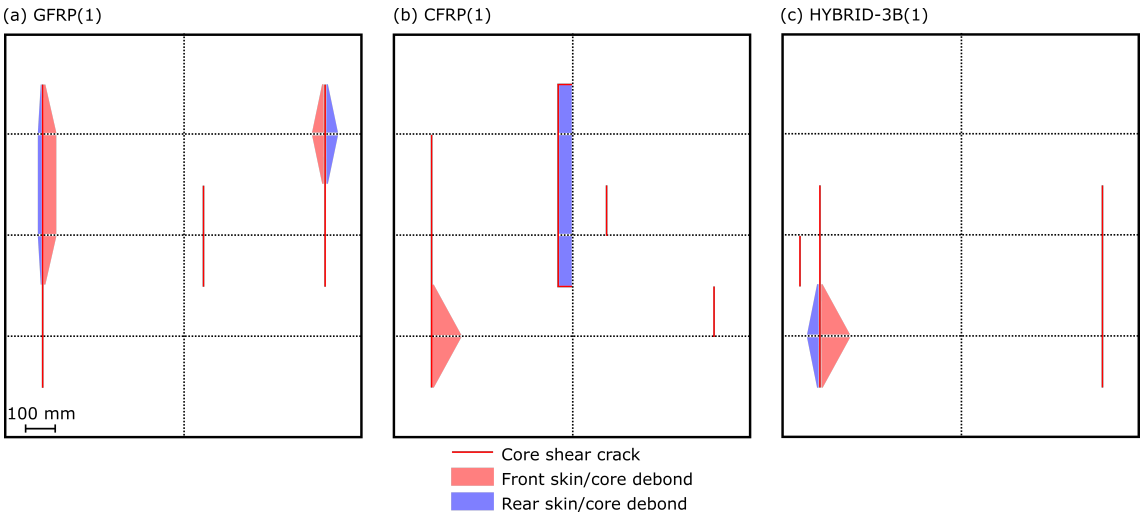


Figure 5.30: Schematic diagram showing the location and extent of internal panel damage for (a) GFRP(1), (b) CFRP(1) and (c) Hybrid-3B(1).

5.4.2.1.2 Post-Blast Compression

Figure 5.31 shows the effective modulus for the specimen taken from the highlighted locations on GFRP(1), CFRP(1) and Hybrid-3B(1). The graph shows that three GFRP(1) specimen have a higher modulus compared to all other specimen. This is due to the high compressive modulus of glass-fibre. CFRP(1) and Hybrid-3B(1) demonstrate a lower variation in modulus results. The mean and median effective modulus values for Hybrid-3B(1) are greater than those for CFRP(1). Figure 5.32 shows the maximum compressive stress for the three panel types. The compressive stress values are comparable for all three panel types. As mentioned previously, compressive strength is often the critical design criterion in naval composites. These results, therefore, indicate that Hybrid-3B(1) achieves comparable values for this critical property despite being subjected to a greater impulse.

Prior to compression testing, the edges and front of each 300 mm $\times$ 200 mm specimen were photographed. Each specimen was visually inspected for damage using the same method and MATLAB script as for the larger panel sections. A damage percentage was calculated for each specimen. This damage percentage takes into account front skin breakage, skin debonding and core shear cracks. All damage types are given an equal weighting in the damage percentage calculation. Figure 5.33 shows a plot of damage percentage against post-blast effective modulus. Undamaged GFRP(1) specimen have a higher modulus than either undamaged CFRP(1) or Hybrid-3B(1) specimen. This is due to the superior compressive properties of glass-fibre. The low undamaged modulus for Hybrid-3B(1) could be due to a weakness at the interfaces between disimilar materials or due to damage existing but not being identified visually. For all three panel types, an increase in panel damage results in a decrease in effective modulus. There is one GFRP(1) outlier which has a high modulus despite sustaining a relatively high level of damage. This result highlights that the type of damage sustained affects the resulting effective modulus. However, each specimen sustained a combination of skin breakage, skin/core debonding and core cracking. The damage types are not isolated, therefore, it is not possible to tell which damage type dominates a reduction in effective modulus. Figure 5.34 shows maximum compressive stress versus damage percentage for GFRP(1), CFRP(1) and Hybrid-3B(1). Beyond 10 % damage there is a general reduction in maximum compressive stress. All Hybrid-3B(1) specimen achieve compressive strength over 66 MPa despite sustaining damage. Again, it should be considered that Hybrid-3B(1) underwent a greater blast impulse. With this in mind, the results demonstrate the high blast resilience of Hybrid-3B.

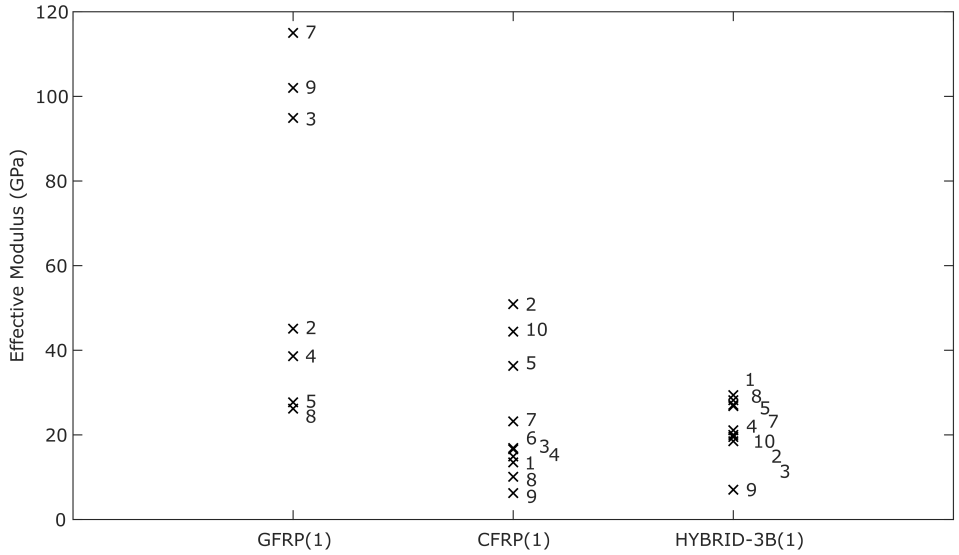


Figure 5.31: Post-blast effective modulus for the specimen taken from GFRP(1), CFRP(1) and Hybrid-3B(1).

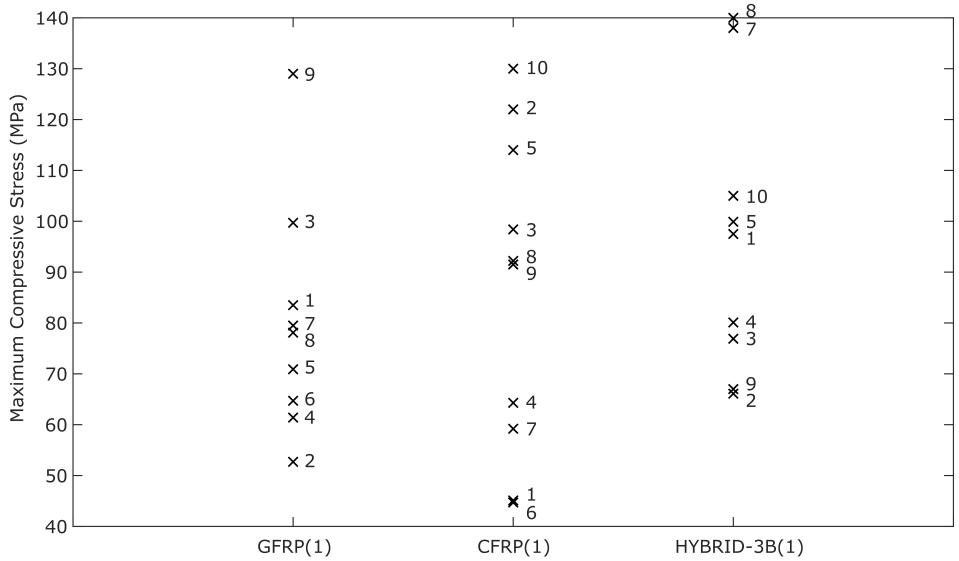


Figure 5.32: Post-blast maximum compressive stress for the ten specimen taken from GFRP(1), CFRP(1) and Hybrid-3B(1).

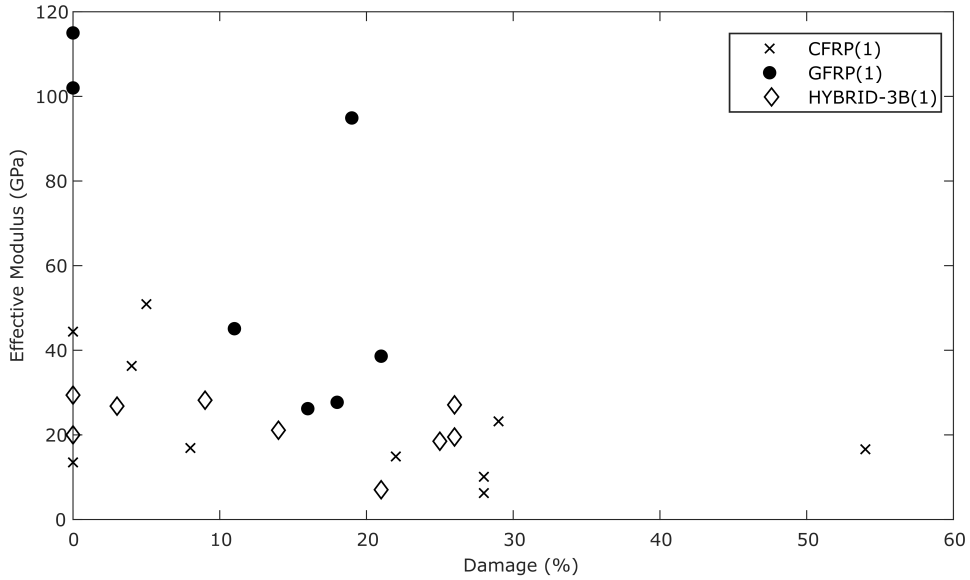


Figure 5.33: Post-blast effective modulus versus damage percentage for the specimen taken from GFRP(1), CFRP(1) and Hybrid-3B(1).

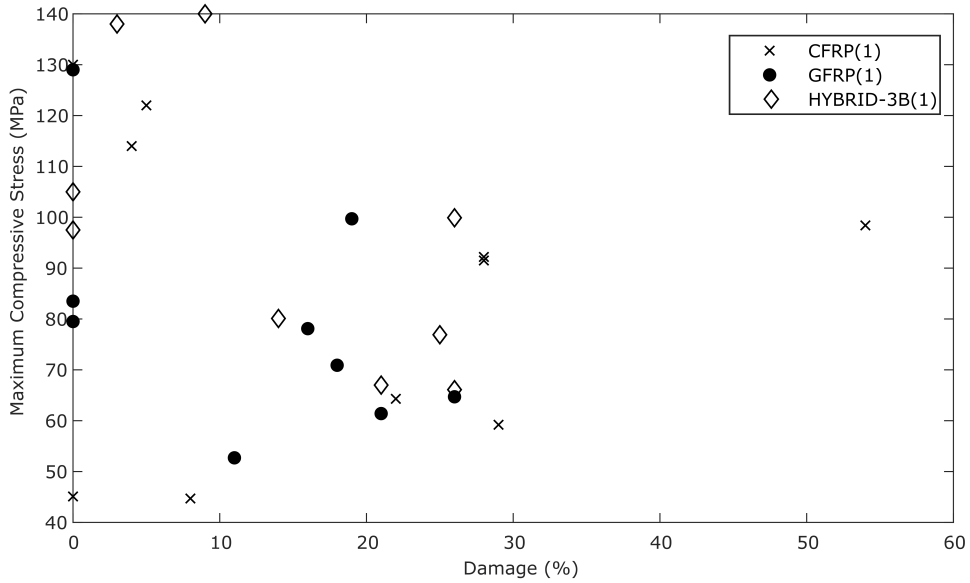


Figure 5.34: Post-blast maximum compressive stress versus damage percentage for the specimen taken from GFRP(1), CFRP(1) and Hybrid-3B(1).

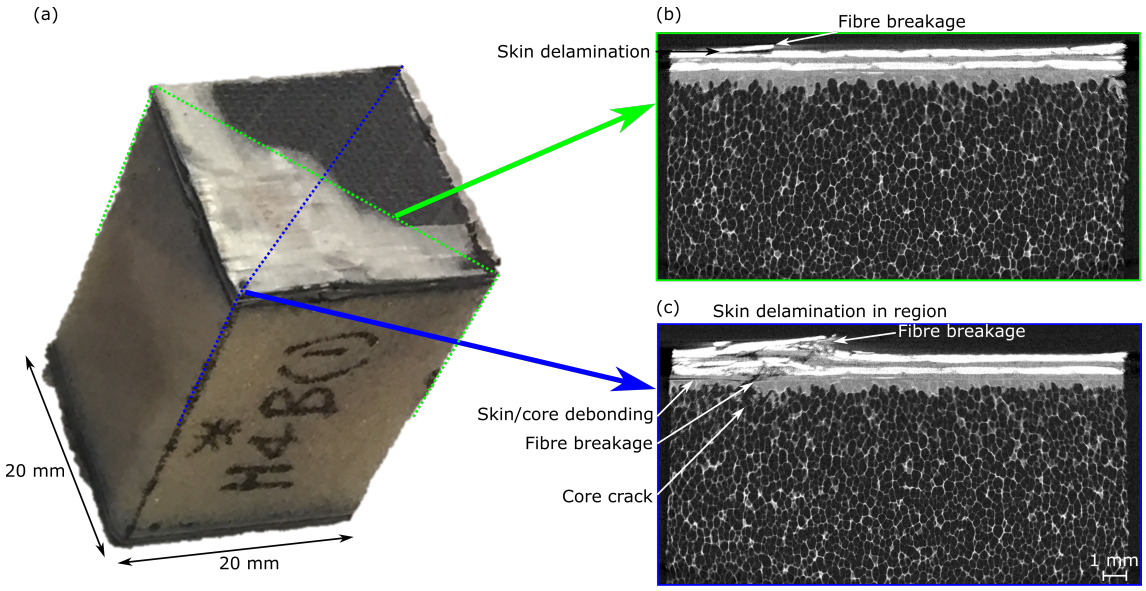


Figure 5.35: Post-blast damage analysis showing: (a) photograph of Hybrid-3B(1) specimen, (b) 2D cross-sectional view in relatively undamaged region and (c) cross-sectional view in highly damaged region.

5.4.2.1.3 X-ray CT Analysis

Figure 5.35 (a) shows a photograph of the 20 × 20 mm Hybrid-3B(1) specimen. Figure 5.35 (b) and (c) show perpendicular x-ray CT cross-sections of the specimen through the front skin and upper half of the foam core. In Figure 5.35 (b) damage to the glass-fibre plies is visible. The glass-fibre plies appear white in the images due to their higher density. Delamination between the perpendicular glass-fibre plies occurs along with fibre breakage. The carbon-fibre plies remain in tact. There is a clear foam crack in Figure 5.35 (c) which reduces the bending stiffness of the panel in this region and leads to skin damage. Around the crack there is a region of debonding between the innermost carbon-fibre ply and the foam. Some glass-fibre tows bridge a portion of the crack, however, the glass-fibre suffers from delamination between its perpendicular layers. Some tows in the next carbon-fibre layer bridge the crack at 45° to the previous glass-fibre bridging. The outermost glass-fibre plies exhibit clear fibre breakage. However, this fibre breakage is not directly above the foam core crack. The interactions between the two fibrous materials have caused debonding, delamination and crack bridging. This prevents a direct crack through the skin thickness and results in energy absorption.

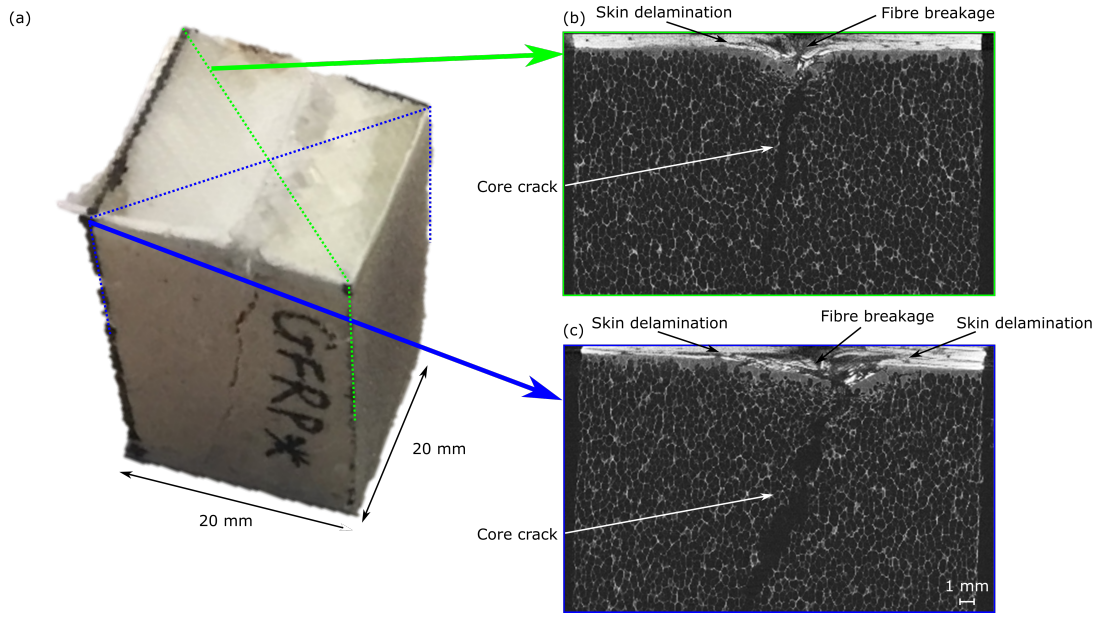


Figure 5.36: Post-blast damage analysis showing: (a) photograph of GFRP(1) specimen, (b) 2D cross-sectional view across highly damaged region and (c) perpendicular cross-sectional view across highly damaged region.

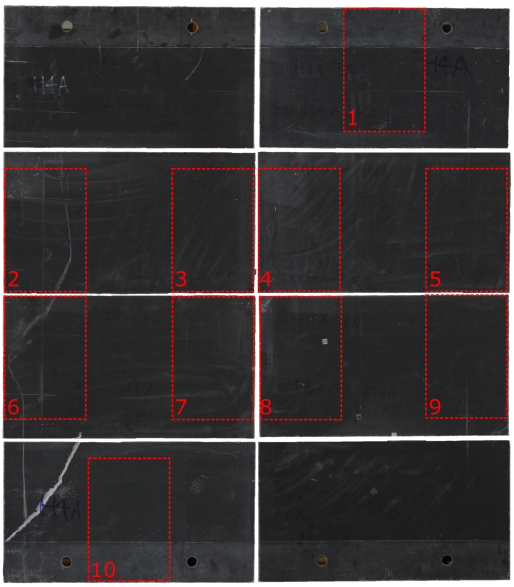
In contrast the photograph and x-ray CT scans of GFRP(1), in Figure 5.36, show a core crack travelling directly through the glass-fibre skin. Skin delamination occurs, particularly between the glass-fibre layers which are not stitched. However, debonding between the skin and core is not observed in this specimen. The crack propagates directly through the skin following the shortest path. Delamination has not absorbed sufficient blast energy to redirect the crack. These x-ray CT scans demonstrate that hybrid skins introduce extra failure mechanisms which aid panel blast resilience.

5.4.2.2 Test Series B

5.4.2.2.1 Damage Analysis

The front views of Hybrid-3B(2) and Hybrid-4(1) are shown in Figure 5.37. The 300 mm $\times$ 200 mm specimen with varying amounts of damage that were removed from the panel for edgewise compression are shown by the red dashed boxes. Hybrid-4(1) suffers from a severe front skin crack travelling vertically from one bolt hole to another. This front skin damage directly correlates with the sharp gradient discontinuity and deflection peak observed in the DIC analysis of Hybrid-4(1) in Figure 5.17. This crack begins to emerge during the rebound of Hybrid-4(1) during

(a) HYBRID-3B(2)



(b) HYBRID-4(1)

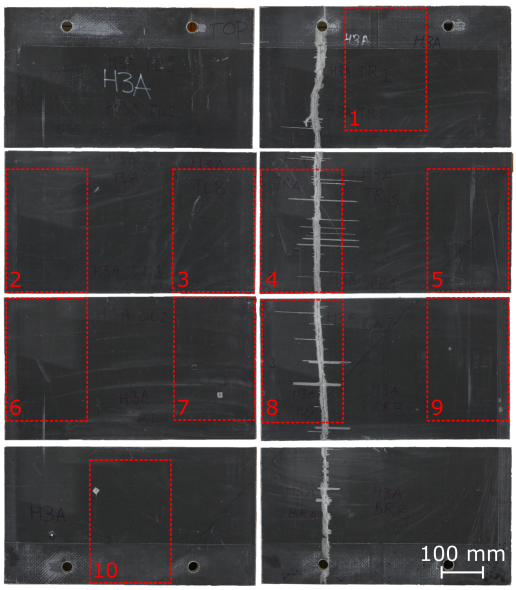


Figure 5.37: Photographs showing the front skin following blast of (a) Hybrid-3B(2) and (b) Hybrid-4(1).

the first 8 kg blast load, shown in Figure 5.16 (c). The crack is clearly visible in the contour plot and cross-sectional view of Figure 5.17. Hybrid-3B(2) suffers from a front skin crack in the bottom left corner of the panel. The cross-sections of Hybrid-4(1) are shown in Figure 5.38. For both Hybrid-3B(2) and Hybrid-4(1), core cracks were located around 150 mm in from the panel edges. In Figure 5.38 (b) the front skin breakage and resulting foam crack travelling perpendicular to the skins through the thickness are highlighted. Table 5.10 details the extent of damage to each panel using visual damage assessment based on these photographs. Furthermore, a schematic diagram showing the locations of the internal panel damage for each panel is shown in Figure 5.39.

Hybrid-3B(2) has a greater proportion of carbon-fibre leading to higher panel stiffness and lower deflection under blast loading. The visual damage inspection has revealed that this also leads to less damage. The slight increase in panel stiffness over Hybrid-4(1) is beneficial in preventing excessive deflection and damage.

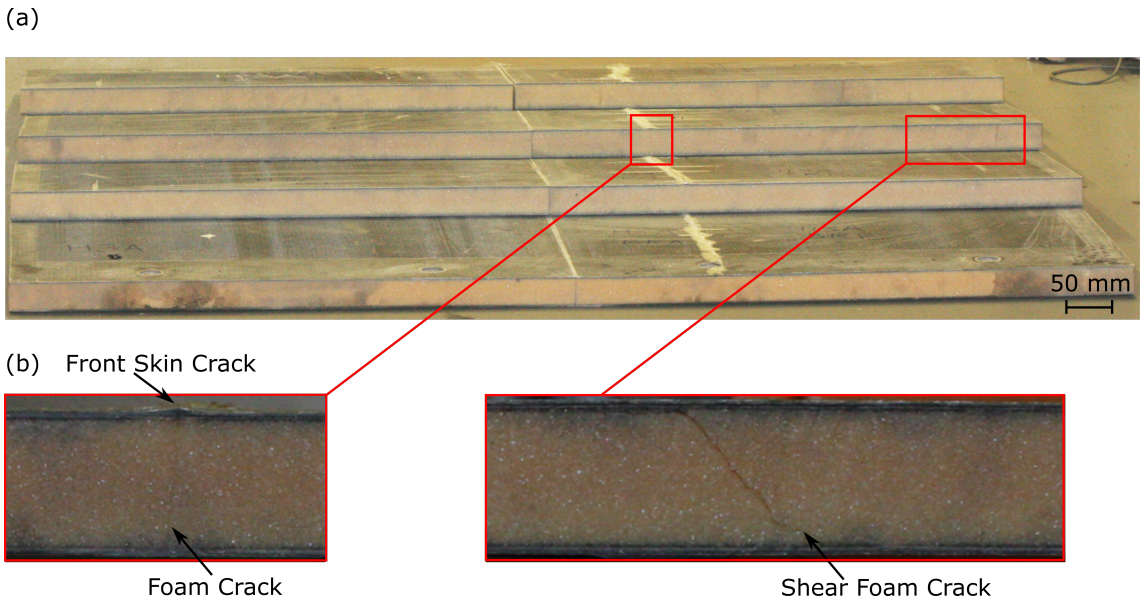


Figure 5.38: Photographs showing the damage to the core of Hybrid-4(1) as viewed from the bottom.

Table 5.10: Visual inspection of damage sustained by the panels subjected to 2 × 8 kg PE7 charge.

Panel type	No. of core cracks	Length of core cracks (mm)	No. of core/front skin debonds	Length of front debonds (mm)	No. of core/rear skin debonds	Length of rear debonds (mm)	Length of front skin cracks (mm)
Hybrid-3B(2)	7	270	1	29	0	0	320
Hybrid-4(1)	8	305	3	77	0	0	1368

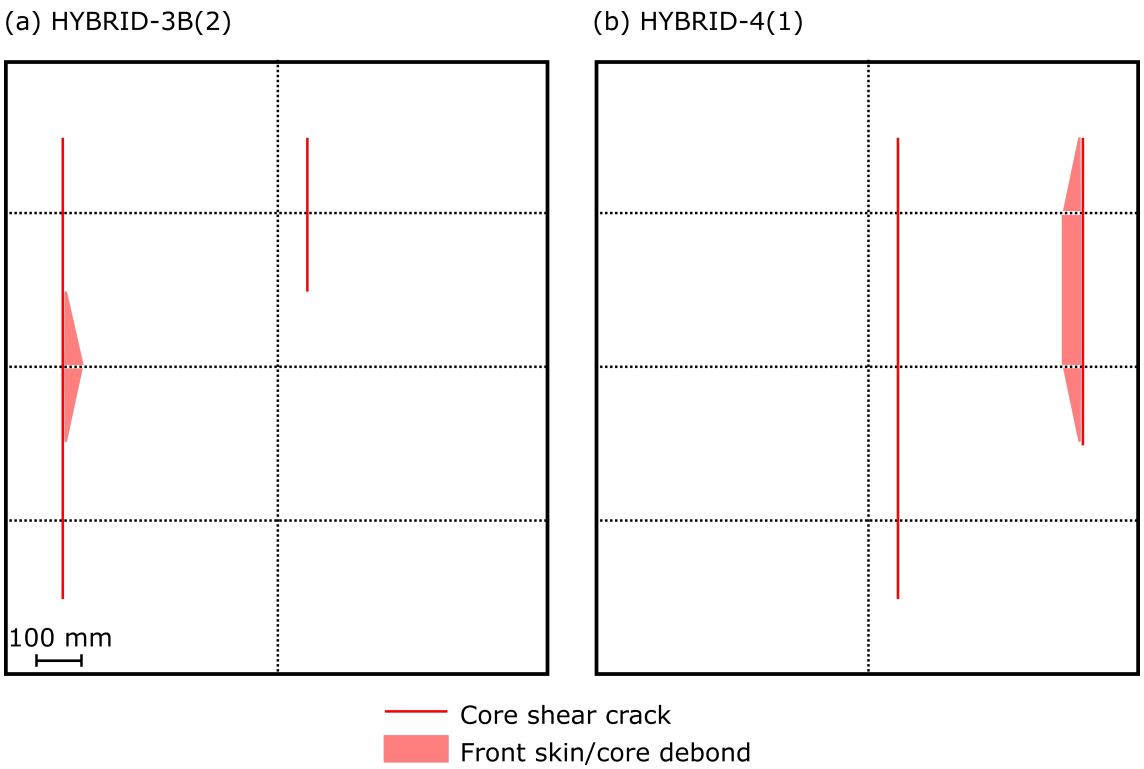


Figure 5.39: Schematic diagram showing the internal panel damage for (a) Hybrid-3B(2) and (b) Hybrid-4(1).

5.4.2.2.2 Post-Blast Compression

Figure 5.40 shows a plot of the effective modulus for the ten specimen taken from the same locations on each panel. Overall, the moduli of Hybrid-4(1) specimen are greater. This is, again, due to the superior compressive properties of glass-fibre as Hybrid-4(1) contains a greater proportion of glass-fibre. Two Hybrid-3B(2) specimen have a significantly lower effective modulus. These specimen were taken from the left-hand side of Hybrid-3B(2) which was the outside edge of the cubicle. This edge experienced greater constraint accounting for the damage. However, specimen taken from the equivalent position on Hybrid-4(1), did not sustain the same amount of damage. Hybrid-4(1) suffers from a front skin crack spanning the length of the panel and spanning the length of two compression specimen. This skin crack and resulting core crack could have acted as a stress relief and could account for the lower damage identified on the constrained side of Hybrid-4(1). However, the presence of the crack does not dominate the compression results for these two Hybrid-4(1) specimen. This highlights that shear core cracking in Hybrid-3B(2) has a greater effect on post-blast modulus than skin failure and direct core cracking in Hybrid-4(1). Figure 5.41 compares the maximum compressive stress achieved by the specimen taken from Hybrid-3B(2) and Hybrid-4(1). Except for the two more damaged Hybrid-3B(2) specimen detailed previously, the two hybrid types achieve similar maximum compressive strengths.

Figure 5.42 shows the specimen damage percentage versus effective modulus for Hybrid-3B(2) and Hybrid-4(1). Generally, the moduli for undamaged Hybrid-4(1) specimen are greater than those of Hybrid-3B(2) specimen. The effective modulus for both hybrid types reduces as damage percentage increases. The Hybrid-4(1) specimen with damage percentages of 18 % and 21 % have high moduli compared to other specimen. These two specimen were assigned a high damage percentage due to the front skin cracks running the length of the specimen, however, these results show that the front skin crack does not have a significant effect on post-blast modulus. A plot of maximum compressive stress versus damage percentage is shown in Figure 5.43 for Hybrid-3B(2) and Hybrid-4(1). Figure 5.43 shows that damage has no clear effect on the maximum compressive stress for Hybrid-4(1). The two Hybrid-3B(2) specimen which suffer from a significant amount of core cracking and skin/core debonding experience a significant drop in maximum compressive stress.

Although Hybrid-3B(2) has two significantly damaged specimen, it suffers from lower overall damage and no front skin cracking. Most Hybrid-3B(2) specimen demonstrate a comparable post-blast compressive strength to the Hybrid-4(1) spec-

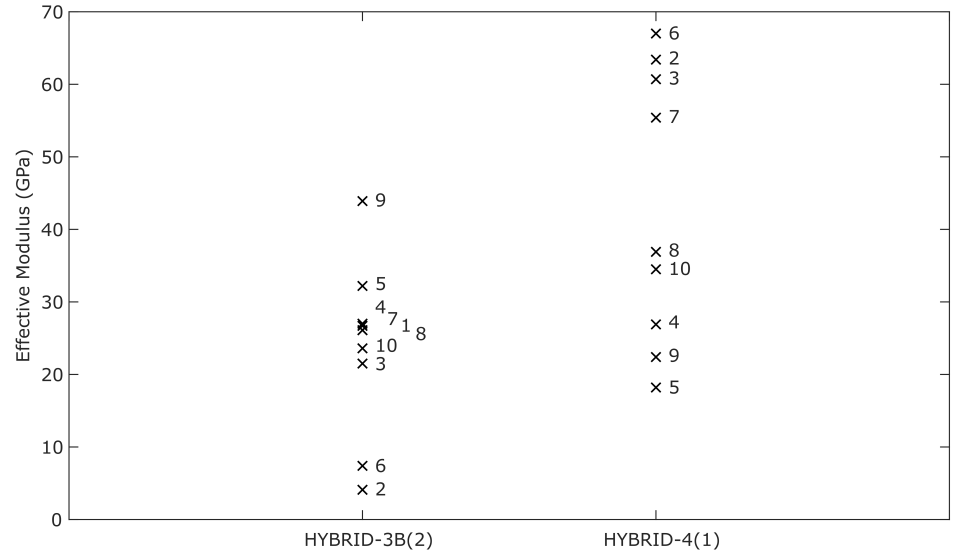


Figure 5.40: Post-blast effective modulus for the ten specimen taken from Hybrid-3B(2) and Hybrid-4(1).

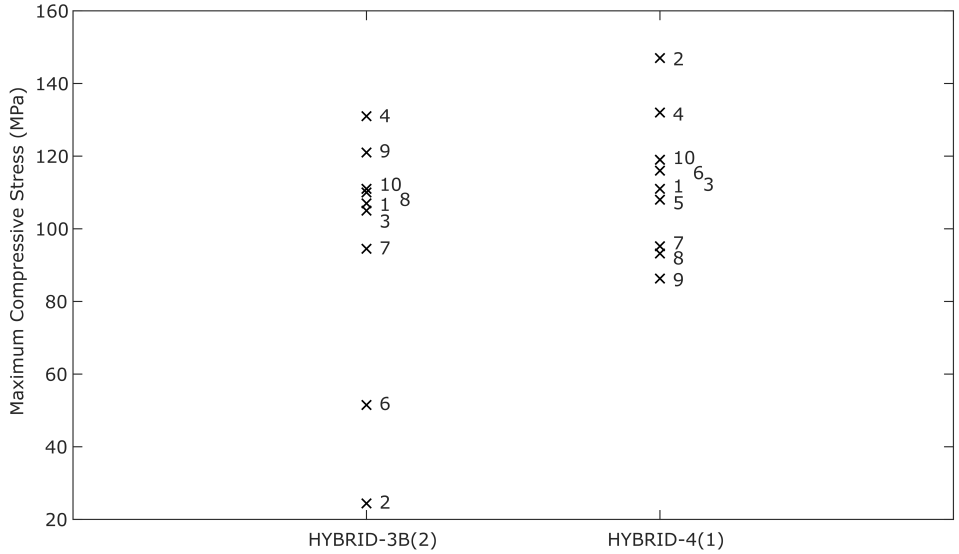


Figure 5.41: Post-blast maximum compressive stress for the ten specimen taken from Hybrid-3B(2) and Hybrid-4(1).

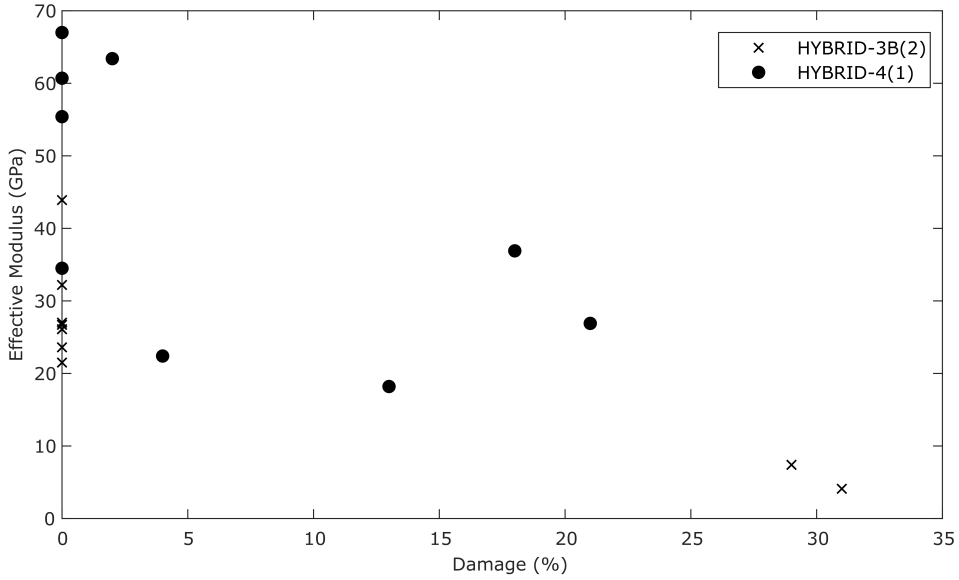


Figure 5.42: Post-blast effective modulus versus damage percentage for the ten specimen taken from Hybrid-3B(2) and Hybrid-4(1).

imen. Although the front skin crack does not appear to be detrimental on post-blast compressive modulus and strength for Hybrid-4(1), a severe skin crack is highly undesirable for marine applications.

Despite undergoing different blast signatures, the post-blast compressive performance of Hybrid-3B(1) and Hybrid-3B(2) can be compared. Figure 5.44 shows effective compressive modulus versus damage percentage for the two Hybrid-3B panels. The panels show consistent post-blast behaviour. The undamaged specimen, or those with damage that was not visually identifiable, demonstrated moduli between 20 GPa and 45 GPa. Once again, the specimen modulus decreases as damage percentage increases. Figure 5.45 shows a plot of maximum compressive stress versus damage percentage. The specimen with no or low damage demonstrate maximum stress over 95 MPa. Once over 10 % damage is sustained, the maximum compressive stress generally decreases as damage increases. For the Hybrid-3B specimen analysed, two 8 kg PE7 blast loads result in either no visually identifiable damage or severe damage. One 30 kg PE7 blast load results in evenly spread damage between 0 % and 26 %. This indicates that a small charge can damage the panel in a few locations and create areas of weakness. The damage in these weakened areas is then exacerbated under a second blast.

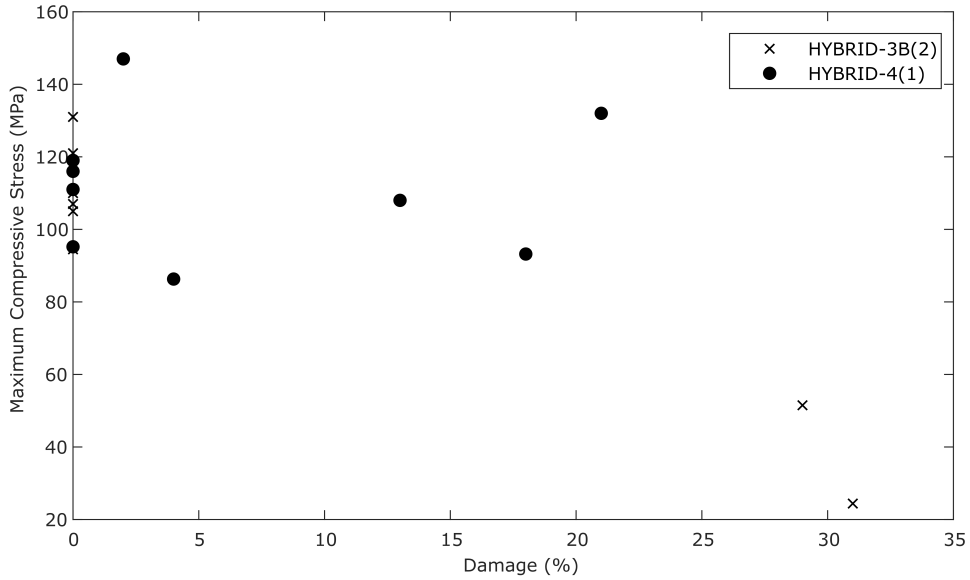


Figure 5.43: Post-blast maximum compressive stress versus damage percentage for the ten specimen taken from Hybrid-3B(2) and Hybrid-4(1).

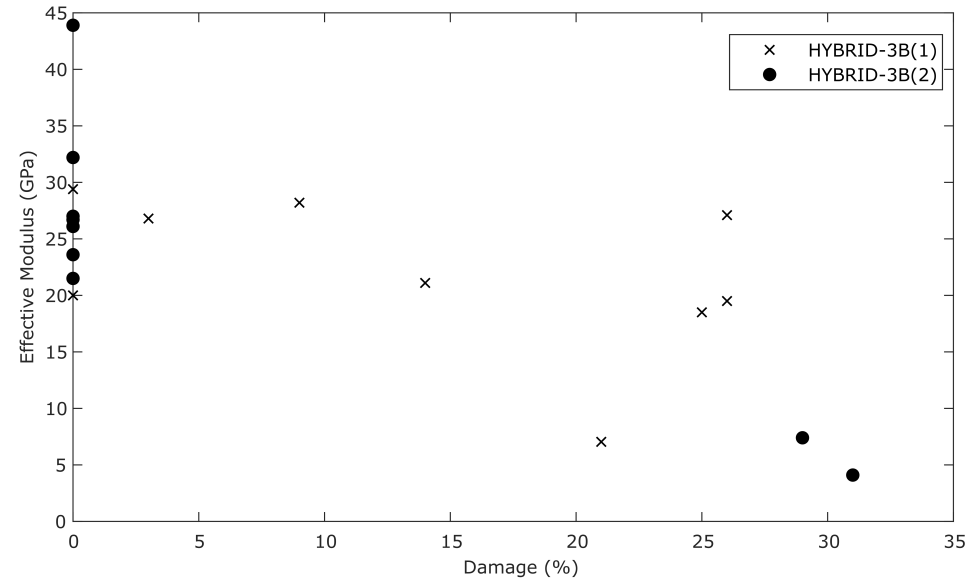


Figure 5.44: Post-blast effective modulus versus damage percentage for the specimen taken from Hybrid-3B(1) and Hybrid-3B(2).

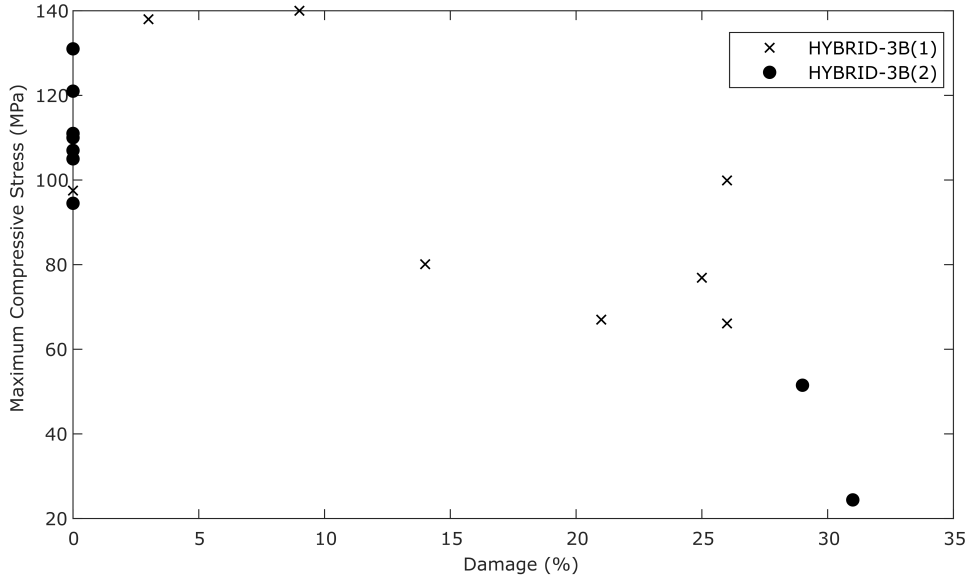


Figure 5.45: Post-blast maximum compressive stress versus damage percentage for the specimen taken from Hybrid-3B(1) and Hybrid-3B(2).

5.5 Discussion

5.5.1 Blast Wave Modelling and Work Done

Pro S Air CFD software was, once again, used to predict the expected pressures experienced at the centre and across the composite sandwich panels. A comparison of the pressure distribution with and without pendine concrete blocks was made. This was used to determine whether comissioning the roof extension and positioning of these blocks was necessary. The Pro S Air predictions revealed that the roof extension and blocks result in a overpressure difference of 25 kPa at 12.58 ms for 8 kg at 8 m. Without the blocks the difference is 50 kPa at the same time. The roof extension and pendine blocks were, therefore, deemed necessary. Even with pendine blocks and roof extension in situ, the model revealed that the panels still do not undergo uniform pressure loading. Areas are loaded radially due to the interactions between the blast wave and the floor.

During test series A, the Pro S Air predicted peak pressure agreed with all PVDF recorded peak pressures to within 8 %. However, the reflected pressure calculated from the side-on gauge is considerably lower than the PVDF recorded pressures and Pro S Air prediction. This could be due to the misalignment of the side-on pressure gauge and possible blast clearing effects around the side-on gauge. This

would lead to pressure lower than the true value being recorded. There is good agreement between the positive phase duration of the first trial in test series A, recorded using the side-on gauge, and the Pro S Air prediction. However, there is a large discrepancy between the positive phase duration values for the Hybrid-3B(1) trial. This could be caused by a change in atmospheric conditions or a number of factors to do with the charge materials or formation.

During test series B, the PVDF gauges were reliably recording peak reflected pressure to within 7 % of one another. However, these PVDF values differed significantly from both the reflected pressure, calculated from the side-on gauge, and from the Pro S Air predicted pressure. As previously detailed, a low side-on pressure reading can be accounted for due to gauge misalignment. However, the difference between the Pro S Air model and PVDF gauges could be due to gauge error or experimental error. The charge could have been incorrectly placed at a reduced stand-off distance or more than 8 kg of explosive could have been in the charge. The explosives were handled and positioned by site staff only so it was not possible to weigh the charge prior to each experiment. Further controlled experiments would be necessary to determine the cause of the disparity in pressure measurements. Nevertheless, Hybrid-3B(2) and Hybrid-4(1) were simultaneously subjected to the charges so their performance can be directly compared regardless of the exact pressure reached. This is also the case for GFRP(2) and CFRP(2).

The Pro S Air pressure distributions were used to help calculate the work done by each panel. The cumulative work done calculations revealed differences in panel performance. GFRP(1) and CFRP(1) were shown to experience a similar cumulative work done. Since both panels experienced the same charge, this indicates that both panels have undergone a similar extent of deflection. CFRP(1) experiences deflection with a lower overall magnitude but across a more widespread area. GFRP(1) experiences a greater deflection in the central region but less deflection elsewhere. These two deflection behaviours lead to differing panel damage distributions. Hybrid-3B(1) undergoes greater work done. This is partially caused by a greater impulse delivered to the panel along with high deflection of a damaged region running diagonally across the panel. During test series B, Hybrid-3B(2) undergoes less cumulative work done compared to Hybrid-4(1) for both blast loads. This is due to the reduced deflection experienced by Hybrid-3B(2) as a result of its increased stiffness. Hybrid-3B(2) and Hybrid-4(1) were simultaneously subjected to the same charge enabling a direct work done comparison.

5.5.2 Digital Image Correlation

RBMC was implemented across all the DIC data to remove cubicle movement. Since the vertical edges of the panels were clamped during these experiments, panel slip occured and some motion of the panels is visible in the DIC data. The DIC data clearly reveals that all three panels undergo damage as a result of blast loading. However, Hybrid-3B(1) spreads the damage across a wider area resulting in a shallower gradient discontinuity. As expected, the centre point deflection and strain of Hybrid-3B(1) lies between that of CFRP(1) and GFRP(1). The centre point displacement trace for CFRP(1) indicates that it has suffered damage due to a double deflection peak and long time period of return. The return time period of Hybrid-3B(1) has also increased due to damage that it has sustained.

During test series B, Hybrid-4(1) experiences greater deflection under both blast loads and DIC reveals the presence of a significant panel crack. Damage within Hybrid-3B(2) is also identified through DIC deflection but this remains as a core crack. The reduced size of GFRP(2) and CFRP(2) resulted in incomparable deflections. The smaller panels required a greater steel front sheet which deflects under blast loading and absorbs greater blast energy than expected. The deflection of GFRP(2) and CFRP(2) relative to their boundaries is, therefore, significantly lower than the larger panels tested. Since the deflection is so low, there are no clear signs of panel damage. As expected, the lower stiffness of GFRP(2) results in greater centre point deflection compared to CFRP(2). The time period of response for all four panels tested in test series B correlate with their mass and stiffness as expected for both initial and repeated blast loads. This indicates, along with the relatively smooth centre point displacement traces, that these panels have sustained less damage compared to the panels in test series A.

5.5.3 Post Blast Damage & Strength

Firstly, the experiments have revealed that DIC deflection maps and cross-sections accurately capture the location of severe damage and, equally, severe front skin damage has a significant effect on panel deflection. Once again, the support conditions dictate the location of core cracks. The rigidity of the support conditions result in high bending moments causing core cracks to occur. The fixing method, bolts and bolt holes, act as the initiation locations for front skin cracks. The design of the support structure can significantly aid in blast resilence.

Post blast damage assessment for test series A revealed that GFRP(1), CFRP(1) and Hybrid-3B(1) all suffer from a similar extent of damage. GFRP(1) suffers from 50 % more front skin/core debonding compared to Hybrid-3B(1). Considering Hybrid-3B(1) has undergone a greater impulse, the panel has only sustained comparable levels of damage demonstrating good blast resilience. Two GFRP(1) specimen had no visual damage indicating that the concentrated deflection of GFRP(1) leads to localised regions of damage. Due to the combination of all damage types in all the specimen, it is difficult to deduce which mechanism dominates reductions in modulus and strength. The post-blast compressive strength for all panels in test series A was similar. Hybrid-3B(1) achieved this strength despite undergoing a greater blast impulse. Finally, the x-ray CT scan of Hybrid-3B(1) indicate that interactions between the skin layers prevents a direct through thickness crack. By redirecting the crack and causing delamination, debonding and fibre breakage, energy is absorbed by the hybrid skin.

Following test series B, Hybrid-4(1) demonstrated a high post-blast compressive modulus due a greater proportion of glass-fibre. However, post-blast strength for Hybrid-3B(2) and Hybrid-4(1) were similar, this is a more critical property. Additionally, Hybrid-4(1) suffers from greater overall damage including a severe front skin crack. This is highly undesirable for a marine application due to water ingress. Despite a highly damaged region of Hybrid-3B(2) suffering from low post-blast compressive strength, overall Hybrid-3B(2) achieves a good balance between deflection, damage and post-blast performance. Furthermore, if Hybrid-3B(2) were tested as a whole panel, the damaged regions could be compensated for. Overall, the proportions of glass-fibre and carbon-fibre fabrics in Hybrid-3B result in a good trade-off between strength and stiffness.

The damage inspection has revealed the shear core crack angles along with the direction in which debonding propagates. Additionally, it has been observed that the first internal damage mechanism that occurs is core shear cracking, followed by front skin/core debonding and then rear skin/core debonding. Core shear cracking also leads to front skin damage due to the resulting local reduction in panel bending stiffness. Skin damage takes the form of delamination and fibre breakage. To accurately capture the response of hybrid composite sandwich panels under blast loading beyond their elastic limit in numerical simulations, all of these failure mechanisms need to be included.

All visible panel damage sustained during air blast loading resulted in compressive modulus and compressive strength reductions. Due to the nature of air blasts

and the global panel response required, any damage sustained becomes widespread. This differs from impact loading where the damage remains localised. Following the air blast experiments performed in this chapter, the panels achieved at least 24.2 MPa compressive strength and 4.10 GPa compressive modulus. This implies that if these panels are expected to sustain an air blast of this nature, the structural requirements on these panels must not exceed these values. Furthermore, it is recommended that a vessel with any visible damage following an air blast of similar magnitude to these experiments returns for repair.

These experiments, and those in Chapter 4, show that hybrid skins constructed from 50 % glass-fibre and 50 % carbon-fibre by volume result in a good blast resilience. These 50:50 hybrid skins achieve the necessary strength to prevent excessive skin damage whilst allowing reasonable deflection. Increasing the proportion of glass-fibre, as shown in Hybrid-4(1), results in decreased panel stiffness. This leads to greater panel deflection, core damage and skin damage. Conversely, increasing the proportion of carbon-fibre would increase panel stiffness and reduce deflection. However, this would come with the risk of increasing the brittle behaviour of the panel. The bending stiffness of the 50:50 hybrids can be marginally adjusted by changing their layup. As shown in Chapter 4, a change in layup can alter the bending stiffness by 0.2 kN m^{-2}. This was shown to have a minor effect on panel damage. Overall, both Hybrid-1A and Hybrid-2 sustained minimal damage. Due to the multiple differences between the experiments, it was not possible to directly compare Hybrid-3B to Hybrid-1A or Hybrid-2. However, based on the results in Chapter 4, the presence of the two fibres in 50:50 proportions is the key factor during air blast loading. One comparison between the first and second air blast studies which can be made is that the asymmetry of Hybrid-3B was shown to have no detrimental effects on blast performance, similar to Hybrid-1A, even with its considerably reduced skin thickness.

5.6 Conclusion

Seven hybrid composite sandwich panels were subjected to air blast loads. The investigations were carried out to compare the blast resilience of different hybrid skin layups along with their performance under different blast severities and repeat loads. Although direct comparisons between panels were intended, the complex nature of blast experiments resulted in variability and complications. For example, Hybrid-3B(1) underwent a greater blast impulse compared to GFRP(1) and

CFRP(1). Despite this, the deflection of Hybrid-3B(1) was found to lie between that of GFRP(1) and CFRP(1), as expected from their panel bending stiffnesses. Hybrid-3B(1) sustained a similar extent of damage and comparable post-blast compressive strength values to both GFRP(1) and CFRP(1). Furthermore, x-ray CT scanning of a Hybrid-3B sample demonstrated the energy absorption mechanisms that can occur in its skin layup.

Due to a difference in panel size, and resulting deflection, repeat blast performance of Hybrid-3B(2) and Hybrid-4(1) could not be compared to GFRP(2) and CFRP(2). Nevertheless, the hybrid panels could still be compared to one another. The results demonstrate that the higher bending stiffness of Hybrid-3B(2) results in lower deflection and hence lower damage. Hybrid-4(1) suffers from a severe front skin crack. Although this does not affect the post-blast compressive performance of Hybrid-4(1), it is undesirable in marine applications due to potential water ingress. Hybrid-3B was shown to have advantages over other panels under both blast scenarios. The 50:50 proportion of glass-fibre and carbon-fibre, as used in Hybrid-3B, results in a good trade-off between strength and stiffness.

Large scale air blast experiments were performed at Radnor Range. Some aspects of the equipment, instrumentation and setup had not been used before at Radnor. The results demonstrated that the previously developed experimental methods could be successfully adapted to a new test site. Areas for further improvement were highlighted.

Chapter 6

Full Scale Underwater Blast Testing

6.1 Introduction

The aim of this investigation was to develop a preliminary underwater blast experiment with high-speed cameras recording full-field panel response. The experiment was carried out at Radnor Range Ltd using equipment available at the site. As detailed previously, the hull of a naval vessel may be subjected to underwater blast loading. Underwater blast results in a more severe loading regime and hence more devastating damage than air blast loading. Once again, scaling the underwater blast response of composite sandwich panels from small to large scale is challenging. Therefore, gathering large scale data to validate analyses and predictions is important. Previous large scale underwater blast testing has relied on foil strain gauge data. The design of the previous test facility meant underwater camera use was not possible [19], [20]. This chapter details the successful full-field displacement and strain tracking of a panel during large scale underwater blast loading.

One hybrid composite sandwich panel was subjected to 1 kg PE7 charge at a stand-off distance of 1 m. The charge was fully submerged to a depth of 275 mm. It was only possible to partially submerge the panel. Nevertheless, the experiment simulates an underwater blast on a panel partially above and below the waterline. The same dimensions and foam core material as used in the hybrid composite sandwich panels in Chapter 5 were adopted. This means the air and underwater blast performance of the selected hybrid composite sandwich panel can be qualitatively compared. Once again, post-blast damage and strength analysis was carried out.

This post-blast analysis highlights the significant change in failure mechanisms between and air and underwater blast caused by the change in fluid medium.

Although only one underwater blast test was carried out, the experiment has revealed the possibility of creating a test setup using existing equipment available at a test range. This shows that similar experiments could be carried out at other test ranges without the requirement for specialised experimental ponds. Furthermore, the preliminary experiment has highlighted the underwater blast resilience of a hybrid composite sandwich panel.

6.2 Experimental

6.2.1 Materials

One hybrid composite sandwich panel was subjected to full-scale underwater blast testing. The panel adopted a Hybrid-4 layup, the schematic of which is shown in Figure 6.1. Hybrid-4 was selected due to its higher proportion of glass-fibre plies which have a greater strain to failure than the carbon-fibre plies. Previous underwater blast testing has demonstrated the disadvantages of using CFRP skins during underwater blast. This is due to their brittle behaviour leading to greater damage and failure [38]. Based on the analysis mentioned, it was desired to investigate whether the inclusion of a small proportion of carbon-fibre would improve panel strength yet result in acceptable levels of damage. The panel was 1.39 m $\times$ 1.23 m in size and it was constructed from four layers of bi-axial stitched fabric either side of a 30 mm thick, 100 kg m^{-3} PVC foam core (Divinycell H100). The fabric layers were arranged quadriaxially. The same fibres, matrix and fabrication method, as detailed in Chapters 4 and 5, were used again. 600 gsm E-glass-fibre and 400 gsm HexTow AS4 carbon-fibre were used along with SR8100 epoxy resin and SD8824 hardener. The panels were fabricated using resin infusion and were ambient cured and then held under vacuum for 24 h before being demoulded. As in Chapter 4, the properties of the materials used and face-sheet properties calculated using the rule of mixtures are detailed in Table 6.1. The laminate compressive strengths are certainly overpredictions as the calculation neglects the effects of voids, fibre misalignment or fibre bunching. The measured areal density of the panel was 9.88 kg m^{-2}, the panel equivalent bending stiffness was 38.9 kN m^{-2} and the fibre volume fraction was 0.39.

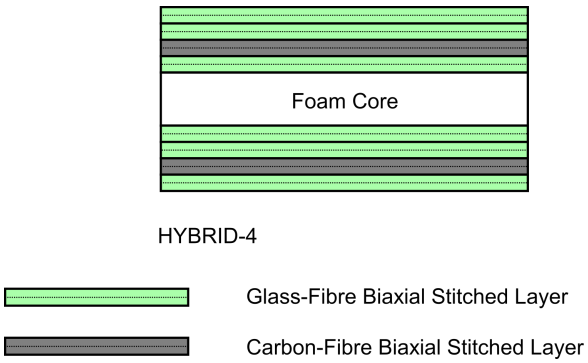


Figure 6.1: Layup configuration of the hybrid composite sandwich panel fabricated for full-scale underwater blast testing.

Table 6.1: Mechanical properties of the composite sandwich panel materials and plies.

Material	Density (kg m^{-3})	Elastic modulus (GPa)	Tensile strength (MPa)	Shear strength (MPa)	Compressive strength (MPa)
Glass-fibres	2555 [96]	78.5 [96]	2000.0 [96]	-	4500.0[96]
Carbon-fibres (HexTowAS4)	1790 [105]	230.0 [105]	4410.0 [105]	-	4950.0 [96]
SR8100 epoxy & SD8824 hardener	1119 [106]	2.7 [106]	50.0 [106]	48.0 [106]	103.0 [96]
BX600/epoxy bi-axial GFRP ply	1913	22.9	574.9	48.0	1289.3
FCIM105/epoxy bi-axial CFRP ply	1425	53.9	1032.4	48.0	1184.3
PVC H100 foam core	100 [107]	0.1 [107]	3.0 [107]	2.1 [107]	2.7 [107]

6.2.2 Methods

The panel was mounted onto one side of the steel cubicle. The panel was bolted to the front steel sheet along the top and bottom edges using 8 × M12 bolts and clamped along the vertical edges using the cubicle clamps. A 5 mm thick steel frame was placed up against the panel to help distribute the bolting and clamping forces. In addition, a custom made epalyn rubber, box welded pond liner was adhered to the inside of the steel frame using Sikaflex 291i marine sealing adhesive and Loctite 406. This created a seal when the frame was tightened up against the panel using the bolts and clamps. An enclosure for the body of water was created from pendine concrete blocks. This block enclosure had the same dimensions as the pond liner and provided support for the liner. A photograph of the test setup under construction is shown in Figure 6.2. Water was pumped into the enclosure to a depth of 1525 mm. The charge was placed at a depth of 275 mm and at 1 m stand-off distance from the panel. A 1 kg spherical PE7 charge was used for the underwater experiment. Due to set up constraints, it was not possible to fully submerge the entire panel hence 420 mm of the panel was above the water level. A schematic of the test setup for this experiment is shown in Figure 6.3. The variation of pressure with time for an underwater shock-wave is given by Equation 6.1, where $P(t)$ is the pressure acting at time t, P_m is the maximum pressure at the shock wavefront and θ is the time constant for $P(t)$ to fall to P_m/e. It is possible to calculate P_m from equations fitted to experimental data expressed in terms of scaled distance, such as in Equation 6.2 [5]. Here Z is the scaled distance as given in Equation 5.1. Using Equation 6.2, the expected pressure loading on the panel for the experimental setup detailed was 52.63 MPa.

$$P(t) = P_m \exp\left(\frac{-t}{\theta}\right) \tag{6.1}$$

$$P_m = \frac{355}{Z} + \frac{115}{Z^2} - \frac{2.44}{Z^3} \tag{6.2}$$

6.2.2.1 Instrumentation

6.2.2.1.1 Three-Dimensional Digital Image Correlation

3D DIC was implemented in an attempt to capture the response of the panel during underwater blast loading. A pair of Photron SAX2s recording at 12,500 fps were placed behind the panel. The camera signal circuit input was connected to a trigger



Figure 6.2: Photograph showing cubicle and pendine concrete block setup whilst under construction.

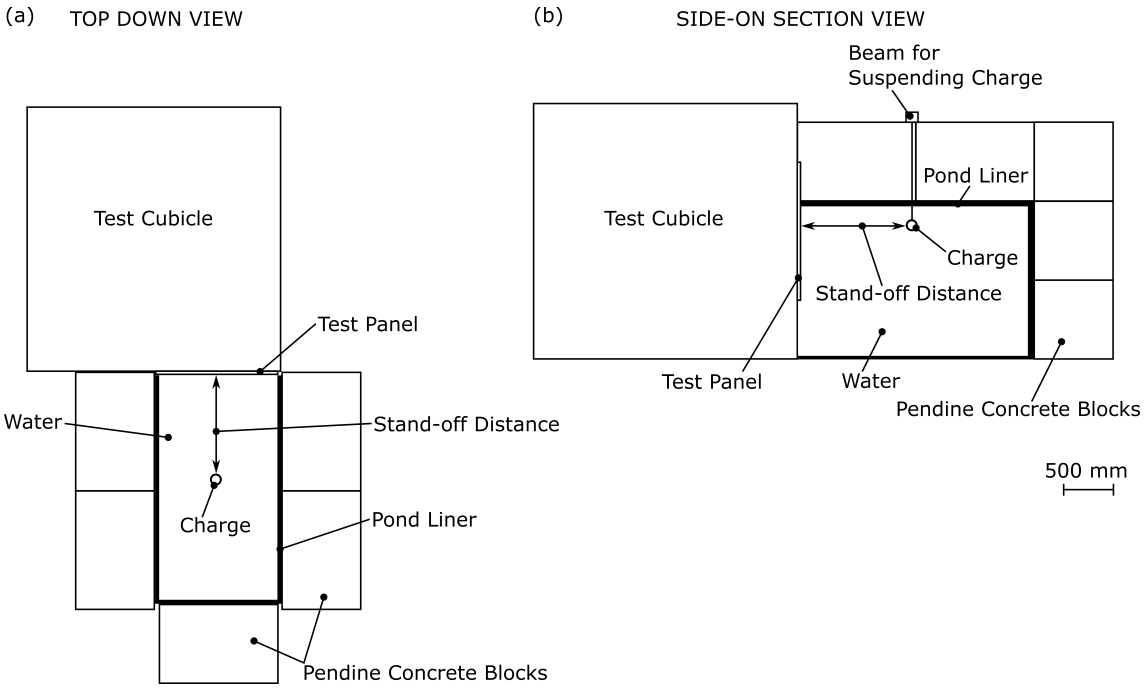


Figure 6.3: Schematic diagram of the test setup showing: (a) view of setup from above and (b) side-on section view of setup.

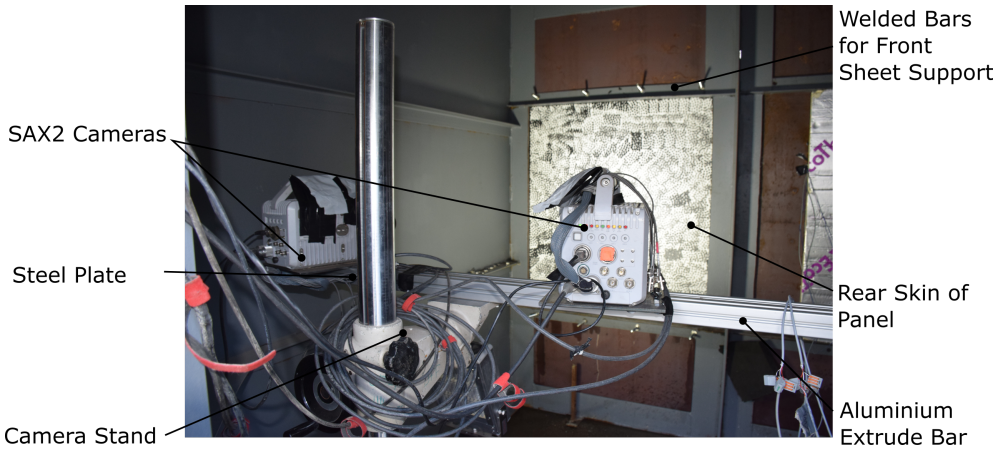


Figure 6.4: Photograph showing the camera setup for the full-scale underwater blast experiment.

switch. This camera trigger switch was pressed at the same time as the charge detonation switch.

The cameras were, once again, housed within the test cubicle. As only one panel was being tested, there was increased space within the cubicle. The cameras were, therefore, mounted horizontally on an aluminium extrude bar attached to a heavy duty camera stand. Furthermore, horizontal camera mounting increased the distance between the cameras and the ground in the eventuality that the cubicle would become flooded. 24 mm camera lenses were used to ensure the panel was entirely within the camera FOV. The perpendicular distance between the panel and the cameras was calculated as 1.74 m and the distance between the two cameras was 0.77 m. Banks of LED lights were used to illuminate the back skin of the panel during blast testing. The power cables for all cameras and lights were lifted off the ground to prevent them from being submerged if the cubicle were to become flooded. Calibration of the cameras was carried out using a 700 mm CC coded calibration cross supplied by GOM UK. The rear skin of the panel was painted matt white and a random black speckle pattern was applied to facilitate DIC processing. The speckles were required to be between 4 mm and 7 mm. A photograph of the camera and light setup within the cubicle, along with the panel speckle pattern is shown in Figure 6.4.

During the experiment, an additional high speed Photron SA1 colour camera was setup to record the progression of the explosion. This camera was mounted on a tripod on the bank of the test arena. The camera recorded at a frame rate of 2,000 fps.

6.2.2.1.2 Foil Strain Gauges

The panel was instrumented with two single axis gauges (CEA-06-250UW-350) at its centre. One gauge was aligned with the major vertical axis of the panel and the second was aligned with the minor horizontal axis. The same surface preparation and adhesion technique as described in Chapter 4 was used. Once again, a three wire quarter-bridge circuit was implemented for the strain gauges. 5 m long three-core shielded cables with a DIN connector were soldered to the gauge terminal pads and ran into the cubicle into a high frequency Flyde H379TA bridge amplifier. The amplifier was placed in an ammunition box padded with foam and was placed on a raised surface in the event that the cubicle would become flooded. The strain gauges were coated with M-Coat A and then the gauges and lead wires were liberally covered with a silicone rubber coating to ensure waterproofing. 200 m of coaxial cable with BNC connectors were used between the amplifier in the cubicle and the oscilloscopes recording the data in a reinforced cabin.

6.2.2.1.3 PVDF Pressure Gauges

PVDF film pressure sensors were implemented during the blast experiment. Three PVDF sensors were taped to the front of the panel. One at the centre, one 350 mm vertically below the centre point and one 350 mm vertically above the centre point. A liberal silicone rubber coating was applied over the PVDF gauges to ensure waterproofing. The PVDF sensors were connected via a 5 m long low noise coaxial cable to a charge amplifier. The charge amplifier was housed within the ammunition box in the steel cubicle. The PVDF cables were fixed to the panel front using self-adhesive cable ties. 200 m of coaxial cable with BNC connectors was used between the charge amplifier and the oscilloscope recording the data. A photograph of the panel front with PVDF and strain gauges mounted, whilst the water enclosure was being filled, is shown in Figure 6.5.

6.3 Results

6.3.1 Digital Image Correlation

The progression of the underwater blast is shown in Figure 6.6. The images show the detonation of the charge and a column of water travelling upwards from the water surface. This water column is very typical for a shallow explosion.



Figure 6.5: Photograph showing the setup of the strain gauges and PVDF pressure gauges whilst the enclosure was being filled with water.

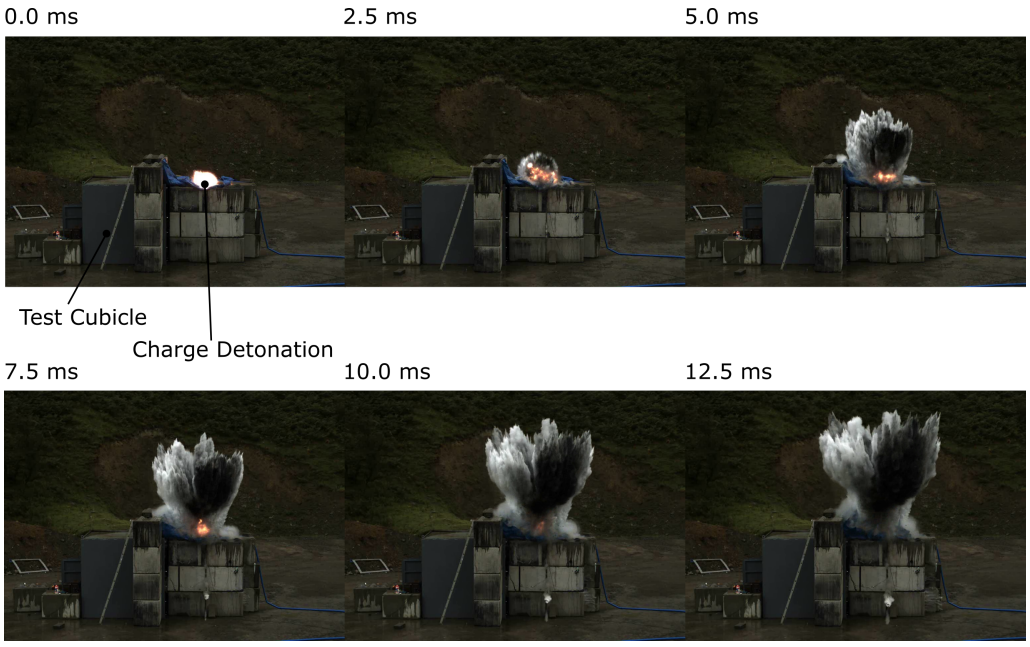


Figure 6.6: Photograph showing the detonation of the charge and progression of the water column.

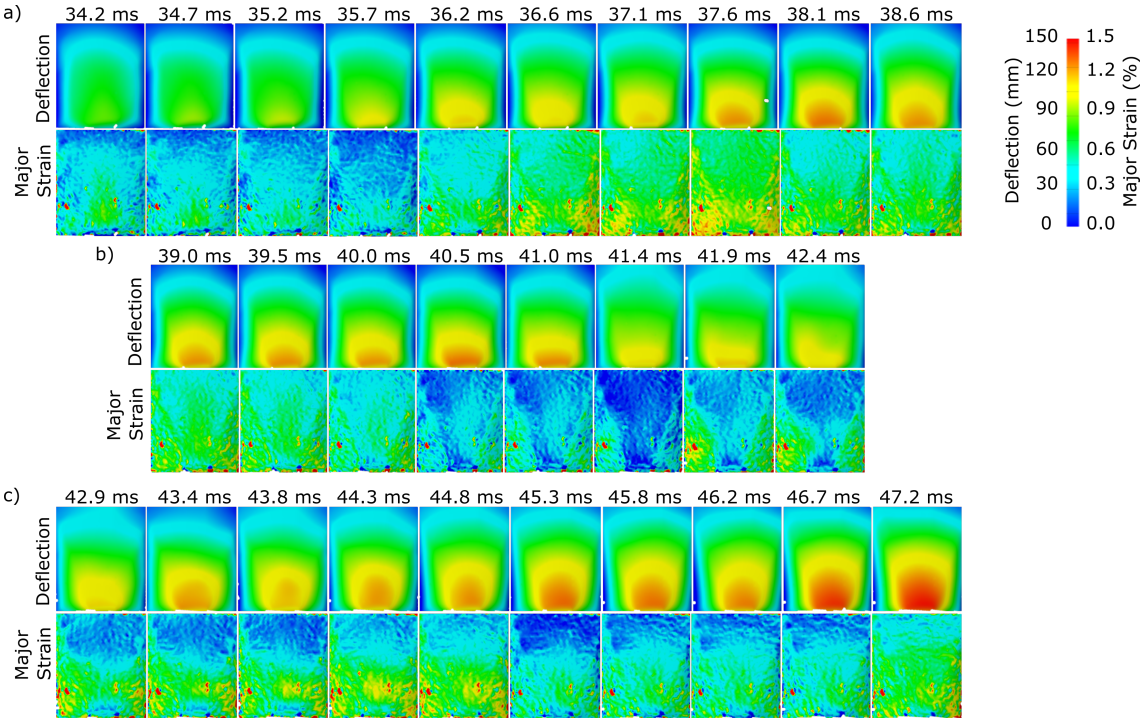


Figure 6.7: DIC image series of the out-of-plane displacement and major strain showing: (a) deflection at intervals of time, (b) short rebound and (c) second deflection.

6.3.1.1 Full-field Analysis

A series of images illustrating the back skin deflection and major strain at approximately 0.5 ms time intervals is shown in Figure 6.7. The images in Figure 6.7 (a) show an initial out-of-plane deflection of the panel. This is followed by a short rebound of the panel, shown in Figure 6.7 (b). The panel deflection remains positive overall. In Figure 6.7 (c) the panel experiences increasing deflection once again. The panel continues to deflect beyond 47.2 ms and remains permanently deformed.

In all image series, the lower portion of the panel experiences a greater deflection and strain compared to the upper portion. This is due to the influence of water depth. When an underwater shock wave reaches the water surface, rarefaction occurs and the water pressure drops. This results in a near surface target experiencing a lower impulse loading than a submerged target [5]. Additionally, the hydrostatic pressure of the water increases with water depth. Even without the detonation of an explosive charge, the deepest point of the panel experiences 9.5 kPa greater pressure than the point at the water surface. The detonation of a charge in this body of water, and hence the introduction of a high pressure wave, is likely to increase

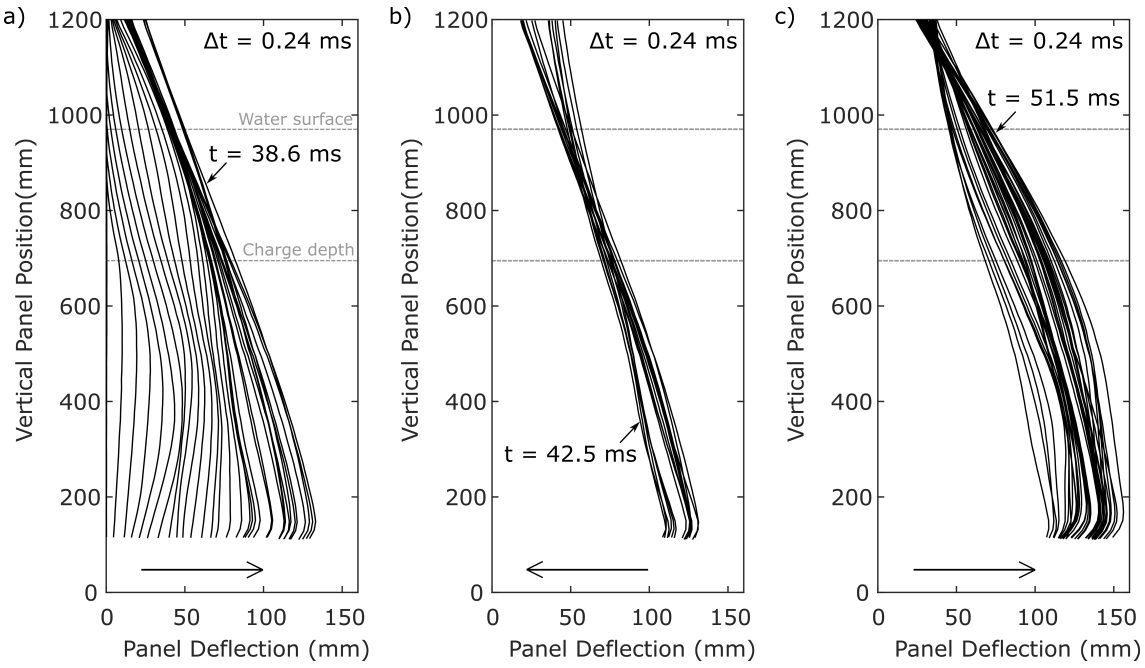


Figure 6.8: DIC results for the vertical centre cross-section showing: (a) deflection at intervals of time, (b) short rebound and (c) second deflection.

this pressure difference. Lastly, the water at the base of the enclosure is confined and is unable to vent away unlike at the surface. All of these effects will result in a variation of loading with panel depth.

Figure 6.8 shows the deflection of the vertical cross-section at the centre of the panel at intervals of time. This cross-section clearly illustrates the greater deflection of the lower portion of the panel. The deflection of the lowest 150 mm of the panel was not captured as the deformation profile of the panel obstructed this area from the cameras' line of sight. From Figure 6.8 (a), the deflection curves show that the panel beneath the surface of the water experiences deflection before the panel above the water surface responds. Figures 6.8 (b) and (c) show that the deformation profile of the panel becomes more curved with increasing time up to its maximum deflection at 51.5 ms.

Figure 6.9 shows the deflection of the horizontal cross-section at the centre of the panel at intervals of time. In Figure 6.9 (a) the panel initially responds by adopting a parabolic deflection profile before the deflection changes to a typically observed 'bathtub' profile. The sharp gradient discontinuities at approximately 200 mm and 900 mm across the panel width illustrate that damage to the foam core and composite laminate skins has occurred at these locations. The panel retains this deflection shape during rebound in Figure 6.9 (b), indicating that the panel

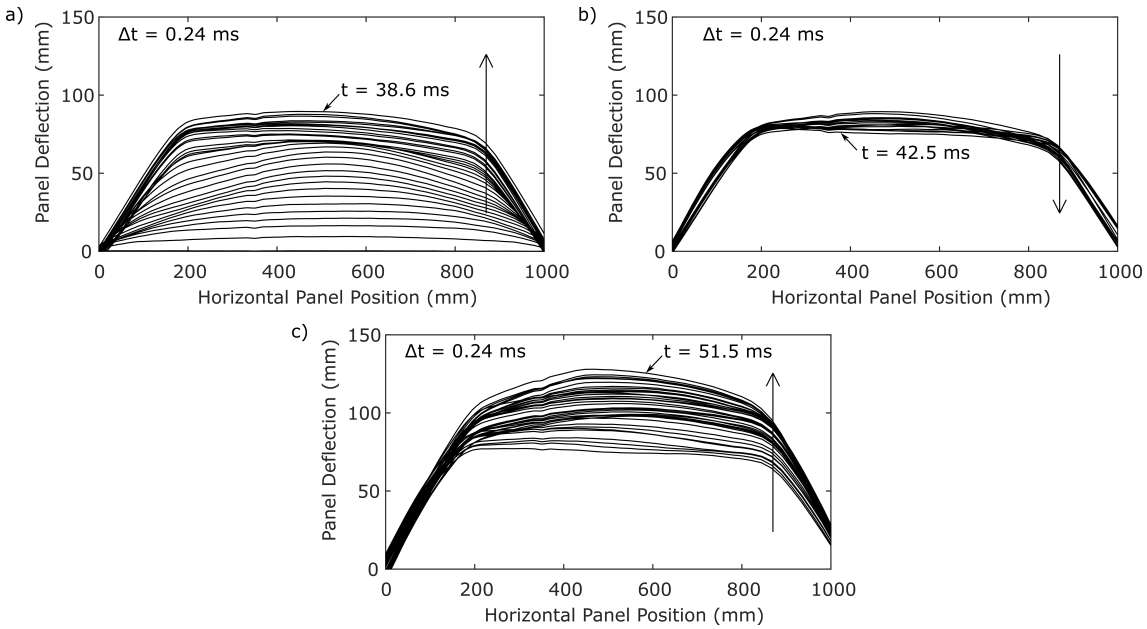


Figure 6.9: DIC results for the horizontal centre cross-section showing: (a) deflection at intervals of time, (b) short rebound and (c) second deflection.

is permanently damaged at these locations. Figure 6.9 (c) shows the second panel deflection between 42.74 ms and its maximum at 51.5 ms. The steep deflection profile at the panel edges and sharp gradient discontinuities at around 200 mm and 900 mm across the panel width result in areas of high major strain as shown in Figure 6.7.

6.3.1.2 Central Point Displacement

Figure 6.10 shows a displacement versus time plot for the central point. The three phases of movement can be clearly seen. These phases have been labelled to correspond with the other DIC data shown in Figures 6.7 to 6.9. There is an initial deflection to 90.4 mm, followed by a small rebound to 75.6 mm. The panel then continues to deflect and remains permanently deformed to around 125 mm. The initial panel deflection is caused by the underwater blast wave, whilst the second panel deflection is most likely caused by pulsation of the underwater gas bubble. Shockwave reflections off the pendine blocks could also contribute to this second panel deflection. Beyond 51 ms after detonation the data becomes significantly noisy. This is due to vibrations from the ground caused by the charge and subsequent movement of the cubicle and pendine blocks. This affects the cameras and causes them to move relative to their initial positions. Figure 6.10 also shows the velocity of the

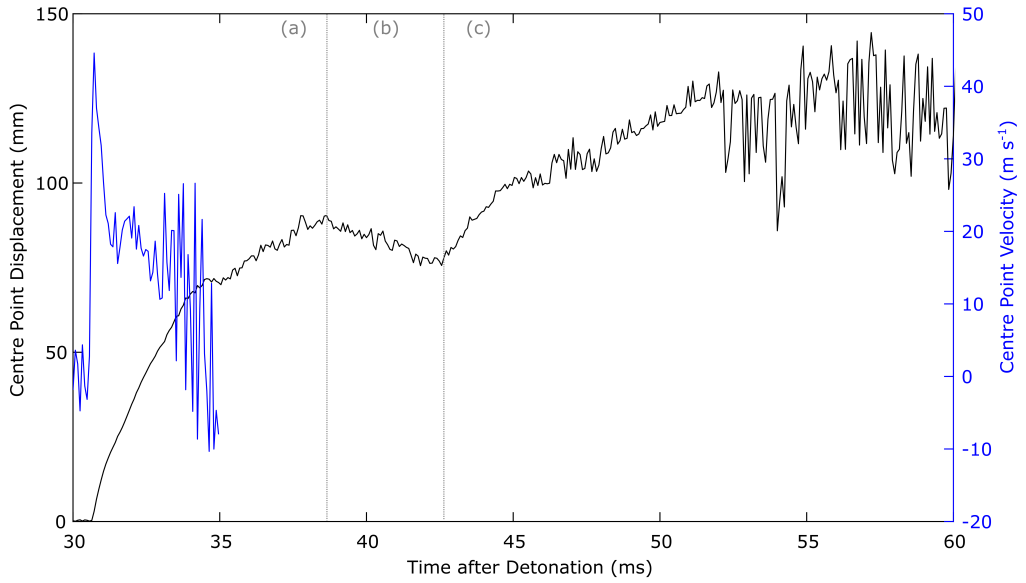


Figure 6.10: Central out-of-plane displacement against time for Hybrid-4(2) during underwater blast loading along with calculated initial central point velocity against time.

centre point between 30 ms and 35 ms after charge detonation. After 35 ms the noise in the displacement trace results in significant noise in the calculated centre point velocity. Despite this, the peak velocity of the panel is captured at 30.7 ms and is 44.6 m s^{-1}. This is a similar peak velocity to those reached during air blast loading under 100 kg nitromethane at 15 m stand-off and 30 kg PE7 at 10.5 m.

6.3.2 Strain Gauges & PVDF Pressure Gauges

Due to an unidentifiable issue, the oscilloscope failed to trigger and record strain gauge or PVDF pressure gauge data during the experimental trial. Since no pressure data was recorded, Equation 6.3 was used to determine the time at which the underwater shock wave would reach the panel front using the pressure prediction from Section 6.2.2. This was carried out to verify whether the DIC time signatures were correct. In Equation 6.3, u is the particle velocity in the water, ρ_w is water density which is assumed to be 997 kg m^{-3} and c_w is the speed of sound in water which is approximately 1400 m s^{-1}. By dividing the known distance between the charge and panel front by the water particle velocity calculated using this equation, the underwater shockwave is expected to reach the panel front 26.5 ms after detonation. This assumes exact positioning of the charge and ideal conditions. According

to DIC data, the panel begins to deflect 30.4 ms after detonation. This correlates well with the pressure prediction, as conditions were not ideal and the panel will require time to respond. Since no pressure data was recorded it was not possible to calculate the underwater blast impulse as the decay rate was unknown.

$$u = \frac{P(t)}{\rho_w c_w} \tag{6.3}$$

6.3.3 Comparison of Air and Underwater Blast

The hybrid composite sandwich structure provided significant resistance to blast loading both in air and underwater. Hybrid-4(1) sustained a peak pressure of 310.4 kPa during air blast loading without resulting in catastrophic failure, as detailed in Chapter 5. During the underwater blast experiment, Hybrid-4(2) was subjected to a peak pressure of around 50 MPa. This pressure is over one hundred and fifty times greater than the peak pressure experienced by the same panel during the air blast experiment. The Hopkinson-Cranz scaled distance for the underwater blast was 0.91, whereas for the 8 kg PE4 charge at 8 m stand-off air blast the scaled distance was 2.99. The reduced stand-off distance during this underwater blast already significantly increases the severity of the load conditions before fluid medium is even considered. The time period of an underwater pressure impulse is far shorter than the time period of an air blast impulse giving the panel less time to respond. This is a result of the increased density of the fluid medium in which the blast is occuring. The speed of the blast wave is not only dependent on the ambient pressure and static overpressure but also on the change in density in front of and behind the wave front in a compressible fluid [113]. The wave front velocity is expected to be twice as great during underwater blast compared to air blast. The underwater blast wave acts like a hammer due to its large stress magnitude and high velocity. This causes the through-thickness stresses to rise leading to different mechanisms of failure and deformation compared to air blast loading. The reduced reaction time available also means the panel can not activate flexural response. During underwater blast, the rear skin experienced peak strains of 6.36 %. This leads to visible fibre breakage on the rear skin. Fibre breakage on the front skin also occurs. In air blast loading, the peak rear skin strain was recorded as 0.78 %. In this loading regime, core shear failure occurred along with front skin failure, however, the back skin of the panel remained intact.

6.4 Post Blast Damage & Compression

6.4.1 Methods

6.4.1.1 Damage Analysis

Hybrid-4(2) was cut into eight sections following underwater blast testing and all edges were photographed. The core cracks, debonding and delaminations were identified and recorded using the same MATLAB script as detailed previously. Following this, eight 300 mm × 200 mm sections were removed from the panel for edgewise compression testing. These compression specimen were taken from various locations across the panel and had sustained varying amounts of damage during the blast test.

6.4.1.2 Edgewise Compression Testing

The same edgewise compression method as detailed in Chapter 5 was adopted. The 300 mm × 200 mm specimen were tested under quasi-static compression loading to simulate the structural loads caused by the weight of the vessel. Testing was performed using an Instron 5985 universal testing machine. A Nikon D7100 DSLR camera was used to capture one photograph every second to measure the strain using 2D DIC. A speckle pattern was painted along one edge of each specimen to facilitate DIC. To ensure even loading, 10 mm thick rubber spacers were placed between the machine plattens and the steel plates. 2D DIC was adopted due to potential slipping at the plattens resulting in inaccurate machine displacement readings. As detailed in Chapter 5, an effective edgewise stiffness was calculated from the in-plane engineering stress and average strain. The in-plane engineering stress in the skins was calculated as negligible stress would be present in the foam core compared to in the skins.

6.4.2 Results

6.4.2.1 Damage Analysis

Figure 6.11 shows the front view of Hybrid-4(2) following sectioning, the red dashed boxes highlight the sections subjected to edgewise compression testing. The panel suffers from a number of skin breakages and cracks initiating from the bolt holes. Tearing through both skins and the foam core has occurred at all four of the bottom bolt holes. There are regions of front skin delamination across the panel. Unlike the air blast results, the DIC deflection contour images do not highlight the locations

Table 6.2: Damage sustained by Hybrid-4(2) following underwater blast testing identified using visual inspection.

Panel type	No. of core cracks	Length of core cracks (mm)	No. of core/front skin debonds	Length of front debonds (mm)	No. of core/rear skin debonds	Length of rear debonds (mm)	Length of front skin cracks (mm)
Hybrid-4(2)	19	808	17	2163	13	555	2993

of severe front skin cracks. This is caused by the significant panel deflection which masks the deflection peaks in localised regions. The DIC contour images, however, do highlight the areas of debonding and core shear cracking one-quarter and three-quarters across the width direction. Sharp changes in deflection gradient and high areas of strain are visible in these regions. Figure 6.12 (a) shows the cross-sections of Hybrid-4(2) as viewed from the bottom of the panel. The permanent dishing of the panel is visible along with extensive core shear cracking and debonding between the skins and core. It is evident that the near-field underwater blast has resulted in far more severe panel damage compared to far-field air blast loading. Figure 6.12 (b) highlights a cross-section at the mid-plane where a shear core crack is visible approximately 150 mm in from the panel edge along with debonding. The core shear crack is at approximately 45° to the through thickness direction. Front skin debonding propagates towards the panel centre and rear skin debonding towards the panel edge as observed previously. The dished shape of this section can also be clearly seen. Table 6.2 details the visual damage assessment based on these photographs.

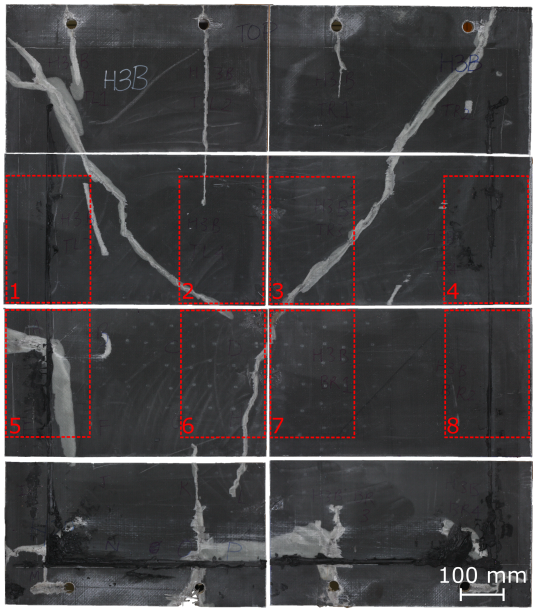


Figure 6.11: Photographs showing the front skin following underwater blast of Hybrid-4(2). The red dashed boxes highlight the sections removed for edgewise compression testing.

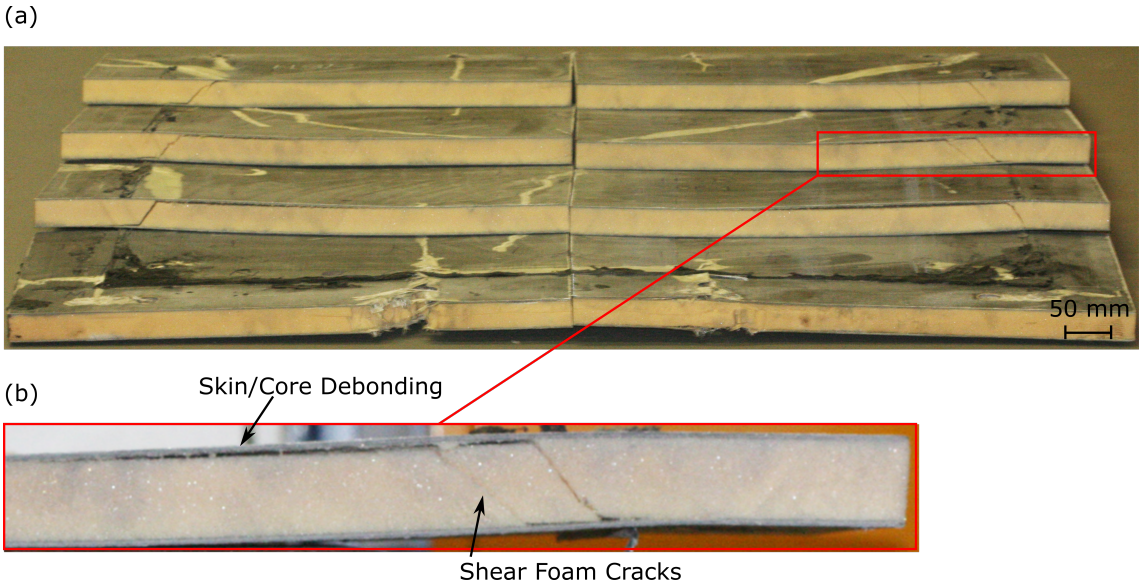


Figure 6.12: Photographs showing the damage to the core and skins of Hybrid-4(2) following underwater blast.

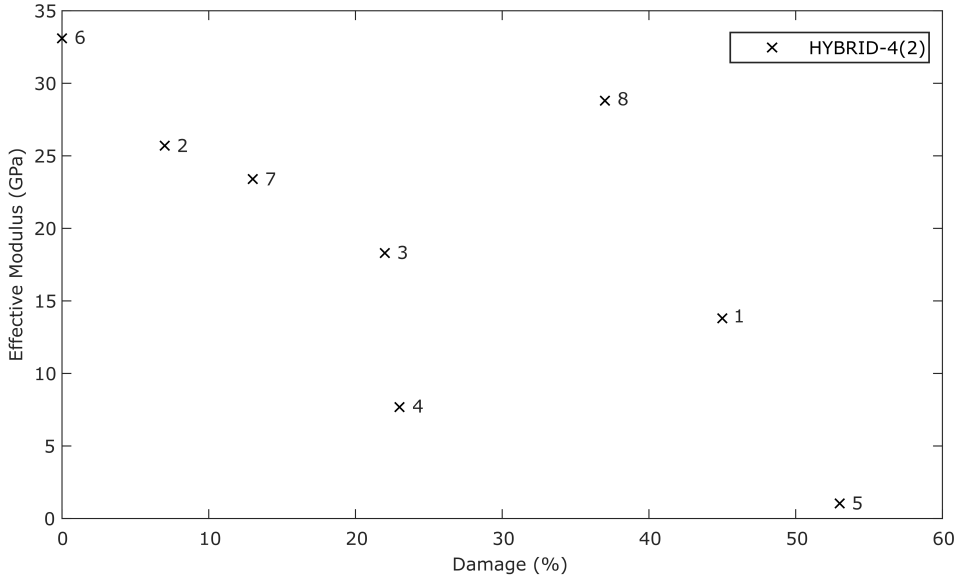


Figure 6.13: Post-blast effective modulus versus damage percentage for the eight specimen taken from Hybrid-4(2).

6.4.2.2 Post-Blast Compression

The edges and front of each 300 mm × 200 mm specimen were photographed before compression testing. This was carried out to record the visual damage to the specimen using the same method and MATLAB script as for the larger panel sections. A damage percentage was then calculated for each specimen which took front skin breakage, skin/core debonding and core shear cracks equally into account. Figure 6.13 shows damage percentage versus effective compressive modulus for Hybrid-4(2) following underwater blast loading. As damage increases, the effective modulus decreases. The graph highlights two outliers. The specimen with 23 % damage and modulus of 7.7 GPa sustained a small amount of all damage types. The low compressive modulus of this specimen could be caused by the interaction of the different damage types. The specimen with modulus 28.8 GPa and 37 % damage was one of two specimen with no front skin breakage, the other specimen demonstrated the highest effective modulus and 0 % damage. This indicates that retaining an intact front skin is advantageous following an underwater blast load.

Figure 6.14 plots maximum compressive stress against damage percentage. There is a trend between increasing damage and decreasing maximum compressive stress. The presence and interaction of different damage types results in four specimen lying above or below the general trend line. However, since the damage types were not

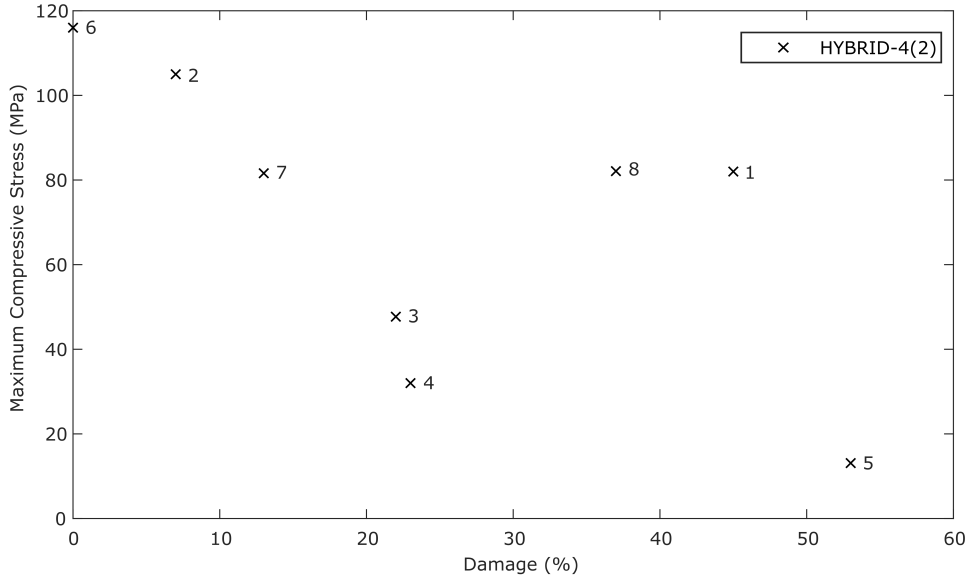


Figure 6.14: Post-blast maximum compressive stress versus damage percentage for the eight specimen taken from Hybrid-4(2).

isolated in these specimen and since the damage inspection is only visual, it is not possible to determine which damage mechanism is most detrimental to post-blast compressive strength.

6.4.2.2.1 Comparison of Air and Underwater Blast

The post-blast compressive performance of Hybrid-4(1) and Hybrid-4(2) can be compared, taking differing damage levels into account, to reveal some differences between air and underwater blast loading. Figure 6.15 shows effective compressive modulus versus damage percentage for the two Hybrid-4 panels. The figure shows that the underwater blast causes greater panel damage ranging between 0 % and 53 % whereas the two 8 kg PE7 air blast loads cause damage between 0 % and 21 % only. This is due to the more severe regime that is created with the presence of water and reduced stand-off to the charge. The only significant difference between Hybrid-4(1) and Hybrid-4(2) occurs for the undamaged specimen. The two undamaged specimen with moduli values around 34 GPa are achieving modulus values comparable to those of damaged specimen. It could be possible that damage in these specimen is present but has not been identified visually. There is a significant drop in effective compressive modulus between specimen with zero damage, the

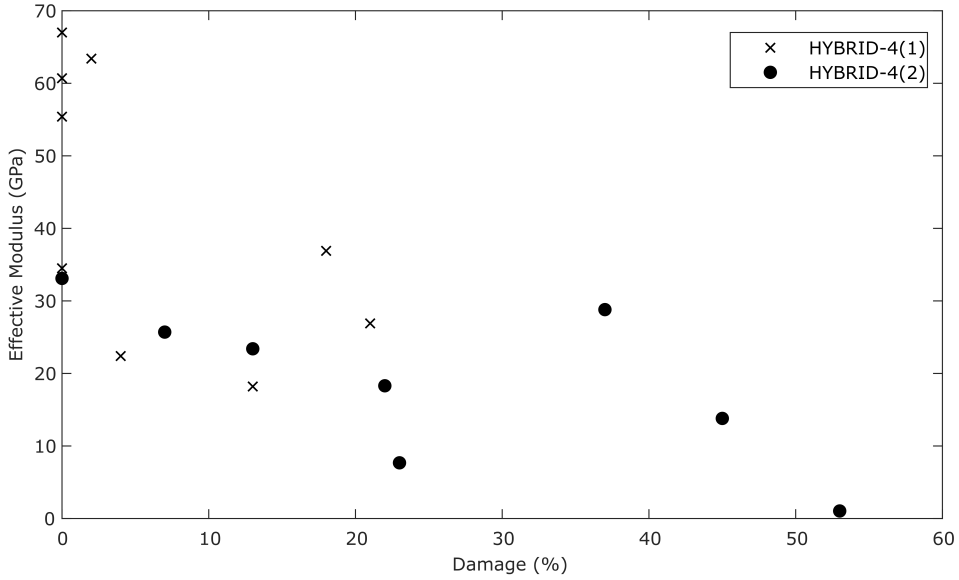


Figure 6.15: Post-blast effective modulus versus damage percentage for the specimen taken from Hybrid-4(1) and Hybrid-4(2).

Hybrid-4(1) specimen exceeding modulus of 55 GPa, and those with damage. This is a disadvantage for Hybrid-4.

Figure 6.16 shows a plot of maximum compressive stress versus damage percentage. The air blast and underwater blast panels show consistent post-blast behaviour. The specimen maximum compressive stress decreases as damage percentage increases with no clear significant drop following the onset of damage. As detailed before, the underwater blast creates a more severe loading regime which results in greater damage. This leads to a significant reduction in post-blast compressive strength for the most damaged Hybrid-4(2) specimen compared to the least damaged specimen. Post-blast testing revealed that sustaining no front skin breakage was advantageous for retaining a high proportion of the compressive modulus for Hybrid-4(2) following underwater blast. This is in direct contrast to the post-blast assessment results for Hybrid-4(1) following air blast. During air blast loading, Hybrid-4(1) suffered from a significant front skin and core crack yet these specimen demonstrated high post-blast compressive performance. The Hybrid-4(1) specimen which suffered from a front skin and core crack did not sustain other damage, therefore, the overall integrity of the specimen was controlled. Conversely, the Hybrid-4(2) underwater blast panels with front skin cracking also suffer from delamination and debonding. Therefore, the front skin damage interacts with other mechanisms

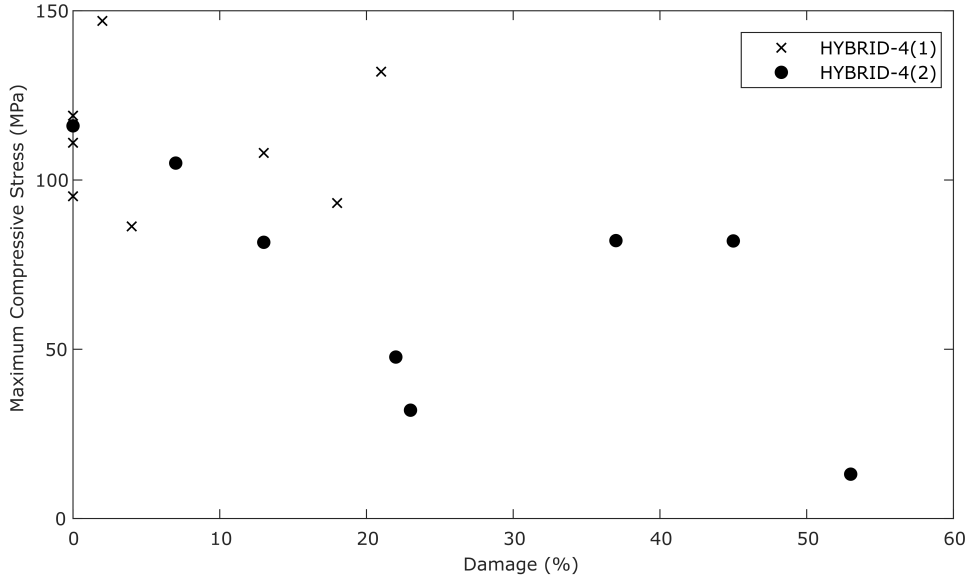


Figure 6.16: Post-blast maximum compressive stress versus damage percentage for the specimen taken from Hybrid-4(1) and Hybrid-4(2).

and reduces the strength of the specimen. Avoiding front skin damage in Hybrid-4(2) specimen would prevent these interactions and would, therefore, be beneficial. Whereas front skin damage in Hybrid-4(1) specimen were not able to interact with other damage types.

6.5 Discussion

6.5.1 Experimental Design

This investigation was carried out to develop a preliminary underwater blast setup with implementation of DIC to record full-field panel response. In general, the trial proved a success as full-field DIC was successfully captured. The trial highlighted areas of improvement for future testing. Initial observations of the DIC data shows that the cameras successfully captured the response of a large area of the panel. The camera frame rate, which was 12,500 fps, was sufficient to capture the panel response during underwater blast. However, the bottom-most section of the panel was not captured as it was not in the line of sight of the cameras. Mounting the cameras vertically, as in Chapters 4 and 5, would not alleviate this issue as the lower section of the panel would be hidden from the top-most camera. A potential

solution would be to mount the cameras horizontally but positioned closer to the ground and angled upwards.

A large amount of slip occured at the vertical edges where the panel was only clamped. The use of bolts around the whole panel perimeter would be recommended. Additionally, a fully submerged panel should ideally be tested. This could be achieved by reducing the panel size or increasing the pondliner size. A number of pendine blocks were damaged by the force of the charge. A layer of structural foam, or other energy absorbing material, between the epalyn rubber and pendine blocks would be recommended to prevent damage in future experiments. Alternatively, a reduction in the charge size would prevent damage to the blocks. Finally, the cause for the trigger failure of the strain gauges and pressure gauges should be identified. The successful use of PVDF gauges at different depths would reveal the pressure variation and would aid in the explanation of the displacement and damage profiles.

6.5.2 Digital Image Correlation

Only one composite sandwich panel was subjected to underwater blast testing due to time and experimental constraints. This data set is too small to definitively quantify the underwater blast behaviour of hybrid composite sandwich panels. Nevertheless, the results provide an insight into key observations. DIC enabled full-field rear skin deflection and strain tracking. RBMC was implemented to remove the movement of the cubicle and fixing system and to isolate the panel response relative to its boundaries. The DIC results showed a small pulsation in panel deflection and strain during blast. The panel centre point was shown to deflect to 90.4 mm then rebound slightly to 75.6 mm before deflecting again to approximately 125 mm. This pulsation is likely to be caused by underwater bubble formation, a typical phenomenon for underwater explosions. However, due to the failure of the pressure gauges it is not possible to determine this for certain.

The strain contour maps and deflection cross-sections highlighted that the horizontal cross-section of the panel deforms in a parabolic shape until excessive deflection causes core shear cracking. The panel then forms the commonly observed 'bath tub' deformation shape. These areas of core cracking and core/skin debonding are regions of weakness for the panel. These damaged areas could be lessened if the mounting structure was able to undergo deflection to some extent. Once again, these results reinforce the importance of support structure design on overall blast resilience. Unlike the air blast experiments, the horizontal cross-sectional DIC does not capture regions of high deflection caused by front skin cracks. This is due to

the localised regions of high deflection being masked by the large deflection of the whole panel. Finally, the DIC results capture the response of the panel vertical cross-section. The panel section 300 mm beneath the charge experiences deflection first. At this time, the upper and lower edges of the panel experience little displacement. Following this, the deflection profile becomes parabolic as the entire panel length experiences deflection. The greatest point of deflection remains around 300 mm beneath the charge. Due to the presence of water more severely loading the lower portion of the panel, severe damage occurs approximately 600 mm beneath the charge depth. This weak point then experiences the greatest out-of-plane displacement.

Full-field DIC has revealed that water depth significantly influences panel deflection, strain and hence damage sustained. The results have shown that it is incorrect to assume a symmetric response around the panel mid-plane for a large scale panel near the water surface.

6.5.3 Post Blast Damage & Compression

Post-blast visual inspection revealed significant panel damage. Front skin cracks, regions of debonding and through thickness tearing were identified. The panel remained permanently deformed and shear core cracks, 150 mm in from both edges running the entire panel length were observed. As expected, significantly more damage occurred as a result of underwater blast testing compared to air blast testing. This is due to the increased severity of underwater blast loading compared to air. The increased density and compressibility of the fluid medium gives the panel less time to respond and increases the blast wave pressure. Post-blast testing revealed that sustaining no front skin breakage was advantageous for retaining a high proportion of the compressive modulus for Hybrid-4(2) following underwater blast. This is contradictory to the results found for post air blast performance of Hybrid-4(1). However, the front skin and core crack in Hybrid-4(1) was an isolated damage type, whereas Hybrid-4(2) specimen suffer from front skin and core cracking along with delamination and debonding. The lack of front skin breakage in Hybrid-4(2) prevents damage interactions and is beneficial. Whereas the presence of only front skin breakage in Hybrid-4(1) was not detrimental. Clear trends were observed for increasing damage and both decreasing compressive modulus and decreasing compressive strength. Furthermore, the post-blast air and underwater compressive strength and moduli from Hybrid-4(1) and Hybrid-4(2) were consistent. Since the damage types were not isolated, it was not possible to determine which

damage mechanism is most detrimental to post-blast panel performance. Following underwater blast loading, the compressive strength and modulus of certain panel sections fell to 13.1 MPa and 1.04 GPa, respectively. Immediate repair following an underwater blast of this nature is recommended, even if damage is not visible, unless the structural requirements on the panel do not exceed these values.

6.6 Conclusion

This experiment was conducted to demonstrate whether DIC could be successfully implemented during underwater blast testing. Furthermore, the experiment was performed to determine whether a hybrid composite sandwich panel could resist an underwater blast load. DIC data was successfully generated and the full-field response reveals more detailed results compared to previous underwater blast experiments. The pulsation of the panel, the asymmetry of the panel deflection profiles and the change in deflection profile with time have been captured for the first time using DIC. The panel response was found to significantly differ from the behaviour of such panels under air blast. Due to the change in fluid medium and reduced stand-off distance, the strain and deflection reached by the panel during underwater blast far exceeds that reached during air blast. This also results in far more significant damage. Overall, the panel showed good blast resilience considering it withstood a pressure loading of around 50 MPa and water did not breach the panel. Despite the failure of pressure and strain gauges, the high speed cameras recorded informative DIC data and improvements for future experiments have been identified. Furthermore, it was demonstrated that an instrumented underwater blast test can be conducted at a test range without the requirement for a specialist underwater test facility.

Chapter 7

Conclusions

This research aimed to improve the understanding of the role that hybrid composite skins can play in the blast resilience of composite sandwich panels. The composite sandwich panels studied would be suitable for use in naval vessels. Naval vessels are expected to withstand blast loading from sea mines that are detonated by proximity methods, along with other challenging loads. Therefore, the main deliverable of this research was to perform full scale blast loading on composite sandwich panels to simulate the air and underwater blast loads that could result from mine detonation.

A number of hybrid composite sandwich panels were assessed using analytical calculations and high velocity impact loading. This was performed to determine which composite sandwich panels would be most suitable for full scale blast testing, as blast testing opportunities were limited. A total of 11 composite sandwich panels were subjected to full scale air blast loading. The blast experiments were performed at RAF Spadeadam and Radnor Range. The blast experiments primarily compared the performance of different hybrid composite sandwich panels. Benchmark panels with solely GFRP or CFRP skins were also subjected to blast loads where possible. The effect of hybrid laminate layup, with constant areal density, was investigated. Asymmetrical layups were tested to determine the benefits of asymmetry with known loading direction. In another trial, the areal density was varied by adjusting proportions of glass-fibre and carbon-fibre within the hybrids. The presence and interactions of the different fibrous layers results in variations of energy absorption. The performance of hybrid composite sandwich panels under both single shot and repeat blast loads was investigated. A consistent foam core was adopted in the composite sandwich panels throughout the experimental trials.

Following blast testing, post-blast damage analysis and compression testing was performed. This was carried out to determine the residual properties of the compos-

ite sandwich structures for continued service in naval vessels. X-ray CT scans were performed on selected samples to compare the failure mechanisms and interactions of fibrous materials.

Finally, one large-scale underwater blast experiment was performed. This experiment demonstrated that DIC could be implemented during an underwater blast experiment. The DIC data captured the full-field deflection and strain response of a panel during underwater blast loading illustrating the influence of water depth.

7.1 Preliminary Analysis of Hybrid Composites

An analytical method for calculating composite laminate properties was outlined and performed. Engineering constants for 13 different laminates were calculated using the laminate stiffness method. The number of carbon-fibre plies has a clear effect on the laminate moduli. As the number of carbon-fibre plies increases, the in-plane and transverse moduli increase. As expected, the addition of [0/90] layers increases the in-plane and transverse moduli more than the addition of [+45/-45] layers. It is widely reported in literature that placing the highest energy absorbing fibre type as the outermost layer on a laminate or sandwich panel skin is advantageous for impact performance. Analytical panel calculations were then carried out for seven different composite sandwich panel variations with glass-fibre as the outermost layer. This included symmetric and asymmetric panel layups. The hybrid panel stiffnesses were found to lie between the benchmark GFRP and CFRP panels, as expected. The stiffness matrices revealed differences between the hybrid panels along with stretching/bending coupling for the asymmetric panels. The analytical calculations revealed that certain hybrid layups with equal proportions of glass-fibre and carbon-fibre could reach moduli values of up to 80 % of a carbon-fibre laminate. Impact and blast loading does not result in solely in-plane loading, therefore, simply including more carbon-fibre plies will not necessarily improve impact or blast performance. However, the increased modulus, coupled with energy absorbing failure mechanisms from layer interactions, illustrates the potential for blast and impact resilient hybrid composite sandwich panels.

Following analytical calculations, four hybrid composite sandwich panels, along with benchmark GFRP and CFRP sandwich panels, were subjected to high velocity impact testing. All panels had an identical 20 mm PET foam core. The impact experiments aimed to reveal the relative high strain rate performance of the hybrid composite panels selected and the damage sustained under impact. These experi-

ments were carried out to aid with material selection for large scale blast testing. A gas gun apparatus was used to perform the impact experiments. The composite sandwich panels were subjected to projectiles at two velocities of 75 ± 3 m s^{-1} and 90 ± 3 m s^{-1}. These velocities were selected as this would lead to a 30 % increase in projectile kinetic energy between the lower and higher velocity. Furthermore, 90 m s^{-1} impact was shown to be on the threshold of causing rear skin damage in the CFRP panel. A further increase in projectile velocity would result in damage to the speckle pattern preventing DIC analysis.

The DIC results revealed that the deflection, strain and damage response of the hybrid composite sandwich panels lies between those of the benchmark GFRP and CFRP panels as expected. The asymmetrical layup of Hybrid-1A resulted in improved impact resilience and asymmetry did not result in any observable detrimental effects. The results showed that the symmetric skin configuration of Hybrid-1B offers no advantages if loading direction is known. The CFRP panels experienced among the lowest deflection and strain. However, due to the brittle behaviour of the carbon-fibres, the CFRP panels suffer from the most extensive damage. The results show that GFRP skins have a superior impact resistance when areal density is constant. Under impact loading lower panel stiffness led to greater deflection but lower impact damage. Furthermore, the greater strain to failure of the glass-fibres allows the panel to absorb and redistribute impact energy. However, blast loading results in a more global panel response. During previous blast testing, the lower stiffness and strength of GFRP panels has led to greater damage and reduced post-blast performance. Post-impact testing demonstrated that a combination of dissimilar glass-fibre and carbon-fibres does not increase the likelihood of post-impact delamination propagation under edgewise compression. The compression results revealed that a less intricate hybridisation may be beneficial. For Hybrid-1A, a large cross-section of carbon-fibre remained intact at the rear of the panel. This significantly contributes to the high post-impact panel stiffness. Hybrid-1A and Hybrid-2 were selected for large scale air blast experiments. These two hybrid types would reveal the effects of a symmetric versus asymmetric layup, of hybridisation intricacy and of distance of carbon-fibre plies from the neutral axis.

7.2 Full Scale Air Blast Testing

Quantitative comparisons between the air blast response of four types of hybrid composite sandwich panels, along with GFRP and CFRP composite sandwich pan-

els, were performed. Full field 3D DIC data was captured using pairs of high-speed cameras. A 30 mm PVC foam core with density 100 kg m^{-3} was adopted for the majority of the panels to maintain consistency. Two panels had a 130 kg m^{-3} PVC foam core. A number of air blast tests were performed to capture the performance of the hybrid composite sandwich panels under various conditions.

When subjected to a 100 kg nitromethane charge at 15 m stand-off distance, the maximum displacement of Hybrid-1A and Hybrid-2 was 74.6 mm and 72.8 mm, respectively. The repeat samples demonstrated agreement within 1.8 mm, confirming that the large scale test method is reliable to within 2.5 %. The centre-point deflection, full field deflection and strain response of the hybrid panels showed little difference. Damage locations were dictated by the panel support conditions and blast wave clearing along the cubicle outer edge. The front skin strain data captured on Hybrid-1A(1) and Hybrid-2(1) was similar. High strain magnitudes were recorded on the outer panel edges. Although the magnitude differed, the front skin strain gauge data and rear skin DIC strain data showed a temporal and spatial agreement. The only difference identified between the two panels was the more widespread deflection experienced by Hybrid-2. This was a result of its reduced stiffness. The increased global deflection led to greater damage. Hybrid-1A(1) suffered from 8 core cracks and 1 debond whilst Hybrid-2(1) suffered from 12 core cracks and 1 larger debond. Despite adopting different skin layups, there was no significant difference in skin damage observed between the two panel types following blast. Furthermore, both panel types withstood a significant blast load with minimal damage overall. This demonstrates the high blast resilience of hybrid composite sandwich panels. Under small scale impact, these two hybrids exhibited more significant differences. This is due to the localised load experienced under impact. The front skin, core and rear skin are sequentially loaded preventing a global bending response. During large scale air blast, the panel size was far greater and the pressure load was more uniform. The blast panels respond globally making use of their inherent bending stiffness. During air blast loading, low panel stiffness was found to result in greater deflection and this led to greater damage. This is opposite to what was observed during impact loading. In comparison to previous blast testing, performance indices demonstrated that the hybrid panels were advantageous. However, a direct comparison between a hybrid and a GFRP or CFRP panel was deemed necessary.

A direct comparison between GFRP(1), CFRP(1) and Hybrid-3B(1) under 30 kg PE7 at 10.5 m stand-off distance was then performed. During this experiment, PVDF film pressure sensors were implemented to record the pressure experienced

during blast at the centre of the sandwich panels. Pendine concrete blocks and a roof extension were positioned to reduce blast wave clearing compared to the previous experiment.

The centre point deflection and strain of Hybrid-3B(1) lay between that of CFRP(1) and GFRP(1), which was expected based on the panel bending stiffnesses. The return time periods for CFRP(1) and Hybrid-3B(1) were greater than expected due to damage suffered by the panels. Post-blast damage assessment, however, identified that all three panels suffered from a similar extent of damage. GFRP(1) suffered from greater front skin/core debonding. Considering Hybrid-3B(1) underwent a greater impulse, the panel only sustained comparable levels of damage demonstrating the high blast resilience of its hybrid skin. The work done calculation reveals that CFRP(1) underwent more widespread deflection whilst the deflection of GFRP(1) is more localised. Two GFRP(1) compression specimen were observed to have no visual damage. This indicates that the more localised deflection of this panel also leads to localised regions of damage. The deflection and damage within CFRP(1) and Hybrid-3B(1) is more widespread. The x-ray CT scan of Hybrid-3B(1) indicates that this widespread damage absorbs blast energy by preventing direct through thickness cracks. By redirecting the crack through delamination, debonding and fibre breakage, energy is absorbed by the hybrid skin. The compressive strength of Hybrid-3B(1), CFRP(1) and GFRP(1) was found to be similar. The energy absorbing damage mechanisms in the Hybrid-3B skin do not have a detrimental affect on the post blast compressive strength.

Lastly, two hybrid composite sandwich panels were subjected to repeat loads of 8 kg PE7 at 8 m stand-off distance. A GFRP and CFRP panel were also subjected to repeat loading. However, due to a difference in size, a direct comparison between all four panels was not possible. The greater stiffness of Hybrid-3B(2) resulted in reduced deflection and subsequently reduced panel damage compared to Hybrid-4(1). For both panels, damage that was initiated by an initial blast was exacerbated by the second blast. Although Hybrid-4(1) was shown to have a higher post-blast compressive modulus, due to the greater proportion of glass-fibre and less intricate hybridisation, the panel suffered from a severe front skin crack. This is undesirable for marine applications due to presence of water. The post-blast compressive strength for Hybrid-3B(2) and Hybrid-4(1), however, are similar. Overall, the air blast experiments demonstrate that hybrid skins constructed from 50 % glass-fibre and 50 % carbon-fibre by volume achieve good blast resilience. These 50:50 hybrid skins achieve the necessary strength and stiffness to permit reasonable deflection

whilst minimising core and skin damage. Variations in the layup of 50:50 hybrid skins result in slight variations in panel performance, as shown in Chapter 4. These variations are caused by changes in bending stiffness and material interactions from the skin layup. However, under blast loading the presence of both fibre types dominates the panel response rather than the position of each fabric layer.

The sequence of damage types that occur during air blast testing of composite sandwich panels was identified. Their typical locations, angles and direction of propagation were determined. In addition, it was established that skin delamination and fibre breakage are key energy absorbing mechanisms in the hybrid skins. Any numerical models seeking to reproduce the air blast loading of hybrid composite sandwich panels beyond their elastic limit should include all these damage mechanisms. The post-blast damage analysis performed in this research can be used to determine whether numerical models have accurately captured panel damage. Furthermore, although the damage characteristics are dictated by the support structure and boundary conditions, numerical models that accurately recreate the location and extent of damage under identical boundary conditions can be extended to other boundary conditions with confidence. These experiments were performed to investigate the blast performance of the panels alone. However, it is well known that the blast resilience of an entire structure can be improved by allowing a permissible level of support structure deflection.

7.3 Full Scale Underwater Blast Testing

A preliminary underwater blast experiment implementing full field 3D DIC was developed and performed. Previous underwater blast testing has relied on the interpretation of strain gauge data at discrete locations. Although only one experiment was performed in this investigation, the full-field results generated will aid in determining whether previous strain interpretations are logical. Furthermore, the experiment was performed to assess the performance of a hybrid composite sandwich panel during underwater blast loading.

One hybrid composite sandwich panel was subjected to 1 kg PE7 charge at 1 m stand-off distance. The panel was partially submerged and the charge was lowered in the water to the panel centre-point. Although strain gauges and PVDF pressure gauges were setup, the instrumentation failed to trigger. It is recommended that the cause of this failure is identified and rectified for future underwater blast testing. The high-speed cameras successfully triggered and recorded the panel response at

12,500 fps. Due to the severe loading imparted by the underwater blast wave, significant panel deflection occurred along with slip at the boundaries. The panel deflection obscured sections of the panel itself from the cameras. The bottom-most section of the panel was not captured in the high-speed camera images. The camera mounting position could be altered in future experiments to overcome this issue. The slip at the panel edges could be alleviated by using bolts around the whole panel perimeter. Alternatively, a smaller charge could be used. This would reduce the boundary slip, panel deflection and damage to the concrete pendine blocks that occured. Even with a smaller charge size, a significant blast pressure would be generated that would cause panel loading and damage. The final improvement to the experimental setup would be to investigate a fully submerged panel. The panel was intended to be fully submerged, however, the pondliner did not have a sufficient border. A fully submerged panel could be achieved by either increasing the size of the pondliner or decreasing the size of the panel.

The DIC results demonstrated that the panel underwent a small pulsation before reaching maximum displacement. Due to the failure of the pressure gauges, it is not possible to tell what caused this pulsation. It is likely, however, that this was caused by the formation of an underwater bubble which is a typical phenomenon for underwater explosion. The DIC data revealed that across its horizontal cross-section, the panel deforms in a parabolic shape. Shear cracking towards the boundaries results in the panel adopting the commonly observed 'bath tub' deformation shape. The vertical cross-section also experiences a transition in deflection profile. Initially, a section 300 mm beneath the charge experiences deflection. The profile then becomes parabolic as the deflection extends towards the boundaries. The greatest point of deflection then shifts down to 600 mm beneath the charge. This area has clearly suffered from a core shear crack and panel damage resulting in a weak point. The full-field DIC results revealed that a symmetric deflection and strain response during underwater blast can not be assumed for a panel of this size. During underwater blast, the panel response was found to significantly differ from panel response during air blast. The strain and deflection reached by the panel during underwater blast exceeds that reached during air blast due to the denser fluid medium and reduced stand-off distance.

The post-blast modulus and strength of the air and underwater Hybrid-4 panels showed consistency. Undamaged specimen from each panel achieved similar properties. As damage percentage increased, the modulus and strength consistently decreased for both panels. Underwater blast loading results in a more severe load-

ing regime and hence more devastating damage than air blast loading. Post-blast damage inspection revealed that the Hybrid-4(2) samples with an intact front skin achieved a higher compressive modulus. However, since all samples sustained a variety of damage, the most detrimental damage type could not be identified.

The panel sucessfully withstood an underwater blast pressure of around 50 MPa without allowing water ingress. Although the pressure and strain gauges failed to trigger, informative DIC data was captured. This full-field DIC data will significantly aid in determining whether numerical underwater blast models are accuartely recreating the underwater blast phenomenon, including influence of water depth and cross-sectional deflection. Furthermore, it was demonstrated that instrumented blast tests can be conducted at a test range without specialised underwater testing facilities.

7.4 Future Work

This research has contributed to the current understanding of blast response of hybrid composite sandwich panels and new experimental techniques have been adopted to quantify the panel responses. The results and methods have revealed topics which would benefit from further research.

Recommended laboratory work includes investigating the interlaminar toughness of the hybrid composite skins. As detailed, delamination between the fibre types is an effective method for absorbing blast energy. The hybrid skins tested in these experiments have been selected based on qualitative failure predictions and subsequent failure identification using x-ray CT scanning. Quantification of the hybrid interlaminar toughness will be beneficial for numerical simulations of hybrid composite sandwich panels. Furthermore, an improved understanding of the hybrid interlaminar toughness could enable damage mechanisms to be predicted or even certain mechanisms to be promoted. X-ray CT analysis should be performed on specimen from all sandwich panels tested to compare the failure behaviour of the different hybrid types and when subjected to differing charges. Quantitative data should be extracted from the CT scans, such as area of debonding, area of delamination and extent of fibre breakage. Debonding between the laminate skins and foam core occurs extensively during blast loading. This debonding also absorbs blast energy, however, unstable debond propagation is detrimental to the panel for repeat blast or post-blast loading. Quantifying and improving the interface between the skins and core is a key area of investigation. This could be achieved by investigating

alternative core materials with properties which more closely match those of the skins.

The development of a soft projectile impact experiment is recommended. The use of a soft projectile will more closely simulate blast loading due to the increased load duration and more widespread area of impact. The experimental setup and panel dimensions could be altered such that a strain rate more representative of blast loading is achieved. The soft projectiles could be manufactured from metal foam, as used by Fleck and coworkers [28], or could be 3D printed polymers with a hollow internal structure. This experiment would be beneficial in providing laboratory based data that is more representative of blast loads. These impact experiments would help to make informed decisions for a reduced number of full-scale blast tests. Furthermore, PVDF film pressure sensors could be implemented to record the pressure signature delivered by the soft projectile and determine how closely it matches that of a blast load.

Progress in future blast experiments could be made. Test methods could be improved by rectifying the strain gauge recording issue at Radnor Range along with the underwater blast pressure gauge trigger. The data recorded by these gauges would have supplemented the DIC data. Aspects of the experiments, in particular the underwater blast, could be explained if gauge data had been recorded. Use of a cubicle with one centrally mounted panel is recommended. This would eliminate asymmetrical boundary conditions. Furthermore, bolting around the entire panel perimeter would result in consistent boundary conditions and prevent panel slip. Data gathering methods could be extended in future experiments by placing strain gauges between the skins and core. This would provide information on the through thickness response of the panels. The front and rear skin data captured a difference in strain magnitude. This energy absorption was attributed to the core. Through thickness strain monitoring would reveal whether this is indeed caused by the foam core. If underwater blast testing is carried out, a comparison of multiple panels should be performed. Additionally, the underwater blast experiment could be improved by using a reduced charge size. This would cause less catastrophic damage to the panel. Less intense loading would lead to a more elastic panel response, greater differences between the panel performances and hence more comparable data.

Extending the post-blast experiments carried out would be beneficial for further understanding how the different panels have stood up to blast loading. The damage sustained by the panels would be exacerbated by edgewise compression, which is why it was selected. However, this involves sectioning the panel. Following a blast

load, the whole panel would have to withstand loads. Edgewise compression testing of larger samples, or the whole panel, would be more representative of in service loads expected. A uniform pressure applied to the surface of the panel, or large sections of the panel, would reveal the remaining static bending strength of the panels. A rubber bladder filled with water or air could be loaded against the panel using a compression machine. Since the load is uniform, there is no single point of applied load dictating the likely location of failure. Instead, the results will reveal the post-blast bending stiffness of the entire panel.

The blast response of the entire structure deserves further research. As mentioned previously, the blast resilience of a structure is vastly improved if it is able to deform elastically under blast to some extent. The blast resilience of the composite sandwich panels can not be developed alone.

A major area for future development is FE modelling. Laboratory based experiments along with full scale blast tests are expensive and time consuming. The role of these experiments is to provide data such that reliable and accurate computational simulations can be developed. The findings presented in this thesis provide blast response results for validation of simulations. FE models which capture the elastic response of the panels have been sufficiently developed by other researchers [82]. However, in order to capture the panel response beyond peak deflection, damage models must be incorporated. This includes damage mechanisms in the laminate skins, debonding and core cracking. Accurately capturing these failures requires extensive material characterisation. However, the characterisation experiments and model development would be highly valuable. Once reliable FE models are created and validated, multiple experimental variables can be altered. This could include charge size, stand-off distance, panel geometry, boundary conditions, panel materials and layup. It is not possible to vary all these parameters experimentally due to the time and cost associated with such large scale experiments.

7.5 Research Impact

The research presented in this thesis has contributed to the knowledge base of composite sandwich material use in naval vessels. The outcomes have demonstrated the significant blast resilience possessed by composite sandwich panels. Hybrid laminate skins can absorb a significant amount of blast energy by allowing moderate panel deflection and permissible skin damage. Additional instrumentation used in these air blast experiments, film pressure gauges and strain gauges, have extended the

data captured compared to previous experimental work. A new underwater blast experiment implementing 3D DIC was devised. The results revealed the previously unknown deflection development, from a flat panel to the 'bath tub' deformation shape. Only one hybrid composite sandwich panel was subjected to underwater blast, however, the panel demonstrated significant blast resilience. Overall, the findings have provided quantitative comparisons of various sandwich constructions under blast loading and following blast. The results could be used to validate numerical or analytical simulations. The results would also be valuable for validating the models used in the design of a whole naval vessel.

References

[1] Kable, *Naval Technology: Visby Class*, 2018. [Online]. Available: https://www.naval-technology.com/projects/visby/.

[2] ——, *Naval Technology: La Fayette Class Frigate*. [Online]. Available: https://www.naval-technology.com/projects/lafayette/.

[3] ——, *Naval Technology: Type 45 Daring Class Destroyer*. [Online]. Available: https://www.naval-technology.com/projects/horizon/.

[4] ——, *Naval Technology: Skjold Class Missile Fast Patrol Boats, Norway*, 2018. [Online]. Available: http://www.naval-technology.com/projects/skjold.

[5] P. D. Smith and J. G. Hetherington, *Blast and ballistic loading of structures*. Butterworth-Heinemann, 1994, ISBN: 9780750620246.

[6] O. Gullberg and K. A. Olsson, "Design and construction of GRP sandwich ship hulls," *Marine Structures*, vol. 3, no. 2, pp. 93–109, Jan. 1990, ISSN: 0951-8339. DOI: 10.1016/0951-8339(90)90006-D.

[7] B. Hayman, "Underwater Explosion Response of Sandwich Structures with Compliant Cores," in *Blast Mitigation Strategies in Marine Composite and Sandwich Structures*, S. Gopalakrishnan and Y. Rajapakse, Eds., Singapore: Springer Singapore, 2018, pp. 23–52, ISBN: 978-981-10-7170-6. DOI: 10.1007/978-981-10-7170-6_2.

[8] A. P. Mouritz, E. Gellert, P. Burchill, and K. Challis, "Review of advanced composite structures for naval ships and submarines," *Composite Structures*, vol. 53, no. 1, pp. 21–42, 2001, ISSN: 0263-8223. DOI: http://dx.doi.org/10.1016/S0263-8223(00)00175-6.

[9] K. E. Mäkinen, S. E. Hellbratt, and K. A. Olsson, "The Development of Sandwich Structures for Naval Vessels During 25 Years," in *Mechanics of Sandwich Structures*, A. Vautrin, Ed., Dordrecht: Springer Netherlands, 1998, pp. 13–28, ISBN: 978-94-015-9091-4.

[10] D. Zenkert, A. Shipsha, P. Bull, and B. Hayman, "Damage tolerance assessment of composite sandwich panels with localised damage," *Composites Science and Technology*, vol. 65, pp. 2597–2611, Dec. 2005. DOI: 10.1016/j.compscitech.2005.05.026.

[11] L. J. Gibson and M. F. Ashby, *Cellular Solids*. Cambridge: Cambridge University Press, 1997, ISBN: 9781139878326. DOI: 10.1017/CBO9781139878326.

[12] D. A. Crowl, *Understanding Explosions*. Wiley, 2003.

[13] J. L. R. Comtois, M. R. Edwards, and M. C. Oakes, "The effect of explosives on polymer matrix composite laminates," *Composites Part A: Applied Science and Manufacturing*, vol. 30, no. 3, pp. 181–190, Mar. 1999, ISSN: 1359-835X. DOI: 10.1016/S1359-835X(98)00172-9.

[14] M. Y. Yahya, W. J. Cantwell, G. S. Langdon, and G. N. Nurick, "The Blast Behavior of Fiber Reinforced Thermoplastic Laminates," *Journal of Composite Materials*, vol. 42, no. 21, pp. 2275–2297, 2008. DOI: 10.1177/0021998308094968.

[15] ——, "The blast resistance of a woven carbon fiber-reinforced epoxy composite," *Journal of Composite Materials*, vol. 45, no. 7, pp. 789–801, 2011. DOI: 10.1177/0021998310376103.

[16] A. Gargano, K. Pingkarawat, M. Blacklock, V. Pickerd, and A. P. Mouritz, "Comparative assessment of the explosive blast performance of carbon and glass fibre-polymer composites used in naval ship structures," *Composite Structures*, vol. 171, pp. 306–316, Jul. 2017, ISSN: 0263-8223. DOI: 10.1016/J.COMPSTRUCT.2017.03.041.

[17] A. Kerber, A. Gargano, K. Pingkarawat, and A. P. Mouritz, "Explosive blast damage resistance of three-dimensional textile composites," *Composites Part A: Applied Science and Manufacturing*, vol. 100, pp. 170–182, Sep. 2017, ISSN: 1359-835X. DOI: 10.1016/J.COMPOSITESA.2017.05.005.

[18] T. Franz, G. N. Nurick, and M. J. Perry, "Experimental investigation into the response of chopped-strand mat glassfibre laminates to blast loading," *International Journal of Impact Engineering*, vol. 27, no. 6, pp. 639–667, Jul. 2002, ISSN: 0734-743X. DOI: 10.1016/S0734-743X(01)00158-0.

[19] H. Arora, "Blast loading of fibre reinforced polymer composite structures," PhD thesis, Imperial College London, 2012.

[20] M. Kelly, "Comparing the blast tolerance of different composite structures," PhD thesis, Imperial College London, 2016, p. 293.

[21] M. Kelly, H. Arora, A. Worley, M. Kaye, P. Del Linz, P. A. Hooper, and J. P. Dear, "Sandwich Panel Cores for Blast Applications: Materials and Graded Density," *Experimental Mechanics*, pp. 1–22, Apr. 2015, ISSN: 0014-4851. DOI: 10.1007/s11340-015-0058-5.

[22] G. S. Langdon, D. Karagiozova, C. J. von Klemperer, G. N. Nurick, A. Ozinsky, and E. G. Pickering, "The air-blast response of sandwich panels with composite face sheets and polymer foam cores: Experiments and predictions," *International Journal of Impact Engineering*, vol. 54, pp. 64–82, Apr. 2013, ISSN: 0734-743X. DOI: 10.1016/J.IJIMPENG.2012.10.015.

[23] S. A. Tekalur, K. Shivakumar, and A. Shukla, "Mechanical behavior and damage evolution in E-glass vinyl ester and carbon composites subjected to static and blast loads," *Composites Part B: Engineering*, vol. 39, no. 1, pp. 57–65, Jan. 2008, ISSN: 1359-8368. DOI: 10.1016/J.COMPOSITESB.2007.02.020.

[24] S. A. Tekalur, A. E. Bogdanovich, and A. Shukla, "Shock loading response of sandwich panels with 3-D woven E-glass composite skins and stitched foam core," *Composites Science and Technology*, vol. 69, no. 6, pp. 736–753, May 2009, ISSN: 0266-3538. DOI: 10.1016/J.COMPSCITECH.2008.03.017.

[25] E. Wang, N. Gardner, and A. Shukla, "The blast resistance of sandwich composites with stepwise graded cores," *International Journal of Solids and Structures*, vol. 46, no. 18-19, pp. 3492–3502, Sep. 2009, ISSN: 0020-7683. DOI: 10.1016/J.IJSOLSTR.2009.06.004.

[26] N. Gardner, E. Wang, P. Kumar, and A. Shukla, "Blast Mitigation in a Sandwich Composite Using Graded Core and Polyurea Interlayer," *Experimental Mechanics*, vol. 52, no. 2, pp. 119–133, Jan. 2012, ISSN: 0014-4851. DOI: 10.1007/s11340-011-9517-9.

[27] M. Hoo Fatt, X. Ouyang, and R. J. Dinan, "Blast response of walls retrofitted with elastomer coatings," *Structures under Shock and Impact VIII: Proceedings of the Eighth International Conference on Structures under Shock and Impact*, pp. 129–138, 2004.

[28] D. D. Radford, V. S. Deshpande, and N. A. Fleck, "The use of metal foam projectiles to simulate shock loading on a structure," *International Journal of Impact Engineering*, vol. 31, no. 9, pp. 1152–1171, 2005, ISSN: 0734743X. DOI: 10.1016/j.ijimpeng.2004.07.012.

[29] B. P. Russell, T. Liu, N. A. Fleck, and V. S. Deshpande, "The soft impact of composite sandwich beams with a square-honeycomb core," *International Journal of Impact Engineering*, vol. 48, pp. 65–81, 2012, ISSN: 0734743X. DOI: 10.1016/j.ijimpeng.2011.04.007.

[30] R. Panciroli and S. Abrate, "Dynamic response of sandwich shells to underwater blasts," *Central European Journal of Engineering*, vol. 2, no. 4, pp. 509–522, Dec. 2012, ISSN: 2081-9927. DOI: 10.2478/s13531-012-0024-2.

[31] F. Latourte, D. Grégoire, D. Zenkert, X. Wei, and H. D. Espinosa, "Failure mechanisms in composite panels subjected to underwater impulsive loads," *Journal of the Mechanics and Physics of Solids*, vol. 59, no. 8, pp. 1623–1646, 2011, ISSN: 0022-5096. DOI: http://dx.doi.org/10.1016/j.jmps.2011.04.013.

[32] J. LeBlanc and A. Shukla, "Dynamic response and damage evolution in composite materials subjected to underwater explosive loading: An experimental and computational study," *Composite Structures*, vol. 92, no. 10, pp. 2421–2430, 2010, ISSN: 0263-8223. DOI: http://dx.doi.org/10.1016/j.compstruct.2010.02.017.

[33] J. LeBlanc, N. Gardner, and A. Shukla, "Effect of polyurea coatings on the response of curved E-Glass/Vinyl ester composite panels to underwater explosive loading," *Composites Part B: Engineering*, vol. 44, no. 1, pp. 565–574, 2013, ISSN: 1359-8368. DOI: http://dx.doi.org/10.1016/j.compositesb.2012.02.038.

[34] S. Gupta, V. Parameswaran, M. A. Sutton, and A. Shukla, "Study of dynamic underwater implosion mechanics using digital image correlation," *Proceedings of the Royal Society A: Mathematical, Physical and Engineering Sciences*, vol. 470, no. 2172, p. 20 140 576, Dec. 2014. DOI: 10.1098/rspa.2014.0576.

[35] G. Caprino and R. Teti, "Impact and post-impact behavior of foam core sandwich structures," *Composite Structures*, vol. 29, no. 1, pp. 47–55, Jan. 1994, ISSN: 02638223. DOI: 10.1016/0263-8223(94)90035-3.

[36] F. Edgren, L. E. Asp, and P. H. Bull, "Compressive Failure of Impacted NCF Composite Sandwich Panels - Characterisation of the Failure Process," *Journal of Composite Materials*, vol. 38, no. 6, pp. 495–514, 2004. DOI: 10.1177/0021998304040559.

[37] H. Arora, M. Kelly, A. Worley, P. Del Linz, A. Fergusson, P. A. Hooper, and J. P. Dear, "Compressive strength after blast of sandwich composite materials," *Philosophical Transactions of the Royal Society of London A: Mathematical, Physical and Engineering Sciences*, vol. 372, no. 2015, Jul. 2014.

[38] E. Rolfe, M. Kelly, H. Arora, P. A. Hooper, and J. P. Dear, "Failure analysis using X-ray computed tomography of composite sandwich panels subjected to full-scale blast loading," *Composites Part B*, vol. 129, pp. 26–40, 2017, ISSN: 1359-8368. DOI: 10.1016/j.compositesb.2017.07.022.

[39] Y. Swolfs, L. Gorbatikh, and I. Verpoest, "Fibre hybridisation in polymer composites: A review," *Composites Part A: Applied Science and Manufacturing*, vol. 67, pp. 181–200, 2014, ISSN: 1359835X. DOI: 10.1016/j.compositesa.2014.08.027.

[40] A. Shindo, "130. On the carbonization of polyacrylonitrile fiber," *Carbon*, vol. 1, no. 3, pp. 391–392, Apr. 1964, ISSN: 0008-6223. DOI: 10.1016/0008-6223(64)90421-X.

[41] M. M. Tang and R. Bacon, "Carbonization of cellulose fibers—I. Low temperature pyrolysis," *Carbon*, vol. 2, no. 3, pp. 211–220, Dec. 1964, ISSN: 0008-6223. DOI: 10.1016/0008-6223(64)90035-1.

[42] P. W. Manders and M. G. Bader, "The strength of hybrid glass/carbon fibre composites," *Journal of Materials Science*, vol. 16, no. 8, pp. 2233–2245, 1981, ISSN: 1573-4803. DOI: 10.1007/BF00542386.

[43] G. Kretsis, "A review of the tensile, compressive, flexural and shear properties of hybrid fibre-reinforced plastics," *Composites*, vol. 18, no. 1, pp. 13–23, Jan. 1987, ISSN: 0010-4361. DOI: 10.1016/0010-4361(87)90003-6.

[44] C. Zweben, "Tensile strength of hybrid composites," *Journal of Materials Science*, vol. 12, no. 7, pp. 1325–1337, Jul. 1977, ISSN: 1573-4803. DOI: 10.1007/BF00540846.

[45] S. Pimenta and S. T. Pinho, "Hierarchical scaling law for the strength of composite fibre bundles," *Journal of the Mechanics and Physics of Solids*, vol. 61, no. 6, pp. 1337–1356, Jun. 2013, ISSN: 0022-5096. DOI: 10.1016/J.JMPS.2013.02.004.

[46] R. Murugan, R. Ramesh, and K. Padmanabhan, "Investigation on static and dynamic mechanical properties of epoxy based woven fabric glass/carbon hybrid composite laminates," *Procedia Engineering*, vol. 97, pp. 459–468, 2014, ISSN: 18777058. DOI: 10.1016/j.proeng.2014.12.270.

[47] J. H. Song, "Pairing effect and tensile properties of laminated high- performance hybrid composites prepared using carbon/glass and carbon/aramid fibers," *Composites Part B: Engineering*, vol. 79, pp. 61–66, 2015, ISSN: 13598368. DOI: 10.1016/j.compositesb.2015.04.015.

[48] J. W. Giancaspro, C. G. Papakonstantinou, and P. N. Balaguru, "Flexural Response of Inorganic Hybrid Composites With E-Glass and Carbon Fibers," *Journal of Engineering Materials and Technology*, vol. 132, no. 2, pp. 021005–021005–8, Feb. 2010, ISSN: 0094-4289.

[49] S. Abrate, Ed., *Impact engineering of composite structures*, eng, ser. CISM courses and lectures ; no. 526. Wien: Springer, 2011, ISBN: 9783709105221.

[50] A. Enfedaque, J. M. Molina-Aldareguía, F. Gálvez, C. González, and J. LLorca, "Effect of Glass Fiber Hybridization on the Behavior Under Impact of Woven Carbon Fiber/Epoxy Laminates," *Journal of Composite Materials*, vol. 44, no. 25, pp. 3051–3068, 2010. DOI: 10.1177/0021998310369602.

[51] E. Sevkat, B. Liaw, F. Delale, and B. B. Raju, "Drop-weight impact of plain-woven hybrid glass–graphite/ toughened epoxy composites," *Composites Part A: Applied Science and Manufacturing*, vol. 40, no. 8, pp. 1090–1110, Aug. 2009, ISSN: 1359-835X. DOI: 10.1016/J.COMPOSITESA.2009.04.028.

[52] C. Pavithran, P. S. Mukherjee, M. Brahmakumar, and A. D. Damodaran, "Impact properties of sisal-glass hybrid laminates," *Journal of Materials Science*, vol. 26, no. 2, pp. 455–459, Jan. 1991, ISSN: 1573-4803. DOI: 10.1007/BF00576542.

[53] E. Sevkat, B. Liaw, F. Delale, and B. B. Raju, "Effect of repeated impacts on the response of plain-woven hybrid composites," *Composites Part B: Engineering*, vol. 41, no. 5, pp. 403–413, Jul. 2010, ISSN: 1359-8368. DOI: 10.1016/J.COMPOSITESB.2010.01.001.

[54] R. Park and J. Jang, "Effect of laminate geometry on impact performance of aramid fiber/ polyethylene fiber hybrid composites," *Journal of applied polymer science*, vol. 75, no. 7, pp. 952–959, 2000, ISSN: 0021-8995.

[55] A. A. J. M. Peijs and R. W. Venderbosch, "Hybrid composites based on polyethylene and carbon fibres Part IV Influence of hybrid design on impact strength," *Journal of Materials Science Letters*, vol. 10, no. 19, pp. 1122–1124, Jan. 1991, ISSN: 1573-4811. DOI: 10.1007/BF00744101.

[56] G. Czél and M. R. Wisnom, "Demonstration of pseudo-ductility in high performance glass/epoxy composites by hybridisation with thin-ply carbon prepreg," *Composites Part A: Applied Science and Manufacturing*, vol. 52, pp. 23–30, 2013, ISSN: 1359835X. DOI: 10.1016/j.compositesa.2013.04.006.

[57] K. S. Pandya, J. R. Pothnis, G. Ravikumar, and N. K. Naik, "Ballistic impact behavior of hybrid composites," *Materials and Design*, vol. 44, pp. 128–135, 2013, ISSN: 0261-3069. DOI: 10.1016/j.matdes.2012.07.044.

[58] P. R. S. Reddy, T. S. Reddy, K. Mogulanna, I. Srikanth, V. Madhu, and K. V. Rao, "Ballistic Impact Studies on Carbon and E-glass Fibre Based Hybrid Composite Laminates," *Procedia Engineering*, vol. 173, pp. 293–298, Jan. 2017, ISSN: 1877-7058. DOI: 10.1016/J.PROENG.2016.12.017.

[59] E. Randjbaran, R. Zahari, N. A. Abdul Jalil, and D. L. Abang Abdul Majid, "Hybrid composite laminates reinforced with kevlar/ carbon/ glass woven fabrics for ballistic impact testing.," *The Scientific World Journal*, vol. 2014, p. 413 753, 2014, ISSN: 1537-744X. DOI: 10.1155/2014/413753.

[60] K. Karthikeyan, B. P. Russell, N. A. Fleck, M. O. Masta, H. N. G. Wadley, and V. S. Deshpande, "The soft impact response of composite laminate beams," *International Journal of Impact Engineering*, vol. 60, pp. 24–36, 2013, ISSN: 0734-743X. DOI: 10.1016/j.ijimpeng.2013.04.002.

[61] A. S. Fallah, K. Micallef, G. S. Langdon, W. C. Lee, P. T. Curtis, and L. A. Louca, "Dynamic response of Dyneema® HB26 plates to localised blast loading," *International Journal of Impact Engineering*, vol. 73, pp. 91–100, 2014, ISSN: 0734743X. DOI: 10.1016/j.ijimpeng.2014.06.014.

[62] L. Librescu, S. Y. Oh, and J. Hohe, "Linear and non-linear dynamic response of sandwich panels to blast loading," *Composites Part B: Engineering*, vol. 35, no. 6-8, pp. 673–683, Sep. 2004, ISSN: 1359-8368. DOI: 10.1016/J.COMPOSITESB.2003.07.003.

[63] T. Hause and L. Librescu, "Dynamic response of anisotropic sandwich flat panels to explosive pressure pulses," *International Journal of Impact Engineering*, vol. 31, no. 5, pp. 607–628, May 2005, ISSN: 0734-743X. DOI: 10.1016/J.IJIMPENG.2004.01.002.

[64] L. Librescu, S. Y. Oh, and J. Hohe, "Dynamic response of anisotropic sandwich flat panels to underwater and in-air explosions," *International Journal of Solids and Structures*, vol. 43, no. 13, pp. 3794–3816, Jun. 2006, ISSN: 0020-7683. DOI: 10.1016/J.IJSOLSTR.2005.03.052.

[65] J. Hohe and L. Librescu, "Recent results on the effect of the transverse core compressibility on the static and dynamic response of sandwich structures," *Composites Part B: Engineering*, vol. 39, no. 1, pp. 108–119, Jan. 2008, ISSN: 1359-8368. DOI: 10.1016/J.COMPOSITESB.2007.02.007.

[66] E. W. Andrews and N. A. Moussa, "Failure mode maps for composite sandwich panels subjected to air blast loading," *International Journal of Impact Engineering*, vol. 36, no. 3, pp. 418–425, Mar. 2009, ISSN: 0734743X. DOI: 10.1016/j.ijimpeng.2008.08.005.

[67] G. A. Kardomateas, Y. Frostig, and C. N. Phan, "Dynamic Elasticity Solution for the Transient Blast Response of Sandwich Beams/Wide Plates," *AIAA Journal*, vol. 51, no. 2, pp. 485–491, Dec. 2012, ISSN: 0001-1452. DOI: 10.2514/1.J051885.

[68] C. N. Phan, G. A. Kardomateas, and Y. Frostig, "Blast Response of a Sandwich Beam/Wide Plate Based on the Extended High-Order Sandwich Panel Theory and Comparison With Elasticity," *Journal of Applied Mechanics*, vol. 80, no. 6, pp. 061005–061005–11, Aug. 2013, ISSN: 0021-8936.

[69] R. Li, G. A. Kardomateas, and G. J. Simitses, "Nonlinear Response of a Shallow Sandwich Shell With Compressible Core to Blast Loading," *Journal of Applied Mechanics*, vol. 75, no. 6, pp. 061023–061023–10, Aug. 2008, ISSN: 0021-8936.

[70] R. Li and G. A. Kardomateas, "Nonlinear High-Order Core Theory for Sandwich Plates with Orthotropic Phases," *AIAA Journal*, vol. 46, no. 11, pp. 2926–2934, Nov. 2008, ISSN: 0001-1452. DOI: 10.2514/1.37430.

[71] Z. Yuan and G. A. Kardomateas, "Nonlinear dynamic response of sandwich wide panels," *International Journal of Solids and Structures*, vol. 148-149, pp. 110–121, Sep. 2018, ISSN: 0020-7683. DOI: 10.1016/J.IJSOLSTR.2017.09.028.

[72] V. Birman and G. A. Kardomateas, "Review of current trends in research and applications of sandwich structures," *Composites Part B: Engineering*, vol. 142, pp. 221–240, Jun. 2018, ISSN: 1359-8368. DOI: 10.1016/J.COMPOSITESB.2018.01.027.

[73] M. S. Hoo Fatt and L. Palla, "Analytical Modeling of Composite Sandwich Panels under Blast Loads," *Journal of Sandwich Structures & Materials*, vol. 11, no. 4, pp. 357–380, 2009. DOI: 10.1177/1099636209104515.

[74] M. S. Hoo Fatt and D. Sirivolu, "Blast response of double curvature, composite sandwich shallow shells," *Engineering Structures*, vol. 100, pp. 696–706, Oct. 2015, ISSN: 0141-0296. DOI: 10.1016/J.ENGSTRUCT.2015.06.054.

[75] M. Z. Hassan, Z. W. Guan, W. J. Cantwell, G. S. Langdon, and G. N. Nurick, "The influence of core density on the blast resistance of foam-based sandwich structures," *International Journal of Impact Engineering*, vol. 50, pp. 9–16, Dec. 2012, ISSN: 0734-743X. DOI: 10.1016/J.IJIMPENG.2012.06.009.

[76] Z. W. Guan, A. Aktas, P. Potluri, W. J. Cantwell, G. Langdon, and G. N. Nurick, "The blast resistance of stitched sandwich panels," *International Journal of Impact Engineering*, vol. 65, pp. 137–145, Mar. 2014, ISSN: 0734-743X. DOI: 10.1016/J.IJIMPENG.2013.12.001.

[77] V. Tagarielli, V. Deshpande, and N. Fleck, "Prediction of the dynamic response of composite sandwich beams under shock loading," *International Journal of Impact Engineering*, vol. 37, no. 7, pp. 854–864, Jul. 2010, ISSN: 0734-743X. DOI: 10.1016/J.IJIMPENG.2009.11.008.

[78] S. Hong and J. McConnell, "Influences of Material Properties on Energy Absorption of Composite Sandwich Panels under Blast Loads," *Journal of Composites for Construction*, vol. 16, no. 4, pp. 464–476, Aug. 2012. DOI: 10.1061/(ASCE)CC.1943-5614.0000269.

[79] Y. A. Bahei-El-Din, G. J. Dvorak, and O. J. Fredricksen, "A blast-tolerant sandwich plate design with a polyurea interlayer," *International Journal of Solids and Structures*, vol. 43, no. 25-26, pp. 7644–7658, Dec. 2006, ISSN: 0020-7683. DOI: 10.1016/J.IJSOLSTR.2006.03.021.

[80] Y. A. Bahei-El-Din and G. J. Dvorak, "Enhancement of blast resistance of sandwich plates," *Composites Part B: Engineering*, vol. 39, no. 1, pp. 120–127, Jan. 2008, ISSN: 1359-8368. DOI: 10.1016/J.COMPOSITESB.2007.02.006.

[81] H. Arora, P. Hooper, P. Del Linz, H. Yang, S. Chen, and J. P. Dear, "Modelling the behaviour of composite sandwich structures when subject to air-blast loading," *The International Journal of Multiphysics*, vol. 6, pp. 199–218, 2012. DOI: 10.1260/1750-9548.6.3.199.

[82] H. Arora, P. Del Linz, and J. P. Dear, "Damage and deformation in composite sandwich panels exposed to multiple and single explosive blasts," *International Journal of Impact Engineering*, vol. 104, pp. 95–106, Jun. 2017, ISSN: 0734-743X. DOI: 10.1016/J.IJIMPENG.2017.01.017.

[83] A. Schiffer and V. Tagarielli, "The dynamic response of composite plates to underwater blast: Theoretical and numerical modelling," *International Journal of Impact Engineering*, vol. 70, pp. 1–13, Aug. 2014, ISSN: 0734-743X. DOI: 10.1016/J.IJIMPENG.2014.03.002.

[84] A. Schiffer and V. L. Tagarielli, "One-dimensional response of sandwich plates to underwater blast: Fluid-structure interaction experiments and simulations," *International Journal of Impact Engineering*, vol. 71, pp. 34–49, Sep. 2014, ISSN: 0734-743X. DOI: 10.1016/J.IJIMPENG.2014.04.001.

[85] A. Schiffer and V. Tagarielli, "The response of circular composite plates to underwater blast: Experiments and modelling," *Journal of Fluids and Structures*, vol. 52, pp. 130–144, Jan. 2015, ISSN: 0889-9746. DOI: 10.1016/J.JFLUIDSTRUCTS.2014.10.009.

[86] A. Schiffer and V. L. Tagarielli, "Underwater blast loading of water-backed sandwich plates with elastic cores: Theoretical modelling and simulations," *International Journal of Impact Engineering*, vol. 102, pp. 62–73, Apr. 2017, ISSN: 0734-743X. DOI: 10.1016/J.IJIMPENG.2016.11.014.

[87] M. S. Hoo Fatt and D. Sirivolu, "Marine composite sandwich plates under air and water blasts," *Marine Structures*, vol. 56, pp. 163–185, Nov. 2017, ISSN: 0951-8339. DOI: 10.1016/J.MARSTRUC.2017.08.004.

[88] X. Wei, P. Tran, A. De Vaucorbeil, R. B. Ramaswamy, F. Latourte, and H. D. Espinosa, "Three-dimensional numerical modeling of composite panels subjected to underwater blast," *Journal of the Mechanics and Physics of Solids*, vol. 61, no. 6, pp. 1319–1336, 2013. DOI: 10.1016/j.jmps.2013.02.007.

[89] G. S. Langdon, W. J. Cantwell, Z. W. Guan, and G. N. Nurick, "The response of polymeric composite structures to air-blast loading: a state-of-the-art," *International Materials Reviews*, vol. 59, no. 3, pp. 159–177, Apr. 2014, ISSN: 0950-6608. DOI: 10.1179/1743280413Y.0000000028.

[90] F. L. Matthews, *Composite materials : engineering and science*. Boca Raton : Cambridge: CRC Press ; Woodhead Publishing Ltd., 2002, ISBN: 1855734737.

[91] L. Iannucci, "Progressive failure modelling of woven carbon composite under impact," *International Journal of Impact Engineering*, vol. 32, pp. 1013–1043, 2006, ISSN: 0734-743X. DOI: 10.1016/j.ijimpeng.2004.08.006.

[92] M. V. Donadon, L. Iannucci, B. G. Falzon, J. M. Hodgkinson, and S. F. M. de Almeida, "A progressive failure model for composite laminates subjected to low velocity impact damage," *Computers & Structures*, vol. 86, pp. 1232–1252, 2008, ISSN: 0045-7949. DOI: 10.1016/j.compstruc.2007.11.004.

[93] A. Faggiani and B. G. Falzon, "Predicting low-velocity impact damage on a stiffened composite panel," *Composites Part A: Applied Science and Manufacturing*, vol. 41, pp. 737–749, 2010, ISSN: 1359-835X. DOI: 10.1016/j.compositesa.2010.02.005.

[94] A. T. Nettles, "Basic Mechanics of Laminated Composite Plates," NASA, Alabama, Tech. Rep., 1994.

[95] J. M. Bertholet, *Composite materials : mechanical behavior and structural analysis*, ser. Mechanical engineering series. New York ; London: Springer, 1999, ISBN: 0387984267.

[96] Granda Design Limited, *CES EduPack 2018*, 2018.

[97] Gurit, "Gurit Product Catalogue - Europe, Middle East and Africa - GPC-22-0216," no. January, pp. 1–97, 2018.

[98] ——, *Datasheet/PRIME^{TM} 20LV*, 2015.

[99] E. Rolfe, C. Kaboglu, R. Quinn, P. A. Hooper, H. Arora, and J. P. Dear, "High velocity impact and blast loading of composite sandwich panels with novel carbon and glass construction," *Journal of Dynamic Behavior of Materials*, 2018.

[100] Armacell, "ArmaForm Core ®," 2018.

[101] GOM GmbH, "User Manual Hardware ARAMIS Adjustable Base 6M," Tech. Rep. 1, 2016.

[102] M. A. Sutton, *Image correlation for shape, motion and deformation measurements : basic concepts, theory and applications*. New York: Springer, 2009, ISBN: 9780387787466.

[103] M. S. Rajput, M. Burman, and S. Hallstroem, "Impact resistance and damage tolerance assessment of composite sandwich materials for aircraft," in *12th International Conference on Sandwich Structures (ICSS-12)*, vol. 1, 2018, pp. 261–263. DOI: 10.5075/epfl-ICSS12-2018-261-263.

[104] E. Rolfe, R. Quinn, A. Sancho, C. Kaboglu, A. Johnson, H. Liu, P. A. Hooper, J. P. Dear, and H. Arora, "Blast resilience of composite sandwich panels with hybrid glass-fibre and carbon-fibre skins," *Multiscale and Multidisciplinary Modeling, Experiments and Design*, vol. 1, no. 3, pp. 197–210, 2018, ISSN: 2520-8160. DOI: 10.1007/s41939-018-0025-9.

[105] Hexcel, "Hexcel HexTow AS4 Carbon Fiber Data Sheet," vol. 000, pp. 1–2, 2018.

[106] Sicomin Epoxy Systems, "SR 8100," vol. 100, no. 0, pp. 1–7, 2014.

[107] Diab Group, "Divinycell H Technical Data," vol. 1, no. 2, p. 132, 2018, ISSN: 10004750. DOI: 10.1016/j.clinph.2009.04.024.Identification.

[108] S. Forth, "ProSAir 2018.4 User Guide," 2018.

[109] T. A. Rose, "A computational tool for air blast calculations: Air3d version 9 users' guide.," 2006.

[110] VishayPG, "The Three-Wire Quarter-Bridge Circuit TT-612," 2015.

[111] K. Hoffmann, "Applying the wheatstone bridge circuit," Hottinger Baldwin Messtechnik GmbH, Tech. Rep., 2001. DOI: 10.1016/0029-554X(78)90136-2.

[112] TorayCA, "Technical Data Sheet No. CFA-005 T700S Data Sheet," pp. 6–7,

[113] R. H. Cole, *Underwater Explosions*. Princeton: Princeton University Press, 1948.

Appendix A

Supplementary Data

This Appendix presents additional digital image correlation (DIC) data which supplements the data and findings detailed in the main body of the thesis. A test matrix detailing the panel types used within each experiment is also included.

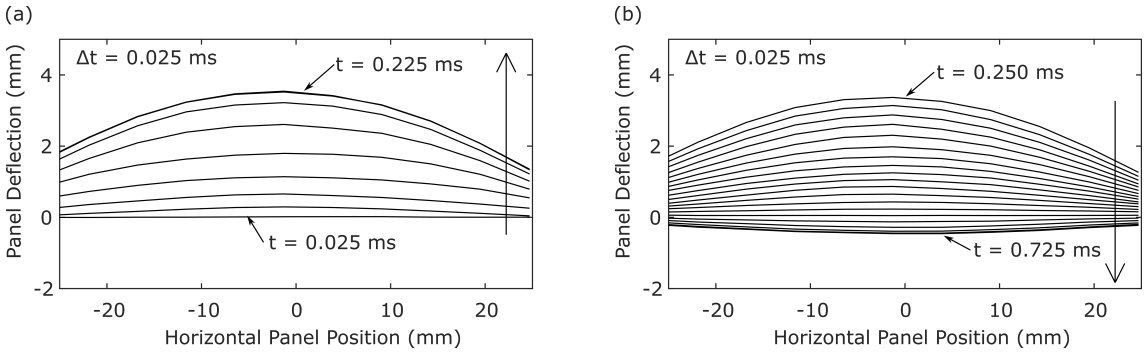


Figure A.1: Central horizontal cross-section of Hybrid-1B panel showing: (a) outward out-of-plane deflection and (b) panel return under impact velocity 75 ± 3 m s^{-1}.

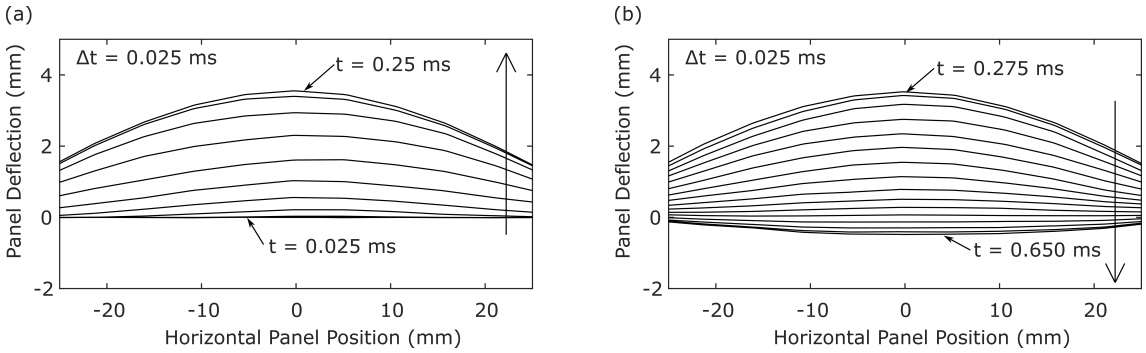


Figure A.2: Central horizontal cross-section of Hybrid-3B panel showing: (a) outward out-of-plane deflection and (b) panel return under impact velocity 75 ± 3 m s^{-1}.

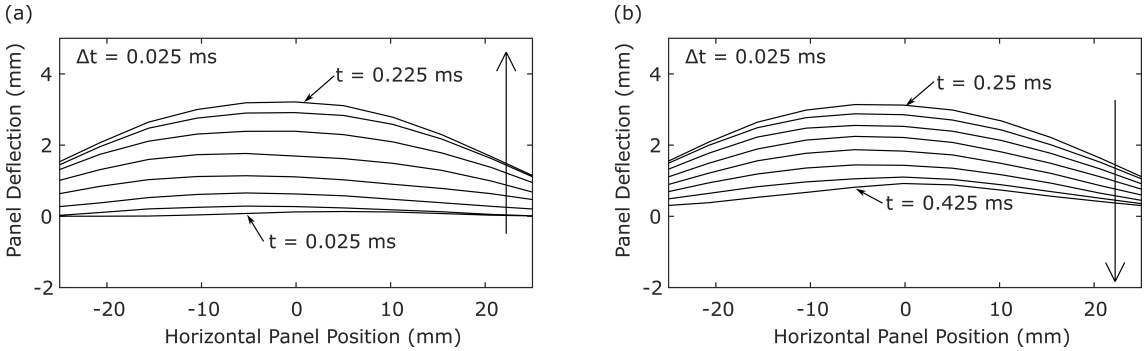


Figure A.3: Central horizontal cross-section of Hybrid-1B panel showing: (a) outward out-of-plane deflection and (b) panel return under impact velocity 90 ± 3 m s^{-1}.

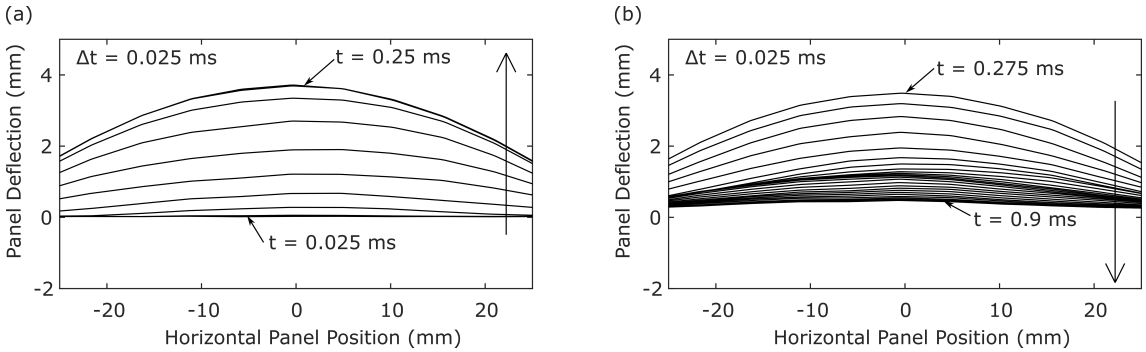


Figure A.4: Central horizontal cross-section of Hybrid-3B panel showing: (a) outward out-of-plane deflection and (b) panel return under impact velocity 90 ± 3 m s^{-1}.

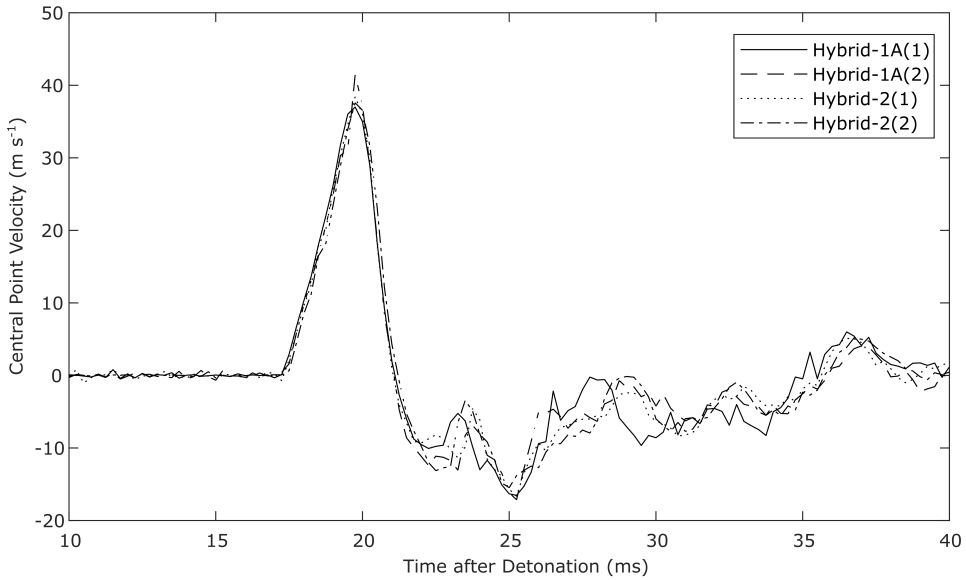


Figure A.5: Central out-of-plane velocity against time for the four composite sandwich panels under 100 kg nitromethane charge at 15 m stand-off.

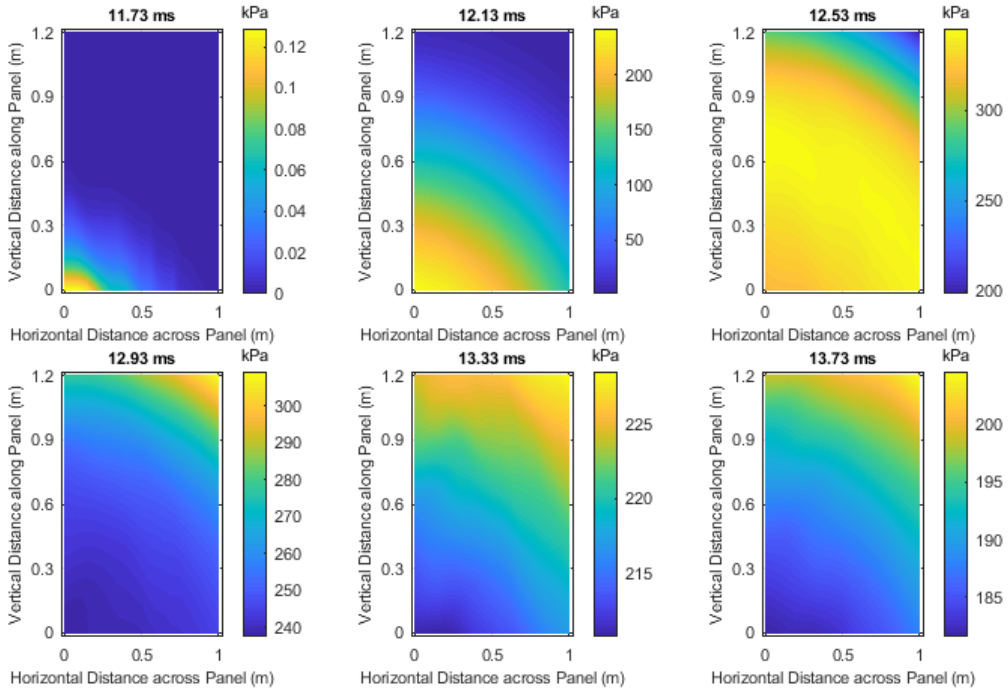


Figure A.6: Comparison of reflected overpressure distribution across the panel for 30 kg PE4 at 10.5 m stand-off with pendine blocks and roof extension.

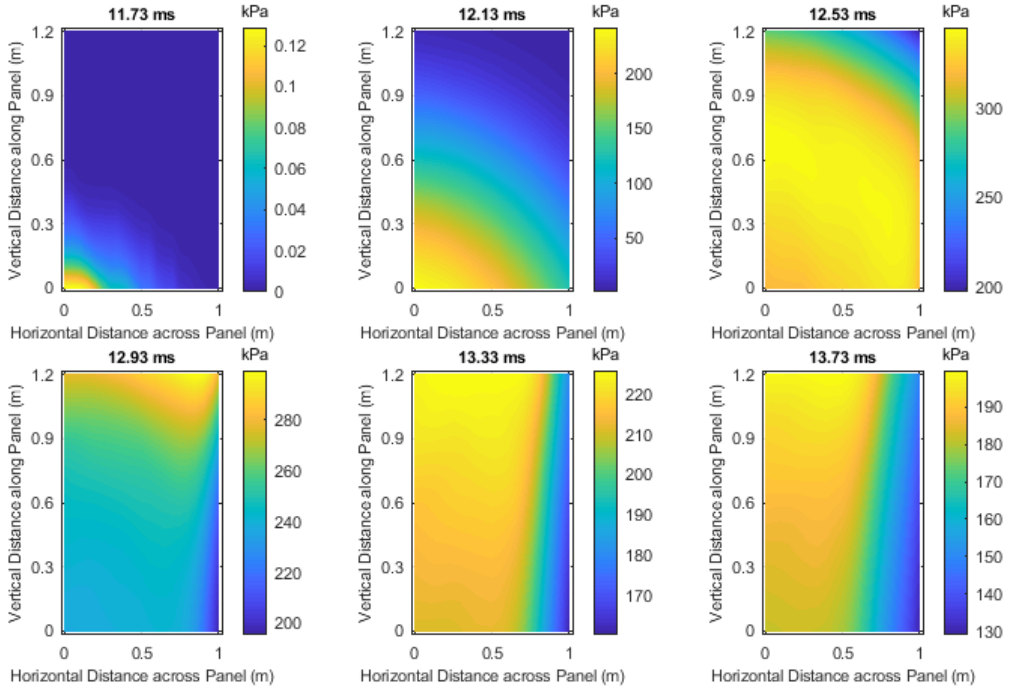


Figure A.7: Comparison of reflected overpressure distribution across the panel for 30 kg PE4 at 10.5 m stand-off without pendine blocks and roof extension.

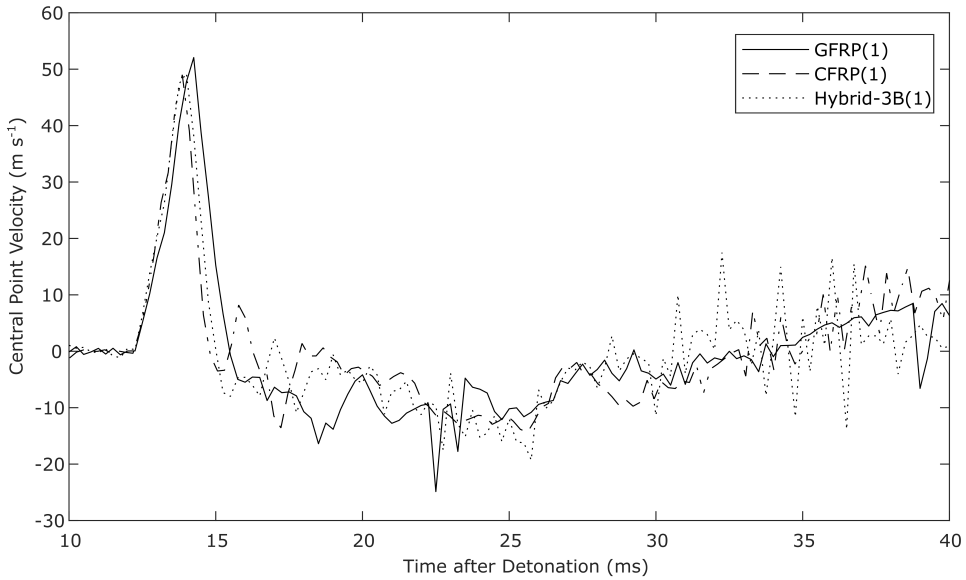


Figure A.8: Central out-of-plane velocity against time for the three composite sandwich panels under 30 kg PE4 charge at 10.5 m stand-off.

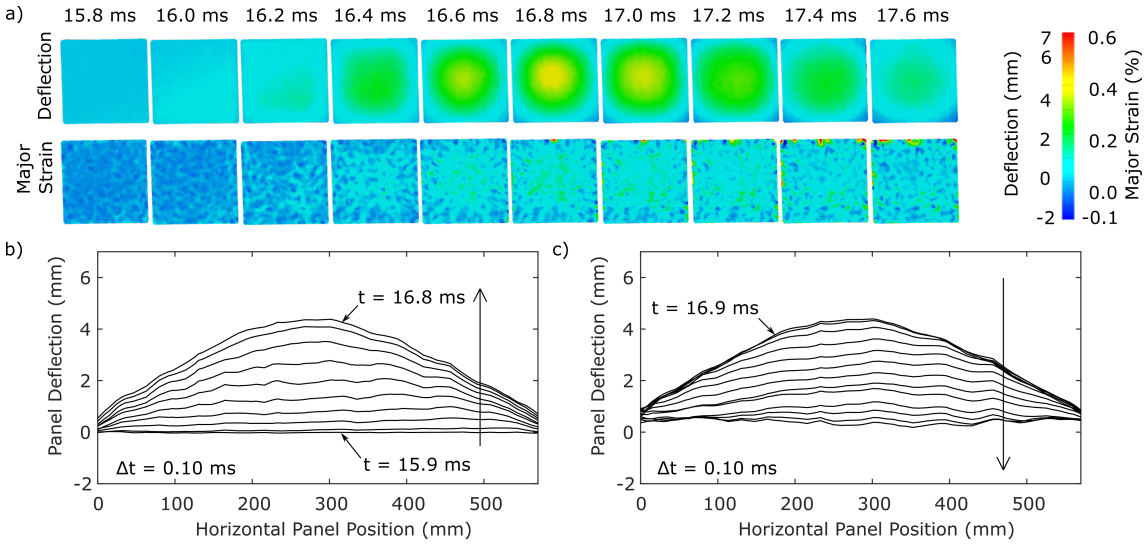


Figure A.9: DIC results for CFRP(2) under the first 8 kg PE7 charge showing: (a) out-of-plane displacement and major strain images, (b) deflection at time intervals for the horizontal centre section and (c) rebound at time intervals for the horizontal centre section.

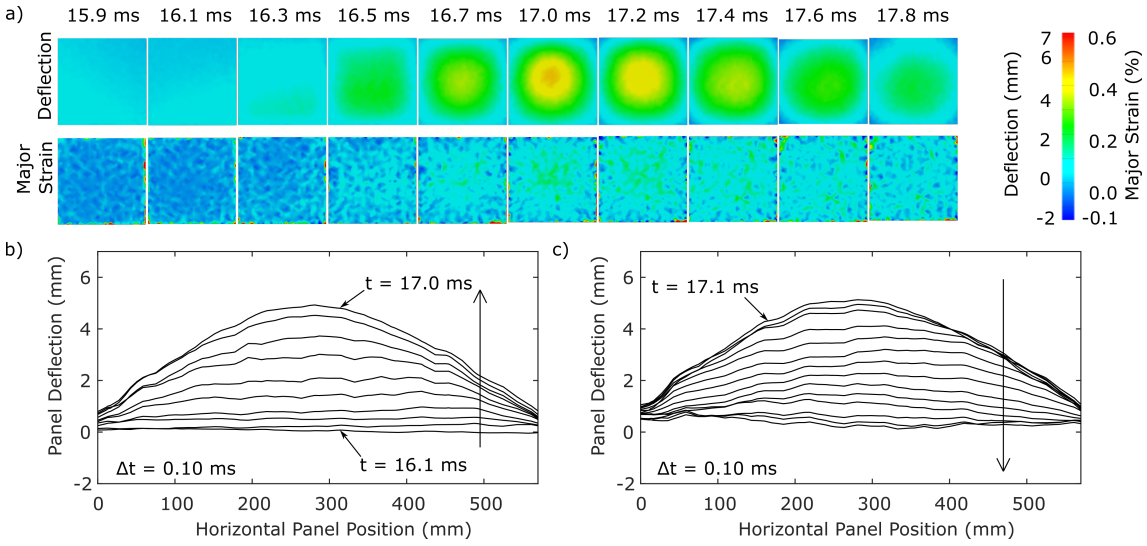


Figure A.10: DIC results for CFRP(2) under the second 8 kg PE7 charge showing: (a) out-of-plane displacement and major strain images, (b) deflection at time intervals for the horizontal centre section and (c) rebound at time intervals for the horizontal centre section.

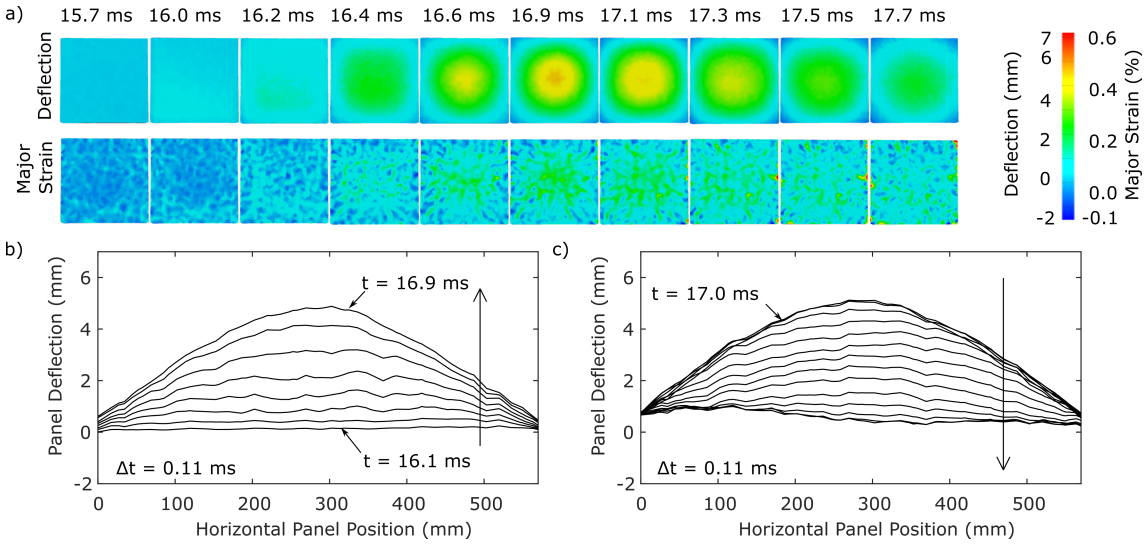


Figure A.11: DIC results for GFRP(2) under the first 8 kg PE7 charge showing: (a) out-of-plane displacement and major strain images, (b) deflection at time intervals for the horizontal centre section and (c) rebound at time intervals for the horizontal centre section.

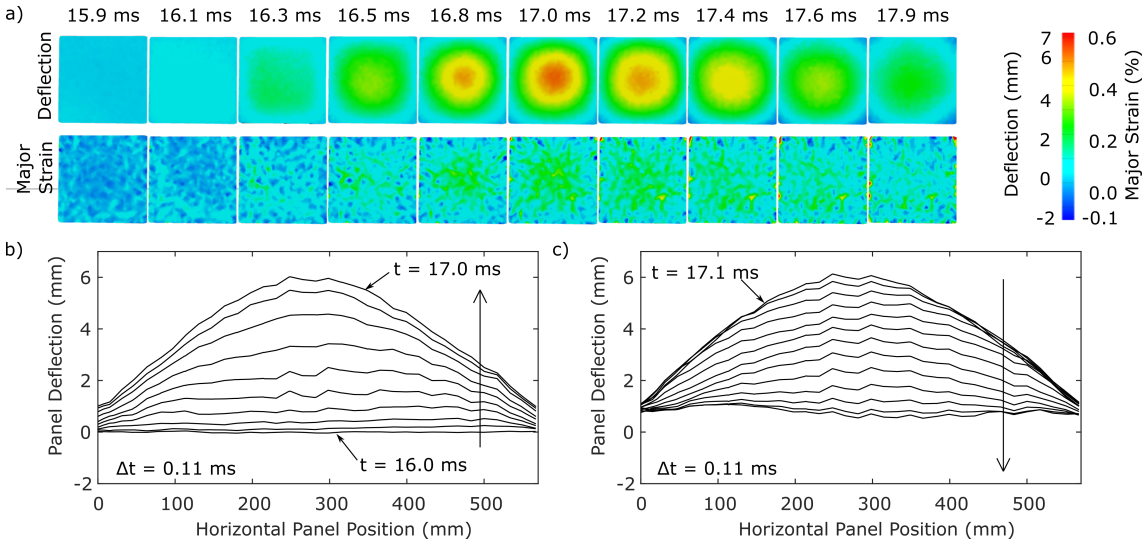


Figure A.12: DIC results for GFRP(2) under the second 8 kg PE7 charge showing: (a) out-of-plane displacement and major strain images, (b) deflection at time intervals for the horizontal centre section and (c) rebound at time intervals for the horizontal centre section.

Table A.1: Test matrix detailing hybrid panel types in each experimental investigation.

Panel type	Panel stiffness calculation	High velocity impact	Air Blast 1	Air Blast 2: Test Series A	Air Blast 2: Test Series B	Underwater blast
GFRP	✓	✓		✓	✓	
CFRP	✓	✓		✓	✓	
Hybrid-1A	✓	✓	✓			
Hybrid-1B	✓	✓				
Hybrid-2	✓	✓	✓			
Hybrid-3A						
Hybrid-3B	✓	✓		✓	✓	
Hybrid-4					✓	✓

Appendix B

Digital Image Correlation Uncertainty

3D DIC was used throughout the experimental methods to obtain test measurements. The uncertainties associated with the DIC measurements were calculated by assessing the noise in the DIC data before projectile impact or blast wave arrival. A number of high-speed camera images were saved during the pre-trigger which makes this possible. The noise in these pre-trigger images accounts for uncertainty in the DIC calculations as well as errors caused by the nature of the field experiments such as wind loading the sandwich panels. The maximum deviation from 0 mm displacement or 0 % major strain during the pre-trigger images was recorded for each set of images. Since a number of different camera models, mounting methods and fields of view were used during the experiments, there is some variation in the uncertainty. Table B.1 summarises the conservative uncertainty estimates for out-of-plane displacement and major strain. There were two trials, however, with greater uncertainties than those detailed in Table B.1. Hybrid-1A under high velocity impact demonstrated a deflection uncertainty of ± 0.05 mm and an increased major strain uncertainty of ± 0.24 %. Additionally, during Air Blast Part 2: Trial B, Hybrid-4(1) demonstrated an increased deflection uncertainty of ± 3.10 mm and a major strain uncertainty of ± 0.50 %.

Table B.1: Summary of the uncertainty estimates for out-of-plane displacement and major strain.

Experimental Trial	Deflection uncertainty (mm)	Major strain uncertainty (%)
High Velocity Impact	±0.05	±0.17
Air Blast Part 1	±0.65	±0.37
Air Blast Part 2: Trial A	±2.85	±0.59
Air Blast Part 2: Trial B	±0.40	±0.50